

Flamelet/Progress Variable Modeling for a Dual-Mode Scramjet Combustor

---

A Dissertation

Presented to  
the faculty of the School of Engineering and Applied Science  
University of Virginia

---

in partial fulfillment  
of the requirements for the degree

Doctor of Philosophy

by

Jesse R. Quinlan

August

2015



## APPROVAL SHEET

The dissertation  
is submitted in partial fulfillment of the requirements  
for the degree of  
Doctor of Philosophy  
in  
Mechanical and Aerospace Engineering

---

Jesse R. Quinlan, Author

The dissertation has been read and approved by the examining committee:

---

James McDaniel, Dissertation Advisor

---

Harsha Chelliah, Committee Chair

---

Christopher Goynes, Committee Member

---

Robert Ribando, Committee Member

---

George Cahen, Committee Member

---

Tomasz Drozda, Committee Member

Accepted for the School of Engineering and Applied Science:



---

Dean, School of Engineering and Applied Science

August  
2015



© 2015 Jesse R. Quinlan

All rights reserved.



UNIVERSITY OF VIRGINIA

# *Abstract*

Department of Mechanical and Aerospace Engineering

Doctor of Philosophy

## **Flamelet/Progress Variable Modeling for a Dual-Mode Scramjet Combustor**

by Jesse R. Quinlan

Hypersonic air-breathing propulsion technologies hold great promise for revolutionizing America's means of accessing space. However, the successful design of hypersonic propulsion systems is hindered by simulation and modeling capabilities. These limitations are most problematic for dual-mode scramjet engines, for which a single engine flowpath may support both dual-mode (i.e. primarily subsonic combustion) and scram-mode (i.e. primarily supersonic combustion) operation. For these engines, the isolator and combustor flowfields may contain a complex shock train, shock-boundary-layer interactions, and large regions of separated flow. Combustion processes are tightly-coupled to the fluid mechanics and are often mixing-limited. It is especially important that designers understand the effect of these phenomena on the flow and combustion physics in order to guarantee vehicle operability. Experimental investigations of these combustors are constrained by technology and affordability limitations, and as a result, computational studies must serve an integral role in the engine design and analysis process, at both the conceptual level and the detailed, flight-experiment level. The current dissertation addresses the problem of accurately and affordably simulating the combustion physics for a dual-mode scramjet combustor of engineering-complexity.

To significantly reduce the computational costs, the state-of-the-practice in combustion modeling for practical devices is to reduce the detailed chemical kinetics to a single step mechanism, such as through the use of a global reaction or the eddy dissipation concept. While these approaches require low computational overhead, these models could be at most relied upon to produce only qualitative representations of scramjet flowfields. Alternatively, state-of-the-art approaches typically involve closing the governing

transport equations using a reduced chemical kinetics reaction mechanism requiring the transport of tens of chemical species for which the reaction kinetics are derived from a detailed reaction mechanism. While more accurate, the computational cost associated with these direct approaches increases substantially with both the number of transported species and the reaction mechanism complexity and associated numerical stiffness. One approach for capturing detailed kinetics effects while also maintaining low numerical stiffness is through the use of a flamelet/progress variable (FPV) model. FPV models currently available in the literature, however, are typically only valid in the low Mach number limit, and recent attempts at extending these models to compressible flows fail to include adequate corrections for compressibility and flamelet boundary condition variability.

The current dissertation used an experimental dual-mode scramjet combustor, referred to as the Hypersonic International Flight Research and Experimentation (HIFiRE) Direct Connect Rig (HDCR), as a testbed for *a priori* analysis and *a posteriori* testing of several compressible FPV model formulations. First, Favre-averaged RANS simulations of the HDCR for test points characterizing both dual- and scram-mode operation were performed using the Viscous Upwind aLgorithm for Complex flow ANalysis and Computational Fluid Dynamics (VULCAN-CFD) with a 22-species finite-rate kinetics reaction mechanism for the simulation of a JP-7 fuel surrogate. These baseline RANS solutions were validated against available experimental data and were then used for *a priori* analysis of the HDCR combustion dynamics and subsequent investigation into the applicability of FPV models. Based on this analysis, a new compressible FPV model was proposed, hereafter referred to as the CFPVX model, which utilized a four-dimensional flamelet manifold incorporating compressibility effects on composition via parameterization on static pressure and effects of flame reactants variability via parameterization on static enthalpy. The CFPVX model, a standard incompressible FPV (IFPV) model, and most recent compressible FPV (CFPV) models were then evaluated using the baseline RANS data with an *a priori* flamelet-modeled-RANS (APFM-RANS) analysis method. These FPV models were subsequently implemented in the VULCAN-CFD solver, and *a posteriori* testing supported the findings of the *a priori* analysis.

# *Acknowledgements*

This dissertation would have been impossible to complete without the help of many friends, family, and colleagues. Special acknowledgement must be made foremost to those who had a direct hand in helping me complete this work. I will remain long-indebted to my NASA mentor Dr. Tomasz Drozda and NASA colleagues Dr. Robert Baurle, Mike Bynum, and Jeff White for their collective guidance, advice, and patience. I also owe many thanks to Drs. Joe Oefelein and Guilhem Lacaze for the great opportunity to visit Sandia National Laboratories and collaborate on this work over the past several years. I would also like to thank Prof. Johan Larsson of the University of Maryland for many helpful discussions regarding modeling with flamelets. Finally, I am most grateful to my faculty advisor, Prof. James McDaniel, and the members of my dissertation committee.

This work would have been impossible to complete without the support of my friends and colleagues at the National Institute of Aerospace, NASA Langley Research Center, and the University of Virginia. Without their support, the many tribulations facing a PhD student would have been quite overwhelming.

I must also acknowledge the overwhelming support from my wife, Charlotte, and my parents. Without their empowering confidence in me, this dissertation would have been made immensely more difficult. I also acknowledge my eight month old triplets, who helped to convince me that sometimes one can indeed fit more than twenty-four hours of work into a single day.

Financial support for this research was provided primarily by a NASA Space Technology Research Fellowship (Grant #NNX11AM86H) and the NASA Pathways Program. Additional support was provided by the Virginia Space Grant Consortium and a Virginia Commonwealth Fellowship. Computational resources were provided by the NASA Advanced Supercomputing division.

With abundant gratitude,

Jesse R. Quinlan

*To my wife, Charlotte, and our three little engineers-in-training,  
Barrett, Lorelei, and Russell.*

# Contents

<b>Abstract</b>	<b>vii</b>
<b>Acknowledgements</b>	<b>ix</b>
<b>Contents</b>	<b>xi</b>
<b>List of Figures</b>	<b>xv</b>
<b>List of Tables</b>	<b>xxv</b>
<b>Abbreviations</b>	<b>xxvii</b>
<b>Symbols</b>	<b>xxix</b>
<b>1 Introduction</b>	<b>1</b>
1.1 Statement of the Problem . . . . .	3
1.2 Dissertation Outline . . . . .	6
<b>2 Background</b>	<b>9</b>
2.1 Scramjet Fundamentals . . . . .	9
2.1.1 Operational Overview . . . . .	9
2.1.2 Overview of Recent Research Campaigns . . . . .	11
2.2 Governing Equations . . . . .	13
2.2.1 Compressible Navier-Stokes Equations . . . . .	14
2.2.2 Compressible RANS Equations . . . . .	16
2.3 Flamelet-Based Combustion Modeling . . . . .	18
2.3.1 Flamelet Modeling Theory . . . . .	18
2.3.2 Steady Laminar Flamelet Model . . . . .	21
2.3.3 Flamelet/Progress Variable Model . . . . .	23
2.3.4 Efforts Toward a Compressible FPV Model . . . . .	25
2.3.4.1 FPV with Total Energy Transport . . . . .	25
2.3.4.2 FPV with Compressibility Correction . . . . .	26
<b>3 Compressible RANS Simulations of the HDCR</b>	<b>29</b>
3.1 The HDCR Ground Experiment . . . . .	30

3.2	Compressible RANS Simulations . . . . .	31
3.2.1	Numerical Formulation . . . . .	34
3.2.2	Dual-Mode Operation . . . . .	35
3.2.3	Scram-Mode Operation . . . . .	36
<b>4</b>	<b><i>A Priori</i> Study of the HDCR Combustion Dynamics</b>	<b>43</b>
4.1	Flame Index . . . . .	44
4.2	Combustion Mode . . . . .	47
4.3	Compressibility . . . . .	55
4.4	Wall Heat Losses . . . . .	57
4.5	Considerations for a Compressible FPV Model . . . . .	59
<b>5</b>	<b><i>A Priori</i> FPV Model Analysis</b>	<b>63</b>
5.1	Methodology . . . . .	63
5.1.1	FPV Model Implementation Considerations . . . . .	63
5.1.2	APFM-RANS Analysis Method and FPV Model Formulations . . . . .	64
5.1.3	Flamelet Table Generation . . . . .	66
5.2	Results . . . . .	69
5.2.1	Progress Variable Trade Study . . . . .	70
5.2.1.1	Dual-Mode Operation . . . . .	73
5.2.1.2	Scram-Mode Operation . . . . .	85
5.2.2	Progress Variable Production Models . . . . .	98
5.2.3	FPV Model Coupling . . . . .	101
5.2.4	CFPVX Model . . . . .	106
5.2.4.1	Dual-Mode Operation . . . . .	107
5.2.4.2	Scram-Mode Operation . . . . .	115
<b>6</b>	<b><i>A Posteriori</i> Model Assessment</b>	<b>125</b>
6.1	FPV Model Implementation . . . . .	126
6.2	Results . . . . .	127
6.2.1	Dual-Mode Operation . . . . .	130
6.2.2	Scram-Mode Operation . . . . .	142
6.2.3	FPV Model Performance . . . . .	155
<b>7</b>	<b>Conclusion</b>	<b>157</b>
7.1	Concluding Discussion . . . . .	157
7.2	Contributions Summary . . . . .	161
7.3	Future Research Plans . . . . .	162
<b>A</b>	<b>Documentation for VULCAN-CFD with FPV Modeling</b>	<b>165</b>
A.1	Implementation Architecture . . . . .	165
A.2	FPV Model Configuration . . . . .	168
A.3	Solution Post-Processing . . . . .	169
A.4	Example Input Deck . . . . .	170
<b>B</b>	<b>Flux Jacobian Transformation Matrices for FPV Models</b>	<b>175</b>
B.1	General System of Governing Equations . . . . .	176

---

B.2 FPV Model Transformation Matrices . . . . .	179
<b>Bibliography</b>	<b>187</b>



# List of Figures

2.1	A notional schematic detailing the four primary components of a scramjet engine. . . . .	10
2.2	Notional schematic of a non-premixed laminar flame approximation to a turbulent flame configuration for which local turbulent eddies serve to wrinkle a thin and locally laminar flame surface. . . . .	19
2.3	Notional S-shaped curve demonstrating the multivaluedness in $Z-\chi_{st}$ space for the steady flamelet model formulation. . . . .	22
2.4	Notional S-shaped curve demonstrating the improved mapping of flame states by using the $Z-C$ parameterization with the FPV model. . . . .	23
3.1	Side view and key dimensions of the HDCR combustor flowpath, where $\varnothing$ is internal diameter of the injectors. . . . .	31
3.2	Looking upstream, isometric, and side views of the structured, quarter-geometry, grid used for RANS of the HDCR combustor coarsened four times for visual clarity. . . . .	34
3.3	Comparisons of streamwise ( $x$ ) wall static pressure ( $p$ ) data obtained from simulations D584A and D584I and experimentally for dual-mode operation of the HDCR combustor. . . . .	36
3.4	Contours of the Mach number at spanwise ( $z$ ) center plane and middle injector centerline for case D584A. Dark black lines correspond to the sonic isocontour. . . . .	37
3.5	Contours of the logarithm of chemical heat release ( $Q$ ) normalized by its global maximum for simulation D584A. Dark black lines correspond to the sonic isocontour. . . . .	38
3.6	Comparisons of streamwise ( $x$ ) wall static pressure ( $p$ ) data obtained from simulations S800A and S800I and experimentally for scram-mode operation of the HDCR combustor. . . . .	39
3.7	Contours of the Mach number at spanwise ( $z$ ) center plane and middle injector centerline for case S800A. Dark black lines correspond to the sonic isocontour. . . . .	40
3.8	Contours of the logarithm of chemical heat release ( $Q$ ) normalized by its global maximum for simulation S800A. Dark black lines correspond to the sonic isocontour. . . . .	41
4.1	Contours of the logarithm of flame index, $f$ , for simulation D584A. Dark black lines correspond to the sonic isocontour. . . . .	45
4.2	Contours of the logarithm of flame index, $f$ , for simulation S800A. Dark black lines correspond to the sonic isocontour. . . . .	46

4.3	Isosurfaces corresponding to a flame index of 0.1 colored by OH mass fraction for both primary and secondary injector flames for cases D584A (a) and S800A (b). . . . .	47
4.4	Damköhler number, $Da$ , versus flame-weighted Takeno index, $\Lambda_f$ , data sized by chemical heat release, $\tilde{Q}$ , and colored by normalized Favre-averaged production rate of water, $\tilde{\omega}_{H_2O}$ , for case D584A. Data are plotted for the primary injector flames, which correspond to the gray regions on the included flowpath mold line. . . . .	50
4.5	Damköhler number, $Da$ , versus flame-weighted Takeno index, $\Lambda_f$ , data sized by chemical heat release, $\tilde{Q}$ , and colored by normalized Favre-averaged production rate of water, $\tilde{\omega}_{H_2O}$ , for case D584A. Data are plotted for the secondary injector flames, which correspond to the gray regions on the included flowpath mold line. . . . .	51
4.6	Damköhler number, $Da$ , versus flame-weighted Takeno index, $\Lambda_f$ , data sized by chemical heat release, $\tilde{Q}$ , and colored by normalized Favre-averaged production rate of water, $\tilde{\omega}_{H_2O}$ , for case S800A. Data are plotted for the primary injector flames, which correspond to the gray regions on the included flowpath mold line. . . . .	52
4.7	Damköhler number, $Da$ , versus flame-weighted Takeno index, $\Lambda_f$ , data sized by chemical heat release, $\tilde{Q}$ , and colored by normalized Favre-averaged production rate of water, $\tilde{\omega}_{H_2O}$ , for case S800A. Data are plotted for the secondary injector flames, which correspond to the gray regions on the included flowpath mold line. . . . .	53
4.8	Borghi diagram for case D584A, whose data are colored by flame index sized by chemical heat release and shown for $\Lambda_f > 0.05$ . . . . .	54
4.9	Borghi diagram for case S800A, whose data are colored by flame index sized by chemical heat release and shown for $\Lambda_f > 0.05$ . . . . .	54
4.10	Static temperature, $\bar{T}$ , versus mixture fraction, $\tilde{Z}$ , colored by the logarithm of static pressure, $\bar{P}$ , and sized by chemical heat release rate, $\tilde{Q}$ , for (a) case D584A and (b) case S800A primary injector flames and for (c) case D584A and (d) case S800A secondary injector flames. . . . .	56
4.11	Static temperature and variance conditionally-averaged on mixture fraction ( $\langle \bar{T}   \tilde{Z} \rangle$ and $\langle \bar{T}'^2   \tilde{Z} \rangle$ , respectively) for dual-mode (a) and scram-mode (b) cases. . . . .	57
4.12	Static temperature plotted in mixture fraction space and colored by logarithm of velocity magnitude, $V_s$ , for cases (a) D584A, (b) D584I, (c) S800A, and (d) S800I, showing the effect of heat losses on the combustion. . . . .	58
4.13	PDFs of static temperature and pressure ( $f_T$ and $f_P$ , respectively) for fuel ( $Z > 0.99$ ) and oxidizer ( $Z < 0.01$ ) conditions for cases D584A (top) and S800A (bottom). Regions from which the data are sampled are shown above the respective plots, with the leftmost representing the primary injector flames and the rightmost representing the secondary injector flames. . . . .	61
5.1	Flowchart depicting the APFM-RANS analysis method. . . . .	66
5.2	PDF of $T_{ox}$ for the HDCR in dual-mode operation, including both the primary and secondary injector combustion regions. . . . .	68
5.3	Stoichiometric temperature, $T_{st}$ , and $\chi_{st}$ for flamelet solutions in table FT1 demonstrating the embedded S-shaped curve. . . . .	68

5.4	Line plots of $Y$ [cm] versus $T$ [K] obtained using the APFM-RANS analysis method and from the baseline RANS simulations of the HDCR combustor at several locations through the primary and secondary injector flames at the injector centerline nearest to the combustor centerline for cases corresponding to DIFPV1-DIFPV4 and DCFPV1-DCFPV4. Units on each subfigure are the same as those shown on the top-row, left-most subfigure. . . . .	74
5.5	Line plots of $Y$ [cm] versus $Y_{CO_2}$ obtained using the APFM-RANS analysis method and from the baseline RANS simulations of the HDCR combustor at several locations through the primary and secondary injector flames at the injector centerline nearest to the combustor centerline for cases corresponding to DIFPV1-DIFPV4 and DCFPV1-DCFPV4. Units on each subfigure are the same as those shown on the top-row, left-most subfigure. . . . .	75
5.6	Line plots of $Y$ [cm] versus $Y_{CO}$ obtained using the APFM-RANS analysis method and from the baseline RANS simulations of the HDCR combustor at several locations through the primary and secondary injector flames at the injector centerline nearest to the combustor centerline for cases corresponding to DIFPV1-DIFPV4 and DCFPV1-DCFPV4. Units on each subfigure are the same as those shown on the top-row, left-most subfigure. . . . .	76
5.7	Line plots of $Y$ [cm] versus $Y_{H_2O}$ obtained using the APFM-RANS analysis method and from the baseline RANS simulations of the HDCR combustor at several locations through the primary and secondary injector flames at the injector centerline nearest to the combustor centerline for cases corresponding to DIFPV1-DIFPV4 and DCFPV1-DCFPV4. Units on each subfigure are the same as those shown on the top-row, left-most subfigure. . . . .	77
5.8	Line plots of $Y$ [cm] versus $Y_{OH}$ obtained using the APFM-RANS analysis method and from the baseline RANS simulations of the HDCR combustor at several locations through the primary and secondary injector flames at the injector centerline nearest to the combustor centerline for cases corresponding to DIFPV1-DIFPV4 and DCFPV1-DCFPV4. Units on each subfigure are the same as those shown on the top-row, left-most subfigure. . . . .	78
5.9	Scatter plots of the temperature, $T$ [K], obtained using the APFM-RANS analysis method versus that from the baseline RANS simulations of the HDCR combustor for the full computational domain for cases DIFPV1-DIFPV4. The red line denotes a line with slope of one. . . . .	80
5.10	Scatter plots of $Y_{CO_2}$ obtained using the APFM-RANS analysis method versus that from the baseline RANS simulations of the HDCR combustor for the full computational domain for cases DIFPV1-DIFPV4. The red line denotes a line with slope of one. . . . .	80
5.11	Scatter plots of $Y_{CO}$ obtained using the APFM-RANS analysis method versus that from the baseline RANS simulations of the HDCR combustor for the full computational domain for cases DIFPV1-DIFPV4. The red line denotes a line with slope of one. . . . .	81

- 5.12 Scatter plots of  $Y_{H_2O}$  obtained using the APFM-RANS analysis method versus that from the baseline RANS simulations of the HDCR combustor for the full computational domain for cases DIFPV1-DIFPV4. The red line denotes a line with slope of one. . . . . 81
- 5.13 Scatter plots of the temperature,  $Y_{OH}$ , obtained using the APFM-RANS analysis method versus that from the baseline RANS simulations of the HDCR combustor for the full computational domain for cases DIFPV1-DIFPV4. The red line denotes a line with slope of one. . . . . 82
- 5.14 Scatter plots of  $T$  [K] obtained using the APFM-RANS analysis method versus that from the baseline RANS simulations of the HDCR combustor for the full computational domain for cases DCFPV1-DCFPV4. The red line denotes a line with slope of one. . . . . 82
- 5.15 Scatter plots of  $Y_{CO_2}$  obtained using the APFM-RANS analysis method versus that from the baseline RANS simulations of the HDCR combustor for the full computational domain for cases DCFPV1-DCFPV4. The red line denotes a line with slope of one. . . . . 83
- 5.16 Scatter plots of  $Y_{CO}$  obtained using the APFM-RANS analysis method versus that from the baseline RANS simulations of the HDCR combustor for the full computational domain for cases DCFPV1-DCFPV4. The red line denotes a line with slope of one. . . . . 83
- 5.17 Scatter plots of  $Y_{H_2O}$  obtained using the APFM-RANS analysis method versus that from the baseline RANS simulations of the HDCR combustor for the full computational domain for cases DCFPV1-DCFPV4. The red line denotes a line with slope of one. . . . . 84
- 5.18 Scatter plots of  $Y_{OH}$  obtained using the APFM-RANS analysis method versus that from the baseline RANS simulations of the HDCR combustor for the full computational domain for cases DCFPV1-DCFPV4. The red line denotes a line with slope of one. . . . . 84
- 5.19 Line plots of  $Y$  [cm] versus  $T$  [K] obtained using the APFM-RANS analysis method and from the baseline RANS simulations of the HDCR combustor at several locations through the primary and secondary injector flames at the injector centerline nearest to the combustor centerline for cases corresponding to SIFPV1-SIFPV4 and SCFPV1-SCFPV4. Units on each subfigure are the same as those shown on the top-row, left-most subfigure. . . . . 87
- 5.20 Line plots of  $Y$  [cm] versus  $Y_{CO_2}$  obtained using the APFM-RANS analysis method and from the baseline RANS simulations of the HDCR combustor at several locations through the primary and secondary injector flames at the injector centerline nearest to the combustor centerline for cases corresponding to SIFPV1-SIFPV4 and SCFPV1-SCFPV4. Units on each subfigure are the same as those shown on the top-row, left-most subfigure. . . . . 88
- 5.21 Line plots of  $Y$  [cm] versus  $Y_{CO}$  obtained using the APFM-RANS analysis method and from the baseline RANS simulations of the HDCR combustor at several locations through the primary and secondary injector flames at the injector centerline nearest to the combustor centerline for cases corresponding to SIFPV1-SIFPV4 and SCFPV1-SCFPV4. Units on each subfigure are the same as those shown on the top-row, left-most subfigure. 89

5.22	Line plots of $Y$ [cm] versus $Y_{H_2O}$ obtained using the APFM-RANS analysis method and from the baseline RANS simulations of the HDCR combustor at several locations through the primary and secondary injector flames at the injector centerline nearest to the combustor centerline for cases corresponding to SIFPV1-SIFPV4 and SCFPV1-SCFPV4. Units on each subfigure are the same as those shown on the top-row, left-most subfigure. . . . .	90
5.23	Line plots of $Y$ [cm] versus $Y_{OH}$ obtained using the APFM-RANS analysis method and from the baseline RANS simulations of the HDCR combustor at several locations through the primary and secondary injector flames at the injector centerline nearest to the combustor centerline for cases corresponding to SIFPV1-SIFPV4 and SCFPV1-SCFPV4. Units on each subfigure are the same as those shown on the top-row, left-most subfigure. . . . .	91
5.24	Scatter plots of the temperature, $T$ [K], obtained using the APFM-RANS analysis method versus that from the baseline RANS simulations of the HDCR combustor for the full computational domain for cases SIFPV1-SIFPV4. The red line denotes a line with slope of one. . . . .	93
5.25	Scatter plots of $Y_{CO_2}$ obtained using the APFM-RANS analysis method versus that from the baseline RANS simulations of the HDCR combustor for the full computational domain for cases SIFPV1-SIFPV4. The red line denotes a line with slope of one. . . . .	93
5.26	Scatter plots of $Y_{CO}$ obtained using the APFM-RANS analysis method versus that from the baseline RANS simulations of the HDCR combustor for the full computational domain for cases SIFPV1-SIFPV4. The red line denotes a line with slope of one. . . . .	94
5.27	Scatter plots of $Y_{H_2O}$ obtained using the APFM-RANS analysis method versus that from the baseline RANS simulations of the HDCR combustor for the full computational domain for cases SIFPV1-SIFPV4. The red line denotes a line with slope of one. . . . .	94
5.28	Scatter plots of the temperature, $Y_{OH}$ , obtained using the APFM-RANS analysis method versus that from the baseline RANS simulations of the HDCR combustor for the full computational domain for cases SIFPV1-SIFPV4. The red line denotes a line with slope of one. . . . .	95
5.29	Scatter plots of $T$ [K] obtained using the APFM-RANS analysis method versus that from the baseline RANS simulations of the HDCR combustor for the full computational domain for cases SCFPV1-SCFPV4. The red line denotes a line with slope of one. . . . .	95
5.30	Scatter plots of $Y_{CO_2}$ obtained using the APFM-RANS analysis method versus that from the baseline RANS simulations of the HDCR combustor for the full computational domain for cases SCFPV1-SCFPV4. The red line denotes a line with slope of one. . . . .	96
5.31	Scatter plots of $Y_{CO}$ obtained using the APFM-RANS analysis method versus that from the baseline RANS simulations of the HDCR combustor for the full computational domain for cases SCFPV1-SCFPV4. The red line denotes a line with slope of one. . . . .	96
5.32	Scatter plots of $Y_{H_2O}$ obtained using the APFM-RANS analysis method versus that from the baseline RANS simulations of the HDCR combustor for the full computational domain for cases SCFPV1-SCFPV4. The red line denotes a line with slope of one. . . . .	97

5.33	Scatter plots of $Y_{OH}$ obtained using the APFM-RANS analysis method versus that from the baseline RANS simulations of the HDCR combustor for the full computational domain for cases SCFPV1-SCFPV4. The red line denotes a line with slope of one. . . . .	97
5.34	Scatter plot of $\dot{\omega}_C$ [kg/m <sup>3</sup> s] calculated using the APFM-RANS analysis method for case DIFPV4 with the pressure-scaling model in Eq. (2.40) as compared to that of case DCFPV4, for which $\dot{\omega}_C$ is parameterized explicitly by pressure. The red line denotes a line with slope of one. . . .	99
5.35	Scatter plot of $\dot{\omega}_C$ [kg/m <sup>3</sup> s] calculated using the APFM-RANS analysis method for case SIFPV4 with the pressure-scaling model in Eq. (2.40) as compared to that of case SCFPV4, for which $\dot{\omega}_C$ is parameterized explicitly by pressure. The red line denotes a line with slope of one. . . .	99
5.36	Line plot $Y$ [cm] versus $\dot{\omega}_C$ [kg/m <sup>3</sup> s] calculated using the APFM-RANS analysis method for case DIFPV4 with the use of Eq. (2.40), case DCFPV4, and case DIFPV4 with the use of Eq. (5.8) to baseline RANS data at selected locations for the primary and secondary injectors spanning the flame regions. Locations of the sampled data planes are shown on the combustor geometry cross-section. . . . .	100
5.37	Scatter plot comparisons of APFM-RANS analysis results and the baseline RANS data for $\dot{\omega}_C$ [kg/m <sup>3</sup> s] for the entire computational domain for cases: (top-left) DIFPV4, (top-right) DIFPV4 with the pressure-scaling model shown in Eq. (2.40), (bottom-left) DIFPV4 with the pressure- and temperature-scaling models shown in of Eq. (5.8), and (bottom-right) DCFPV4 with the temperature-scaling model shown in Eq. (5.8). . . . .	102
5.38	Scatter plot comparisons of APFM-RANS analysis results and the baseline RANS data for $\dot{\omega}_C$ [kg/m <sup>3</sup> s] for the entire computational domain for cases: (top-left) SIFPV4, (top-right) SIFPV4 with the pressure-scaling model shown in Eq. (2.40), (bottom-left) SIFPV4 with the pressure- and temperature-scaling models shown in of Eq. (5.8), and (bottom-right) SCFPV4 with the temperature-scaling model shown in Eq. (5.8). . . . .	102
5.39	Scatter plot of energy interdiffusion using the $\beta_{ii}$ formulation for case DCFPV4 compared to the baseline RANS data. The red line denotes a line with slope of one. . . . .	104
5.40	Scatter plot of energy interdiffusion using the $\beta_{iii}$ formulation for case DCFPV4 compared to the baseline RANS data. The red line denotes a line with slope of one. . . . .	105
5.41	Scatter plot of energy interdiffusion using the $\beta_{ii}$ formulation for case SCFPV4 compared to the baseline RANS data. The red line denotes a line with slope of one. . . . .	105
5.42	Scatter plot of energy interdiffusion using the $\beta_{iii}$ formulation for case SCFPV4 compared to the baseline RANS data. The red line denotes a line with slope of one. . . . .	106
5.43	The flamelet manifold embedded in table FT3 presented in $Z$ - $C$ - $T_{ox}$ space where points are colored by $h$ to demonstrate the monotonic nature of the $T_{ox}$ - $h$ mapping. . . . .	107

5.44	Line plots of $Y$ [cm] versus $T$ [K] obtained using the APFM-RANS analysis method and from the baseline RANS simulations of the HDCR combustor at several locations through the primary and secondary injector flames at the injector centerline nearest to the combustor centerline for cases corresponding to DIFPV4, DCFPV4, and DCFPVX4. . . . .	109
5.45	Line plots of $Y$ [cm] versus $Y_{CO_2}$ obtained using the APFM-RANS analysis method and from the baseline RANS simulations of the HDCR combustor at several locations through the primary and secondary injector flames at the injector centerline nearest to the combustor centerline for cases corresponding to DIFPV4, DCFPV4, and DCFPVX4. . . . .	110
5.46	Line plots of $Y$ [cm] versus $Y_{H_2O}$ obtained using the APFM-RANS analysis method and from the baseline RANS simulations of the HDCR combustor at several locations through the primary and secondary injector flames at the injector centerline nearest to the combustor centerline for cases corresponding to DIFPV4, DCFPV4, and DCFPVX4. . . . .	111
5.47	Line plots of $Y$ [cm] versus $Y_{CO}$ obtained using the APFM-RANS analysis method and from the baseline RANS simulations of the HDCR combustor at several locations through the primary and secondary injector flames at the injector centerline nearest to the combustor centerline for cases corresponding to DIFPV4, DCFPV4, and DCFPVX4. . . . .	112
5.48	Line plots of $Y$ [cm] versus $Y_{OH}$ obtained using the APFM-RANS analysis method and from the baseline RANS simulations of the HDCR combustor at several locations through the primary and secondary injector flames at the injector centerline nearest to the combustor centerline for cases corresponding to DIFPV4, DCFPV4, and DCFPVX4. . . . .	113
5.49	Scatter plots of $T$ obtained using the APFM-RANS analysis method in black versus that from the baseline RANS simulations of the HDCR combustor for the full computational domain for case DCFPVX4. Results for case DCFPV4 are shown in green, and the red line denotes a line with slope of one. . . . .	114
5.50	Scatter plots of $Y_{CO_2}$ , $Y_{CO}$ , $Y_{H_2O}$ , and $Y_{OH}$ obtained using the APFM-RANS analysis method in black versus that from the baseline RANS simulations of the HDCR combustor for the full computational domain for case DCFPVX4. Results for case DCFPV4 are shown in green, and the red line denotes a line with slope of one. . . . .	115
5.51	Scatter plot of $\dot{\omega}_C$ [kg/m <sup>3</sup> s] obtained using the APFM-RANS analysis method for case DCFPVX4 versus that from the baseline RANS simulations of the HDCR combustor for the full computational domain. The temperature-scaling presented in Eq. (5.8) is used to correct the tabulated DCFPVX4 $\dot{\omega}_C$ . . . . .	116
5.52	Line plots of $Y$ [cm] versus $T$ [K] obtained using the APFM-RANS analysis method and from the baseline RANS simulations of the HDCR combustor at several locations through the primary and secondary injector flames at the injector centerline nearest to the combustor centerline for cases corresponding to SIFPV4, SCFPV4, and SCFPVX4. . . . .	117

5.53	Line plots of $Y$ [cm] versus $Y_{CO_2}$ obtained using the APFM-RANS analysis method and from the baseline RANS simulations of the HDCR combustor at several locations through the primary and secondary injector flames at the injector centerline nearest to the combustor centerline for cases corresponding to SIFPV4, SCFPV4, and SCFPVX4. . . . .	118
5.54	Line plots of $Y$ [cm] versus $Y_{H_2O}$ obtained using the APFM-RANS analysis method and from the baseline RANS simulations of the HDCR combustor at several locations through the primary and secondary injector flames at the injector centerline nearest to the combustor centerline for cases corresponding to SIFPV4, SCFPV4, and SCFPVX4. . . . .	119
5.55	Line plots of $Y$ [cm] versus $Y_{CO}$ obtained using the APFM-RANS analysis method and from the baseline RANS simulations of the HDCR combustor at several locations through the primary and secondary injector flames at the injector centerline nearest to the combustor centerline for cases corresponding to SIFPV4, SCFPV4, and SCFPVX4. . . . .	120
5.56	Line plots of $Y$ [cm] versus $Y_{OH}$ obtained using the APFM-RANS analysis method and from the baseline RANS simulations of the HDCR combustor at several locations through the primary and secondary injector flames at the injector centerline nearest to the combustor centerline for cases corresponding to SIFPV4, SCFPV4, and SCFPVX4. . . . .	121
5.57	Scatter plots of $T$ obtained using the APFM-RANS analysis method in black versus that from the baseline RANS simulations of the HDCR combustor for the full computational domain for case SCFPVX4. Results for case SCFPV4 are shown in green, and the red line denotes a line with slope of one. . . . .	122
5.58	Scatter plots of $Y_{CO_2}$ , $Y_{CO}$ , $Y_{H_2O}$ , and $Y_{OH}$ obtained using the APFM-RANS analysis method in black versus that from the baseline RANS simulations of the HDCR combustor for the full computational domain for case SCFPVX4. Results for case SCFPV4 are shown in green, and the red line denotes a line with slope of one. . . . .	123
5.59	Scatter plot of $\dot{\omega}_C$ [kg/m <sup>3</sup> s] obtained using the APFM-RANS analysis method for case SCFPVX4 versus that from the baseline RANS simulations of the HDCR combustor for the full computational domain. The temperature-scaling presented in Eq. (5.8) is used to correct the tabulated SCFPVX4 $\dot{\omega}_C$ . . . . .	124
6.1	Flowchart depicting the application of FPV models using VULCAN-CFD.	129
6.2	Comparisons of streamwise ( $x$ [cm]) wall static pressure ( $p$ [atm]) data at the HDCR combustor centerline for FPV simulation cases DIFPV4, DCFPV4, and DCFPVX4 computed using VULCAN-CFD. The baseline dual-mode RANS case D584A and experimental data are also plotted. . .	131
6.3	Contours of $\tilde{T}$ [K] obtained by solving Eqs. (6.1)-(6.6) using VULCAN-CFD for the HDCR combustor at the injector centerline nearest to the combustor centerline for cases DIFPV4, DCFPV4, and DCFPVX4 and compared to the baseline dual-mode RANS case D584A. . . . .	132
6.4	Contours of $\tilde{Y}_{CO_2}$ obtained by solving Eqs. (6.1)-(6.6) using VULCAN-CFD for the HDCR combustor at the injector centerline nearest to the combustor centerline for cases DIFPV4, DCFPV4, and DCFPVX4 and compared to the baseline dual-mode RANS case D584A. . . . .	133

6.5	Contours of $\tilde{Y}_{CO}$ obtained by solving Eqs. (6.1)-(6.6) using VULCAN-CFD for the HDCR combustor at the injector centerline nearest to the combustor centerline for cases DIFPV4, DCFPV4, and DCFPVX4 and compared to the baseline dual-mode RANS case D584A. . . . .	134
6.6	Contours of $\tilde{Y}_{H_2O}$ obtained by solving Eqs. (6.1)-(6.6) using VULCAN-CFD for the HDCR combustor at the injector centerline nearest to the combustor centerline for cases DIFPV4, DCFPV4, and DCFPVX4 and compared to the baseline dual-mode RANS case D584A. . . . .	135
6.7	Contours of $\tilde{Y}_{OH}$ obtained by solving Eqs. (6.1)-(6.6) using VULCAN-CFD for the HDCR combustor at the injector centerline nearest to the combustor centerline for cases DIFPV4, DCFPV4, and DCFPVX4 and compared to the baseline dual-mode RANS case D584A. . . . .	136
6.8	Line plots of $Y$ [cm] versus $\tilde{T}$ [K] obtained by solving Eqs. (6.1)-(6.6) using VULCAN-CFD for the HDCR combustor at several locations through the primary and secondary injector flames at the injector centerline nearest to the combustor centerline for cases DIFPV4, DCFPV4, and DCFPVX4 and compared to the baseline dual-mode RANS case D584A. . . . .	137
6.9	Line plots of $Y$ [cm] versus $\tilde{Y}_{CO_2}$ obtained by solving Eqs. (6.1)-(6.6) using VULCAN-CFD for the HDCR combustor at several locations through the primary and secondary injector flames at the injector centerline nearest to the combustor centerline for cases DIFPV4, DCFPV4, and DCFPVX4 and compared to the baseline dual-mode RANS case D584A. . . . .	138
6.10	Line plots of $Y$ [cm] versus $\tilde{Y}_{H_2O}$ obtained by solving Eqs. (6.1)-(6.6) using VULCAN-CFD for the HDCR combustor at several locations through the primary and secondary injector flames at the injector centerline nearest to the combustor centerline for cases DIFPV4, DCFPV4, and DCFPVX4 and compared to the baseline dual-mode RANS case D584A. . . . .	139
6.11	Line plots of $Y$ [cm] versus $\tilde{Y}_{CO}$ obtained by solving Eqs. (6.1)-(6.6) using VULCAN-CFD for the HDCR combustor at several locations through the primary and secondary injector flames at the injector centerline nearest to the combustor centerline for cases DIFPV4, DCFPV4, and DCFPVX4 and compared to the baseline dual-mode RANS case D584A. . . . .	140
6.12	Line plots of $Y$ [cm] versus $\tilde{Y}_{OH}$ obtained by solving Eqs. (6.1)-(6.6) using VULCAN-CFD for the HDCR combustor at several locations through the primary and secondary injector flames at the injector centerline nearest to the combustor centerline for cases DIFPV4, DCFPV4, and DCFPVX4 and compared to the baseline dual-mode RANS case D584A. . . . .	141
6.13	Comparisons of streamwise ( $x$ [cm]) wall static pressure ( $p$ [atm]) data at the HDCR combustor centerline for FPV simulation cases SIFPV4, SCFPV4, and SCFPVX4 computed using VULCAN-CFD. The baseline scram-mode RANS case S800A and experimental data are also plotted. . . . .	142
6.14	Contours of $\tilde{T}$ [K] obtained by solving Eqs. (6.1)-(6.6) using VULCAN-CFD for the HDCR combustor at the injector centerline nearest to the combustor centerline for cases SIFPV4, SCFPV4, and SCFPVX4 and compared to the baseline scram-mode RANS case S800A. . . . .	144
6.15	Contours of $\tilde{Y}_{CO_2}$ obtained by solving Eqs. (6.1)-(6.6) using VULCAN-CFD for the HDCR combustor at the injector centerline nearest to the combustor centerline for cases SIFPV4, SCFPV4, and SCFPVX4 and compared to the baseline scram-mode RANS case S800A. . . . .	145

6.16	Contours of $\tilde{Y}_{CO}$ obtained by solving Eqs. (6.1)-(6.6) using VULCAN-CFD for the HDCR combustor at the injector centerline nearest to the combustor centerline for cases SIFPV4, SCFPV4, and SCFPVX4 and compared to the baseline scram-mode RANS case S800A. . . . .	146
6.17	Contours of $\tilde{Y}_{H_2O}$ obtained by solving Eqs. (6.1)-(6.6) using VULCAN-CFD for the HDCR combustor at the injector centerline nearest to the combustor centerline for cases SIFPV4, SCFPV4, and SCFPVX4 and compared to the baseline scram-mode RANS case S800A. . . . .	147
6.18	Contours of $\tilde{Y}_{OH}$ obtained by solving Eqs. (6.1)-(6.6) using VULCAN-CFD for the HDCR combustor at the injector centerline nearest to the combustor centerline for cases SIFPV4, SCFPV4, and SCFPVX4 and compared to the baseline scram-mode RANS case S800A. . . . .	148
6.19	Line plots of $Y$ [cm] versus $\tilde{T}$ [K] obtained by solving Eqs. (6.1)-(6.6) using VULCAN-CFD for the HDCR combustor at several locations through the primary and secondary injector flames at the injector centerline nearest to the combustor centerline for cases SIFPV4, SCFPV4, and SCFPVX4 and compared to the baseline scram-mode RANS case S800A. . . . .	150
6.20	Line plots of $Y$ [cm] versus $\tilde{Y}_{CO_2}$ obtained by solving Eqs. (6.1)-(6.6) using VULCAN-CFD for the HDCR combustor at several locations through the primary and secondary injector flames at the injector centerline nearest to the combustor centerline for cases SIFPV4, SCFPV4, and SCFPVX4 and compared to the baseline scram-mode RANS case S800A. . . . .	151
6.21	Line plots of $Y$ [cm] versus $\tilde{Y}_{H_2O}$ obtained by solving Eqs. (6.1)-(6.6) using VULCAN-CFD for the HDCR combustor at several locations through the primary and secondary injector flames at the injector centerline nearest to the combustor centerline for cases SIFPV4, SCFPV4, and SCFPVX4 and compared to the baseline scram-mode RANS case S800A. . . . .	152
6.22	Line plots of $Y$ [cm] versus $\tilde{Y}_{CO}$ obtained by solving Eqs. (6.1)-(6.6) using VULCAN-CFD for the HDCR combustor at several locations through the primary and secondary injector flames at the injector centerline nearest to the combustor centerline for cases SIFPV4, SCFPV4, and SCFPVX4 and compared to the baseline scram-mode RANS case S800A. . . . .	153
6.23	Line plots of $Y$ [cm] versus $\tilde{Y}_{OH}$ obtained by solving Eqs. (6.1)-(6.6) using VULCAN-CFD for the HDCR combustor at several locations through the primary and secondary injector flames at the injector centerline nearest to the combustor centerline for cases SIFPV4, SCFPV4, and SCFPVX4 and compared to the baseline scram-mode RANS case S800A. . . . .	154

# List of Tables

3.1	Summary of simulated test cases, including flight Mach number, plenum conditions, fuel equivalence ratios ( $\Phi$ ), and wall boundary conditions. . . .	33
4.1	Approximate bounding fuel and oxidizer temperature and pressures derived from corresponding PDFs for simulated test cases. . . . .	62
5.1	APFM-RANS test cases. . . . .	72
6.1	Summary of FPV model performance (IFPV, CFPV, and CFPVX) comparisons to both reacting and non-reacting baseline finite-rate RANS simulations (Reacting Baseline and Non-Reacting Baseline) for VULCAN-CFD. Cost is shown in units of seconds per iteration per CPU [s/it/CPU], and Cost Benefit is shown in percentage points [%] less than the Reacting Baseline case. . . . .	155
A.1	Summary of VULCAN-CFD boundary conditions for which FPV models are supported. . . . .	169



# Abbreviations

<b>AFRL</b>	<b>Air Force Research Laboratory</b>
<b>APFM-RANS</b>	<b>A Priori Flamelet Modeled-Reynolds-Averaged Navier-Stokes</b>
<b>ATMS</b>	<b>Army Tactical Missile System</b>
<b>CFD</b>	<b>Computational Fluid Dynamics</b>
<b>CFPV</b>	<b>Compressible Flamelet Progress Variable</b>
<b>CFPVX</b>	<b>Compressible Flamelet Progress Variable with oxidizer temperature</b>
<b>CPU</b>	<b>Central Processing Unit</b>
<b>DAF</b>	<b>Diagonalized Approximate Factorization</b>
<b>DARPA</b>	<b>Defense Advanced Research Projects Agency</b>
<b>DLR</b>	<b>Deutsches Zentrum für Luft- und Raumfahrt e.V. (German Aerospace Center)</b>
<b>DNS</b>	<b>Direct Numerical Simulation</b>
<b>DOD</b>	<b>Department Of Defense</b>
<b>EDC</b>	<b>Eddy Dissipation Concept</b>
<b>FASTT</b>	<b>Freeflight Atmospheric Scramjet Test Technique</b>
<b>FDF</b>	<b>Filtered Density Function</b>
<b>FGM</b>	<b>Flamelet Generated Manifold</b>
<b>FPV</b>	<b>Flamelet Progress Variable</b>
<b>GASL</b>	<b>General Applied Science Laboratory</b>
<b>HDCR</b>	<b>HIFiRE Direct Connect Rig</b>
<b>HIFiRE</b>	<b>Hypersonic International Flight Research and Experimentation</b>
<b>HyPulse</b>	<b>Hypersonic Pulse Facility</b>
<b>IFPV</b>	<b>Incompressible Flamelet Progress Variable</b>

---

<b>ISAT</b>	<b>In Situ Adaptive Tabulation</b>
<b>JAXA</b>	<b>Japanese Aerospace and EXploration Agency</b>
<b>LaRC</b>	<b>Langley Research Center</b>
<b>LES</b>	<b>Large Eddy Simulation</b>
<b>MPI</b>	<b>Message Passing Interface</b>
<b>MUSCL</b>	<b>Monotone Upstream-centered Scheme for Conservation Laws</b>
<b>NAS</b>	<b>NASA Advanced Supercomputing Division</b>
<b>NASA</b>	<b>National Aeronautics and Space Administration</b>
<b>NCHCCP</b>	<b>National Center for Hypersonic Combined Cycle Propulsion</b>
<b>ONR</b>	<b>Office of Naval Research</b>
<b>PDF</b>	<b>Probability Density Function</b>
<b>PI</b>	<b>Principal Investigator</b>
<b>pyVFPV</b>	<b>python package for VULCAN-CFD Flamelet Progress Variable Modeling</b>
<b>RANS</b>	<b>Reynolds-Averaged Navier-Stokes</b>
<b>scramjet</b>	<b>supersonic combustible ramjet</b>
<b>SED</b>	<b>Scramjet Engine Demonstrator</b>
<b>SLF</b>	<b>Steady Laminar Flamelet</b>
<b>slvAPFM</b>	<b>solver package for APFM-RANS Analysis Method</b>
<b>slvVFPV</b>	<b>solver package for VULCAN-CFD Flamelet Progress Variable Modeling</b>
<b>UVa</b>	<b>University of Virginia</b>
<b>VULCAN-CFD</b>	<b>Viscous Upwind aLgorithm for Complex fluid ANalysis-Computational Fluid Dynamics</b>

# Symbols

## Roman:

$a_{ij}$	Number of atoms of element $i$ in species $j$
$a_p$	FPV model pressure scaling exponent
$a_s$	Stagnation-point velocity gradient for a counterflow diffusion flamelet configuration
$a_\gamma$	FPV model linearization constant
$C$	Progress variable
$C_a$	Modeling constant
$c_p$	Mixture specific heat at constant pressure
$c_{p\alpha}$	Specific heat at constant pressure for species $\alpha$
$c_v$	Mixture specific heat at constant volume
$c_{v\alpha}$	Specific heat at constant volume for species $\alpha$
$d$	Diagonalized flux Jacobian matrix
$D$	Mass diffusion coefficient
$D_\alpha$	Mass diffusion coefficient for species $\alpha$
$Da$	Damköhler number
$E$	Total energy
$e$	Internal energy
$e_0$	Reference flamelet internal energy
$e_{RANS}$	RANS solution internal energy
$erfc$	Inverse of the error function
$f$	Flame sensor index
$f_p$	Probability density function of static pressure

---

$f_T$	Probability density function of static temperature
$f_I, g_I, h_I$	Fluxes in the $x$ , $y$ , and $z$ directions, respectively
$F_I, G_I, H_I$	Generalized fluxes in the $\xi$ , $\eta$ , and $\zeta$ directions, respectively
$h$	Mixture specific enthalpy
$h_\alpha$	Specific enthalpy of species $\alpha$
$H$	Total enthalpy
$it$	Iteration
$J$	Jacobian matrix
$k$	Turbulence kinetic energy
$Ka$	Karlovitz number
$Ka_\delta$	Karlovitz number based on flame reaction zone thickness
$l$	Integral turbulence length scale
$l_F$	Laminar flame thickness
$l_\delta$	Flame reaction zone thickness
$Ka$	Karlovitz number
$Le$	Lewis number
$M$	Flux Jacobian transformation matrix
$MW_\alpha$	Molecular weight of species $\alpha$
$MW_i$	Molecular weight of species $i$
$MW_j$	Molecular weight of species $j$
$N$	Total number of species comprising gas mixture
$p$	Static pressure
$p_0$	Reference flamelet static pressure
$Pr$	Prandtl number
$Pr_t$	Turbulent Prandtl number
$R$	Mixture gas constant
$R_\alpha$	Gas constant for species $\alpha$
$R_u$	Universal gas constant
$R_0$	Reference flamelet mixture gas constant
$Re_t$	Turbulent Reynolds number
$q$	Conserved variables vector

$q^*$	Primitive variables vector
$q_j$	Heat flux vector component in $j$ direction
$q_{smf}$	FPV mapped species mass fractions vector
$Q$	Generalized conserved variables vector
$S$	Source vector
$Sc$	Schmidt number
$Sc_t$	Turbulent Schmidt number
$s$	Second
$s_L$	Laminar flame speed
$t$	Time
$t_0$	Reference time
$T$	Static temperature
$T_a$	FPV model activation temperature
$T_{ox}$	Oxidizer static temperature
$T_{st}$	Stoichiometric static temperature
$T_{RANS}$	RANS solution static temperature
$T_0$	Reference flamelet static temperature
$u_j$	Convective velocities
$u'$	Integral turbulence velocity scale
$V_j^\alpha$	Diffusion velocity for species $\alpha$ in direction $j$
$V_s$	Velocity magnitude
$x, y, z$	Cartesian coordinates
$x_j$	Spatial coordinates in tensor notation
$Y_\alpha$	Mass fraction of species $\alpha$
$Y_{fuel}$	Fuel mass fraction
$Y_{oxidizer}$	Oxidizer mass fraction
$Z$	Mixture fraction
$Z''^2$	Mixture fraction variance

**Greek:**

$\beta$	Energy interdiffusion term found in transport equation
---------	--

---

	for total energy
$\beta_{RANS}$	RANS solution energy interdiffusion
$\beta_i$	Energy interdiffusion model $i$
$\beta_{ii}$	Energy interdiffusion model $ii$
$\beta_{iii}$	Energy interdiffusion model $iii$
$\delta$	Laminar flame thickness
$\delta_{ij}$	Kronecker delta function
$\eta$	Kolmogorov length scale
$\epsilon$	Turbulence dissipation rate
$\gamma$	Ratio of specific heats
$\gamma_0$	Reference flamelet ratio of specific heats
$\lambda$	Mixture thermal conductivity
$\Lambda_f$	Flame-weighted Takeno index
$\Lambda_T$	Takeno index
$\phi$	Flamelet model state vector
$\phi_{FPV}$	FPV model state vector
$\phi_{SLF}$	SLF model state vector
$\varphi$	State property
$\Phi$	Fuel equivalence ratio
$\Phi_p$	Fuel equivalence ratio for the primary injectors
$\Phi_s$	Fuel equivalence ratio for the secondary injectors
$\Omega$	Fuel mass fraction
$\Omega_F$	Fraction of fuel mass in the fuel stream
$\Omega_O$	Fraction of fuel mass in the oxidizer stream
$\rho$	Mass density
$\rho_0$	Reference flamelet mass density
$\sigma_k$	Turbulence modeling parameter representing the ratio of viscous diffusion to that of the turbulence kinetic energy
$\tau$	Generalized time coordinate
$\tau_{ij}$	Stress tensor
$\tau_{chem}$	Characteristic chemical time scale
$\tau_{flame}$	Characteristic flame time scale

$\tau_{flow}$	Characteristic flow time scale
$\tau_{turb}$	Characteristic turbulence time scale
$\mu$	Dynamic molecular viscosity
$\mu_t$	Eddy viscosity
$\nu$	Kinematic molecular viscosity
$\omega$	Turbulence frequency
$\dot{\omega}_\alpha$	Production rate of chemical species $\alpha$
$\dot{\omega}_C$	Production rate of progress variable $C$
$\dot{\omega}_{C_0}$	Reference production rate of the progress variable $C$
$\chi$	Scalar dissipation rate
$\chi_{modeled}$	Modeled scalar dissipation rate
$\chi_{st}$	Stoichiometric scalar dissipation rate
$\xi, \eta, \zeta$	Generalized $x, y,$ and $z$ coordinates
$\nabla$	Divergence operator

### Superscripts:

–	Time-averaged quantity
~	Favre-averaged quantity
→	Vector quantity
'	Fluctuating quantity subject to time-averaging
"	Fluctuating quantity subject to Favre-averaging



# Chapter 1

## Introduction

In light of decades of research and numerous national and international research programs, development of operational supersonic combustion ramjet (scramjet) engines remains an ongoing challenge. Efforts by domestic agencies, including the National Aeronautics and Space Administration (NASA) and the Department of Defense (DOD), and international agencies, such as the German Aerospace Center (DLR) and the Japanese Aerospace Exploration Agency (JAXA), have produced numerous advances in the fundamental technologies and predictive capabilities required to design and fly such engines. These advances are evidenced by the numerous scramjet flight experiments of recent times [1–6]. Though, despite the substantial progress made by these efforts, significant research remains. One particularly challenging area of open research is the prediction of the flow and combustion dynamics within dual-mode scramjet engines, for which the engine flowpath may support both dual-mode (i.e. primarily subsonic combustion) and scram-mode (i.e. primarily supersonic combustion) operation. The current work addresses limitations of existing flamelet-based combustion models for the simulation of dual-mode scramjet combustors of engineering complexity.

Significant computational work has been directed at hydrogen-fueled scramjet engines, historically, due to experimental and flight applications that leverage hydrogen’s relatively short ignition delay times. In fact, researchers routinely use reduced reaction mechanisms for hydrogen directly with three-dimensional Reynolds-averaged Navier-Stokes (RANS) and hybrid RANS/large-eddy simulations (LES) with much success [7–10]. However, recent years have seen a push for scramjet designs utilizing hydrocarbon

fuels, due to their higher densities, which allow for reduced fuel storage requirements, and also due to their relative ease of handling and safety characteristics [11]. Related simulations using mechanisms as large as 14 [12] and 22 [13] species have been performed in recent years; however, such studies are limited to single point analyses due to the considerable computational cost. This increased cost for hydrocarbon-fueled applications has led many researchers to use simpler approaches like the eddy dissipation concept (EDC) [14–16], global reaction mechanisms [17, 18], and equilibrium flamelet solutions [19]. The low-cost of these models make application to state-of-the-art scramjet combustor designs possible, albeit at the expense of excluding limiting combustion physics, while often affording researchers greater discretion in their choice of turbulence and turbulence-chemistry-interaction (TCI) models. Consequently, for researchers interested in engine design-space exploration and analysis, a critical void exists between single-point, high-fidelity, computationally-costly and multi-point, low-fidelity, computationally-inexpensive modeling approaches.

The current dissertation details a comprehensive research effort toward understanding and modeling the combustion dynamics governing a hydrocarbon-fueled dual-mode scramjet engine using flamelet/progress-variable (FPV)-based modeling techniques [20–24], which are proposed as a means of bridging the gap between the high-cost, high-fidelity (i.e. detailed reaction mechanisms) and low-cost, low-fidelity (i.e. EDC, global reaction mechanisms, and equilibrium flamelets) approaches described above. In this research, the experimental Hypersonic International Flight Research and Experimentation (HIFiRE) Direct Connect Rig (HDCR) dual-mode scramjet combustor is used for a computational modeling campaign and the development of a compressible FPV combustion model. Fully three-dimensional compressible RANS simulations are performed using a 22-species finite-rate reaction mechanism for the combustion of a JP-7 surrogate mixture, and the results are *a priori* analyzed to characterize the fundamental nature of the combustion through the dual-mode regime. Using these findings, several current FPV combustion models are evaluated using a novel *a priori* flamelet-modeled RANS (APFM-RANS) analysis method, and the results of this study lead to the proposal of a new compressible FPV model for application to high-speed reacting flows. Finally, the proposed compressible FPV model is implemented in the Viscous Upwind aLgorithm for Complex flow ANalysis-Computational Fluid Dynamics (VULCAN-CFD) [25] solver, and *a posteriori* testing of the proposed compressible FPV model is performed

for both dual-mode and scram-mode operation of the HDCR. These *a posteriori* simulations demonstrate the physical accuracy and affordability of the FPV models and suggest substantial utility for design and analysis efforts where significant physics are required, but computational affordability is paramount, such as design-space exploration and multidisciplinary optimization.

In the following section, 1.1, a brief statement of the problem addressed by this work is presented, as well as a summary of the supporting research objectives. A detailed outline of this dissertation follows in section 1.2.

## 1.1 Statement of the Problem

Numerous complex flow features complicate the study of dual-mode scramjet engines. These features include laminar-to-turbulent transition along the forebody and within the inlet, shock wave/boundary layer interactions within the isolator, flow separation, turbulent mixing, finite rate reactions, turbulence-chemistry interactions, wall heat transfer, compressibility effects, and additional shock wave/boundary layer interactions within the combustor. Since efficient operation of the engine depends upon these features, predicting the onset and understanding the dynamics of these features is critical to the design and analysis of a flight vehicle. Unfortunately, the current state-of-the-practice and state-of-the-art simulation tools are unable to address the entirety of these complexities, and as such, sometimes gross approximations have to be made for the sake of progress.

The gaps in capability presented by current simulation methods are complemented by the limitations of ground facilities in recreating the conditions within a scramjet engine during flight. While experimentation is often performed in support of engine development and analysis, the results are generally limited to wall pressure and temperature data, and experiments are generally limited to short duration runs at isolated test points and in some cases use vitiated supply air due to the methods used for matching the high total temperatures experienced in flight. Optical- and laser-based diagnostics have made considerable strides in recent years, but still fall short of providing complete tool development and validation data sets.

In practice, RANS solvers continue to serve as the primary means of simulation, as computational affordability remains one of the most limiting factors. The great expense associated with simulating these high-speed, compressible, reacting flows is largely associated with modeling the turbulent combustion. In particular, the numerical stiffness associated with finite-rate reaction mechanisms for realistic fuels often severely limits the solver integration time steps, thereby necessitating alternative methods of modeling the combustion. Some alternative approaches used in prior studies include the eddy dissipation concept [16], equilibrium chemistry flamelet [19], and FPV formulations [20, 24].

FPV models are a particularly intriguing approach for scramjet combustion. While FPV models were originally developed for incompressible reacting flows [26], the approach holds great promise for reducing the cost of simulating supersonic combustion, while simultaneously including significant physical information, if the methodology can be extended to these high-speed, compressible flows. The great strength of the FPV modeling approach is the unique coupling of the thermochemistry to the flow transport equations. Instead of solving for the transported reactive scalars along with transported continuity, momentum, and energy, the FPV formulation relies on computing solutions to the system of one-dimensional, laminar, flamelet equations [27, 28] in the pre-processing step and independently of a CFD solution. The state-space embedded in these flamelet solutions is tabulated and accessed at runtime using transported tracking scalars, such as mixture fraction and progress variable, in place of the original transported reactive scalars. This approach allows for the use of arbitrarily complex reaction mechanisms, at no additional cost to the CFD solver. These models are highly extensible, as well, since the final tabulation can be over an arbitrary number of tracking scalar dimensions. Common practical implementations generally rely on two- and three-dimensional tabulations based on mixture fraction, progress variable, and mixture fraction variance for TCI modeling [26, 29].

Some attempts at extending the standard incompressible FPV model formulation [28] to flows exhibiting strong compressibility effects have been made in recent years [20, 24]; however, these efforts neglect several critical features governing dual-mode scramjet combustion. In each of these studies, the role of static pressure on the thermochemistry has been reduced to a correction on the progress variable production rate, whereas in reality, the entirety of the thermochemistry is a function of pressure. By tabulating the thermochemistry without using static pressure as an independent variable, and rather

simply correcting the tabulated progress variable source term upon extraction, this approach only partially accounts for the effects of compressibility on the combustion. The second major limitation of other efforts regards the calculation of the local static temperature at runtime. Since the total energy varies considerably across space and time for scramjet flowfields, the local temperature must be computed using the transported total energy, along with the local composition. Current, commonly used, FPV models rely on computing the local temperature using linearizations around the tabulated flamelet temperature data or by simply using the flamelet temperature directly. The final, and perhaps most important, problem with existing compressible FPV models is the omission of any variability in oxidizer and fuel pressures and temperatures as seen by the flames. These parameters are generally held fixed for all existing FPV models. However, in a scramjet combustor, the local thermodynamic state can change significantly from region to region due to the influence of compression waves, expansions, and heat losses at the walls. Without considering the variability in these flamelet boundary conditions, any FPV model may misrepresent the thermochemical state-space embedded in the flowfield.

The primary objective of the current dissertation is to evaluate FPV modeling for application to dual-mode scramjet combustors of engineering complexity. Achieving this primary objective relies on satisfying four supporting research objectives, which include:

#### **Research Objective One**

Construct a database of realistic flow solutions for an experimental dual-mode scramjet combustor of engineering complexity using RANS with finite-rate chemical kinetics and validate using experimental data.

#### **Research Objective Two**

Assess fundamental flamelet theory and FPV model assumptions *a priori* for an experimental dual-mode scramjet combustor flowfield.

#### **Research Objective Three**

Develop a compressible FPV model formulation for application to dual-mode scramjet combustors after *a priori* analyzing the efficacy of state-of-the-art FPV model formulations.

### **Research Objective Four**

Assess the accuracy and performance of compressible FPV model formulations *a posteriori* using a production-level CFD solver for an experimental scramjet combustor.

The research contributions presented in detail throughout the remainder of this dissertation support these research objectives and thereby advance the state-of-the-art for computationally affordable modeling and simulation for hydrocarbon-fueled dual-mode scramjet combustors of engineering complexity using FPV methods. The results of this research will provide researchers and designers a critical new capability where low-cost, higher-fidelity combustion modeling is required.

## **1.2 Dissertation Outline**

The dissertation consists of seven chapters and two appendices, in addition to the front matter. A brief outline is presented below.

Following the current introductory chapter, Chapter 2 establishes the background material required to assimilate the work presented in subsequent chapters. Section 2.1 presents an overview of fundamental scramjet operation principles and recent major research efforts, with particular emphasis on dual-mode scramjet engines. Next, section 2.2 presents the transport equations governing high-speed, compressible, reacting flows. Finally, FPV-based approaches for modeling turbulent combustion are described in section 2.3.

Chapter 3 begins by providing an overview of the HDCR experiment, including both an overview of the experimental tests and flow diagnostics and also the major flow features governing the combustor's operation at test points spanning both dual-mode and scram-mode operation. Details of the combustor flowpath are presented. The chapter also details three-dimensional, compressible, finite-rate RANS simulations of the HDCR combustor at test points characterizing both dual- and scram-mode operation, which correspond to simulated flight Mach numbers of 5.84 and 8.00, respectively. The simulation results are validated against experimental measurements, and major flow features are discussed. The results shown in this chapter represent the baseline data sets for subsequent model development and validation purposes.

Chapter 4 describes an *a priori* characterization of the HDCR's combustion dynamics. First, the flame structures are identified through the use of a flame index. Once isolated, a detailed study of the flame structure is performed using a mode index designed to indicate dominant combustion modes, and fundamental assumptions of flamelet theory are evaluated. The construction of relevant flame regime diagrams yields critical information on the efficacy of flamelet-based modeling for the HDCR. Theorized flamelet boundary conditions are elicited from the RANS data set of Chapter 3, and probability density functions (PDFs) of these properties are used to estimate their importance in recovering prominent HDCR combustion dynamics.

Chapter 5 presents the development and application of the APFM-RANS analysis method. Applications of the APFM-RANS analysis method include a trade study on progress variable definitions, validation of several progress variable production rate correction models, investigation of several FPV model coupling approaches, and assessment of IFPV and CFPV models from the literature. The CFPVX model is proposed, and applications to the HDCR combustor are demonstrated using the APFM-RANS analysis method.

Following the development and *a priori* validation of the CFPVX model, *a posteriori* testing is performed in Chapter 6. In support of this analysis, an FPV modeling capability is implemented in VULCAN-CFD. Earlier APFM-RANS analyses of the HDCR combustor are repeated by solving the three-dimensional, FPV-modeled, Favre-averaged RANS equations using VULCAN-CFD. These *a posteriori* results are shown to support the observations made in prior chapters using the *a priori* approaches.

The dissertation concludes in Chapter 7 with a summary of important findings and research contributions, as well as a discussion of planned follow-on work.



## Chapter 2

# Background

In this chapter, the fundamentals of scramjet engine design and operation, as well as an overview of recent research campaigns, are presented in section 2.1, with an emphasis on dual-mode scramjet engines. In section 2.2, the governing equations for compressible reacting flows are presented, along with brief discussion of relevant closure models. Finally, section 2.3 provides an overview of current FPV models available in the literature, with an emphasis on the limitations of existing compressible formulations.

### 2.1 Scramjet Fundamentals

#### 2.1.1 Operational Overview

Conceptually developed as an efficient means of hypersonic flight via utilization of atmospheric oxygen, scramjet engines generally require few moving parts and, in their most basic form, are comprised of four primary functional components. These components include the inlet, the isolator, the combustor, and the exit nozzle, and each is designed to uniquely process the flow. A notional layout of a scramjet engine showing these four basic components is shown in Fig. 2.1.

As the incoming supersonic or hypersonic air enters the engine, the inlet first acts to compress and slow the air. If the engine is operating in a ramjet-mode, which typically includes vehicle speeds less than approximately Mach 4, this compression drives the air

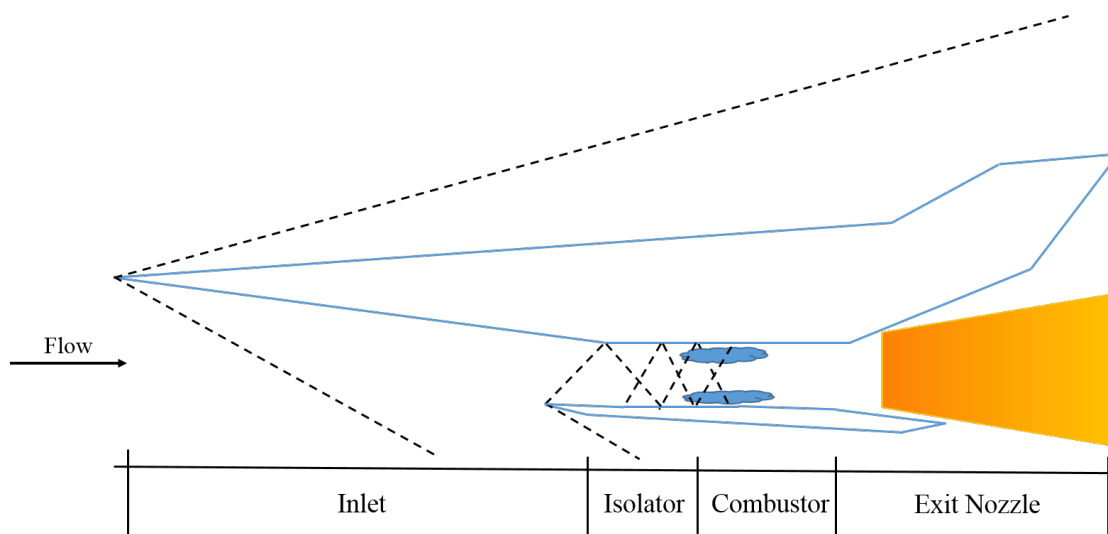


FIGURE 2.1: A notional schematic detailing the four primary components of a scramjet engine.

velocity to subsonic speeds. If, on the other hand, the engine is operating in scram-mode, the inlet compresses the air without driving it below the sonic limit.

The inlet leads to the isolator, which generally consists of a straight duct used to damp any substantial fluidic disturbances in the free stream prior to entering the combustion chamber during dual-mode engine operation. A system of oblique shocks in the isolator helps to provide this damping effect, and the positioning of this shock train is generally a critical design consideration. Without proper margin, the isolator shock train could exit the entrance to the isolator and anchor in the inlet leading to inefficient engine operation, or even worse, exit also the inlet and form a bow shock ahead of the vehicle leading to catastrophic failure.

Upon leaving the isolator section, the air enters the combustor where it is mixed with fuel and burned. For scram-mode operation, the mixing of fuel and air must occur on relatively short time scales due to the incoming supersonic air velocities, and the combustion in many cases is mixing-limited. Thus, efficient combustion within the engine relies on efficient mixing of the fuel and air. Designing scramjet combustors to minimize mixing length and maximize mixing efficiency is a critical requirement for successful engine operation. Once the fuel and oxidizer have reacted within the combustor, the resultant hot gases exit the engine through the exit nozzle resulting in a net thrust force, which propels the vehicle forward.

As a scramjet accelerates from approximately Mach 4 to Mach 6 from dual- to scram-mode, the flow within the engine undergoes critical changes. The combustor swallows any shocks residing upstream in the isolator, and large regions of separated flow, shock-boundary-layer interactions, and shock reflections may develop and subsequently dissipate throughout the engine. During this transition, the combustor must still maintain efficient combustion to maintain positive thrust and prevent engine flame-out. The interplay among these complex fluid phenomena makes predicting combustor characteristics a critical element of the vehicle design process. As will be described below, experimental investigation of combustors operating in both dual- and scram-mode is significantly limited due to facility hardware and available diagnostic techniques. As a result, recent decades have seen a shift toward the development of higher-fidelity modeling and simulation tools for such purposes.

### 2.1.2 Overview of Recent Research Campaigns

Despite the many difficulties associated with experimentally-testing scramjet engines, several fruitful efforts have been made over the past several decades. Due to the significant resources required, these experiments have largely been the result of concentrated efforts by governmental research agencies and consortia of private and public research entities. Several of these programs are summarized here.

Hyper-X was a particularly visible program led by NASA in the late 1990s and early 2000s whose intent was to demonstrate the viability of state-of-the-art design tools and experimental techniques for the design and testing of an airframe-integrated scramjet fueled by hydrogen [1, 2]. The eight-year campaign included numerous ground tests and three flight tests. These three flights included one failure in June 2001, a record-breaking flight in March of 2004 that marked the first ever air-breathing engine to reach hypersonic speeds, and a second successful flight in November of 2004. The successful flights reached speeds of Mach 6.8 and 9.6, respectively. Significant ground-testing was performed at several research facilities around the country using both blowdown and continuously-run, combustion heated tunnels, including the Arc-Heated Scramjet Test Facility at NASA Langley Research Center [30], the Hypersonic Pulse Facility (HyPulse) operated at the General Applied Science Laboratory (GASL) in New York [31], and the 8' High Temperature Tunnel at NASA Langley Research Center [30], among others.

The Hyper-X program resulted in a wealth of data for use by designers, modelers, and technologists of scramjet vehicle systems.

Following the success of the Hyper-X program, the Office of Naval Research (ONR) and the Defense Advanced Research Projects Agency (DARPA) launched the Freeflight Atmospheric Scramjet Test Technique (FASTT) [32] vehicle in December 2005, which became the first air-breathing, liquid hydrocarbon fueled scramjet engine to fly successfully. Launched from NASA Wallops Flight Facility aboard a two-stage Terrier-Orion solid-rocket, the missile-like vehicle flew at Mach 5.5 for approximately 15 seconds. The mission was a success and demonstrated low-cost flight techniques while obtaining in-flight performance data at hypersonic vehicle velocities.

The Air Force Research Laboratory (AFRL) followed years of ground-based experimentation and analysis of scramjet engines with the X-51A Scramjet Engine Demonstrator (SED)-WaveRider program [33] in 2009. The X-51 scramjet marked the first hydrocarbon fuel-cooled scramjet to accelerate and free-fly under scramjet propulsion after being launched from an Army Tactical Missile System (ATMS) missile from the underside of a B-52. Upon separating from the ATMS missile at Mach 4.5, the X-51 vehicle accelerated to approximately Mach 6.5, and the X-51A demonstrated the viability of an endothermically fueled, free-flying, scramjet-powered vehicle.

Targeting the dual-mode transition, specifically, the Hypersonic International Flight Research and Experimentation (HIFiRE) program [5, 6] was a combination computational and experimental campaign targeted at better understanding the physics governing the efficient operation of a scramjet flight vehicle accelerating through the dual-mode transition regime. Considerable computational studies were performed supporting the design of the experiments and benchmarking vehicle flight characteristics prior-to, during, and after the flight experiments [16, 34, 35]. Perhaps the most important of the flights, HIFiRE flight 2 successfully demonstrated dual-mode transition for a hydrocarbon-fueled scramjet by changing the aerodynamic conditions at the inlet. Over 700 instruments on board the test article collected and transmitted data to ground stations, and these data are being used to better understand the process of dual-mode transition and to develop higher-fidelity tools for the design and analysis of dual-mode scramjets.

The latest major effort toward understanding the mechanics of dual-mode scramjet engines at the combustor-level is the National Center for Hypersonic Combined Cycle

Propulsion (NCHCCP) [36]. The NCHCCP is one of three centers of technical excellence in hypersonics and is led by the University of Virginia (UVa). It is comprised of a consortium of universities that was founded and funded jointly by NASA and the United States Air Force. The NCHCCP is dedicated to advancing the understanding of critical mode transitions required by proposed scramjet vehicle concepts using both experimental and modeling research efforts. Experiments for several dual-mode scramjet combustors were undertaken at UVa, where advanced diagnostics were developed by UVa and George Washington University. Computational investigations of the same configurations were undertaken by researchers at UVa, Cornell University, the University of Buffalo, North Carolina State University, and the University of Pittsburgh, where a major focus was on modeling of turbulent reacting flows and extending higher-fidelity simulation techniques like hybrid RANS/LES and LES to such flows. The guiding objective of this effort was to increase understanding of fundamental dual-mode combustion physics through targeted experimentation and enhanced computational modeling and predictive capabilities.

The past two decades have resulted in considerable gains in the understanding, measuring, and modeling of the flow and combustion physics important for scramjet engines of engineering complexity, as evidenced by the numerous successful research campaigns both domestically and internationally. And while the gains made were significant, for example HIFiRE 2's successful hydrocarbon-fueled, in-flight, dual-mode transition, significant limitations remain. Specifically, computational expense is a major limiting factor for the advanced models developed through these research campaigns, and the current dissertation focuses on developing a combustion model that is *enabling*, rather than simply *higher-fidelity*.

## 2.2 Governing Equations

High-speed, reacting, compressible flows are governed by conservation equations for mass, momentum, energy, and the reactive scalars comprising the chemical mixture. These transport equations, which are comprised of the full Navier-Stokes equations paired with the set of reactive scalar transport equations, are generally computationally intractable for problems of engineering interest. That is, resolving all the time and length scales necessary for flows at high Reynolds numbers would require prohibitive grid densities. Therefore, these equations are typically modeled using the Reynolds decomposition

and time-averaging. Following presentation of the full set of equations governing compressible flows below in section 2.2.1, the Reynolds-averaged Navier-Stokes equations governing compressible reacting flows are presented in section 2.2.2 with accompanying discussion of models required for system closure.

### 2.2.1 Compressible Navier-Stokes Equations

The compressible, unsteady, three-dimensional Navier-Stokes equations along with mass continuity equations for a set of reactive scalars are shown below in Eqs. (2.1)-(2.4) using Einstein index summation notation

$$\frac{\partial \rho}{\partial t} + \frac{\partial \rho u_j}{\partial x_j} = 0 \quad (2.1)$$

$$\frac{\partial \rho u_i}{\partial t} + \frac{\partial \rho u_i u_j}{\partial x_j} = -\frac{\partial p}{\partial x_i} + \frac{\partial \tau_{ij}}{\partial x_j} \quad (2.2)$$

$$\frac{\partial \rho E}{\partial t} + \frac{\partial \rho u_j H}{\partial x_j} = \frac{\partial \tau_{ij} u_i}{\partial x_j} - \frac{\partial q_j}{\partial x_j} \quad (2.3)$$

$$\frac{\partial \rho Y_\alpha}{\partial t} + \frac{\partial \rho u_j Y_\alpha}{\partial x_j} = -\frac{\partial \rho Y_\alpha V_j^\alpha}{\partial x_j} + \dot{\omega}_\alpha \quad (2.4)$$

where  $\rho$  is static density,  $t$  is time,  $u_j$  are the component velocities,  $x_j$  are the Cartesian coordinates,  $p$  is static pressure,  $\tau_{ij}$  is the stress tensor,  $E$  is total energy,  $H$  is total enthalpy,  $q_j$  are the component heat flux vectors,  $Y_\alpha$  is the mass fraction for species  $\alpha$ ,  $V_j^\alpha$  is the diffusion velocity for species  $\alpha$ , and  $\dot{\omega}_\alpha$  is the production rate for species  $\alpha$ .

The total energy,  $E$ , is the sum of the internal energy,  $e$ , and the kinetic energy,  $\frac{1}{2}u_i u_i$ , as shown in Eq. (2.5), and similarly, the total enthalpy,  $H$ , is the sum of the static enthalpy,  $h$ , and the kinetic energy, as shown in Eq. (2.6).

$$E \equiv e + \frac{1}{2}u_i u_i \quad (2.5)$$

$$H \equiv h + \frac{1}{2}u_i u_i \quad (2.6)$$

The mixture static enthalpy,  $h$ , is given by Eq. (2.7), where  $h_\alpha$  are the species static enthalpies given by NASA polynomial curve fits [37].

$$h = \sum_{\alpha} Y_\alpha h_\alpha \quad (2.7)$$

For the large class of flows meeting the assumption of a Newtonian fluid, the stress tensor,  $\tau_{ij}$ , is proportional to the fluid strain rate and is given by the constitutive relation shown in Eq. (2.8), where  $\mu$  is the mixture viscosity and  $\delta_{ij}$  is the Kronecker delta function.

$$\tau_{ij} = \mu \left( \frac{\partial u_i}{\partial x_j} + \frac{\partial u_j}{\partial x_i} \right) - \frac{2}{3} \mu \delta_{ij} \frac{\partial u_k}{\partial x_k} \quad (2.8)$$

The heat flux vector,  $q_j$ , is comprised of two terms representing the transport of  $E$  due to heat conduction and energy interdiffusion processes, shown in Eq. (2.9), where  $\lambda$  is the mixture thermal conductivity and  $T$  is the static temperature. In the current formulation, the Dufour effect is neglected [38].

$$q_j = -\lambda \frac{\partial T}{\partial x_j} + \rho \sum_{\alpha} h_{\alpha} Y_{\alpha} V_j^{\alpha} \quad (2.9)$$

Fick's law of diffusion is used to model the diffusion velocities,  $V_j^{\alpha}$ , as shown in Eq. (2.10), where  $D_{\alpha}$  is the mass diffusion coefficient for species  $\alpha$ .

$$V_j^{\alpha} = -\frac{D_{\alpha}}{Y_{\alpha}} \frac{\partial Y_{\alpha}}{\partial x_j} \quad (2.10)$$

The species production rates,  $\dot{\omega}_{\alpha}$ , are typically computed using the law of mass action in combination with the Arrhenius model for forward reaction rate coefficients and the equilibrium constant to compute the backward reaction rate coefficients. Additional details of this process can be found in many textbooks on the simulation of reacting flows, such as in Ref. 39.

The transport properties  $\mu$ ,  $\lambda$ , and  $D_{\alpha}$  required to close Eqs. (2.8), (2.9), and (2.10), respectively, are primarily functions of the composition and temperature. For the current study,  $\mu$  and  $\lambda$  for individual species are modeled using Sutherland's Law [40]. Mixture based  $\mu$  is computed using Wilke's Law [41], and mixture-based  $\lambda$  is computed using Wassilej's Law [41]. The diffusion coefficients,  $D_{\alpha}$  are assumed equal in accordance with the assumption of constant Lewis number,  $Le$ , for which the mixture diffusion coefficient,  $D$ , may be computed using Eq. (2.11)

$$D = \frac{Pr}{Sc} \frac{\lambda}{\rho C_p} = \frac{1}{Le} \frac{\lambda}{\rho C_p} \quad (2.11)$$

where  $Pr$  is the Prandtl number,  $Sc$  is the Schmidt number, and  $C_p$  is the mass-based specific heat at constant pressure. Finally, the set of governing equations is closed using

an equation of state following the assumption of a mixture of thermally perfect gases. This equation of state relates the thermodynamic properties and is shown below in Eq. (2.12)

$$p = \rho T R = \rho T \sum_{\alpha} R_{\alpha} = \rho T R_u \sum_{\alpha} \frac{Y_{\alpha}}{MW_{\alpha}} \quad (2.12)$$

where  $R$  is the mixture gas constant,  $R_{\alpha}$  is the gas constant for species  $\alpha$ ,  $R_u$  is the universal gas constant, and  $MW_{\alpha}$  is the molecular weight for species  $\alpha$ .

## 2.2.2 Compressible RANS Equations

For flows at Reynolds numbers characteristic of dual-mode scramjet engines, direct solution of Eqs. (2.1)-(2.4) remains computationally unfeasible. In this section, the development of the Favre-averaged RANS equations is briefly summarized, and the governing equations currently solved by VULCAN-CFD are presented with discussion of relevant closure models. A complete derivation of these equations can be found in Ref. 42.

As is commonly done for compressible flows, a combination of both time- and Favre-averaging of Eqs. (2.1)-(2.4) is used for the Reynolds decomposition. This decomposition splits the flow variables into two signals comprising a mean and a fluctuating component, defined below in Eq. (2.13) for both time- and Favre-averaging, where  $\varphi$  is the instantaneous property,  $\bar{\varphi}$  is the mean property component,  $\varphi'$  is the fluctuating property component,  $\tilde{\varphi}$  is the density-based mean property component,  $\varphi''$  is the density-based fluctuating property component, and  $t_0$  is a reference time.

$$\text{Time-Average: } \varphi = \bar{\varphi} + \varphi' \quad \text{where} \quad \bar{\varphi} = \lim_{\Delta t \rightarrow \infty} \frac{1}{\Delta t} \int_{t_0}^{t_0 + \Delta t} \varphi dt \quad (2.13)$$

$$\text{Favre-Average: } \varphi = \tilde{\varphi} + \varphi'' \quad \text{where} \quad \tilde{\varphi} = \frac{1}{\bar{\rho}} \lim_{\Delta t \rightarrow \infty} \frac{1}{\Delta t} \int_{t_0}^{t_0 + \Delta t} \rho \varphi dt$$

The resulting equations form the complete set of unclosed, Favre-averaged RANS equations, as shown in Eqs. (2.14)-(2.17).

$$\frac{\partial \bar{\rho}}{\partial t} + \frac{\partial \bar{\rho} \tilde{u}_j}{\partial x_j} = 0 \quad (2.14)$$

$$\frac{\partial \bar{\rho} \tilde{u}_i}{\partial t} + \frac{\partial \bar{\rho} \tilde{u}_i \tilde{u}_j}{\partial x_j} = - \frac{\partial \bar{p}}{\partial x_i} + \frac{\partial \bar{\tau}_{ij}}{\partial x_j} - \frac{\partial \widetilde{\bar{\rho} u''_i u''_{jj}}}{\partial x_j} \quad (2.15)$$

$$\frac{\partial \bar{\rho} \tilde{E}}{\partial t} + \frac{\partial \bar{\rho} \tilde{H} \tilde{u}_j}{\partial x_j} = -\frac{\partial \bar{\rho} \widetilde{H'' u_j''}}{\partial x_j} + \frac{\partial \bar{\tau}_{ij} \tilde{u}_i}{\partial x_j} + \frac{\partial \overline{\tau_{ij} u_i''}}{\partial x_j} - \frac{\partial \bar{q}_j}{\partial x_j} \quad (2.16)$$

$$\frac{\partial \bar{\rho} \tilde{Y}_\alpha}{\partial t} + \frac{\partial \bar{\rho} \tilde{Y}_\alpha \tilde{u}_j}{\partial x_j} = -\frac{\partial \bar{\rho} \tilde{Y}_\alpha \tilde{V}_j^\alpha}{\partial x_j} - \frac{\partial \overline{\rho Y_\alpha'' V_j^{\alpha''}}}{\partial x_j} - \frac{\partial \bar{\rho} \widetilde{Y_\alpha'' u_j''}}{\partial x_j} + \bar{\omega}_\alpha \quad (2.17)$$

Several terms in these equations require closure, and by using the closure models described in Ref. 42, the complete set of equations solved by VULCAN-CFD may be written as shown below in Eqs. (2.18)-(2.22).

$$\frac{\partial \bar{\rho}}{\partial t} + \frac{\partial \bar{\rho} \tilde{u}_j}{\partial x_j} = 0 \quad (2.18)$$

$$\begin{aligned} \frac{\partial \bar{\rho} \tilde{u}_i}{\partial t} + \frac{\partial \bar{\rho} \tilde{u}_i \tilde{u}_j}{\partial x_j} = & -\frac{\partial \bar{p}}{\partial x_i} \\ & + \frac{\partial}{\partial x_j} \underbrace{\left\{ (\mu + \mu_t) \left[ \left( \frac{\partial \tilde{u}_i}{\partial x_j} + \frac{\partial \tilde{u}_j}{\partial x_i} \right) - \frac{2}{3} \delta_{ij} \frac{\partial \tilde{u}_k}{\partial x_k} \right] - \frac{2}{3} \delta_{ij} \bar{\rho} \tilde{k} \right\}}_{\bar{\tau}_{ij} - \bar{\rho} \widetilde{u_i'' u_j''}} \end{aligned} \quad (2.19)$$

$$\begin{aligned} \frac{\partial \bar{\rho} \tilde{E}}{\partial t} + \frac{\partial \bar{\rho} \tilde{H} \tilde{u}_j}{\partial x_j} = & \frac{\partial}{\partial x_j} \underbrace{\left\{ \tilde{u}_i \left[ \mu \left( \frac{\partial \tilde{u}_i}{\partial x_j} + \frac{\partial \tilde{u}_j}{\partial x_i} \right) - \frac{2}{3} \delta_{ij} \mu \frac{\partial \tilde{u}_k}{\partial x_k} \right] \right\}}_{\tilde{u}_i \bar{\tau}_{ij}} \\ & + \frac{\partial}{\partial x_j} \underbrace{\left[ \left( \lambda + \frac{\mu_t c_p}{Pr_t} \right) \frac{\partial \tilde{T}}{\partial x_i} + \left( \frac{\mu}{Sc} + \frac{\mu_t}{Sc_t} \right) \sum_\alpha \tilde{h}_\alpha \frac{\partial \tilde{Y}_\alpha}{\partial x_j} \right]}_{\bar{q}_j - \bar{\rho} \widetilde{h'' u_j''}} + \frac{\partial}{\partial x_j} \underbrace{\left[ \left( \frac{\mu}{\sigma_k} + \frac{\mu_t}{\sigma_k} \right) \frac{\partial \tilde{k}}{\partial x_j} \right]}_{\overline{\tau_{ij} u_i''}} \end{aligned} \quad (2.20)$$

$$\begin{aligned} \frac{\partial \bar{\rho} \tilde{Y}_\alpha}{\partial t} + \frac{\partial \bar{\rho} \tilde{Y}_\alpha \tilde{u}_j}{\partial x_j} = & \frac{\partial}{\partial x_j} \underbrace{\left[ \left( \frac{\mu}{Sc} + \frac{\mu_t}{Sc_t} \right) \frac{\partial \tilde{Y}_\alpha}{\partial x_j} \right]}_{-\bar{\rho} \tilde{Y}_\alpha \tilde{V}_j^\alpha - \overline{\rho Y_\alpha'' V_j^{\alpha''}} - \bar{\rho} \widetilde{Y_\alpha'' u_j''}} + \bar{\omega}_\alpha \end{aligned} \quad (2.21)$$

$$\bar{p} = \bar{\rho} \tilde{T} R_u \sum_\alpha \frac{\tilde{Y}_\alpha}{MW_\alpha} \quad (2.22)$$

where  $\mu_t$  is the eddy viscosity,  $c_p$  is the specific heat at constant pressure,  $Pr_t$  is the turbulent Prandtl number,  $Sc_t$  is the turbulent Schmidt number,  $\sigma_k$  is a turbulence modeling parameter, and  $\tilde{k}$  is the turbulence kinetic energy. The instantaneous terms from

Eqs. (2.14)-(2.17) are annotated below the corresponding modeled terms in Eqs. (2.18)-(2.22). The static temperature,  $\tilde{T}$ , is computed by performing a Newton-Raphson iteration on Eq. (2.23).

$$0 = \tilde{E} - \sum_{\alpha} \tilde{h}_{\alpha}(\tilde{T})Y_{\alpha} + R_u\tilde{T} \sum_{\alpha} \frac{\tilde{Y}_{\alpha}}{MW_{\alpha}} - \tilde{k} - \frac{1}{2}\tilde{u}_i\tilde{u}_i \quad (2.23)$$

With user-supplied values for  $Pr_t$ ,  $Sc$ , and  $Sc_t$  and an appropriate turbulence model for computing  $\mu_t$ ,  $\sigma_k$ , and  $\tilde{k}$ , these equations are completely closed. For the current work, the two equation turbulence model of Menter [43] is used, for which additional transport equations are solved for turbulence kinetic energy,  $\tilde{k}$ , and frequency,  $\tilde{\omega}$ .

## 2.3 Flamelet-Based Combustion Modeling

Flamelet-based combustion modeling techniques like flamelet-generated manifolds [44] and FPV models [26] leverage the flamelet concept [27] to dramatically reduce the computational cost of reacting flow simulations. This cost reduction is achieved by parameterizing the entire relevant thermochemical state-space using a small set of tracking scalars, for which transport equations may then be solved at simulation runtime. This class of models relies on the assumption that all gradients not orthogonal to the turbulent flame sheet are negligible, thereby effectively representing the turbulent flame region as a one-dimensional laminar flame. As will be seen in section 2.3.1, this simplification allows one to effectively couple the flame chemistry to the flowfield using a single, mixing-based parameter known as scalar dissipation rate,  $\chi$ , while still retaining much of the complexity offered by detailed finite-rate reaction mechanism models. Overviews of the steady laminar flamelet (SLF) and the incompressible FPV (IFPV) models are included in sections 2.3.2 and 2.3.3, respectively. The final section, 2.3.4, discusses recent efforts at extending the incompressible flamelet modeling framework to the types of high-speed, compressible, reacting flows typical of scramjet engines.

### 2.3.1 Flamelet Modeling Theory

From a physical perspective, under certain conditions, it is reasonable to posit that three-dimensional, turbulent flames can be approximately described as one-dimensional

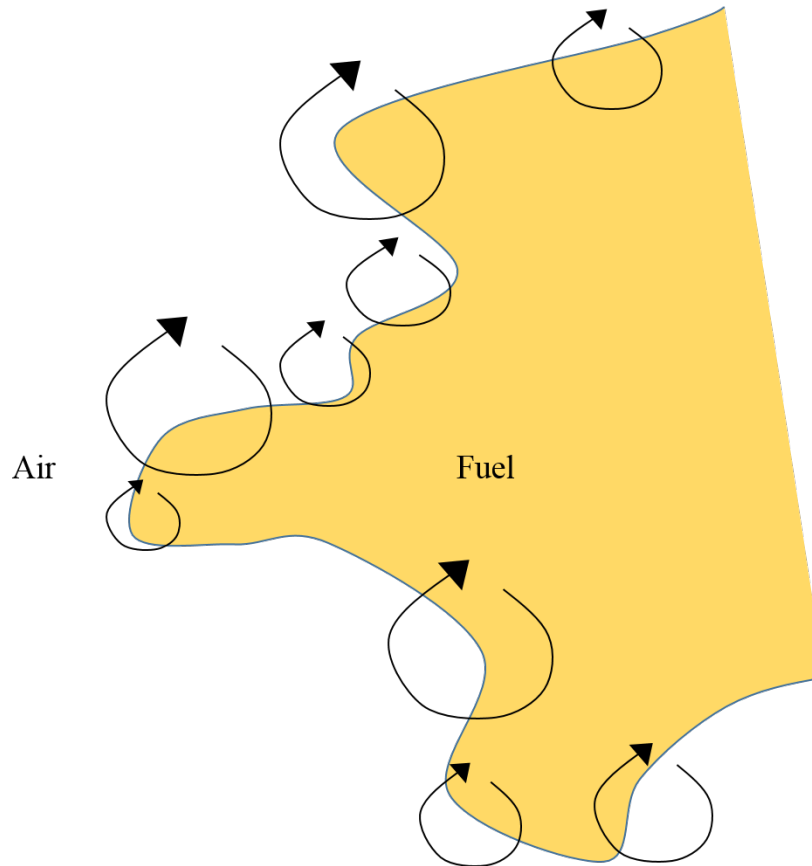


FIGURE 2.2: Notional schematic of a non-premixed laminar flame approximation to a turbulent flame configuration for which local turbulent eddies serve to wrinkle a thin and locally laminar flame surface.

laminar flames subjected to wrinkling and stretching by local turbulent eddies. Such an interpretation may be especially appropriate when the reaction chemistry occurs much more quickly than the characteristic eddy turnover time. While perhaps fast enough to warp the flame sheet, these characteristic eddies may not significantly alter the internal structure of the flame, as shown conceptually in Fig. 2.2. In fact, under certain conditions, the gradients orthogonal to the flame sheet may be all that is necessary to accurately describe the local reaction chemistry. In this theoretical situation, complex three-dimensional turbulent flames may be approximated using an ensemble of locally-embedded, one-dimensional, laminar flames, and it is this physical argument that gave rise to the idea of using one-dimensional laminar flames—or *flamelets*—as a way to model complex three-dimensional turbulent combustion.

A more rigorous description of this proposed configuration relies on the use of Damköhler number,  $Da$ , which is defined as the ratio of a characteristic flow time scale,  $\tau_{flow}$ , and

a chemical time scale,  $\tau_{chem}$ , below in Eq. (2.24).

$$Da = \frac{\tau_{flow}}{\tau_{chemical}} \quad (2.24)$$

For the conditions described above to hold true,  $Da$  must be necessarily much greater than unity, and the chemical reactions must occur significantly faster than local turbulent transport processes. In this limit, the rate of scalar dissipation,  $\chi$ , may serve as the primary means of straining the flame surface in response to local fluid mechanical properties. In subsequent discussions, these physical conditions characterized by  $Da \gg 1$  will be generally referenced as the *flamelet limit*.

A fundamental tenant of flamelet-based approaches to combustion modeling is the ubiquitous utility of the mixture fraction,  $Z$ , as a means of tracking local mixture properties. Specifically, for the current discussion,  $Z$  represents the fraction of mass originating in the fuel stream present in the mixture locally. The definition of  $Z$  is shown below in Eq. (2.25) for a generic mixture

$$Z = \frac{\Omega - \Omega_O}{\Omega_F - \Omega_O} \quad (2.25)$$

where  $\Omega_F$  and  $\Omega_O$  are the fractions of fuel mass in the fuel and oxidizer streams. The fuel mass fraction,  $\Omega$ , is defined below in Eq. (2.26) as

$$\Omega = \sum_i \gamma_i \sum_j \frac{a_{ij} MW_i Y_j}{MW_j} \quad (2.26)$$

where  $\gamma_i$  are elemental mixture fraction weights,  $a_{ij}$  is the number of atoms of element  $i$  in species  $j$ ,  $MW_i$  and  $MW_j$  are molecular weights of species  $i$  and  $j$ , respectively, and  $Y_i$  is the mass fraction of species  $i$ . Bilger's definition of  $Z$  for mixtures containing C, H, and O elements requires that  $\gamma_i$  be set according to Eq. (2.27) below [45].

$$\gamma = \begin{bmatrix} \gamma_C \\ \gamma_H \\ \gamma_O \end{bmatrix} = \begin{bmatrix} \frac{2}{MW_C} \\ \frac{1}{2MW_H} \\ -\frac{1}{MW_O} \end{bmatrix} \quad (2.27)$$

Mixture fraction is a passive scalar, for which transport is governed by convection and diffusion processes, only. Accordingly, the Favre-averaged transport equation for  $\tilde{Z}$  may be written assuming constant  $Sc$  and  $Sc_t$  numbers using the principles of section 2.2.2

and is shown below in Eq. (2.28).

$$\frac{\partial \bar{\rho} \tilde{Z}}{\partial t} + \frac{\partial \bar{\rho} \tilde{Z} \tilde{u}_j}{\partial x_j} = \frac{\partial}{\partial x_j} \left[ \left( \frac{\mu}{Sc} + \frac{\mu_t}{Sc_t} \right) \frac{\partial \tilde{Z}}{\partial x_j} \right] \quad (2.28)$$

Flamelet-based models also rely on solutions of the laminar flamelet equations [27, 28]. The derivation of these equations relies on the assumption that time,  $t$ , and mixture fraction,  $Z$ , are the only coordinates required to solve for the dynamics of a chemically-reacting system, which leads to the coordinate transformation shown in Eq. (2.29).

$$(t, x_j) \mapsto (t, Z) \iff \begin{aligned} \frac{\partial}{\partial t} &\mapsto \frac{\partial}{\partial t} + \frac{\partial Z}{\partial t} \frac{\partial}{\partial Z} \\ \frac{\partial}{\partial x_j} &\mapsto \frac{\partial Z}{\partial x_j} \frac{\partial}{\partial Z} \end{aligned} \quad (2.29)$$

After applying this coordinate transformation to the total energy and reactive scalar transport equations shown previously in Eqs. (2.3) and (2.4), respectively, and invoking a low Mach number assumption, an asymptotic analysis [27] leads to the set of partial differential equations in  $Z$  and  $t$  space forming the unsteady, laminar flamelet equations, which are often expressed for  $Y_\alpha$  and  $T$ , as shown in Eqs. (2.30) and (2.31)

$$\rho \frac{\partial Y_\alpha}{\partial t} - \frac{1}{2} \rho \chi \frac{\partial^2 Y_\alpha}{\partial Z^2} - \dot{\omega}_\alpha = 0 \quad (2.30)$$

$$\rho \frac{\partial T}{\partial t} - \frac{1}{2} \rho \chi \frac{\partial^2 T}{\partial Z^2} + \frac{1}{c_p} \sum_{\alpha=1}^N h_\alpha \dot{\omega}_\alpha = 0 \quad (2.31)$$

where  $\chi$  is the scalar dissipation rate and is given by

$$\chi \equiv 2D \frac{\partial Z}{\partial x_j} \frac{\partial Z}{\partial x_j} \quad (2.32)$$

The steady form of these equations is the foundation of steady laminar flamelet models, which are described in the next section.

### 2.3.2 Steady Laminar Flamelet Model

Application of the steady laminar flamelet (SLF) model [27, 28] to a three-dimensional, turbulent combustion simulation requires first solving the transport equation for  $\tilde{Z}$  shown in Eq. (2.28) in place of the reactive scalar transport equations for  $\tilde{Y}_\alpha$ . A functional form for the Favre-averaged scalar dissipation rate,  $\tilde{\chi}$ , is then specified as a function of  $\tilde{Z}$ .

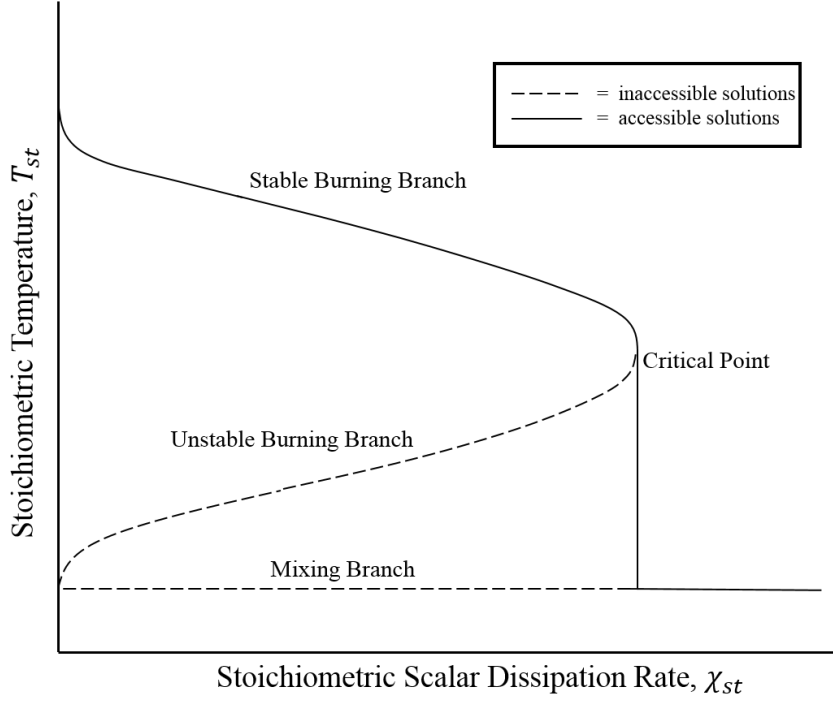


FIGURE 2.3: Notional S-shaped curve demonstrating the multivaluedness in  $Z$ - $\chi_{st}$  space for the steady flamelet model formulation.

The form used by Peters [27] and Kim and Williams [46] is shown below in Eq. (2.33),

$$\tilde{\chi} = 4a_s \tilde{Z}^2 [\text{erfc}^{-1}(2\tilde{Z})]^2 \quad (2.33)$$

where  $a_s$  is the stagnation-point velocity gradient for the counterflow flamelet configuration and  $\text{erfc}$  is the inverse of the error function. Using  $\tilde{Z}$  and  $\tilde{\chi}$ , a fully-three dimensional turbulent combustion simulation solving Eqs. (2.18)-(2.20) with (2.28) and (2.33) may be closed by retrieving  $\tilde{Y}_\alpha$ ,  $\tilde{\omega}_\alpha$ , and  $\tilde{T}$  from tabulated solutions of the flamelet equations using the SLF model vector,  $\phi_{SLF}$ , which is defined in Eq. (2.34).

$$\phi_{SLF} = \begin{bmatrix} \tilde{Z} \\ \tilde{\chi}_{st} \end{bmatrix} \quad (2.34)$$

While all solution states along the curve of stoichiometric temperature,  $T_{st}$ , versus stoichiometric scalar dissipation rate,  $\chi_{st}$ , are embedded in the steady, laminar flamelet equations, only stable burning and mixing solutions are accessible using the SLF model parameterization. The S-shaped curve (i.e.  $T_{st}$  versus  $\chi_{st}$ ) is multivalued in  $Z$ - $\chi_{st}$  space, as shown in Fig. 2.3, and this limitation is one of the primary drawbacks of using the SLF model [27, 28]. Without accessing the unstable branch of solutions, physically-realistic

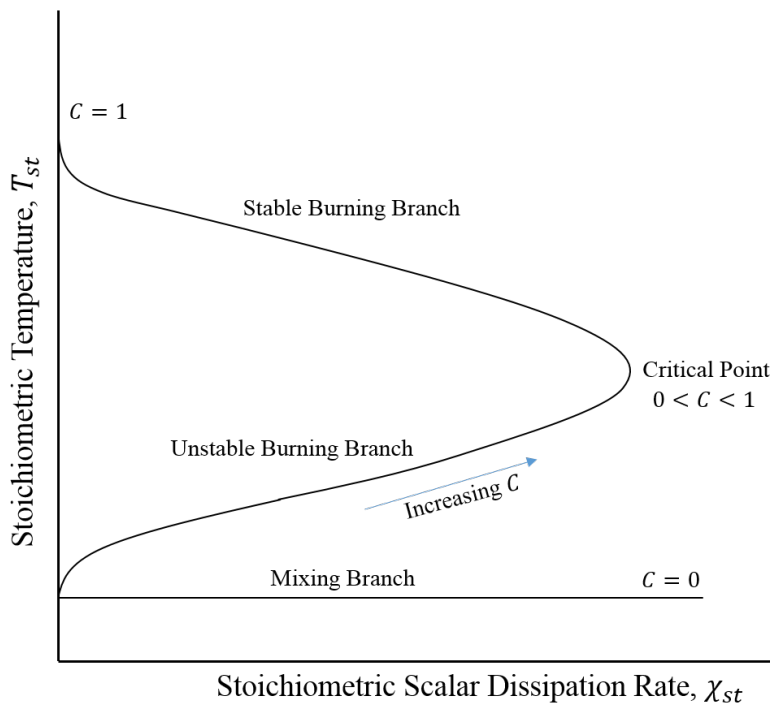


FIGURE 2.4: Notional S-shaped curve demonstrating the improved mapping of flame states by using the  $Z$ - $C$  parameterization with the FPV model.

extinction events are excluded from the thermochemical state-space, and for problems in which extinction and reignition are critical to predicting flame dynamics, a better approach is necessary.

### 2.3.3 Flamelet/Progress Variable Model

Pierce and Moin developed the incompressible FPV modeling approach in response to the limitations of previous incompressible flamelet models [26]. Instead of using  $Z$  and  $\chi_{st}$  to parameterize solutions to the incompressible flamelet equations, a progress variable,  $C$ , was introduced to be used in place of  $\chi_{st}$ . The progress variable is defined in such a way that it tracks the global progress of the combustion and is typically a linear combination of product species mass fractions; though,  $C$  could be defined using any suitable parameters. For mixing states,  $C = 0$ , and for chemical equilibrium states,  $C = 1$ . Most importantly, since  $C$  is defined to track the reaction's progress,  $Z$  and  $C$  uniquely track solutions along the S-shaped curve from mixing to equilibrium. As shown in Fig. 2.4, the  $Z$ - $C$  parameterization permits a consistent functional parameterization of all flame solutions along the S-shaped curve, from the mixing line, along the unstable branch, and up the stable branch to the equilibrium line.

Application of the incompressible FPV model requires solving the transport equations for  $\tilde{Z}$  and  $\tilde{C}$ , in addition to Eqs. (2.18)-(2.20), for which  $\tilde{Z}$  is governed by Eq. (2.28) and  $\tilde{C}$  is governed by Eq. (2.35), below,

$$\frac{\partial \bar{\rho} \tilde{C}}{\partial t} + \frac{\partial \bar{\rho} \tilde{C} \tilde{u}_j}{\partial x_j} = \frac{\partial}{\partial x_j} \left[ \left( \frac{\mu}{Sc} + \frac{\mu_t}{Sc_t} \right) \frac{\partial \tilde{C}}{\partial x_j} \right] + \bar{\omega}_C \quad (2.35)$$

and  $\tilde{Y}_\alpha$ ,  $\bar{\omega}_\alpha$ , and  $\tilde{T}$  are retrieved from the pre-tabulated flamelet solutions using the FPV model state vector,  $\phi_{FPV}$ , which assumes the form given below in Eq. (2.36).

$$\phi_{FPV} = \begin{bmatrix} \tilde{Z} \\ \tilde{C} \end{bmatrix} \quad (2.36)$$

Note that the solution of Eq. (2.35) requires  $\bar{\omega}_C$ , which is tabulated in the flamelet library and retrieved at runtime. While the FPV model of Pierce and Moin improved upon the SLF model of Peters by including extinction and reignition solution states, it left significant room for improvement. Numerous applications have proven its efficacy for low-Mach number turbulent combustion flows [44, 47–54] and in particular lifted flames [29]; however, the model made no correction for compressible effects, non-adiabatic heat transfer effects, or variable flamelet boundary condition effects, all of which are important for high-speed applications.

SLF and FPV models place no limitations on how turbulence-chemistry-interactions are modeled. Both approaches typically use presumed PDF closures, for which presumed- $\beta$  PDFs are formed using the mean and variance of mixture fraction,  $\tilde{Z}$  and  $\tilde{Z}''^2$ , respectively. For these approaches, the SLF and FPV model state vectors are extended to form three dimensional mappings given by Eqs. (2.37) and (2.38), respectively, and a transport equation for  $\tilde{Z}''^2$  must also be solved.

$$\phi_{SLF} = \begin{bmatrix} \tilde{Z} \\ \tilde{\chi}_{st} \\ \tilde{Z}''^2 \end{bmatrix} \quad (2.37)$$

$$\phi_{FPV} = \begin{bmatrix} \tilde{Z} \\ \tilde{C} \\ \tilde{Z}''^2 \end{bmatrix} \quad (2.38)$$

For both models, however, the developers acknowledged the shortcomings of such approaches and suggested the presumed PDF modeling approach may be a significant source of error. In light of this, the current work separates the problem of modeling turbulence-chemistry-interactions from the problem of modeling the reaction chemistry. As a result, the current dissertation addresses the development of an FPV model for application to high-speed, compressible, reacting flows, independent of any detailed turbulence-chemistry-interaction model formulation. In this context, the findings presented in subsequent chapters are applicable regardless of what turbulence-chemistry-interaction model may be used; though, the author acknowledges that the interaction and any modeling errors between a presumed PDF model and either a finite-rate reaction mechanism or a flamelet model may be significantly different.

Recent attempts at correcting the incompressible FPV model for application to compressible flows are summarized in the following section.

### **2.3.4 Efforts Toward a Compressible FPV Model**

While the utility of the incompressible FPV model has been demonstrated extensively for numerous low speed applications, the model in its original form is unable to account for many of the physical processes characteristic of high speed reacting flows, such as heat transfer at solid surfaces, compressibility effects, and shock-processed reactant properties. Several attempts at extending the incompressible FPV model formulation to compressible flows have been made in recent years, and a summary of these efforts is presented below.

#### **2.3.4.1 FPV with Total Energy Transport**

The first attempted compressible FPV model formulation in the literature is that of Terrapon et al. [55], for which a variant of the FPV model of Pierce is applied to the HyShot II ground experiment. This study followed an earlier application of the SLF model formulation to an experimental DLR scramjet combustor by Oevermann [56], who considered the effects of compressibility in a similar manner. Instead of retrieving the temperature from the flamelet table using the FPV model state vector, the researchers computed the local  $\tilde{T}$  directly after retrieving the composition and reaction data from the

flamelet library. A Newton-Raphson iteration on Eq. (2.39), below, using the retrieved  $\tilde{Y}_\alpha$  and the transported  $\tilde{h}$  was then used to compute the local  $\tilde{T}$ .

$$\tilde{h} = \sum_{\alpha} \tilde{h}_{\alpha}(\tilde{T}) \tilde{Y}_{\alpha} \quad (2.39)$$

While this approach was an improvement compared to the incompressible FPV formulation, it did little to correct the major model deficiencies. Within this formulation, the species mass fractions and progress variable production rate are only a function of  $\tilde{Z}$  and  $\tilde{C}$ . It then follows that without an explicit correction for compressibility effects, the modeled  $\tilde{Y}_\alpha$  and  $\tilde{\omega}_C$  are functions of the flamelet pressure and temperature, which are known to be inconsistent with the locally-transported properties in the flowfield. Thus, while the total energy was used to compute the local static temperature, the constituents required for this calculation retrieved from the table serve to drive the temperature toward that embedded in the table. Due to these limitations, comparisons of centerline  $\bar{p}$  for the HyShot II ground experiment showed a general inability to recover the complete pressure rise associated with the combustion.

#### 2.3.4.2 FPV with Compressibility Correction

Later attempts at a compressible FPV model formulation were focused on incorporating explicit corrections for compressibility effects and at reducing the expense of computing  $\tilde{T}$ . The first such attempt was made by Terrapon et al. [21], with supporting work and validation by Saghafian et al. [22] and Pecnik et al. [23]. By noting that the majority of relevant chemical reactions comprising representative kinetic mechanisms for the combustion of hydrogen are bimolecular in nature, the researchers proposed a first order compressibility correction by applying a  $\bar{p}^2$  scaling to the retrieval of  $\tilde{\omega}_C$ . The scaling model is shown below in Eq. (2.40),

$$\tilde{\omega}_C = \frac{\bar{p}^2}{\bar{p}_0^2} \tilde{\omega}_{C_0} \quad (2.40)$$

where  $\bar{p}_0$  and  $\tilde{\omega}_{C_0}$  correspond to the nominal flamelet solution pressure and progress variable production rate, respectively.

The second modification made to the FPV model was regarding the calculation of  $\tilde{T}$ , for which an analytical expression was derived to alleviate the Newton-Raphson iteration

on Eq. (2.39). This analytical expression was the result of a linearization around the flamelet solution corresponding to the local FPV state vector,  $\phi_{FPV}$ , that began by noting the internal energy,  $\tilde{e}$ , could be expressed according to Eq. (2.41) using the definition for  $\tilde{h}$ .

$$\tilde{e} = \tilde{h} - R\tilde{T} = \sum_{\alpha} \tilde{Y}_{\alpha} \tilde{h}_{\alpha} - R\tilde{T} \quad (2.41)$$

For a fixed value of  $\phi_{FPV}$ , and necessarily fixed mixture composition, Eq. (2.41) can be approximated as

$$\tilde{e} = \tilde{e}_0 + \int_{\tilde{T}_0}^{\tilde{T}} c_v(\tilde{T}) d\tilde{T} = \tilde{e}_0 + \int_{\tilde{T}_0}^{\tilde{T}} \frac{R_0}{\gamma(\tilde{T}) - 1} d\tilde{T} \quad (2.42)$$

where  $\tilde{e}_0$ ,  $\tilde{T}_0$ , and  $R_0$  are the internal energy, temperature, and gas constant corresponding to the flamelet solution, respectively. The ratio of specific heats,  $\gamma$ , was then linearly expanded around the corresponding flamelet solution in temperature space according to

$$\gamma(\tilde{T}) = \gamma_0 + a_{\gamma}(\tilde{T} - \tilde{T}_0) \quad (2.43)$$

where  $\gamma_0$  and  $a_{\gamma}$  are the ratio of specific heats at the flamelet solution and a linearization constant, respectively. Substituting Eq. (2.43) into Eq. (2.42) and rearranging yields the analytic, linearized, approximation for  $\tilde{T}$  shown below in Eq. (2.44).

$$\tilde{T} = \tilde{T}_0 + \frac{\gamma_0 - 1}{a_{\gamma}} \left( \tilde{e}^{a_{\gamma}(\tilde{e} - \tilde{e}_0)/R} - 1 \right) \quad (2.44)$$

The researchers claimed the error associated with this approach was less than 1%; though, this approach requires tabulating  $\tilde{e}_0$ ,  $R_0$ ,  $\gamma_0$ ,  $a_{\gamma}$ , and  $\tilde{T}_0$  in the flamelet library, in addition to the  $\tilde{Y}_{\alpha}$  and  $\bar{\omega}_C$  terms, at a minimum. Importantly, the inclusion of the pressure-scaling correction on  $\bar{\omega}_C$  yielded results that compared more favorably with the HyShot II experimental combustor pressure data.

The latest attempt at a compressible FPV model formulation involves the same  $\phi_{FPV}$  as before, but with a scaling correction on  $\bar{\omega}_C$  for  $\tilde{T}$ , in addition to the scaling for  $\bar{p}$  described above [24]. In this approach, Arrhenius behavior of the elementary reactions is assumed, from which the scaling for  $\bar{\omega}_C$  follows below in Eq. (2.45)

$$\bar{\omega}_C = \left( \frac{\bar{p}}{\bar{p}_0} \right)^{a_{\rho}} \exp \left[ -T_a \left( \frac{1}{\tilde{T}} - \frac{1}{T_0} \right) \right] \bar{\omega}_{C_0} \quad (2.45)$$

where  $\bar{\rho}$  is the transported mass density,  $\bar{\rho}_0$  is the flamelet mass density,  $a_\rho$  is a model constant that takes on a value of 2 due to the continued assumption of bimolecular collisional dominance, and  $T_a$  is a modeled activation temperature that is used to best fit the flamelet data. The use of Eq. (2.45) with the linearized analytic expression for  $\tilde{T}$  represents the current state-of-the-art in the development of a compressible FPV model formulation for application to high-speed, reacting flows.

One major issue with this formulation is that while the corrections for compressibility effects are made for  $\bar{\omega}_C$ , no such considerations are made for the composition data,  $\tilde{Y}_\alpha$ . In order to do so, the model state vector would necessarily have to be extended dimensionally to include a proxy for compressibility, such as static pressure,  $\bar{p}$ , since the feasibility of deriving a similar scaling correction for  $\tilde{Y}_\alpha$  is unlikely. Some research into using  $\bar{p}$  as an additional parameterizing dimension in the FPV model has been performed for application to internal combustion engines [57] with considerable success; however, application of such a model to scramjet flowfields has not been forthcoming.

The second major issue with the state-of-the-art compressible FPV formulation is the use of single-point flamelet boundary conditions used to construct the entire flamelet library. In all the studies referenced in this chapter, the oxidizer and fuel pressure and temperature used as the boundary conditions for Eqs. (2.30) and (2.31) were held constant at nominal values set using *trial-and-error* approaches. However, due to the significant complexity of the flowfields within scramjet engines and especially considering the shock-systems residing in the isolator and combustor, one would expect the conditions seen by the flame regions to vary considerably from the values at the nozzle and injector entrances. As the fuel and oxidizer advect to the flame region, they are processed by any flow features in their path, and as will be seen in subsequent chapters, the processing by shocks imparts a significant departure from nominal conditions requiring explicit considerations.

Finally, while the linearization around  $\gamma$  may serve as a reasonable approximation in order to alleviate the Newton-Raphson iteration on  $\tilde{T}$ , it is unnecessary, as this calculation generally consumes a trivial percentage of total computational work. The potential for error outweighs the potential time savings, and therefore, a comprehensive compressible FPV model should solve for the  $\tilde{T}$  directly from the transported  $\tilde{E}$  using an explicit Newton-Raphson iteration, so as to not impart an additional source of modeling error.

## Chapter 3

# Compressible RANS Simulations of the HDCR

As discussed in Chapters 1 and 2, analysis of dual-mode scramjet combustors requires both an understanding of and accurate models for the flow and combustion physics critical to both dual- and scram-mode operating regimes. Understanding and reliably predicting these physics is critical to preventing catastrophic engine unstart conditions, wherein the engine isolator's shock train may be pushed forward of the inlet due to excessive combustor heat release and pressure rise and thereby render the vehicle inoperable. Since experimental investigations of engine conditions characteristic of dual-mode transition are often severely limited due to hardware and test facility capabilities, computational investigations serve a paramount purpose. In most recent research campaigns targeting dual-mode transition, in fact, the experimental and computational research efforts were inextricably linked. Accordingly, enhancing the predictive capability and accuracy of modeling and simulation tools for high-speed reacting flows is necessary for continued progress toward understanding the complete scramjet flight regime.

Since experimental research efforts typically yield little more than centerline static pressure data, the current chapter details a simulation campaign for the HDCR dual-mode scramjet experimental combustor designed to yield a database of flowfield data for use with subsequent *a priori* analysis. For the flowfield characterization and model analysis in Chapters 4 and 5, respectively, the current chapter provides a set of baseline RANS solutions containing detailed, three-dimensional data for the HDCR combustor using a

finite-rate chemical kinetics reaction mechanism. Much of these data are inaccessible by experimental diagnostics, and therefore, any attempt at detailed flowfield analysis for a dual-mode scramjet combustor requires a computational solution database.

In section 3.1, a brief overview of the HDCR experiment is presented with discussion of the experimental objectives, the test article, and the physical flow phenomena governing the combustor flowfield. The following section, 3.2, presents the Favre-averaged RANS simulations performed in support of the current work, beginning with a summary of the cases performed. A description of the numerical formulation is included in section 3.2.1, and simulation results for dual- and scram-mode cases are presented in sections 3.2.2 and 3.2.3, respectively. The final section summarizes the important findings from this effort.

### 3.1 The HDCR Ground Experiment

The HDCR was a ground-based experiment conducted at NASA Langley Research Center (LaRC) in support of flight two of the HIFiRE flight experiments [58]. Of the eight planned HIFiRE flight experiments, the second was a hydrocarbon-fueled scramjet flight test designed to demonstrate dual-mode transition to fully-scram-mode operation and to validate design and analysis tools. The primary performance goal of the flight experiment was to demonstrate scram-mode combustion at an equivalence ratio greater than 0.7, and the projected flight profile included flight numbers from Mach 6.0-8.0. The HDCR ground experiment was performed for the HIFiRE flight two engine to validate the flowpath design and demonstrate operability across the projected range of flight Mach numbers, including achievable margin.

The HDCR test article comprised a cavity-based hydrocarbon-fueled dual-mode scramjet combustor, which was tested in a direct-connect fashion in the NASA LaRC Arc-Heated Scramjet Test Facility [30]. The model included a constant-area cross-section isolator duct attached to a combustor containing five stages of fuel injectors. During the experiment, only the primary injectors and secondary injectors located upstream and downstream of the cavity closeout, respectively, were fueled. A mold line of the engine is shown in Fig. 3.1, in which relevant dimensions and injector locations are illustrated. The engine was fueled by a JP-7 surrogate consisting of 36% methane and 64% ethylene

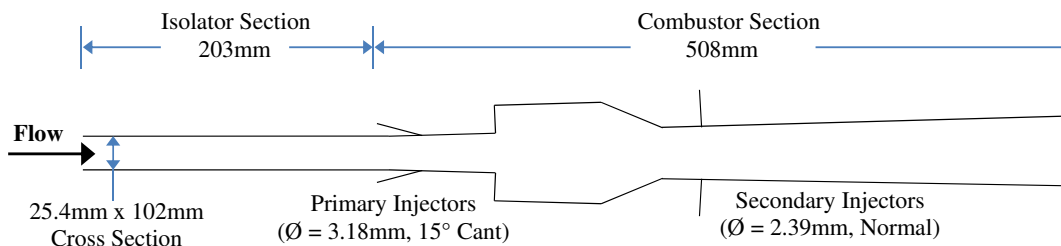


FIGURE 3.1: Side view and key dimensions of the HDCR combustor flowpath, where  $\varnothing$  is internal diameter of the injectors.

by volume. Experimental objectives included demonstrating scram-mode operation of the engine at an equivalence ratio,  $\Phi$ , of 1.0 and combustion efficiency greater than 0.7 and simultaneously developing a fuel distribution schedule to safely operate the subsequent flight engine through dual-mode transition [16]. Based on the estimated flight trajectory, this transition was expected to occur between flight Mach numbers of 6-8. Two computational fluid dynamics (CFD) simulations [34] of the HIFiRE inlet, bounding these flight Mach numbers, were performed to estimate the corresponding Mach numbers at the inlet to the isolator for the direct-connect experiments. The results obtained from the CFD simulations showed that the facility nozzles with Mach numbers of 2.51 and 3.46 produced isolator flows appropriate for the dual-mode and scram-mode experiments, respectively. The total enthalpy of each of the two flows was set to match that of the corresponding flight Mach number. Data collected during the experiments included wall temperatures, heat fluxes, and static pressures. The flowpath was outfitted with 144 static pressure ports, 19 flowpath surface thermocouples, and 4 heat flux gauges.

For the purposes of the current investigation and inline with the experimental efforts, dual-mode operation is marked by the leading combustion-induced compression shock anchoring upstream of the primary injectors. When this leading shock resides downstream of the primary injectors, the engine is operating in scram-mode.

## 3.2 Compressible RANS Simulations

Two experimental tests points were chosen for further analysis that corresponded to archetypal dual- and scram-mode operation of the engine. The dual-mode cases were tested at a flight Mach number of 5.84 and a total equivalence ratio of 0.65, whereas the

scram-mode cases were tested at a flight Mach number of 8.0 and a total equivalence ratio of 1.0. The total equivalence ratio was split between the primary and secondary injectors, respectively, as 0.15 and 0.5 for the dual-mode cases and as 0.4 and 0.6 for the scram-mode cases. Hereafter, simulation cases will be referenced using a case identifier that reflects the operational mode, the flight Mach number, and the imposed wall boundary conditions, as shown in Table 3.1. For example, case *D584A* signifies dual-mode operation, *D*, at a flight Mach number of *5.84* with adiabatic walls, *A*. Similarly, case *S800I* signifies scram-mode operation, *S*, at a flight Mach number of *8.00* with isothermal walls, *I*.

TABLE 3.1: Summary of simulated test cases, including flight Mach number, plenum conditions, fuel equivalence ratios ( $\Phi$ ), and wall boundary conditions.

Case	Flight Mach Number	Plenum Total Temperature [K]	Plenum Total Pressure [atm]	Primary Injector $\Phi$	Secondary Injector $\Phi$	Wall Treatment
D584A	5.84	1550	14.63	0.15	0.5	Adiabatic
D584I	5.84	1550	14.63	0.15	0.5	ID Conduction
S800A	8.00	2570	42.19	0.40	0.6	Adiabatic
S800I	8.00	2570	42.19	0.40	0.6	ID Conduction

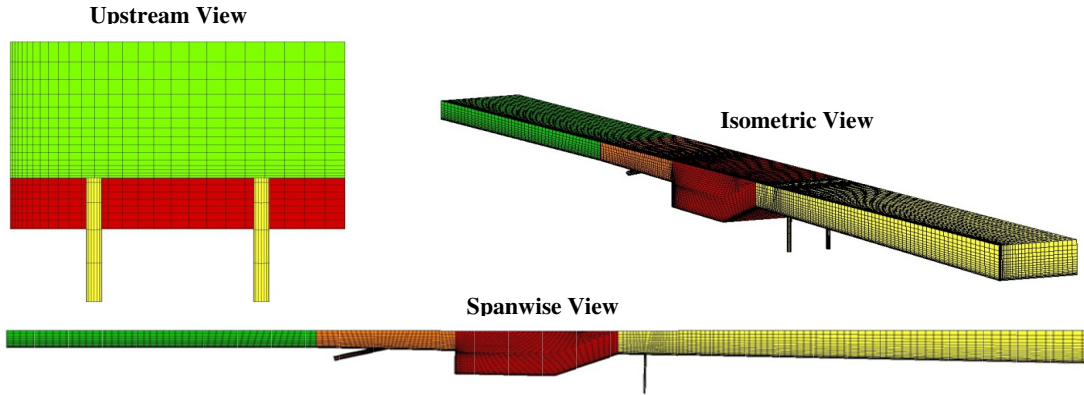


FIGURE 3.2: Looking upstream, isometric, and side views of the structured, quarter-geometry, grid used for RANS of the HDCR combustor coarsened four times for visual clarity.

### 3.2.1 Numerical Formulation

The Favre-averaged RANS equations derived in Chapter 2 and summarized in Eqs. (2.18)-(2.22) were solved using VULCAN-CFD. VULCAN-CFD is a structured grid finite-volume solver that is extensively used for high-speed combustion simulations using RANS techniques [25]. For the current study, a 6.6 million cell, quarter-geometry, structured grid was used, which is illustrated in Fig. 3.2. This grid included the facility nozzle. Wall spacings were set for efficient application of wall-matching functions [59]. At no point in the combustor did the  $y^+$  value exceed approximately 30. Symmetry was enforced at symmetric boundaries, and an extrapolation of transported variables was applied at the outflow plane. Wall functions were used at all solid surfaces, and simulations were performed for both adiabatic and isothermal walls to determine the effect of wall heat losses. In the case of isothermal walls, a one-dimensional heat-conduction equation was solved for the heat transfer through solid surfaces given a wall's external temperature and thermal conductivity, which were set to yield wall temperatures similar to those measured during the experiment [35]. The governing RANS equations were closed using the blended  $k$ - $\omega$ / $k$ - $\epsilon$  turbulence model of Menter [43], where  $k$  is the turbulence kinetic energy,  $\omega$  is the turbulence frequency, and  $\epsilon$  is the turbulence dissipation rate. Inviscid fluxes were calculated using the low-dissipation flux split scheme (LDFSS) of Edwards [60]. The van Leer flux limiter was used, along with a monotone upstream-centered scheme for conservation laws (MUSCL) with an interpolation coefficient ( $\kappa$ )

of 1/3. The equations were integrated in pseudo-time using an implicit diagonalized approximate factorization (DAF) scheme [61] with a maximum local CFL number of 2.0.

Reaction chemistry was modeled using an 18-step reduced chemical reaction mechanism designed for the combustion of ethylene [62]. Transport equations for the 22 species comprising the reaction mechanism were solved implicitly, and laminar chemistry was assumed. The turbulent Prandtl number was set to 0.89 for each case, and the turbulent Schmidt number was set to 0.325 for the dual-mode cases and 0.25 for the scram-mode cases, as suggested by Storch et al. [16]. Laminar Prandtl and Schmidt numbers were set to 0.72 and 0.22, respectively [16].

### 3.2.2 Dual-Mode Operation

Validation of dual-mode cases D584A and D584I is shown using experimental wall pressures,  $p$ , in Fig. 3.3. Both cases agree reasonably well with the centerline experimental static pressure data. The simulations agree well throughout the isolator, and both solutions capture the location of the leading oblique shock due to combustor pressure rise. Case D584A predicts the peak combustor pressure rise and subsequent exit nozzle expansion slightly better than that of case D584I. For this reason, case D584A was subsequently used as the baseline dual-mode solution and to further remove the complexity associated with heat transfer through the walls.

Examining Mach number contours confirms the dual-mode operation of the engine. As illustrated in Fig. 3.4, the leading shock due to combustor pressure rise resides upstream of the primary injectors, which is followed by a series of shock reflections. A black line corresponding to the sonic isocontour is overlaid on the contour maps in Fig. 3.4, which helps to distinguish regions of subsonic flow. Importantly, the leading oblique shock serves to stabilize flames that anchor near the primary injector orifices. The flow subsequently separates downstream of the primary injectors at the rearward-facing step corner, and a shear layer forms over the recirculating flow within the cavity, which reattaches near the point of cavity closeout. This mixture of oxidizer, fuel, and products from the primary injectors mixes with the unburnt fuel injected at the secondary set of injectors after being processed by the flowfield through the cavity region. As suggested by the relative fuel equivalence ratios, the secondary injector flames release considerably

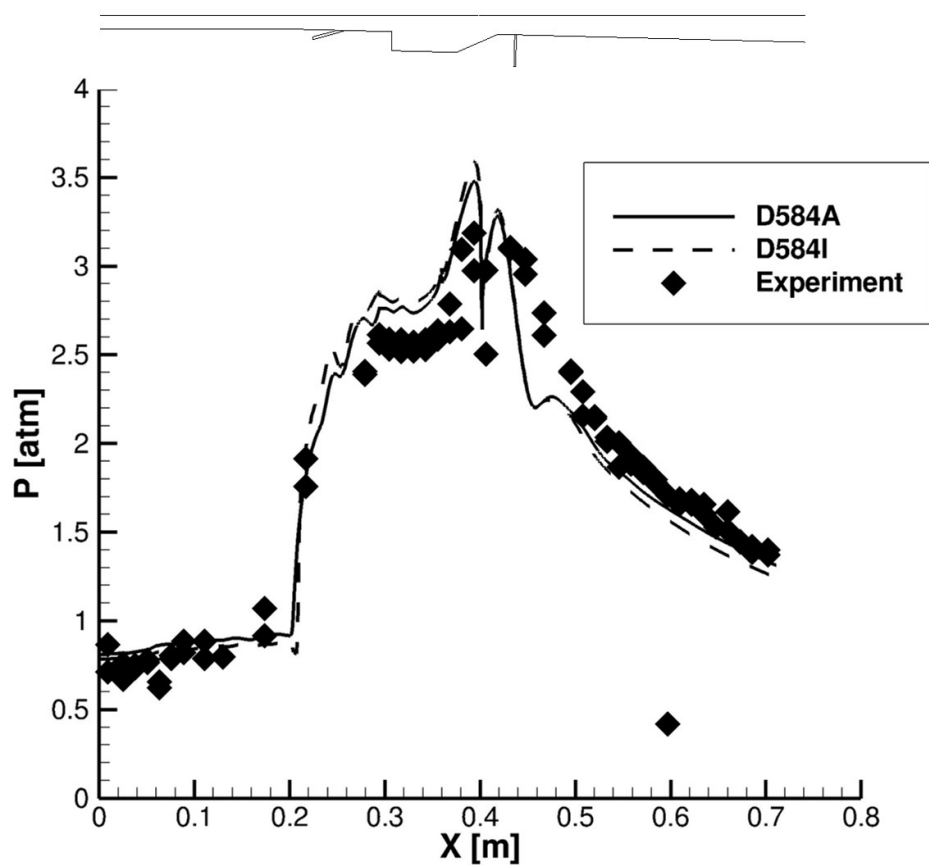


FIGURE 3.3: Comparisons of streamwise ( $x$ ) wall static pressure ( $p$ ) data obtained from simulations D584A and D584I and experimentally for dual-mode operation of the HDCR combustor.

more heat than the primary injector flames, which is illustrated by chemical heat release in Fig. 3.5, before the flow is finally expanded through the exit nozzle.

### 3.2.3 Scram-Mode Operation

For scram-mode operation of the engine, case S800A demonstrates reasonably good agreement with experimental static wall pressure data, while case S800I overpredicts the peak combustor pressure by approximately 0.7 atm, as illustrated in Fig. 3.6. Both solutions predict the pressure drop through the exit nozzle and overpredict the isolator pressure by about 0.1 atm. The differences in these solutions are a direct indication of the sensitivity of the flowfield solution to wall heat transfer, which will be discussed as relevant to flamelet modeling in the following section.

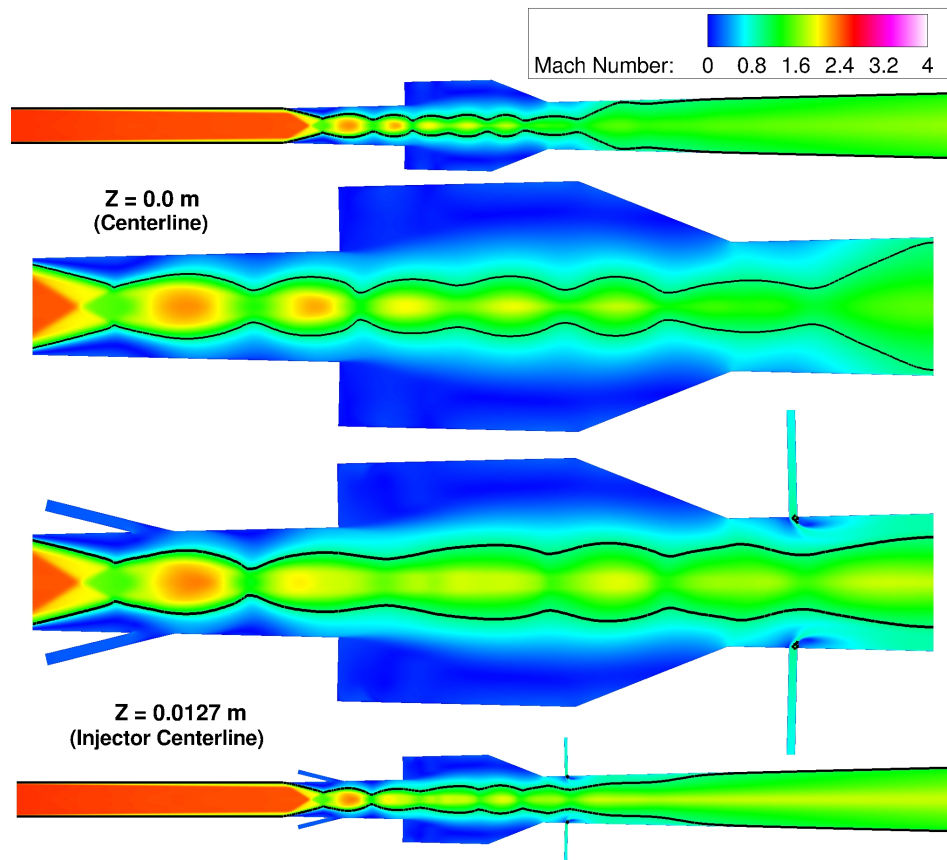


FIGURE 3.4: Contours of the Mach number at spanwise ( $z$ ) center plane and middle injector centerline for case D584A. Dark black lines correspond to the sonic isocontour.

Examining Figs. 3.4 and 3.7 together further supports previously discussed differences between the dual- and scram-modes. Unlike for the dual-mode solution, the combustion occurs predominantly at supersonic flow velocities. Of further importance are the differences in flame location and structure as suggested by the contours of chemical heat release in Fig. 3.8. Whereas in the dual-mode case a strong thin flame anchors directly outside the primary injector orifices, in the scram-mode case the primary injector fuel burns downstream of the injectors in a more distributed fashion. These flames reside behind the leading oblique shock and above the cavity region. The secondary injector flames, on the other hand, appear to be of a similar nature to those of the dual-mode case. Differences in flame structure are investigated in more detail in the following section.

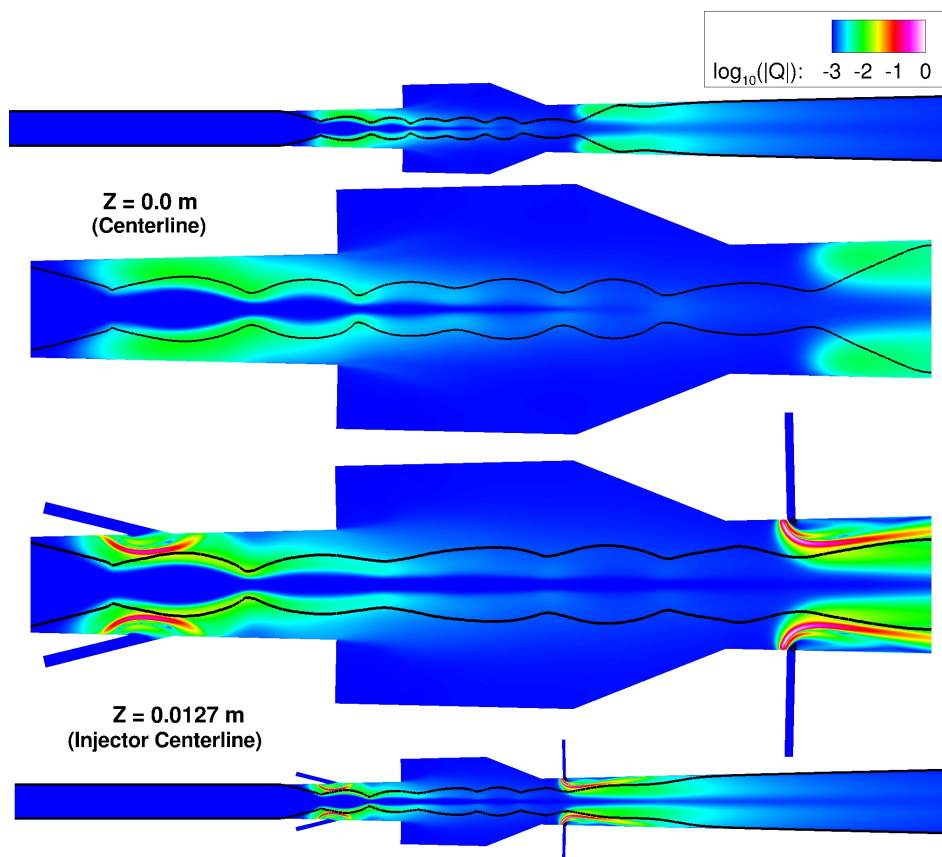


FIGURE 3.5: Contours of the logarithm of chemical heat release ( $Q$ ) normalized by its global maximum for simulation D584A. Dark black lines correspond to the sonic isocontour.

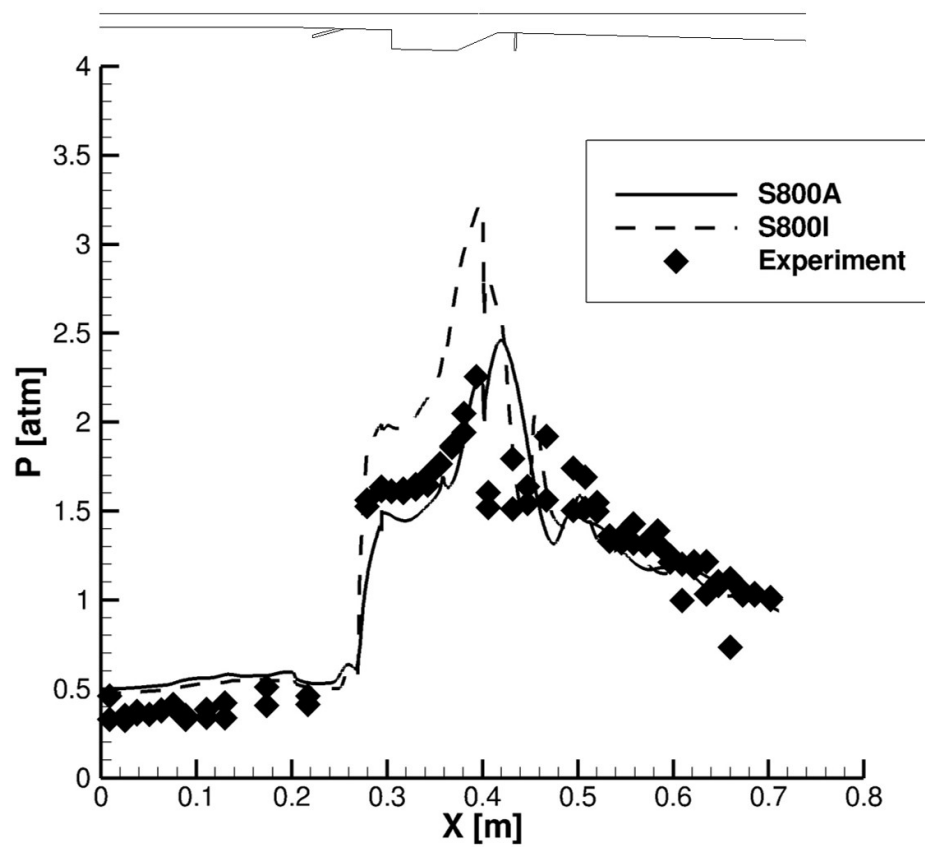


FIGURE 3.6: Comparisons of streamwise ( $x$ ) wall static pressure ( $p$ ) data obtained from simulations S800A and S800I and experimentally for scram-mode operation of the HDCR combustor.

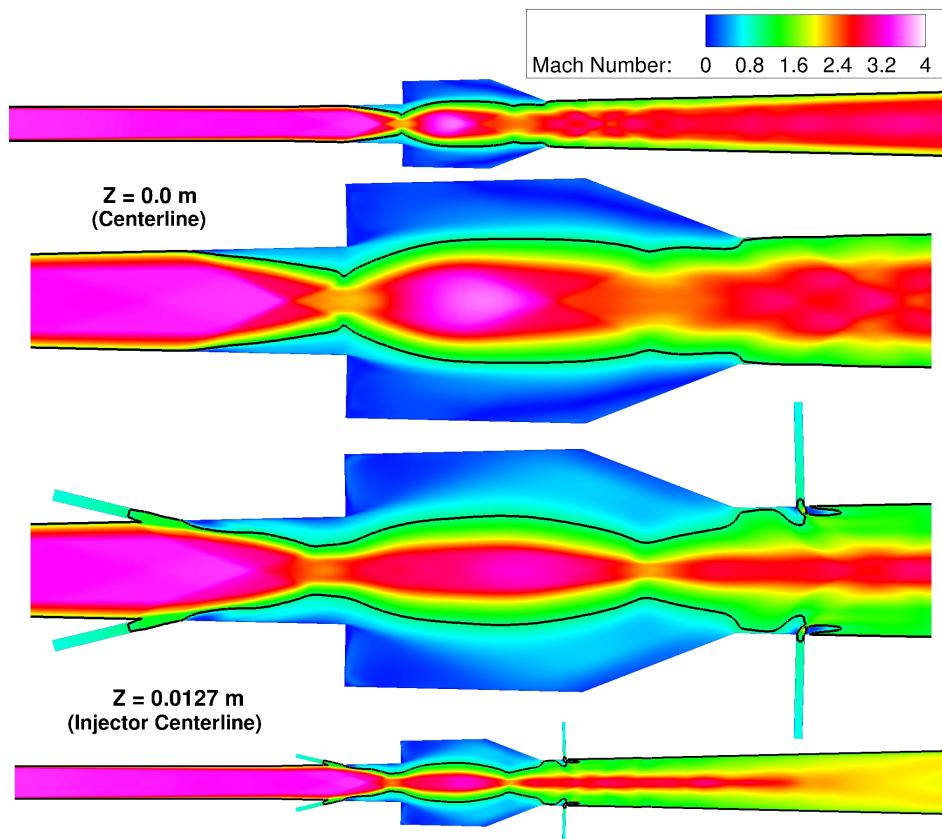


FIGURE 3.7: Contours of the Mach number at spanwise ( $z$ ) center plane and middle injector centerline for case S800A. Dark black lines correspond to the sonic isocontour.

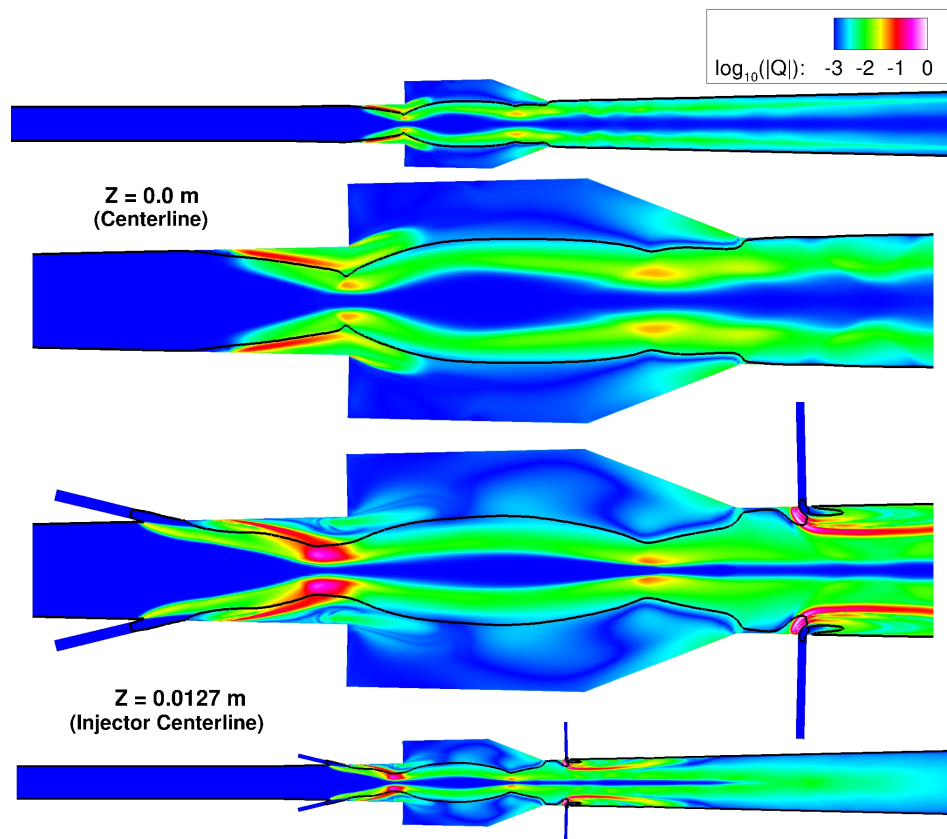


FIGURE 3.8: Contours of the logarithm of chemical heat release ( $Q$ ) normalized by its global maximum for simulation S800A. Dark black lines correspond to the sonic isocontour.



## Chapter 4

# *A Priori* Study of the HDCR Combustion Dynamics

Flamelet-based models for turbulent combustion assume that within a turbulent combustion flowfield are embedded asymptotically-thin locally-laminar flames or *flamelets* [27, 28]. When the flame chemistry can be reasonably assumed to occur much faster than relevant transport processes, the scalar dissipation rate provides the only means of influence for the fluid mechanical processes on the flamelet structure. The flamelet equations may then be used to construct a multidimensional manifold prior to a CFD simulation, which can be parameterized by a small number of scalar variables and tabulated. The resulting table or flamelet library may be accessed at runtime to retrieve relevant thermochemical data. Such an approach requires solving transport equations only for the parameterizing variables in place of the generally much larger system of chemical species transport equations described in Chapter 2, thereby resulting in a significantly less-stiff and less computationally-expensive system of governing equations.

Gauging the applicability of flamelet-models for a turbulent reacting flow requires one to consider the extent to which the flowfield meets the fundamental flamelet-model assumptions. In the case of non-premixed combustion, for which the flamelet is attached to the surface of stoichiometric mixture fraction and for which the scalar dissipation rate couples the flame dynamics to that of the fluid dynamics, the characteristic chemical time scale must be considerably smaller than that of the representative diffusive and turbulent transport processes. Additionally, the Damköhler number,  $Da$ , which was

defined in Eq. (2.24) as the ratio of a characteristic flow time scale,  $\tau_{flow}$ , to that of chemistry,  $\tau_{chem}$ , must be much greater than unity, thereby indicating the characteristic reaction chemistry times are much shorter than those of characteristic flow processes.

In the case of premixed combustion, for which the flame can propagate normal to itself, the chemical time scale and thermal diffusivity effectively govern the flame thickness, which must be considerably smaller than the representative turbulent length scales under the flamelet assumption. Flamelet-models are generally applicable for premixed turbulent flames characterized by a Karlovitz,  $Ka$ , number much less than unity, where  $Ka$  is defined as the ratio of a characteristic flame length scale to a characteristic turbulence length scale. In most cases, the Kolmogorov scale is used as the representative turbulence length scale.

The primary objective of this chapter is to use the Favre-averaged RANS solutions for cases D584A and S800A presented in Chapter 3 to determine whether the fundamental flamelet-model assumptions are valid for a dual-mode scramjet combustor. In doing so, a flame index is first devised in section 4.1 to objectively identify regions of chemical reactivity. Once the data is filtered using the flame index, a flame-weighted Takeno index is presented in section 4.2 that distinguishes regions of premixed and non-premixed conditions. Local  $Da$  and  $Ka$  numbers are subsequently estimated using the approach outlined by Poinot [39] and Peters [28]. Borghi diagrams [63] are constructed for the premixed combustion, and proxy combustion diagrams are devised for the non-premixed combustion using the flame-weighted Takeno index and  $Da$  number. Finally, *a priori* investigation of the effects of compressibility, wall heat losses, and flamelet boundary condition variability on the HDCR flames is presented in sections 4.3, 4.4, and 4.5, respectively.

## 4.1 Flame Index

The first step in characterizing the combustion fields is to devise a metric indicative of flame activity, which can be used to identify regions of combustion. The current study uses the approach of Lacaze [64] and defines a flame index,  $f$ , according to Eq. (4.1)

$$f(x, y, z) = \frac{\max(\bar{\omega}_\alpha(x, y, z))}{\max(|\bar{\omega}_\alpha|)} \quad (4.1)$$

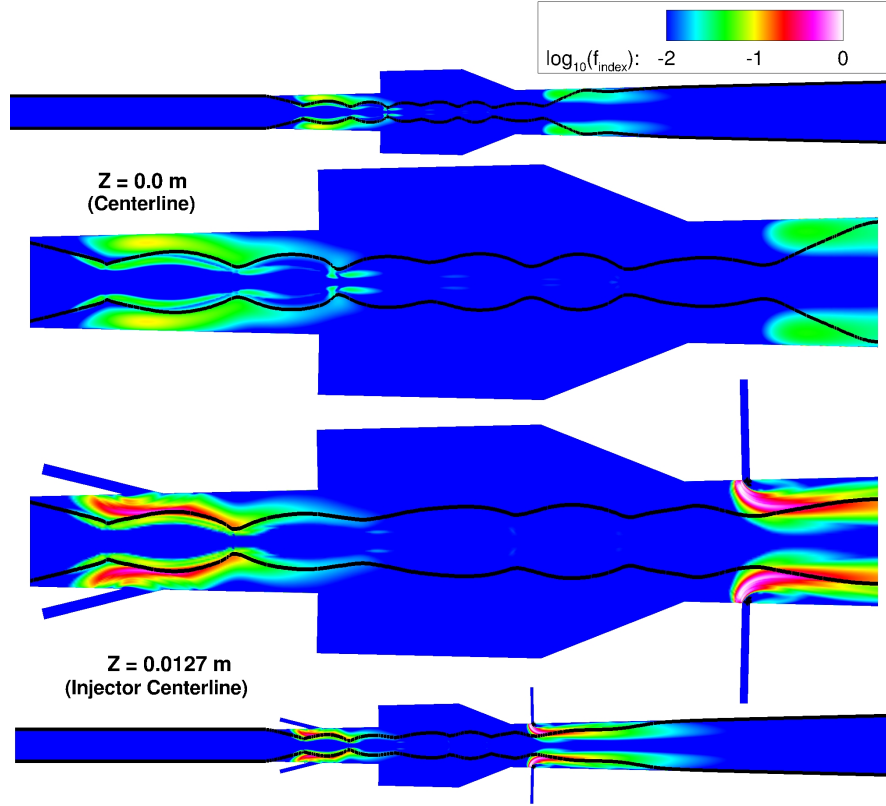


FIGURE 4.1: Contours of the logarithm of flame index,  $f$ , for simulation D584A. Dark black lines correspond to the sonic isocontour.

where  $\bar{\omega}_\alpha$  is the Favre-averaged production rate of species  $\alpha$  and  $x$ ,  $y$ , and  $z$  are Cartesian coordinates. The flame index is defined such that it indicates the level of maximum chemical production over all 22 species. The index takes on a value between 0 and 1, where 0 corresponds to no chemical production and where 1 corresponds to a point at which at least one chemical species is produced at its global maximum. By using the maximum chemical production rate over all the species at each point, the flame index remains unbiased toward any single species. Since the intent of this analysis is to characterize the combustion field in preparation for determining the validity of the fundamental flamelet-model assumptions, the flame index should not impose limiting assumptions as to the oxidizer and fuel compositions or to the chemical kinetics. Furthermore, the general nature of the flame index allows it to be used for the study of additional physics, such as thermal cracking of the fuel species.

Contours of  $\log_{10}(f)$  for cases D584A and S800A are presented in Figs. 4.1 and 4.2, respectively. The index confirms that for dual-mode operation, thin flames anchor near the primary injector orifices, which are stabilized by the leading oblique shock and recirculating fluid directly outside the injectors. Thin flames also burn outside the secondary

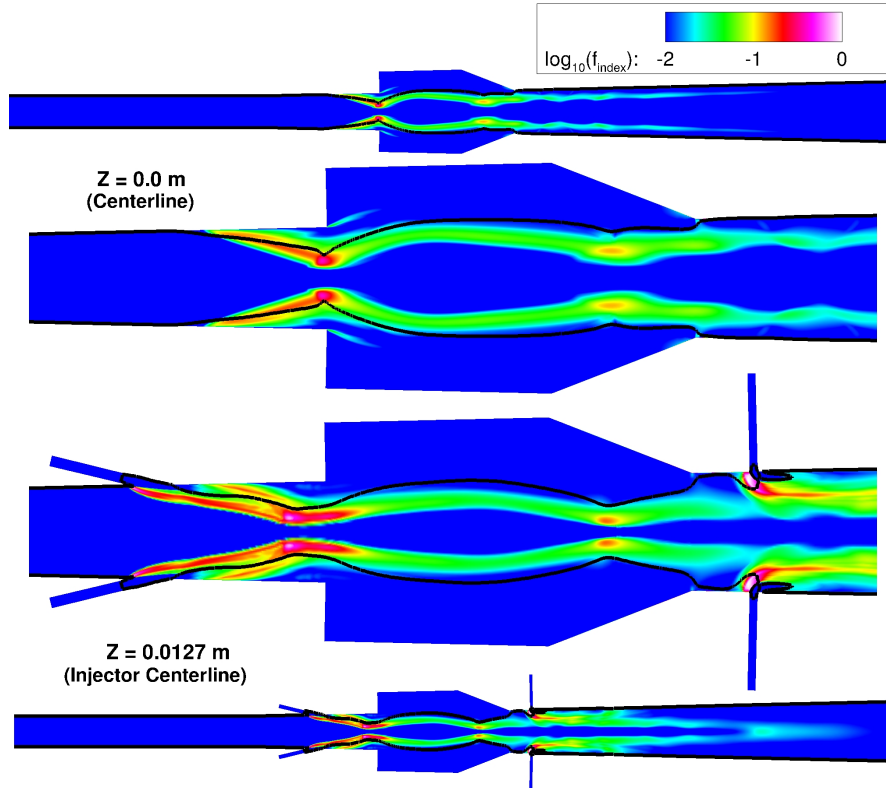


FIGURE 4.2: Contours of the logarithm of flame index,  $f$ , for simulation S800A. Dark black lines correspond to the sonic isocontour.

injector orifices and extend downstream. For case S800A, the flames associated with the primary injectors appear to be fundamentally different than those of the secondary injectors. While there does exist a thin region of combustion near the injectors stabilized by the fuel injection bow shock and fluid recirculation, most of the combustion appears to be distributed from the point of injection to just downstream of the cavity step corner. When compared to the Mach number contours in Fig. 3.7, the combustion appears to track the leading shock fronts until a pronounced increase in flame intensity is seen directly behind the point of leading shock-shock interaction. This observation may suggest the occurrence of shock-induced combustion. Downstream of this intense region of combustion, a weak distributed flame is observed. Note also the difference in equivalence ratio at the primary injectors for the dual- and scram-mode cases, as this may contribute to the difference in flame structure observed. The secondary injector flames are similar in nature to those observed in the dual-mode cases, which suggests a relatively thin flame that extends downstream past the injectors and is angled toward the wall. These observations are further supported by analyzing isosurfaces corresponding to  $f = 0.1$ , which are presented in Figs. 4.3a and 4.3b for cases D584A and S800A,

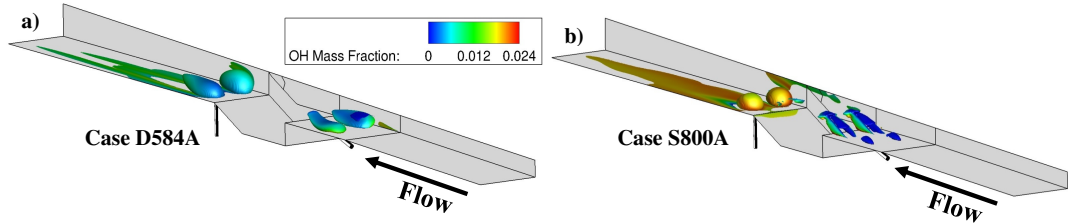


FIGURE 4.3: Isosurfaces corresponding to a flame index of 0.1 colored by OH mass fraction for both primary and secondary injector flames for cases D584A (a) and S800A (b).

respectively. Note that these isosurfaces are colored by mass fraction of  $OH$ , which is also a commonly-used flame identifier.

## 4.2 Combustion Mode

In order to properly determine the applicability of flamelet-models, the combustion mode must first be determined. To isolate the non-premixed combustion data from that of the premixed data, the approach of Yamashita et al. [65] is used. This method assumes that in non-premixed flames, the gradients of oxidizer and fuel species are oriented in opposite directions, while in premixed flames, the gradients are oriented in the same direction. By taking the dot product of the gradients and normalizing, the Takeno index,  $\Lambda_T$ , is calculated according to Eq. (4.2), where  $\tilde{Y}_{oxidizer}$  and  $\tilde{Y}_{fuel}$  are the Favre-averaged oxidizer and fuel species mass fractions, respectively. In the context of RANS, this index indicates the statistically-dominant combustion mode at a given location in the flowfield. Since the RANS solution is an averaged representation of the flowfield, non-premixed regions of the RANS flowfield may exhibit pockets of premixed combustion locally in time and space, and vice versa, which are not captured in this analysis.

$$\Lambda_T = \frac{\nabla \tilde{Y}_{oxidizer} \cdot \nabla \tilde{Y}_{fuel}}{|\nabla \tilde{Y}_{oxidizer} \cdot \nabla \tilde{Y}_{fuel}|} \quad (4.2)$$

The index is recast for the current work using the oxidizer ( $O_2$ ) and fuel ( $CH_4$ ,  $C_2H_4$ ) mixture species. In cases where the oxidizer and fuel species are consumed in the same physical direction, the index returns 1.0, which indicates premixed combustion. Alternatively, when the oxidizer and fuel species are consumed in opposite directions, the

index returns -1.0, which indicates non-premixed combustion. By then weighting the Takeno index by the flame index, a new index,  $\Lambda_f$ , is formed according to Eq. (4.3), which is hereafter referred to as the flame-weighted Takeno index.

$$\Lambda_f = f\Lambda_T \quad (4.3)$$

The value of  $\Lambda_f$  ranges from  $-1.0 < \Lambda_f < 1.0$  and conveys both the flame intensity and dominant combustion mode at each point in the flowfield. Accordingly,  $\Lambda_f$  is used to focus subsequent analysis first at non-premixed regions of combustion and then at regions of premixed combustion.

The characteristic flow time scale is approximated using the scalar dissipation rate,  $\chi$ , which was defined in Eq. (2.32) in Chapter 2. The scalar dissipation rate is representative of a scalar mixing rate and has units of inverse time. It is modeled using the approach of Poinso, who suggests that for RANS applications the scalar dissipation rate plays a similar role to mixture fraction as does the dissipation of turbulent kinetic energy to velocity [39]. Following this analogy, the scalar dissipation rate can be modeled for a RANS solution by applying the Reynolds-decomposition, neglecting the averaged component, and subsequently modeling the fluctuating component using the Favre-averaged turbulence dissipation rate ( $\tilde{\epsilon}$ ), turbulence kinetic energy ( $\tilde{k}$ ), and mixture fraction variance ( $\widetilde{Z'^2}$ ), as shown in Eq. (4.4), where  $C_a$  is a modeling constant.

$$\chi_{modeled} = C_a \frac{\tilde{\epsilon}}{\tilde{k}} \widetilde{Z'^2} \quad (4.4)$$

By using the theoretical upper bound on the mixture fraction variance, the modeled scalar dissipation rate can be rewritten according to Eq. (4.5), where  $\tilde{Z}$  is the Favre-averaged mixture fraction and is reconstructed from the 22 transported species using Bilger's definition [45]. The modeled characteristic flow time scale becomes the inverse of the modeled scalar dissipation rate, as shown in Eq (4.6).

$$\chi_{modeled} = \frac{\tilde{\epsilon}}{\tilde{k}} \tilde{Z}(1 - \tilde{Z}) \quad (4.5)$$

$$\tau_{flow} = \frac{1}{\chi_{modeled}} \quad (4.6)$$

The modeled scalar dissipation rate and characteristic flow time scale represent approximate upper and lower limits, respectively, suggesting this analysis presents a conservative

approach for determining the applicability of flamelet modeling and that correction of any error embedded in these terms would be in favor of flamelet-model viability. The constant  $C_a$  from Eq. (4.4) is assumed to be unity [39]. To estimate a characteristic time scale associated with the flame chemistry, a time scale is formed using the Favre-averaged production rate and mass fraction of a representative species, which in this case is water,  $\bar{\omega}_{H_2O}$  and  $\tilde{Y}_{H_2O}$ , respectively, and mixture density,  $\bar{\rho}$ , according to Eq. (4.7).

$$\tau_{chem} = \frac{\bar{\rho}\tilde{Y}_{H_2O}}{\bar{\omega}_{H_2O}} \quad (4.7)$$

Using Eqs. (4.5) and (4.7), the local non-premixed  $Da$  number,  $Da_{non-premixed}$ , can be calculated directly from the simulation data set by using Eq. (4.8).

$$Da_{non-premixed} = \frac{1}{\chi_{modeled}\tau_{chem}} \quad (4.8)$$

In the case of premixed combustion, both the  $Da$  and  $Ka$  numbers may be used to characterize flame regime; however, care must be taken in the calculation of their constituent components. For a premixed flame, the  $Da$  number is typically defined as the ratio of characteristic turbulence and flame time scales. With the laminar flame thickness ( $l_F$ ) and flame speed ( $s_L$ ), a characteristic flame time scale may be calculated, and using the integral turbulence length ( $l$ ) and velocity ( $u'$ ), a turbulent time scale may be formed. The premixed  $Da$  number,  $Da_{premixed}$ , is then calculated according to Eq. (4.9).

$$Da_{premixed} = \frac{\tau_{turb}}{\tau_{flame}} = \frac{l/u'}{l_F/s_L} \quad (4.9)$$

As Poinot points out, however, the most appropriate turbulence scale for calculating  $Da$  number of a premixed flame is unclear [39]. Since the current investigation is based on RANS data with model development intended for RANS and LES, the premixed  $Da$  number is calculated using the integral turbulence length scale. The laminar flame thickness and laminar flame speed are estimated by solving freely-propagating premixed flames corresponding to the average temperature, pressure, and fuel equivalence ratio characterizing the premixed data within the flowfield, as isolated by the flame-weighted Takeno index.

Combustion diagrams for the primary injector flames for cases D584A and S800A are presented in Figs. 4.4 and 4.6, respectively, and for the secondary injector flames for

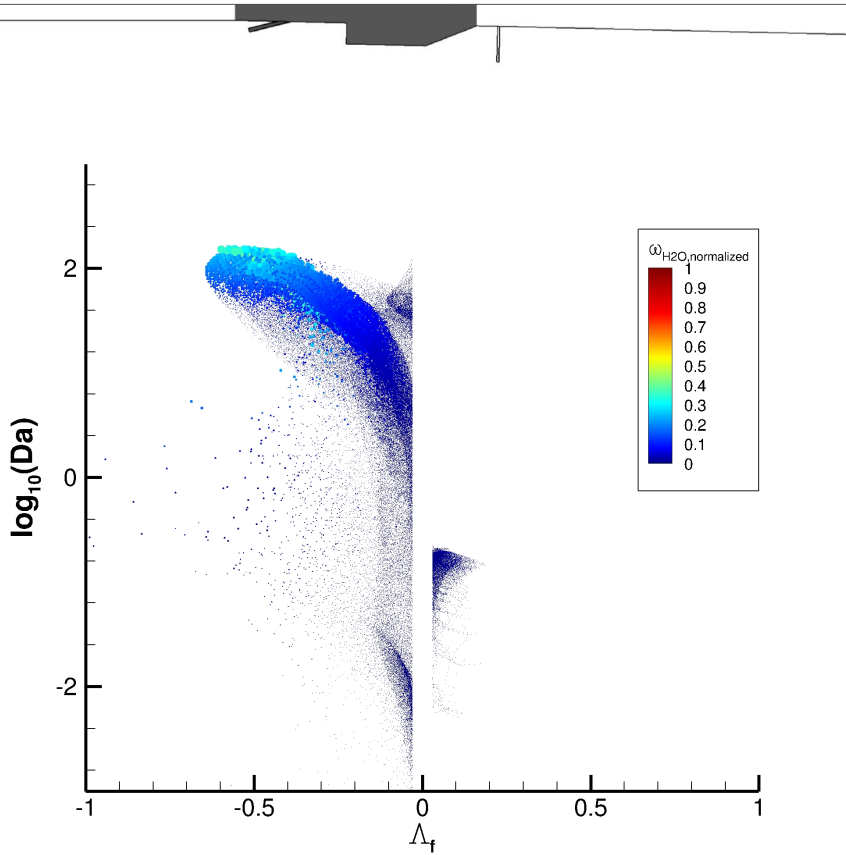


FIGURE 4.4: Damköhler number,  $Da$ , versus flame-weighted Takeno index,  $\Lambda_f$ , data sized by chemical heat release,  $\tilde{Q}$ , and colored by normalized Favre-averaged production rate of water,  $\bar{\omega}_{H_2O}$ , for case D584A. Data are plotted for the primary injector flames, which correspond to the gray regions on the included flowpath mold line.

cases D584A and S800A in Figs. 4.5 and 4.7, respectively. In each of these figures,  $\log_{10}(Da)$  is plotted against the flame-weighted Takeno index. In accordance with the preceding discussion, the non-premixed  $Da$  number is used for data corresponding to  $\Lambda_f < 0$ , and the premixed  $Da$  number is used for  $\Lambda_f > 0$ . On each plot, the data points are sized by the chemical heat release rate and are colored by the production rate of water. For each of the figures, the data are sampled from the shaded regions of the flowpath shown above each plot, and data within 3% of  $\Lambda_f = 0$  are omitted for clarity.

For both the primary and secondary injector flames, Figs. 4.4 and 4.5 suggest that for case D584A the combustion occurs primarily at high  $Da$  numbers ( $Da \gg 1$ ) and in a non-premixed mode ( $\Lambda_f < 0$ ). While limited regions of premixed combustion exist for this case, the heat release is insignificant when compared to that of the non-premixed combustion. These figures suggest that for case D584A, the fundamental assumptions made for non-premixed flamelet-models are likely satisfied and that such models may

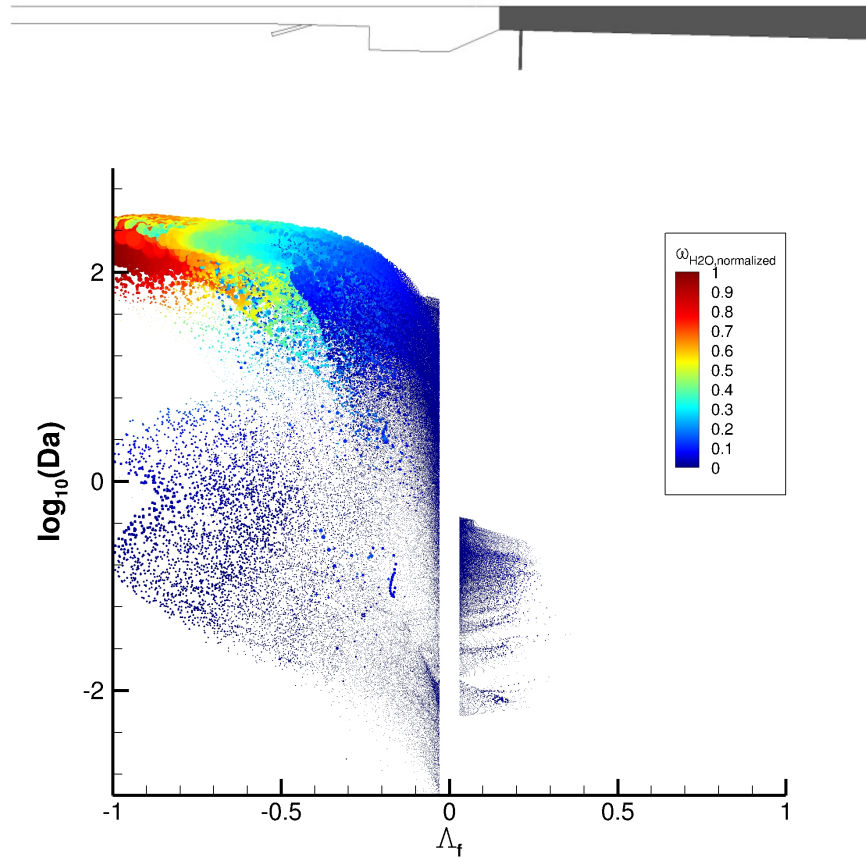


FIGURE 4.5: Damköhler number,  $Da$ , versus flame-weighted Takeno index,  $\Lambda_f$ , data sized by chemical heat release,  $\tilde{Q}$ , and colored by normalized Favre-averaged production rate of water,  $\bar{\omega}_{H_2O}$ , for case D584A. Data are plotted for the secondary injector flames, which correspond to the gray regions on the included flowpath mold line.

sufficiently predict the combustion physics governing dual-mode operation of the HDCR engine. Conversely, analyzing Figs. 4.6 and 4.7 for case S800A suggests that the combustion is of a more complex nature for scram-mode engine operation. For the primary injectors, the combustion occurs over a range of  $Da$  numbers and is split among both non-premixed and premixed modes. In fact, a significant portion of the heat release due to the primary injectors corresponds to premixed regions of combustion occurring near  $Da=1$ , thereby suggesting the characteristic flame time scale is on the same order of magnitude as that of the integral turbulence. However, a significant portion of the combustion occurs at high  $Da$  numbers in a non-premixed mode, as well. For the secondary injectors, the combustion occurs at a range of  $Da$  numbers and primarily in a non-premixed mode. Based on these data, a suitable simulation of the HDCR engine for scram-mode operation would likely require both premixed and non-premixed flamelet models, and the fundamental assumptions made for these models may only be valid for

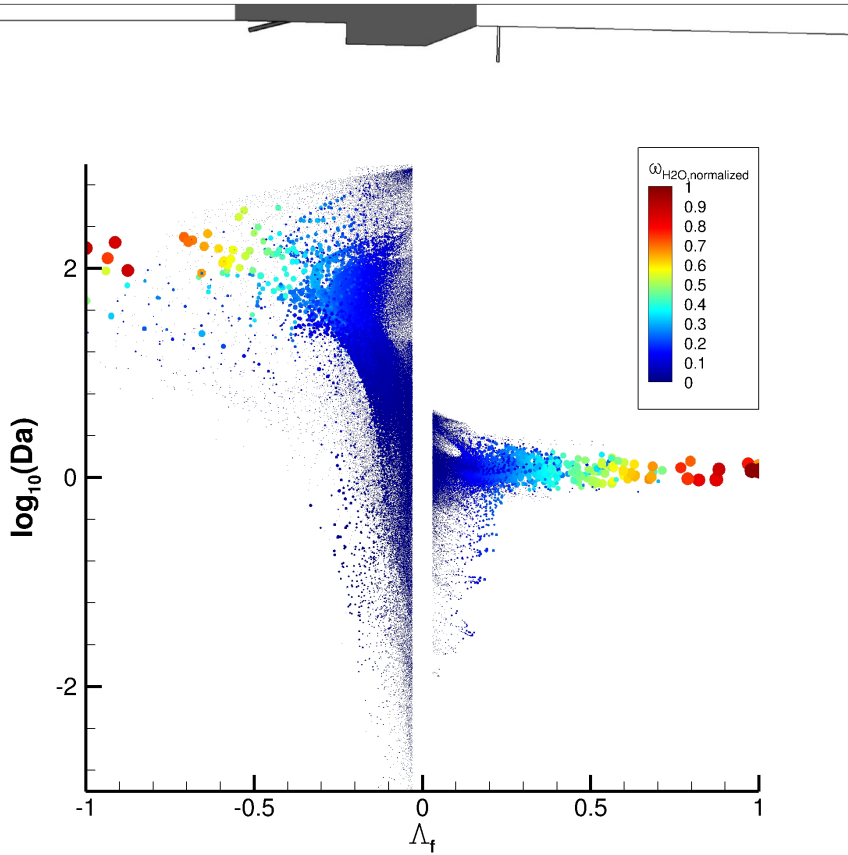


FIGURE 4.6: Damköhler number,  $\text{Da}$ , versus flame-weighted Takeno index,  $\Lambda_f$ , data sized by chemical heat release,  $\tilde{Q}$ , and colored by normalized Favre-averaged production rate of water,  $\bar{\omega}_{H_2O}$ , for case S800A. Data are plotted for the primary injector flames, which correspond to the gray regions on the included flowpath mold line.

limited regions of the combustion.

To better understand the nature of the premixed combustion data, modified Borghi combustion regime diagrams are constructed in Figs. 4.8 and 4.9 for cases D584A and S800A, respectively, following the approach of Peters [28]. The data are sized by chemical heat release rate and colored by flame index. The abscissa corresponds to the logarithm of the ratio of the turbulent length scale to that of the flame, and the ordinate is the logarithm of the ratio of the turbulent velocity scale to the laminar flame speed. Both parameters are recast in terms of transported variables and constants, as shown in Eqs. (4.10) and (4.11).

$$l/l_F = \frac{2^{3/2}}{3} \frac{\tilde{\epsilon}}{\tilde{k}^{1/2} l_F} \quad (4.10)$$

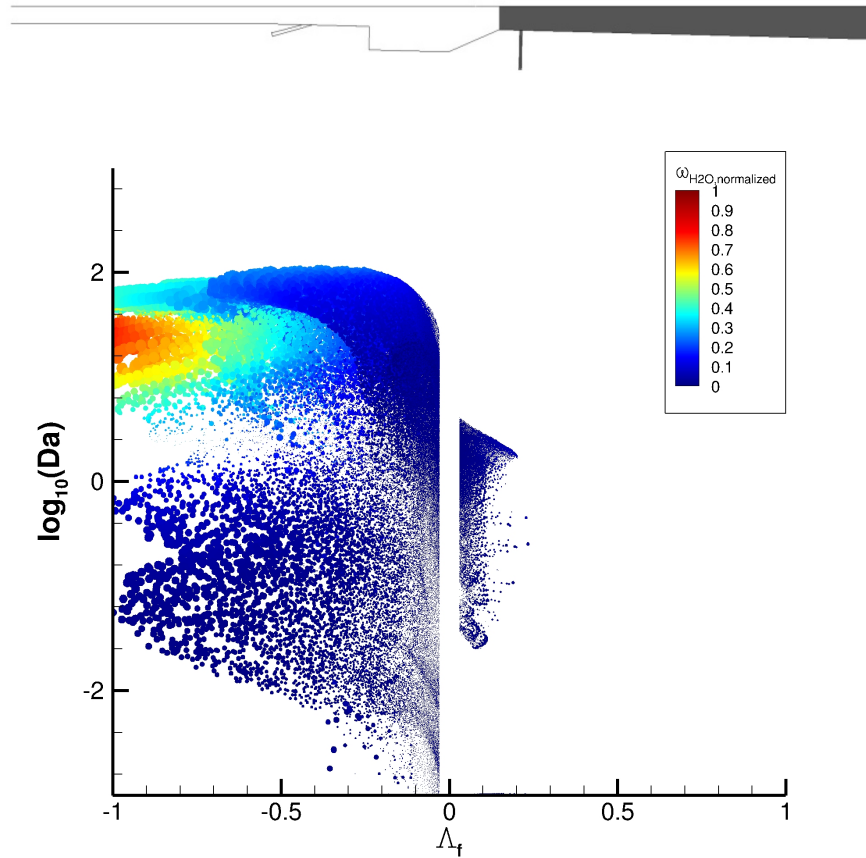


FIGURE 4.7: Damköhler number,  $Da$ , versus flame-weighted Takeno index,  $\Lambda_f$ , data sized by chemical heat release,  $\tilde{Q}$ , and colored by normalized Favre-averaged production rate of water,  $\bar{\omega}_{H_2O}$ , for case S800A. Data are plotted for the secondary injector flames, which correspond to the gray regions on the included flowpath mold line.

$$u'/s_L = \frac{2^{1/2} \tilde{k}^{1/2}}{3 s_L} \quad (4.11)$$

Lines corresponding to  $Ka$  number of unity, turbulent Reynolds number of unity, and  $Ka$  number based on flame reaction zone thickness of unity are overlaid on these figures.

For both cases D584A and S800A, the premixed data reside in the broken reactions and thin reaction regimes, where turbulent Reynolds number,  $Re_t$ , and  $Ka$  are greater than one. Within these regimes, the flame thickness is larger than the Kolmogorov scale, which allows Kolmogorov eddies to penetrate the flame partially for the thin reaction regime or completely for the broken reactions regime. More so, within the broken reactions regime, the smallest turbulent eddies may alter the internal flame structure, causing localized extinction, resulting in segmented, broken flame regions, which do not meet the fundamental assumptions of flamelet-modeling theory. In the case of dual-mode combustion, the heat release corresponding to these premixed data

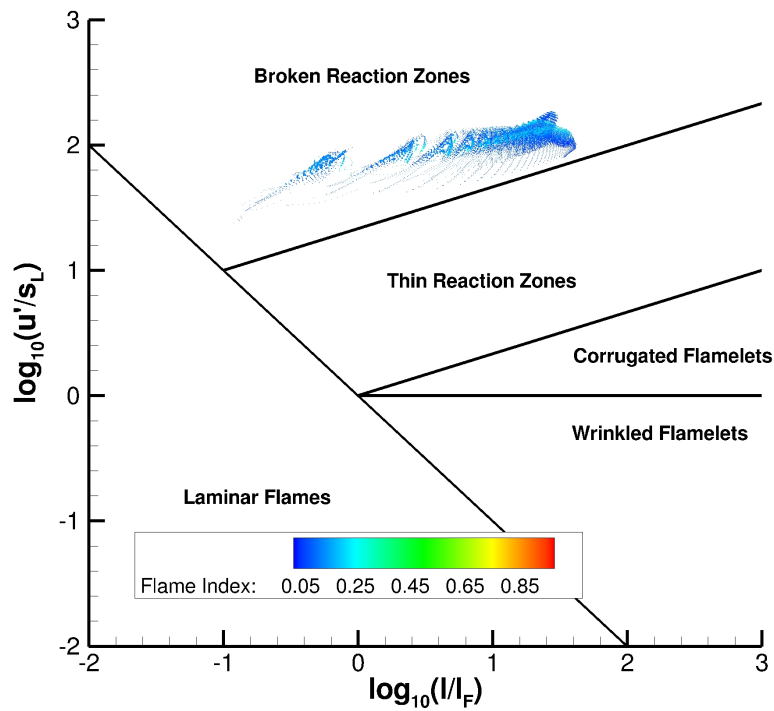


FIGURE 4.8: Borghi diagram for case D584A, whose data are colored by flame index sized by chemical heat release and shown for  $\Lambda_f > 0.05$ .

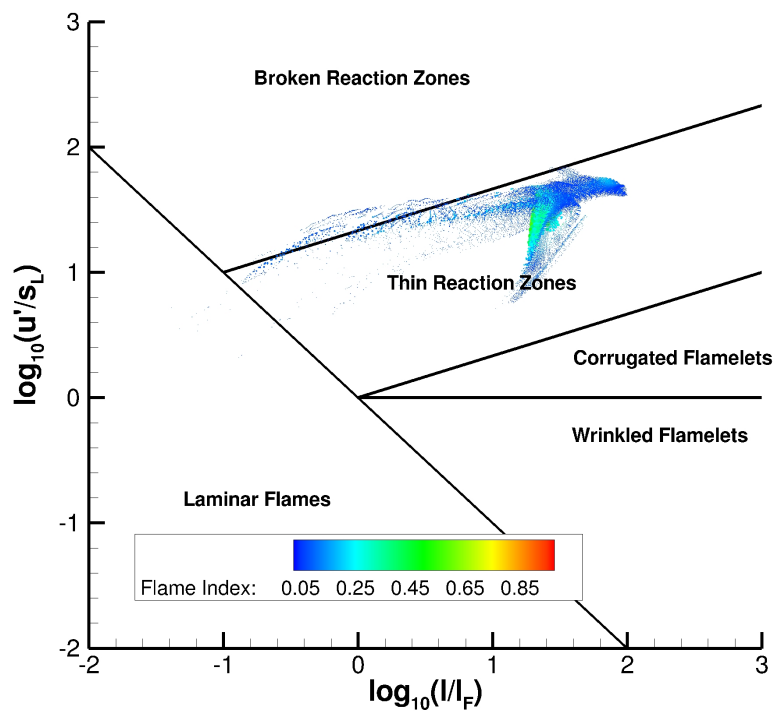


FIGURE 4.9: Borghi diagram for case S800A, whose data are colored by flame index sized by chemical heat release and shown for  $\Lambda_f > 0.05$ .

is relatively insignificant when compared to that of the non-premixed data. Thus, the fact that the combustion may not meet the fundamental flamelet assumptions may be irrelevant. However, for the case of scram-mode combustion where much of the premixed combustion occurs within the thin reactions regime, the heat release due to these premixed data is significant. Therefore, these regions of highly-turbulent premixed thin and broken reaction zones challenge the fundamental assumptions of flamelet-model theory and may suggest alternate modeling techniques are necessary to simulate the HDCR engine primary injector flames during scram-mode operation. It is important to note that recent work by Savard and Blanquart suggests flamelet models may be used successfully even for these premixed combustion regimes by using an effective Lewis number mapping [66]. However, further work is necessary to validate this approach for the current flowfield.

### 4.3 Compressibility

Building on the success of incompressible flamelet-models, researchers have in recent years embarked on efforts to extend flamelet-models for application to high-speed, compressible reacting flows. These efforts have largely focused on modifying the incompressible flamelet-model formulation to account for the effects of compressibility on the thermochemical state space embedded in a flamelet table by either parameterizing the solutions to the incompressible constant-pressure flamelet equations by pressure [67] or by introducing a pressure scaling on the progress-variable source term when extracting it from the flamelet table [23, 68]. In this section, the effects of compressibility on the combustion are illustrated by investigating the flame structure in mixture fraction space and by examining the effects of pressure.

Since the majority of the combustion occurs in a non-premixed mode, mixture fraction provides a convenient parameterization of the three-dimensional flowfield data. In Fig. 4.10, temperature is plotted in mixture fraction space for cases D584A and S800A and is colored by the logarithm of static pressure. Data corresponding to the primary injector flames are included in Figs. 4.10a and 4.10b for cases D584A and S800A, respectively, while data for the secondary injector flames are included in Figs. 4.10c and 4.10d for the same cases, respectively. The variation in pressure appears to be generally higher for case S800A, although case D584A exhibits significant variation as well. The

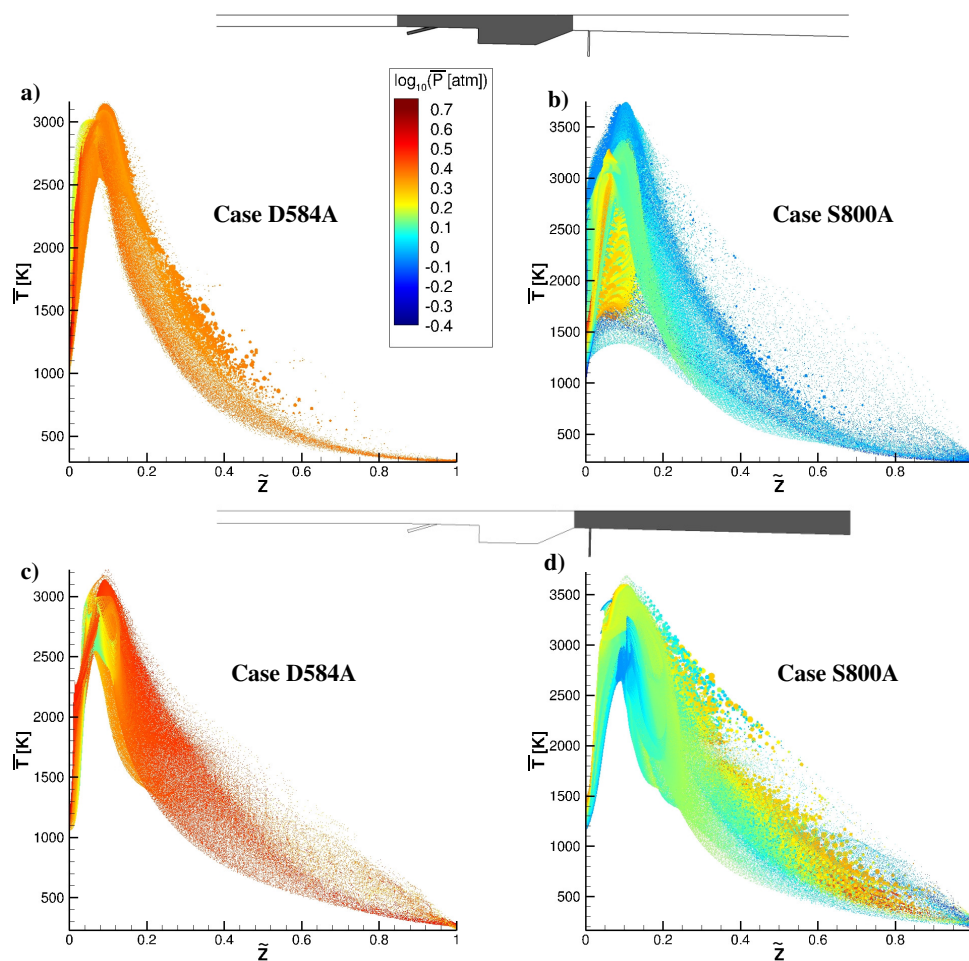


FIGURE 4.10: Static temperature,  $\bar{T}$ , versus mixture fraction,  $\tilde{Z}$ , colored by the logarithm of static pressure,  $\bar{P}$ , and sized by chemical heat release rate,  $\tilde{Q}$ , for (a) case D584A and (b) case S800A primary injector flames and for (c) case D584A and (d) case S800A secondary injector flames.

scram-mode data appear to span approximately half an order more of static pressure as compared to the dual-mode data, for which the static pressure spans nearly an entire order of magnitude. Thus, any suitable flamelet-model must account for the effects of pressure and compressibility for application to a dual-mode scramjet combustor.

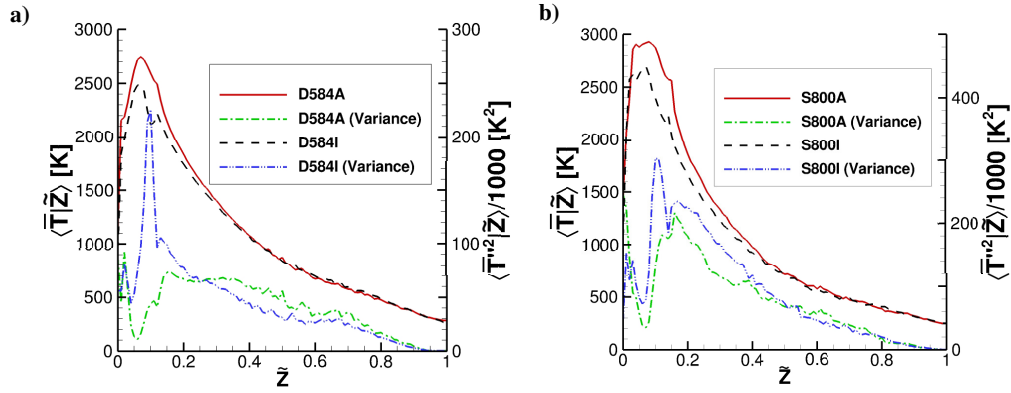


FIGURE 4.11: Static temperature and variance conditionally-averaged on mixture fraction ( $\langle \bar{T} | \tilde{Z} \rangle$  and  $\langle \bar{T}''^2 | \tilde{Z} \rangle$ , respectively) for dual-mode (a) and scram-mode (b) cases.

## 4.4 Wall Heat Losses

In addition to compressibility concerns, recent research efforts have been directed at including the effects of heat losses in flamelet-models for application to flows with non-adiabatic walls. As with compressibility, researchers have focused on developing modifications to existing incompressible flamelet models to account for wall heat losses using various approaches [69–71]. In this section, the effect of heat loss on the flame structure is illustrated for the HDCR combustor by analyzing the simulations computed using adiabatic walls and those computed allowing for one-dimensional heat conduction through the walls, thereby making solution differences precisely an effect of wall heat transfer.

The primary mechanism by which wall heat transfer influences the combustion field is local quenching in the vicinity of the wall. For scramjet engines, in which the core flow is at high velocity and fuel is injected through the walls, a considerable amount of fuel is entrained in the slow-moving near-wall regions. As a result, the fuel has sufficient time to mix with oxidizer and react, thereby creating intense regions of combustion near the wall surfaces. In Figs. 4.11a and 4.11b, temperature conditionally-averaged on mixture fraction is plotted for cases D584A and D584I and cases S800A and S800I, respectively. Also included on both figures is the temperature variance. For both dual-mode and scram-mode operation, the effect of heat loss through the walls is a decrease in average stoichiometric temperature and an increase in temperature variance, which is in accord with the notion that heat loss through the walls results in regions of quenched combustion and reduced boundary layer autoignition. Further, the effect of heat losses through the walls can be clearly seen in Figs. 4.12a and 4.12b for dual-mode operation

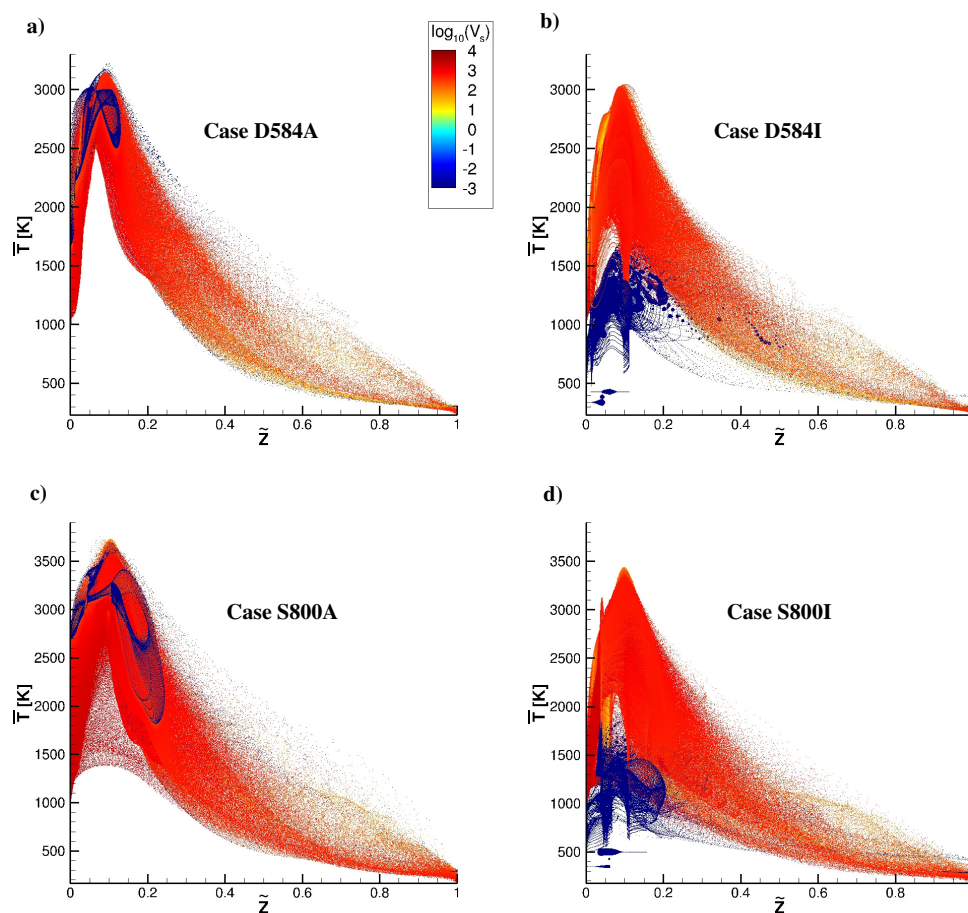


FIGURE 4.12: Static temperature plotted in mixture fraction space and colored by logarithm of velocity magnitude,  $V_s$ , for cases (a) D584A, (b) D584I, (c) S800A, and (d) S800I, showing the effect of heat losses on the combustion.

and in Figs. 4.12c and 4.12d for scram-mode operation by examining the near-wall data. In Fig. 4.12, the static temperature is plotted in mixture fraction space, and data are colored by the velocity magnitude,  $V_s$ . By examining the minimum velocity magnitude data, one can directly observe the effect of near-wall flame quenching by heat losses through the wall; these quenched, near-wall data for cases D584I and S800I reside among the higher temperature data in cases D584A and S800A, respectively. While these differences are pronounced and may possibly suggest the inclusion of such effects in a general compressible flamelet model, adiabatic walls yielded more accurate solutions when compared to experimental static pressure data for the HDCR, thereby suggesting the aggregate effect of wall heat transfer on the combustion is limited.

## 4.5 Considerations for a Compressible FPV Model

Since the analysis presented in the previous section suggests that the fundamental assumptions of flamelet-models are largely valid for the HDCR combustor during dual-mode operation, and potentially for scram-mode operation, subsequent analysis is concerned with some of the more pragmatic issues in applying a flamelet-model to a high-speed, compressible turbulent reacting flow. In this section, a compressible flamelet model methodology is discussed that addresses the problem of boundary condition specification and corresponding table construction.

As was initially discussed in Chapter 2, typical flamelet model parameterizations like  $(Z, \chi)$  or  $(Z, C)$  are generally inadequate due to the wide variations in pressure and temperature. To account for these effects, a suitable manifold must also include pressure, and likely enthalpy, as parameterizing quantities. However, the process of specifying applicable ranges for some of the quantities *a priori* is unclear. For example, since pressure varies with flowpath geometry and across shocks, determining the appropriate pressures at which to build a flamelet table for a scramjet combustor is impossible without prior knowledge of the flowfield. In this regard, a compressible flamelet model is fundamentally different from conventional incompressible flamelet models. A further complication is that pressure and enthalpy are not conveniently defined to vary between zero and unity like mixture fraction and progress variable. In order to use flamelet models to simulate the high-speed compressible flows found within scramjet engines, a new flamelet model methodology is necessary.

The critical component of such a methodology, apart from the details of the model itself, is the use of the *a priori* data in building a suitable flamelet table. After determining the applicability of flamelet models for a given flowfield, *a priori* data regarding the flames must be elicited from either a prior simulation or available experimental data. At a minimum, fuel and oxidizer temperatures (or enthalpies) and pressures must be collected for regions of the flowfield where a flame index indicates the presence of combustion. With this data, one may construct PDFs to determine the range of flamelet conditions required to model the combustion. The flamelet table is subsequently built by solving the flamelet equations across these conditions and by parameterizing the state space by mixture fraction, progress variable, pressure, and enthalpy. At runtime, transport equations are solved for each of these parameterizing variables. For the case of multiple

injectors, it may be prudent to tailor the analysis to each set independently and to determine whether a multiple flamelet approach is best suited [72, 73].

As a first step in estimating the representative flamelet conditions embedded in the HDCR combustor, all data points within 1% of pure oxidizer and pure fuel according to mixture fraction were isolated from the solution. Next, these data were split into two groups according to whether the data resided in the primary or secondary injector flames. PDFs were constructed for pressure and temperature and are shown for cases D584A and S800A in Fig. 4.13. For both dual-mode and scram-mode operation, the fuel temperatures remain fairly constant at their nominal values, while the oxidizer temperatures vary considerably and exhibit multimodal distributions. For the primary injector flames, the fuel pressures are distributed tightly around their nominal values, whereas the oxidizer pressures exhibit multimodal distributions. In the case of the secondary injector flames, both the fuel and oxidizer pressures show multimodal distributions. While the most representative samplings of these distributions are not immediately apparent, bounding conditions for these temperatures and pressures can be quickly determined by examining the span of each PDF. Bounding conditions on fuel and oxidizer temperature and pressure based on these PDFs are summarized in Table 4.1. Sensitivity studies are likely necessary to determine the minimum number of enthalpy and pressure levels required for a given simulation within these bounding values. Additional discussion of the use of *a priori* data in the use of flamelet-based combustion models is included in Chapters 5 and 6 with regards to the proposed CFPVX model.

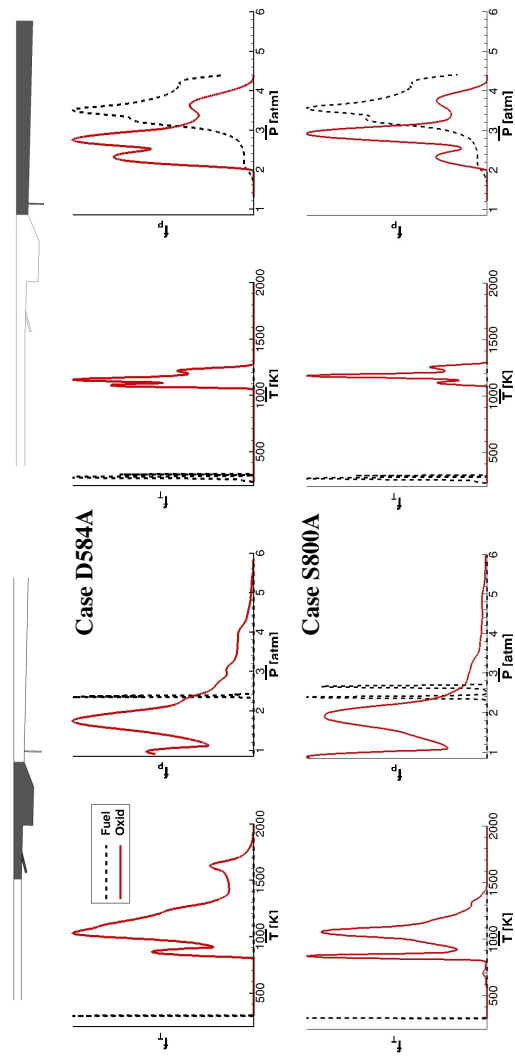


FIGURE 4.13: PDFs of static temperature and pressure ( $f_T$  and  $f_P$ , respectively) for fuel ( $Z < 0.01$ ) and oxidizer ( $Z > 0.99$ ) conditions for cases D584A (top) and S800A (bottom). Regions from which the data are sampled are shown above the respective plots, with the leftmost representing the primary injector flames and the rightmost representing the secondary injector flames.

TABLE 4.1: Approximate bounding fuel and oxidizer temperature and pressures derived from corresponding PDFs for simulated test cases.

Case	Injector Location	Fuel Temperature Range [K]	Fuel Pressure Range [atm]	Oxidizer Temperature Range [K]	Oxidizer Pressure Range [atm]
D584A	Primary	300.0 - 300.0	2.25 - 2.50	800.0 - 1900.0	0.90 - 5.80
D584I	Secondary	230.0 - 300.0	1.60 - 4.40	1050.0 - 1275.0	2.00 - 4.30
S800A	Primary	300.0 - 300.0	2.30 - 2.70	550.0 - 1450.0	0.85 - 6.00
S800I	Secondary	230.0 - 300.0	1.70 - 4.40	1100.0 - 1300.0	2.00 - 4.20

## Chapter 5

# *A Priori* FPV Model Analysis

In this chapter, the details of the novel APFM-RANS analysis method and corresponding results are presented. In doing so, this chapter addresses several of the challenges facing a compressible FPV (CFPV) model identified using the *a priori* analysis of the HDCR combustor data in the previous chapter. First, an overview of the APFM-RANS analysis method is presented in section 5.1, including descriptions of the FPV models chosen for further analysis and the flamelet table generation and data retrieval methods used. In section 5.2.1, the APFM-RANS analysis is used to perform a trade study on the efficacy of several candidate progress variables found in the literature. Next, the use of pressure as a means of accounting for compressibility effects on the combustion is investigated and a summary of this analysis is presented in section 5.2.2. Several numerically-efficient methods of constructing model coupling terms present in the governing equation for the total energy are considered in section 5.2.3. Finally, the variability in the oxidizer temperature observed in the previous chapter is used to propose a novel CFPV model formulation in section 5.2.4.

### 5.1 Methodology

#### 5.1.1 FPV Model Implementation Considerations

The APFM-RANS analysis method was developed to efficiently study the modeling characteristics of a variety of compressible flamelet models. For reacting RANS calculations, the compressible Reynolds-averaged transport equations for mass, momentum,

total energy, and reactive scalars are solved. This system of transport equations is closed using the ideal gas equation of state. For flamelet-based modeling approaches, however, all of the reactive scalar transport equations are replaced by several tracking scalars used to parameterize the thermochemical state-space. This alternative system generally includes a single passive scalar (typically mixture fraction,  $Z$ ) and a single reactive scalar (typically a progress variable,  $C$ ) transport equation of the forms shown earlier in Eqs. (2.28) and (2.35), respectively. In order to close Eq. (2.35),  $\dot{\omega}_C$  must be calculated using the FPV model. In order to close the transport equation for total energy,  $E$ , which was shown previously in Eq. (2.20), and the equation of state, shown in Eq. (2.22), the FPV model must be used to compute the species mass fractions,  $Y_\alpha$ . The form of the energy interdiffusion term used by VULCAN-CFD is shown below in Eq. (5.1) and is hereafter referred to as  $\beta$ .

$$\beta = \frac{\partial}{\partial x_j} \left[ \left( \frac{\mu}{Sc} + \frac{\mu_t}{Sc_t} \right) \sum_{\alpha=1}^N h_\alpha \frac{\partial Y_\alpha}{\partial x_j} \right] \quad (5.1)$$

For incompressible flow simulations with single air and fuel streams, the FPV models have been shown to work well to describe the thermochemical state for a range of problems of engineering interest [44, 47–50]. However, for a compressible flow, the static pressure cannot be assumed constant and may vary by an order of magnitude or more, as was shown in Chapter 4. The effect of  $p$  on the chemical kinetics and composition must be considered within the FPV model. The proper way to account for this dependence requires adding  $p$  to the flamelet library parameterization. When considering the implementation details of such a compressible FPV model, it is helpful to consider terms used to link the model to the governing equations, which include  $Y_\alpha$ ,  $\dot{\omega}_C$ , and the energy interdiffusion term,  $\beta$ , shown above in Eq. (5.1). These linking terms will be considered in more detail in subsequent sections.

### 5.1.2 APFM-RANS Analysis Method and FPV Model Formulations

Application of the APFM-RANS analysis method relies on first performing a baseline RANS simulation of the flow using a finite-rate chemical kinetics reaction mechanism. This RANS solution serves as the truth data set from which  $Z$  and  $C$  are computed and to which subsequent APFM-RANS analysis data are compared. Bilger’s definition is used to calculate  $Z$  for the current work [45]. In a separate but concurrent step,

a flamelet table is constructed by solving the flamelet equations [27]. Details of the flamelet table generation are included in the following section. Once the  $Z$  and  $C$  fields are constructed from the RANS data and the flamelet table is complete, the desired FPV model formulation is used to compute an APFM-RANS solution.

Computing the APFM-RANS solution requires querying the flamelet table using the reconstructed FPV state vector,  $\phi$ , which for the IFPV model used for the current study consists of  $\phi = [Z\ C]^T$ . Compressible models require additional parameters from the RANS solution, as described later. Linearly interpolated values for  $Y_\alpha$  and  $\dot{\omega}_\alpha$  are retrieved from the table based on  $\phi$  and used to update the original RANS values. Using the updated  $Y_\alpha$  and the internal energy from the RANS solution,  $e_{RANS}$ , the APFM-RANS temperature,  $T$ , is calculated by performing a Newton-Raphson solve on Eq. (5.2), where  $e_{RANS}$  is the internal energy for the baseline RANS solution and  $R$  is the mixture gas constant.

$$0 = e_{RANS} - \sum_{\alpha=1}^N Y_\alpha h_\alpha(T) + T \sum_{\alpha=1}^N R \frac{Y_\alpha}{MW_\alpha} \quad (5.2)$$

NASA thermodynamic polynomials were used to compute mixture static enthalpy,  $h$ , as a function of temperature during application of the APFM-RANS analysis method [37]. Pressure can then be updated using the equation of state in Eq. (2.22). A flowchart detailing the APFM-RANS analysis method is included in Fig. 5.1.

In the current study, three FPV model formulations were tested. The first was the standard IFPV model developed by Pierce and Moin [29], in which the flamelet table was built by solving the flamelet equations over a range of  $\chi_{st}$  and subsequently mapping solutions to  $Z$  and  $C$  space. For this model, a single pressure level was used to compute all the flamelet solutions. Contrary to the original formulation,  $T$  was computed using the Newton-Raphson solve on Eq. (5.2), rather than retrieving directly from the flamelet table. The second model was a CFPV model, in which the flamelet table was parameterized by  $Z$ ,  $C$ , and  $p$ . Similar models can be found in the literature for application to diesel engines [67]. For this model, a flamelet table was constructed by solving flamelet solutions across  $\chi_{st}$  and  $p$ , where baseline RANS data [74] was used to identify physically-representative pressure levels. The third model tested using the APFM-RANS analysis method was a novel CFPV model in which flamelet oxidizer temperature was used as an additional parameterizing scalar. Using baseline RANS data

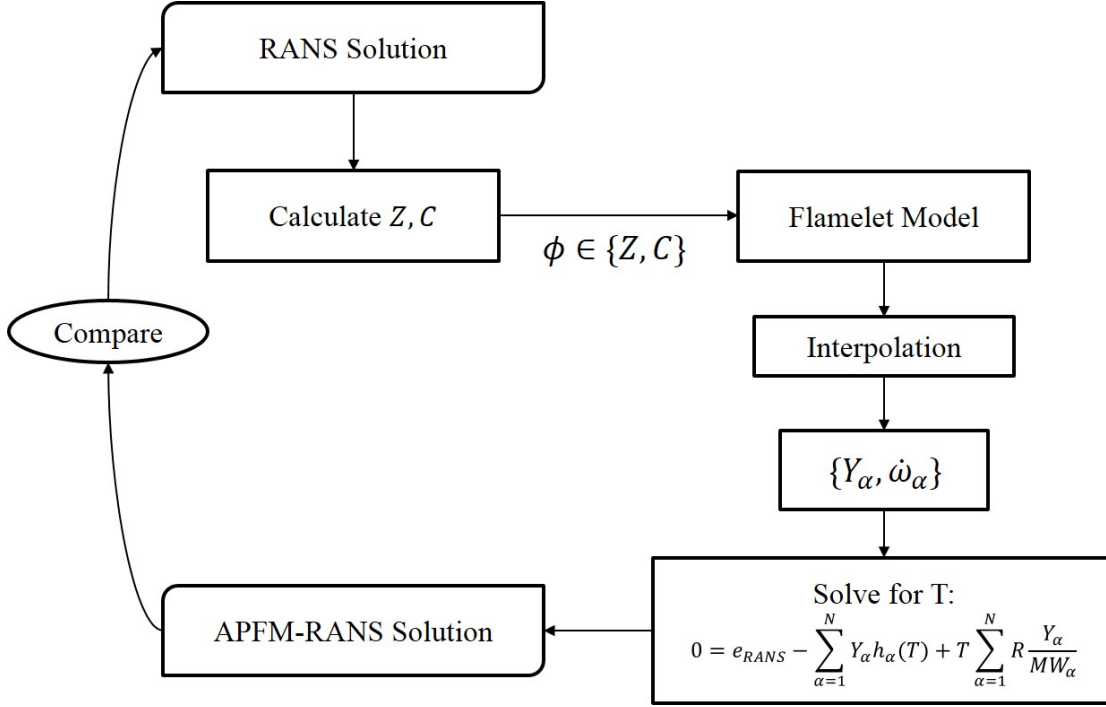


FIGURE 5.1: Flowchart depicting the APFM-RANS analysis method.

as guidance [74], the flamelet table was built by solving the flamelet equations over physically-representative  $\chi_{st}$ ,  $p$ , and  $T_{ox}$  and subsequently mapping the solutions to  $Z$ ,  $C$ ,  $p$ , and  $h$ . In this approach,  $h$  was used as a proxy variable for  $T_{ox}$ . This model, referred hereafter as the CFPVX model, was designed to model the effects of both compressibility and varying flamelet boundary conditions on the combustion. This model is the first for which variation associated with flamelet boundary conditions, which in the current case is oxidizer temperature, is included in an Eulerian FPV model framework.

### 5.1.3 Flamelet Table Generation

A separate flamelet table was constructed for use with each of the three FPV models described in the previous section. For each table, the flamelet equations [27] presented earlier in Eqs. (2.30)-(2.31) were solved using the FlameMaster [75] software. The *pyVFPV* suite of scripts was then used to build the flamelet tables in conjunction with the FlameMaster solutions database. The first table, for use with the IFPV model and hereafter referred to as FT1, consisted of 13 flamelet solutions computed at  $p = 1.0$  atm and varying  $\chi_{st}$ , resulting in a two-dimensional state-space parameterized by  $Z$  and  $C$ . Fuel and oxidizer temperatures were held constant at 300 K and 1100 K, respectively,

which were set to approximately match the average fuel and oxidizer temperatures from the baseline RANS data.

The second table, hereafter referred to as FT2 and used for the CFPV model, consisted of 52 flamelet solutions at pressure levels including  $p = 0.5, 2.5, 4.5,$  and  $6.5$  atm. These  $p$  levels were chosen to best represent the extent of pressure variation observed in the baseline RANS data of the HDCR for dual-mode operation [74]. At each  $p$  level, the solutions were computed by varying  $\chi_{st}$ , resulting in a complete parameterization using  $Z, C,$  and  $p$  and thereby yielding a three-dimensional state-space. Again, for FT2, the fuel and oxidizer temperatures were held constant at 300 K and 1100 K, respectively.

The third flamelet table, hereafter referred to as FT3 and used for the CFPVX model, consisted of 256 flamelet solutions at pressure levels including  $p = 0.5, 2.5, 4.5,$  and  $6.5$  atm and at oxidizer temperature levels including  $T_{ox} = 900, 1100, 1300, 1500,$  and  $1700$  K. Similar to  $p,$   $T_{ox}$  levels were chosen to span the results of the baseline RANS data of the HDCR [74]. These bounds were determined by examining the PDF of  $T_{ox}$  for the baseline RANS data shown in Fig. 5.2, which was computed by calculating  $Z$  and sampling  $T$  at points for  $Z < 0.01$ . Thus, the third table was parameterized by  $Z, C, p,$  and  $T_{ox},$  resulting in a four-dimensional state-space.

Chapter 4 analysis of the HDCR combustor suggested the combustion data was characterized by a wide range of Damköhler number, which thereby supports the existence of strong finite-rate effects [74]. For this reason, it was important to confirm that the FPV models and accompanying flamelet libraries included flamelet solutions along the unstable burning branch of the S-shaped curve, in addition to those along the mixing line and the branch of stable burning solutions. Without the inclusion of the unstable branch, transition from a burning state to the mixing line is non-physical, as was discussed and demonstrated in Chapter 2 in Fig. 2.3. Therefore, each table included flamelet solutions completely traversing the underlying S-shaped curve, as shown by the S-curve for table FT1 in Fig. 5.3.

Since the FPV models used in this study employ a progress variable to model the reaction progress, the  $\chi_{st}$  was subsequently mapped to a corresponding  $C$  for each of the three tables. Candidate  $C$  definitions used for this study are discussed in the following section. In effect, FT1 comprised a two-dimensional state-space parameterized by  $\phi = [ Z C ]^T,$  FT2 comprised a three-dimensional state-space parameterized by  $\phi = [ Z C p ]^T,$  and

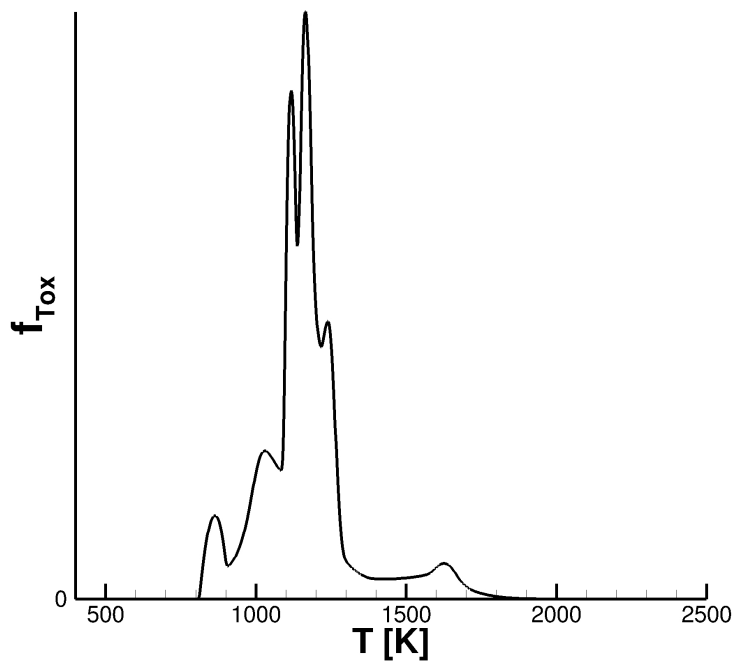


FIGURE 5.2: PDF of  $T_{ox}$  for the HDCR in dual-mode operation, including both the primary and secondary injector combustion regions.

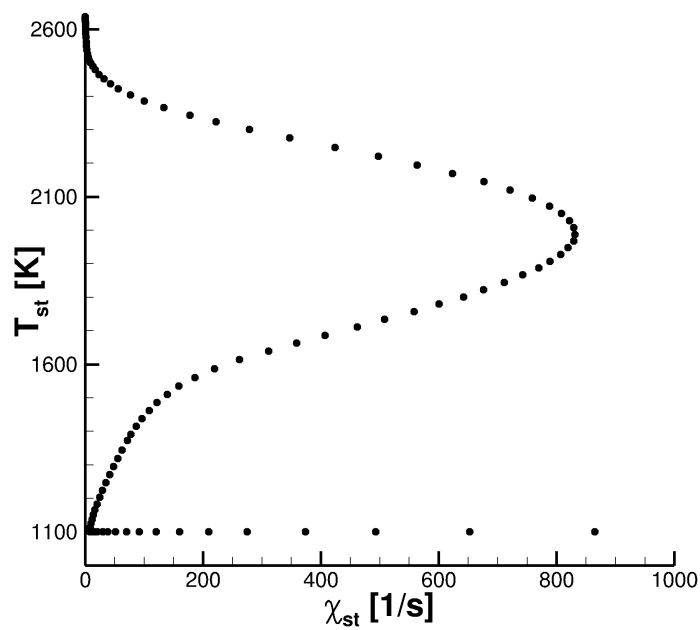


FIGURE 5.3: Stoichiometric temperature,  $T_{st}$ , and  $\chi_{st}$  for flamelet solutions in table FT1 demonstrating the embedded S-shaped curve.

FT3 comprised a four-dimensional state-space parameterized by  $\phi = [ Z C p T_{ox} ]^T$ . However, since a transport equation for  $T_{ox}$  is not easily formed, a further mapping was necessary. It was reasonable to posit that  $h$  varied approximately monotonically with  $T_{ox}$  for constant composition, or constant  $Z$ ,  $C$ , and  $p$ , across the flamelet manifold due to the explicit dependence of  $h$  on  $T$  shown by the definition of  $h$  in Eq. (5.3) for a mixture of thermally perfect gases, where  $\Delta h_f^o$  is the mixture heat of formation,  $T_0$  is the standard state temperature, and  $c_{p\alpha}$  is the specific heat at constant pressure for species  $\alpha$ .

$$h = \sum_{\alpha} h_{\alpha} Y_{\alpha} = \Delta h_f^o + \sum_{\alpha} Y_{\alpha} \int_{T_0}^T c_{p\alpha} dT \quad (5.3)$$

Thus, after building FT3 over  $\phi = [ Z C p T_{ox} ]^T$ , the state-space was subsequently mapped to  $\phi = [ Z C p h ]^T$  for use with the CFPVX model.

For each table, flamelet solution data for  $Y_{\alpha}$ ,  $\dot{\omega}_{\alpha}$ ,  $T$ , and  $\frac{\partial Y_{\alpha}}{\partial Z}$  were stored for use by the APFM-RANS analysis method. The  $\frac{\partial Y_{\alpha}}{\partial Z}$  terms are used to model the energy inter-diffusion term in Eq. (5.1) and will be discussed in the next section. A set of Fortran routines were developed to interface the flamelet table data with VULCAN-CFD and the APFM-RANS software. Because the FlameMaster solutions are grid-adapted to the flame, and are therefore non-uniformly spaced, the analysis tools included binary search routines. In the case of higher-dimension flamelet tables, for which lookup times are considerably more expensive, an index-based search was also developed. In this approach, FlameMaster solutions are mapped onto a uniformly spaced flamelet state-space. The subsequent look up and interpolation are straight forward. The number of grid points in each dimension was then set to 150, 50, 10, and 10 for  $Z$ ,  $C$ ,  $p$ , and  $h$ , respectively, for the current study; these values were representative of the size table that would be used for *a posteriori* simulations on NASA's Pleiades cluster [76] to ensure storage in local memory at runtime. For each call made to the table at runtime, the target  $Z$ ,  $C$ ,  $p$ , and  $h$  are converted to index representations on the uniform grid, and a quadrilinear interpolation is performed prior to returning the requested data.

## 5.2 Results

The current study addresses several research objectives concerning the development and implementation of compressible FPV models. These objectives included: evaluating the

efficacy of progress variable definitions available from the open literature for application to the HDCR combustor; gauging the effectiveness of pressure and temperature scaling techniques for recovering  $\dot{\omega}_C$  from the flamelet table; evaluating model coupling terms embedded in the governing transport equations; and demonstrating the benefits of the proposed CFPVX model. The results for each of these objectives are presented in this section for both the dual-mode (D584A) and scram-mode (S800A) baseline RANS cases described in Chapter 3.

### 5.2.1 Progress Variable Trade Study

In many applications of FPV models,  $C$  is generally defined in an *ad hoc* fashion by the modeler in an attempt to best track the progress of the reaction system. In recent years, some attempts have been made by researchers to more rigorously define  $C$  for a given fuel and reaction mechanism using optimization techniques [77, 78]. Motivated by the deficiencies highlighted by these efforts, a trade study was performed for several definitions of  $C$  commonly used in the literature to model hydrocarbon fuel combustion using flamelet models, and the results are used to select the most appropriate functional form for simulations of the HDCR.

The most general requirement of  $C$  is that it be defined such that it represents the global progress rate of the reaction system being modeled. Some formal requirements for  $C$  were put forth by Ihme et al. [77]. The foremost of these is that all parameters defining the flamelet manifold uniquely identify each point in the thermochemical state-space. In this study, the following commonly used progress variable definitions [29, 79–85] were considered:

$$C = Y_{CO_2} + Y_{CO} \quad (5.4)$$

$$C = Y_{CO_2} + Y_{H_2O} \quad (5.5)$$

$$C = Y_{CO_2} + Y_{H_2O} + Y_{CO} \quad (5.6)$$

$$C = Y_{CO_2} + Y_{H_2O} + Y_{CO} + Y_{H_2} \quad (5.7)$$

For each of these progress variable definitions, APFM-RANS analyses were performed using IFPV, CFPV, and CFPVX models with flamelet tables FT1, FT2, and FT3, respectively. Twenty-four individual cases were analyzed for this study, and each will

hereafter be referred to by its case ID. Each case ID identifies the combustor operational mode, progress variable, and FPV model used. For example, case *DIFPV1* refers to the APFM-RANS analysis for the dual-mode, *D*, configuration (baseline RANS case D584A), with the incompressible FPV model, *IFPV*, and where 1 indicates the first definition for *C* in Eq. (5.4) was used. Similarly, case *SCFPVX4* refers to the APFM-RANS analysis for the scram-mode, *S* configuration (baseline RANS case S800A), with the compressible FPVX model, *CFPVX*, and where the fourth definition for *C* in Eq. (5.7) was used. Additional details regarding these cases are included in Table 5.1. For the current study on *C*, results from cases DIFPV1-DCFPV4 and SIFPV1-SCFPV4 were compared to those of the baseline RANS solutions D584A and S800A, respectively, using  $T$ ,  $Y_{CO_2}$ ,  $Y_{CO}$ ,  $Y_{H_2O}$ , and  $Y_{OH}$ . For each APFM-RANS analysis, the comparisons were made by first inspecting contours at the spanwise centerline of the first injector from the combustor centerline. Scatter plots of the APFM-RANS data were then constructed using the corresponding parameters from the RANS solution over the entire computational domain.

TABLE 5.1: APFM-RANS test cases.

Case	Combustor Configuration	Flamelet Table	Oxidizer Temperature Levels [K]	Static Pressure Levels [atm]	Progress Variable, $C$	Number of Flamelet Solutions
DIFPV1	D584A	FT1	1100	1.0	$CO_2 + CO$	13
DIFPV2	D584A	FT1	1100	1.0	$CO_2 + H_2O$	13
DIFPV3	D584A	FT1	1100	1.0	$CO_2 + H_2O + CO$	13
DIFPV4	D584A	FT1	1100	1.0	$CO_2 + H_2O + CO + H_2$	13
DCFPV1	D584A	FT2	1100	0.5, 2.5, 4.5, 6.5	$CO_2 + CO$	52
DCFPV2	D584A	FT2	1100	0.5, 2.5, 4.5, 6.5	$CO_2 + H_2O$	52
DCFPV3	D584A	FT2	1100	0.5, 2.5, 4.5, 6.5	$CO_2 + H_2O + CO$	52
DCFPV4	D584A	FT2	1100	0.5, 2.5, 4.5, 6.5	$CO_2 + H_2O + CO + H_2$	52
DCFPVX1	D584A	FT3	900, 1100, 1300, 1500, 1700	0.5, 2.5, 4.5, 6.5	$CO_2 + CO$	256
DCFPVX2	D584A	FT3	900, 1100, 1300, 1500, 1700	0.5, 2.5, 4.5, 6.5	$CO_2 + H_2O$	256
DCFPVX3	D584A	FT3	900, 1100, 1300, 1500, 1700	0.5, 2.5, 4.5, 6.5	$CO_2 + H_2O + CO$	256
DCFPVX4	D584A	FT3	900, 1100, 1300, 1500, 1700	0.5, 2.5, 4.5, 6.5	$CO_2 + H_2O + CO + H_2$	256
SIFPV1	S800A	FT1	1100	1.0	$CO_2 + CO$	13
SIFPV2	S800A	FT1	1100	1.0	$CO_2 + H_2O$	13
SIFPV3	S800A	FT1	1100	1.0	$CO_2 + H_2O + CO$	13
SIFPV4	S800A	FT1	1100	1.0	$CO_2 + H_2O + CO + H_2$	13
SCFPV1	S800A	FT2	1100	0.5, 2.5, 4.5, 6.5	$CO_2 + CO$	52
SCFPV2	S800A	FT2	1100	0.5, 2.5, 4.5, 6.5	$CO_2 + H_2O$	52
SCFPV3	S800A	FT2	1100	0.5, 2.5, 4.5, 6.5	$CO_2 + H_2O + CO$	52
SCFPV4	S800A	FT2	1100	0.5, 2.5, 4.5, 6.5	$CO_2 + H_2O + CO + H_2$	52
SCFPVX1	S800A	FT3	900, 1100, 1300, 1500, 1700	0.5, 2.5, 4.5, 6.5	$CO_2 + CO$	256
SCFPVX2	S800A	FT3	900, 1100, 1300, 1500, 1700	0.5, 2.5, 4.5, 6.5	$CO_2 + H_2O$	256
SCFPVX3	S800A	FT3	900, 1100, 1300, 1500, 1700	0.5, 2.5, 4.5, 6.5	$CO_2 + H_2O + CO$	256
SCFPVX4	S800A	FT3	900, 1100, 1300, 1500, 1700	0.5, 2.5, 4.5, 6.5	$CO_2 + H_2O + CO + H_2$	256

### 5.2.1.1 Dual-Mode Operation

Line plots of  $T$ ,  $Y_{CO_2}$ ,  $Y_{CO}$ ,  $Y_{H_2O}$ , and  $Y_{OH}$  at selected streamwise locations along the injector spanwise centerline nearest to the combustor centerline are included for cases DIFPV1-DIFPV4 and cases DCFPV1-DCFPV4 in Figs. 5.4-5.8. The streamwise locations were selected to approximately span the flame regions as indicated by the chemical heat release and flame index in Figs. 3.5 and 4.1, respectively. For each of these figures, the D584A RANS solution (truth model) is shown for comparison. For both the IFPV and CFPV models, the FPV-modeled solutions agree well with the baseline RANS solution for each of the comparison parameters. The line plots of  $T$ ,  $Y_{CO_2}$ , and  $Y_{H_2O}$  obtained using the APFM-RANS analysis method agree well with those obtained from the baseline RANS simulations. The  $Y_{CO}$  and  $Y_{OH}$  fields exhibit weaker agreement with the baseline RANS solution for both the IFPV and CFPV models for all four  $C$  definitions. While the trending of these parameters is similar to that of the RANS solution, it is clear that the FPV models under-predict the production of these minor species. Variation in agreement among the four candidate definitions for  $C$  is less pronounced in these figures, and a more rigorous comparison must be subsequently made. However, it is clear already that the definition for  $C$  given by Eq. (5.5) exhibits significant error due to the multivalued nature of the manifold in  $Z$ - $C$ -space around the stoichiometric curve, as seen in Fig. 5.6 at stations 25.5 cm and 42.0 cm for cases DIFPV2 and DCFPV2. The spikes in concentration of  $Y_{CO}$  occur due to this multivaluedness of the flamelet manifold.

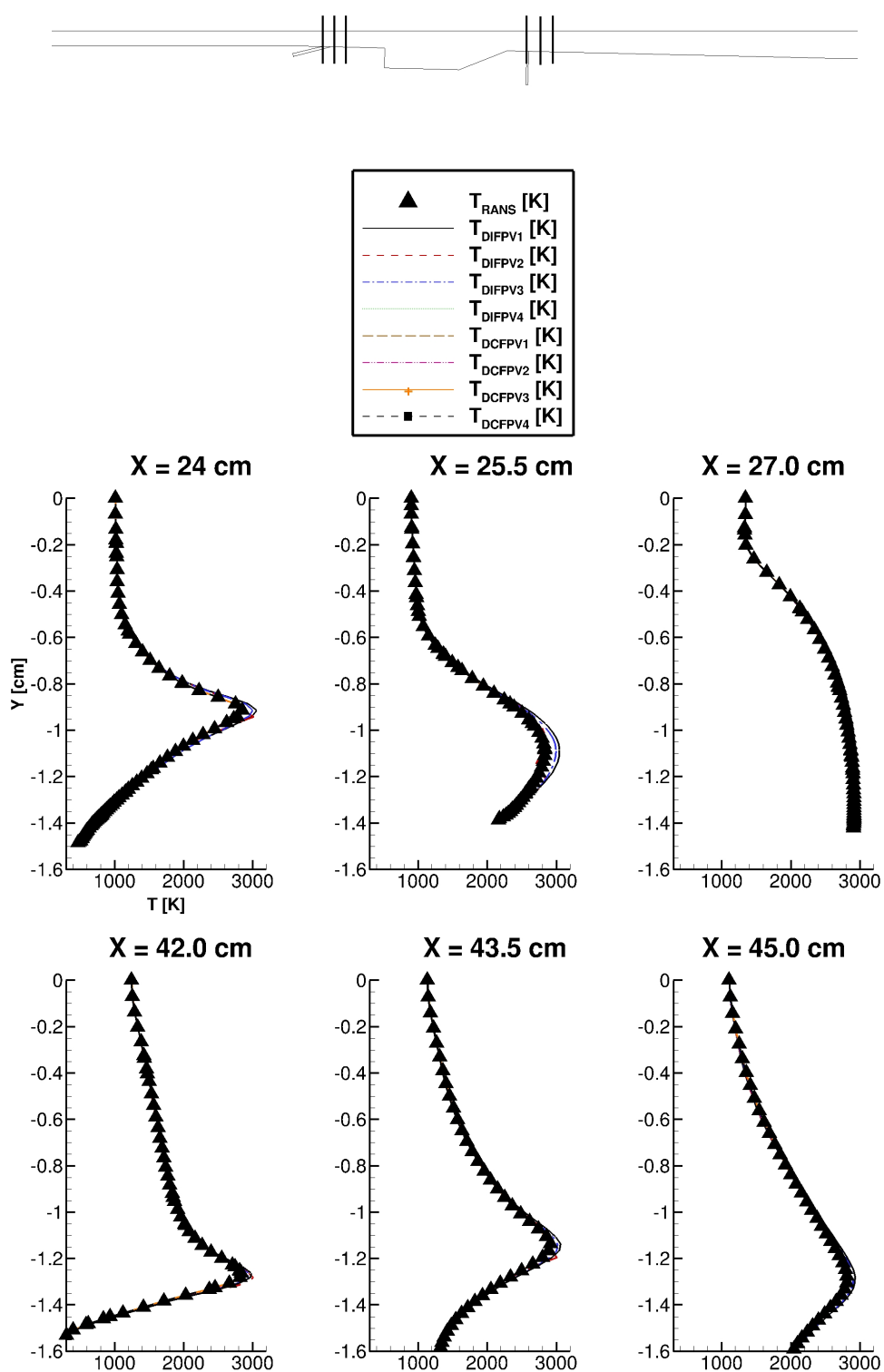


FIGURE 5.4: Line plots of  $Y$  [cm] versus  $T$  [K] obtained using the APFM-RANS analysis method and from the baseline RANS simulations of the HDCR combustor at several locations through the primary and secondary injector flames at the injector centerline nearest to the combustor centerline for cases corresponding to DIFPV1-DIFPV4 and DCFPV1-DCFPV4. Units on each subfigure are the same as those shown on the top-row, left-most subfigure.

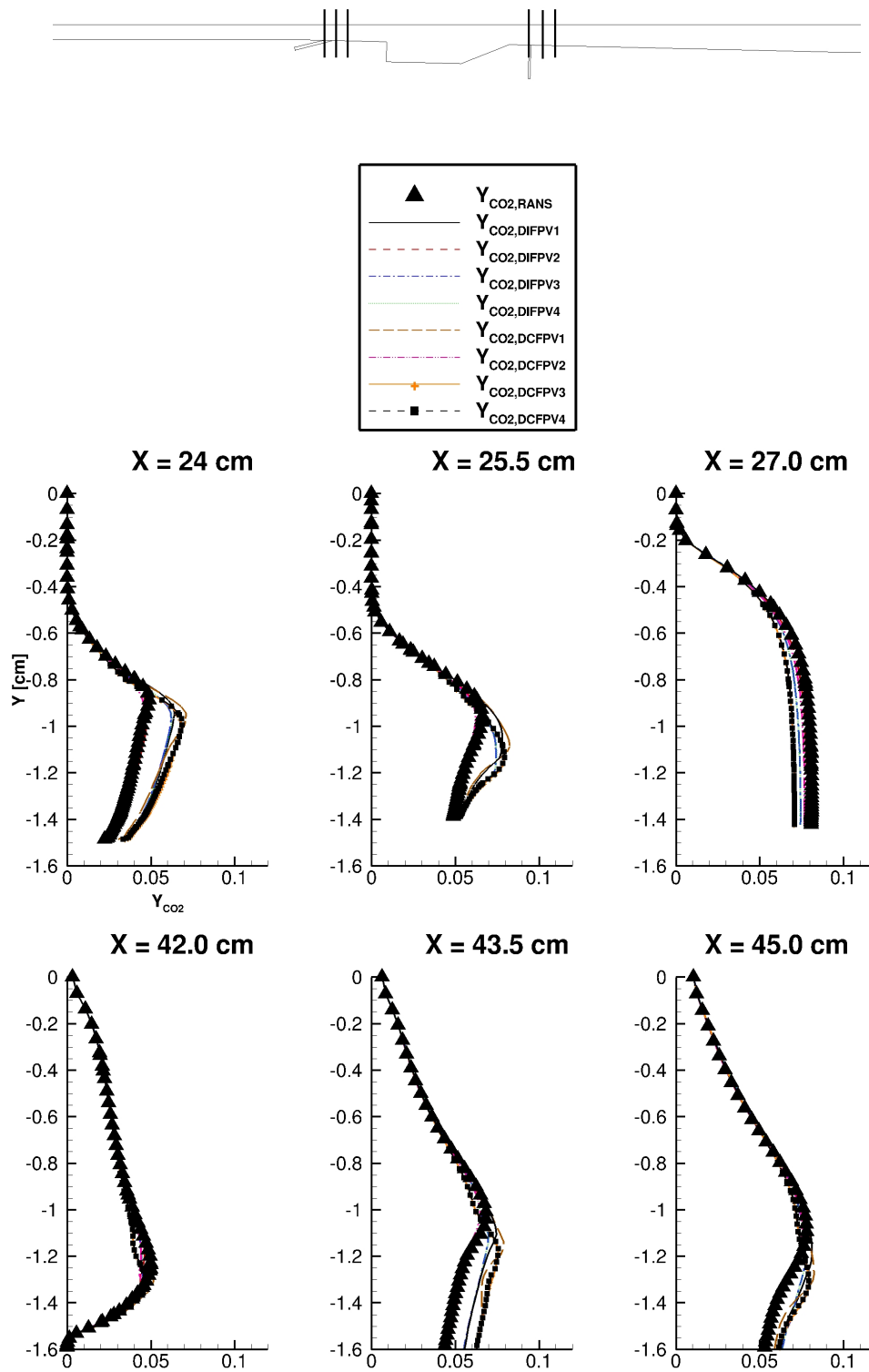


FIGURE 5.5: Line plots of  $Y$  [cm] versus  $Y_{CO_2}$  obtained using the APFM-RANS analysis method and from the baseline RANS simulations of the HDCR combustor at several locations through the primary and secondary injector flames at the injector centerline nearest to the combustor centerline for cases corresponding to DIFPV1-DIFPV4 and DCFPV1-DCFPV4. Units on each subfigure are the same as those shown on the top-left, left-most subfigure.

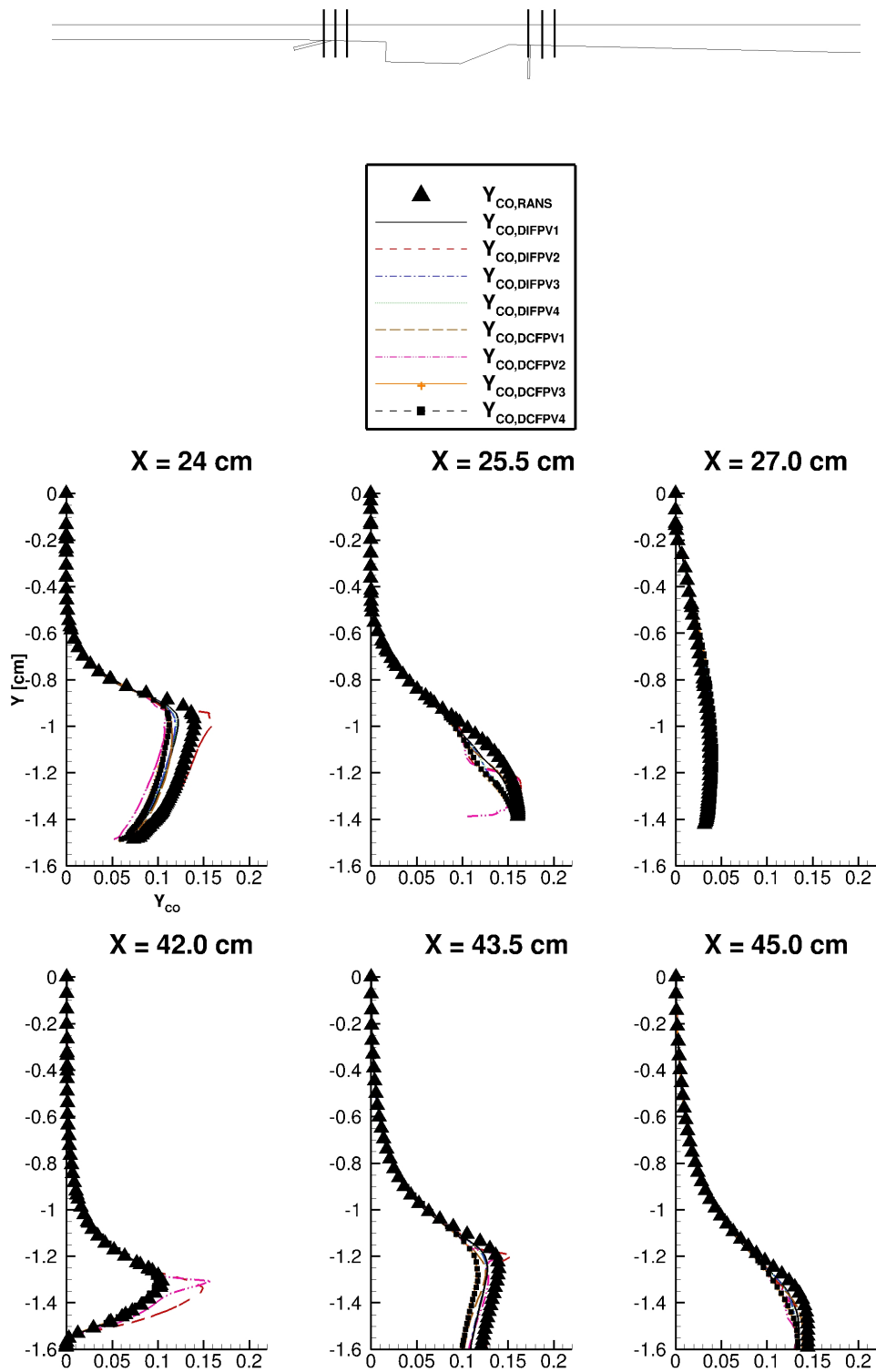


FIGURE 5.6: Line plots of  $Y$  [cm] versus  $Y_{CO}$  obtained using the APFM-RANS analysis method and from the baseline RANS simulations of the HDCR combustor at several locations through the primary and secondary injector flames at the injector centerline nearest to the combustor centerline for cases corresponding to DIFPV1-DIFPV4 and DCFPV1-DCFPV4. Units on each subfigure are the same as those shown on the top-row, left-most subfigure.

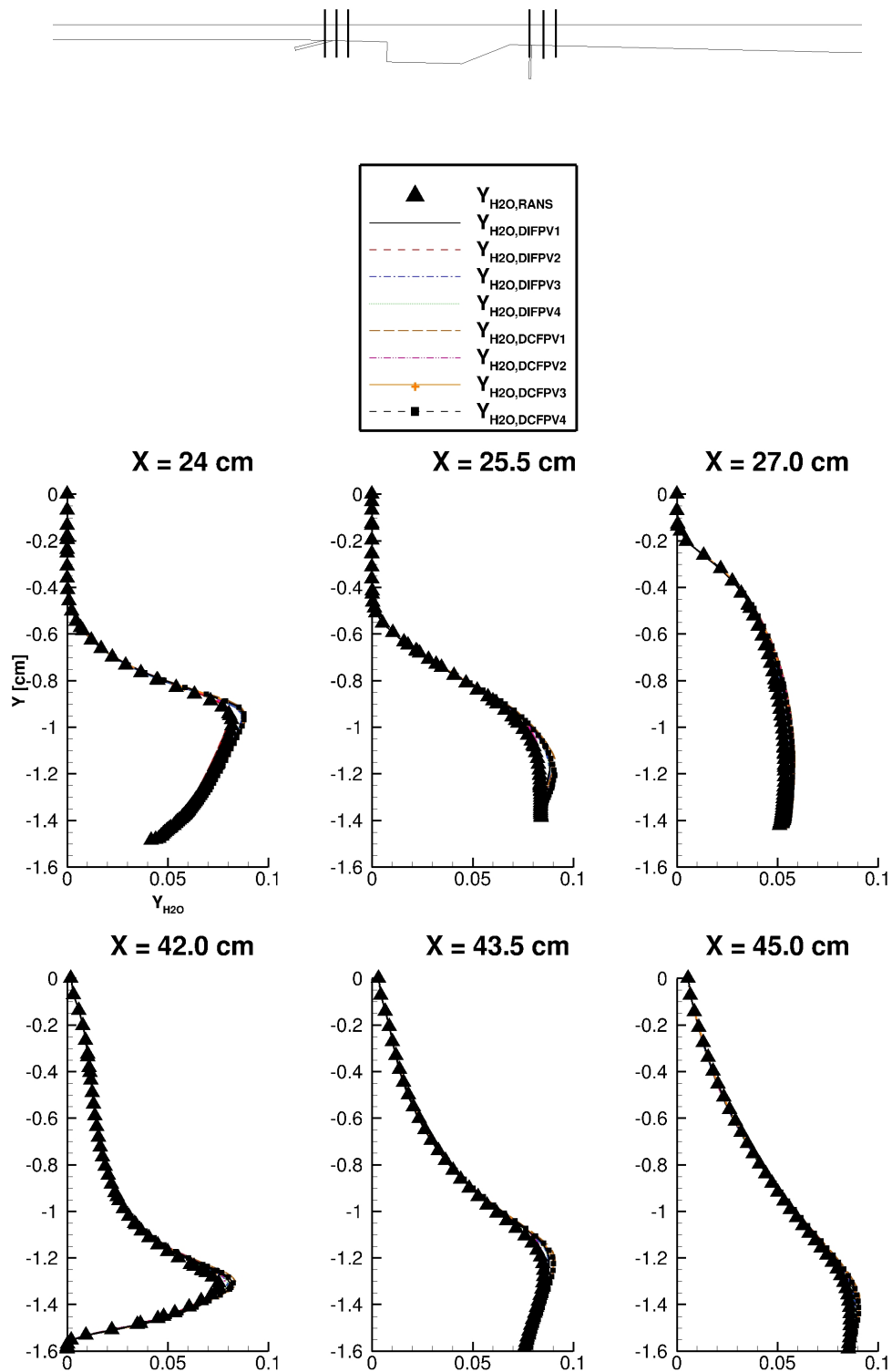


FIGURE 5.7: Line plots of  $Y$  [cm] versus  $Y_{H_2O}$  obtained using the APFM-RANS analysis method and from the baseline RANS simulations of the HDCR combustor at several locations through the primary and secondary injector flames at the injector centerline nearest to the combustor centerline for cases corresponding to DIFPV1-DIFPV4 and DCFPV1-DCFPV4. Units on each subfigure are the same as those shown on the top-row, left-most subfigure.

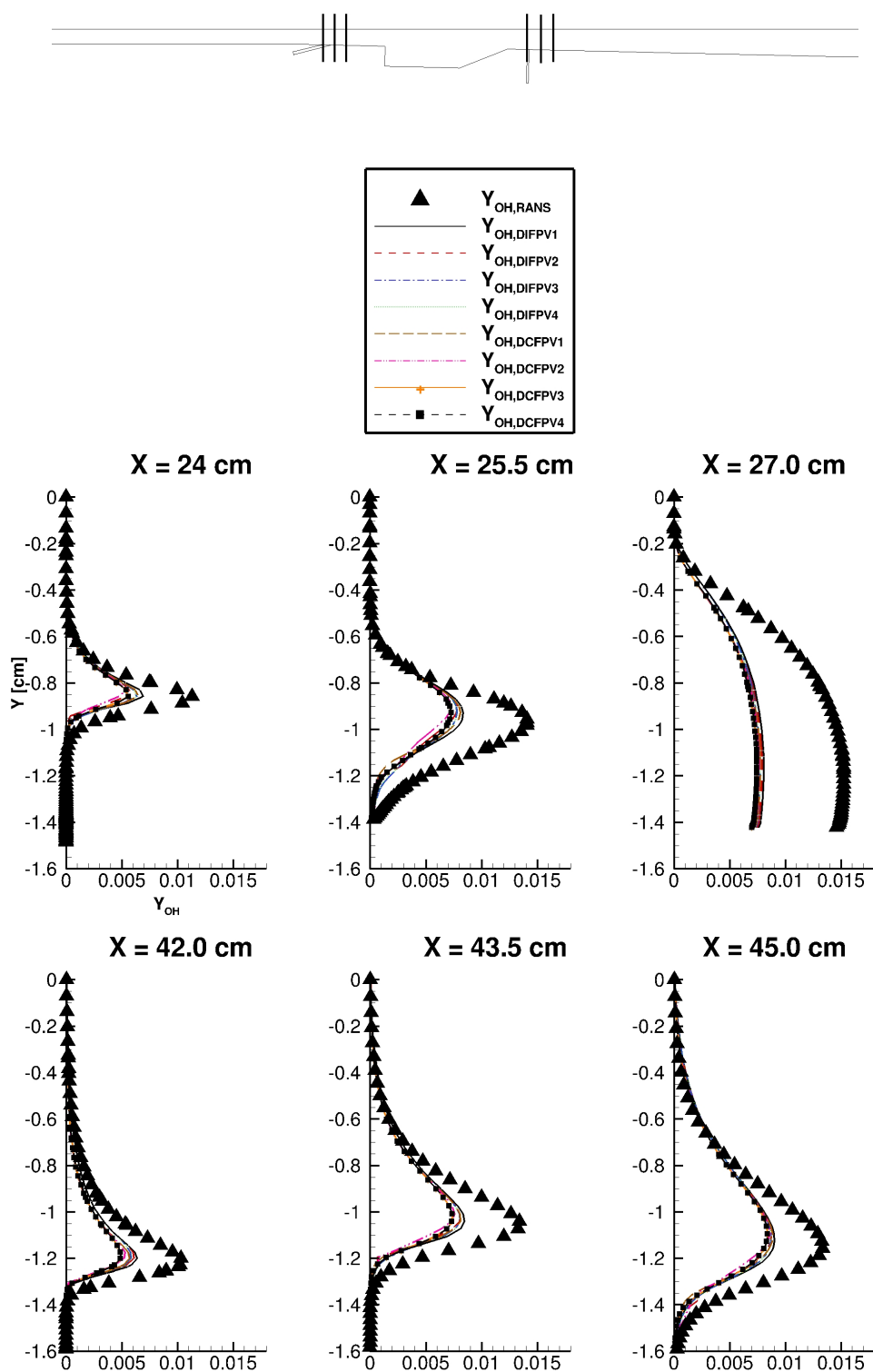


FIGURE 5.8: Line plots of  $Y$  [cm] versus  $Y_{OH}$  obtained using the APFM-RANS analysis method and from the baseline RANS simulations of the HDCR combustor at several locations through the primary and secondary injector flames at the injector centerline nearest to the combustor centerline for cases corresponding to DIFPV1-DIFPV4 and DCFPV1-DCFPV4. Units on each subfigure are the same as those shown on the top-row, left-most subfigure.

A more detailed comparison can be made by scatter plotting FPV-modeled results against those of the baseline RANS case. These plots are shown for cases DIFPV1-DIFPV4 and cases DCFPV1-DCFPV4 in Figs. 5.9-5.13 and Figs. 5.14-5.18, respectively. In each of these figures, a solid red line of slope one is overlaid on the data as a marker for one-to-one agreement. Deviation from this solid red line indicates the extent of disagreement among the modeled data. Analyzing Figs. 5.9 and 5.14 suggests that for IFPV models, the detailed form of  $C$  is critical to recovering the  $T$  field, whereas for CFPV models, the  $T$  field is much less sensitive. Figure 5.9 shows that the scatter plot corresponding to DIFPV4 obtained using Eq. (5.7) results in a significantly more-accurate comparison than the other candidate definitions for  $C$ , whereas in Fig. 5.14, all four candidates for  $C$  result in similarly accurate scatter.

Contrary to the trend in the values of  $T$ , analyzing results for the selected species mass fractions in Figs. 5.10-5.13 and 5.15-5.18 suggests the chemical composition exhibits considerably less sensitivity to the inclusion of  $p$  as a parameterizing variable in the FPV model. Though, for both the IFPV and CFPV models, the chemical composition exhibits a similarly-high sensitivity to the detailed form of  $C$ . Also interesting, though perhaps expected, are the trends among the values of the four  $C$  candidates, which are not static from one species to the next. For example, in the case of  $Y_{CO_2}$  in Figs. 5.10 and 5.15, the results given by Eq. (5.4) in the top-row, left-most subfigure exhibit the best agreement with the baseline RANS solution; however, for  $Y_{H_2O}$  in Figs. 5.12 and 5.17 in the top-row, right-most subfigure, results given by Eq. (5.5) show the best agreement.

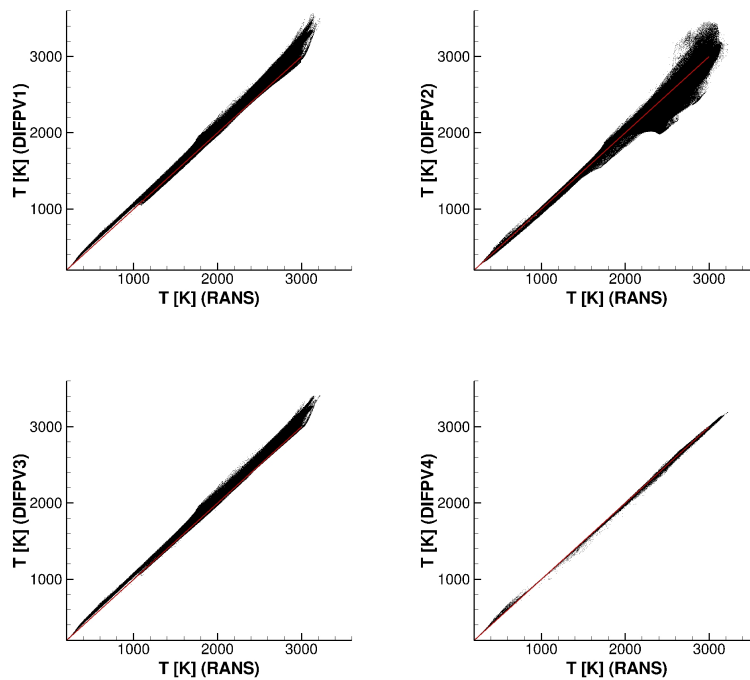


FIGURE 5.9: Scatter plots of the temperature,  $T$  [K], obtained using the APFM-RANS analysis method versus that from the baseline RANS simulations of the HDCR combustor for the full computational domain for cases DIFPV1-DIFPV4. The red line denotes a line with slope of one.

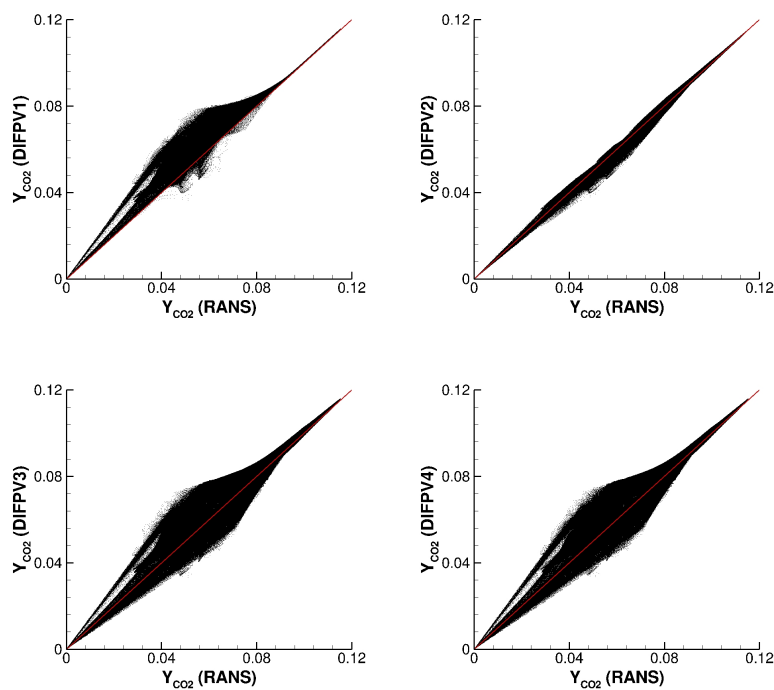


FIGURE 5.10: Scatter plots of  $Y_{CO_2}$  obtained using the APFM-RANS analysis method versus that from the baseline RANS simulations of the HDCR combustor for the full computational domain for cases DIFPV1-DIFPV4. The red line denotes a line with slope of one.

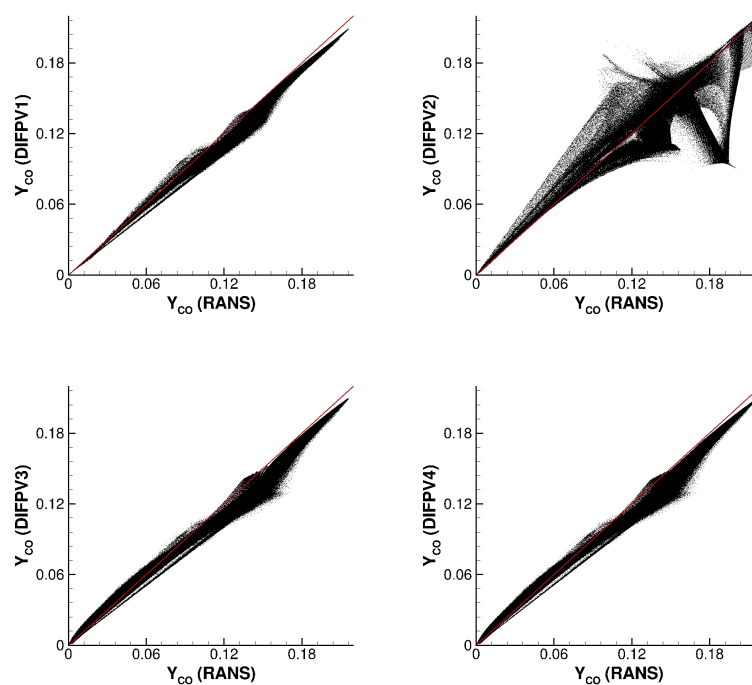


FIGURE 5.11: Scatter plots of  $Y_{CO}$  obtained using the APFM-RANS analysis method versus that from the baseline RANS simulations of the HDCR combustor for the full computational domain for cases DIFPV1-DIFPV4. The red line denotes a line with slope of one.

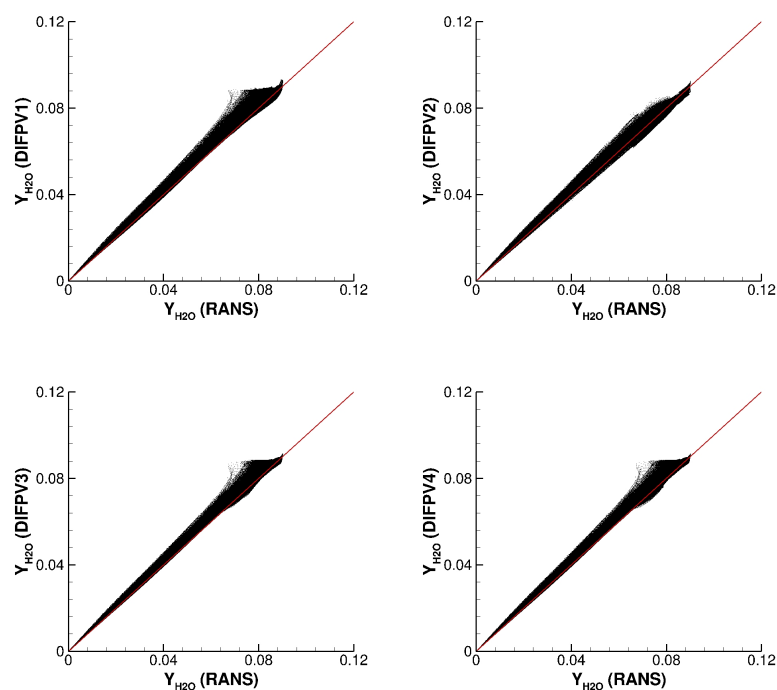


FIGURE 5.12: Scatter plots of  $Y_{H_2O}$  obtained using the APFM-RANS analysis method versus that from the baseline RANS simulations of the HDCR combustor for the full computational domain for cases DIFPV1-DIFPV4. The red line denotes a line with slope of one.

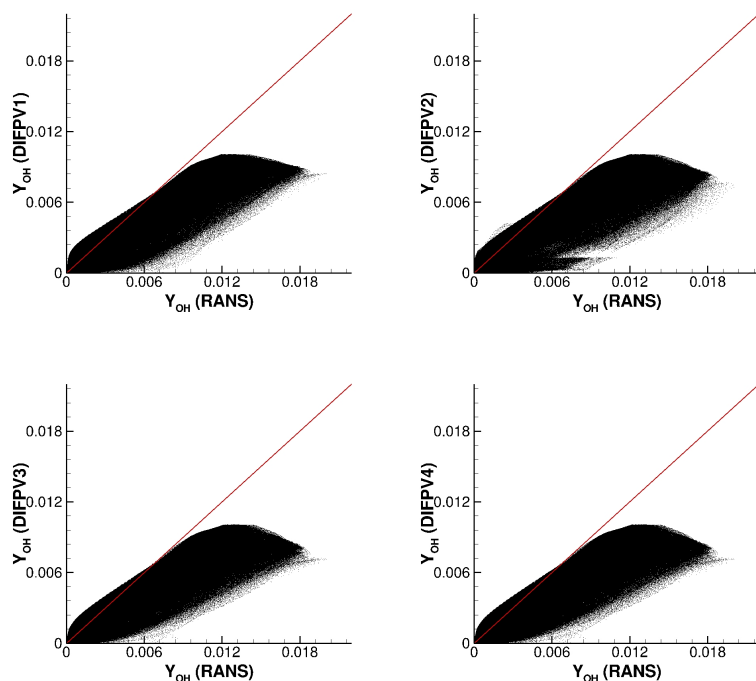


FIGURE 5.13: Scatter plots of the temperature,  $Y_{OH}$ , obtained using the APFM-RANS analysis method versus that from the baseline RANS simulations of the HDCR combustor for the full computational domain for cases DIFPV1-DIFPV4. The red line denotes a line with slope of one.

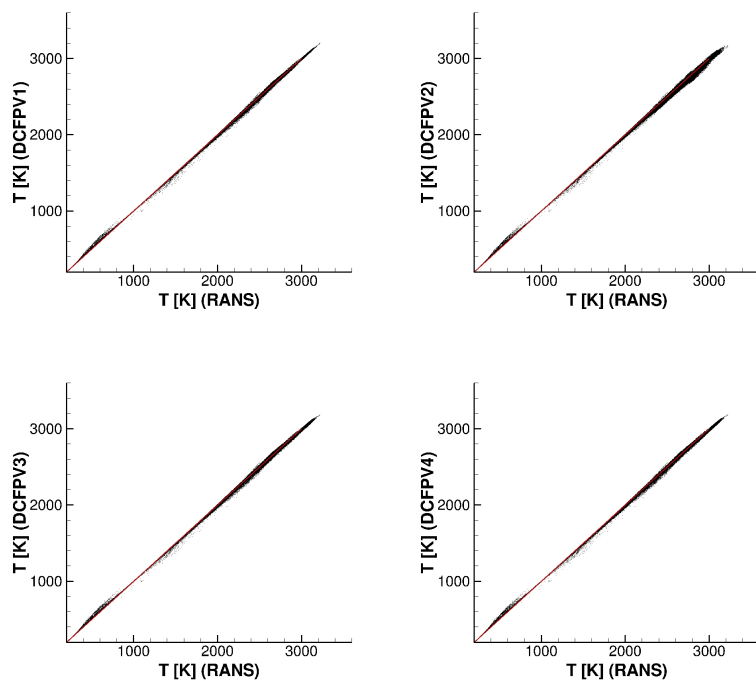


FIGURE 5.14: Scatter plots of  $T$  [K] obtained using the APFM-RANS analysis method versus that from the baseline RANS simulations of the HDCR combustor for the full computational domain for cases DCFPV1-DCFPV4. The red line denotes a line with slope of one.

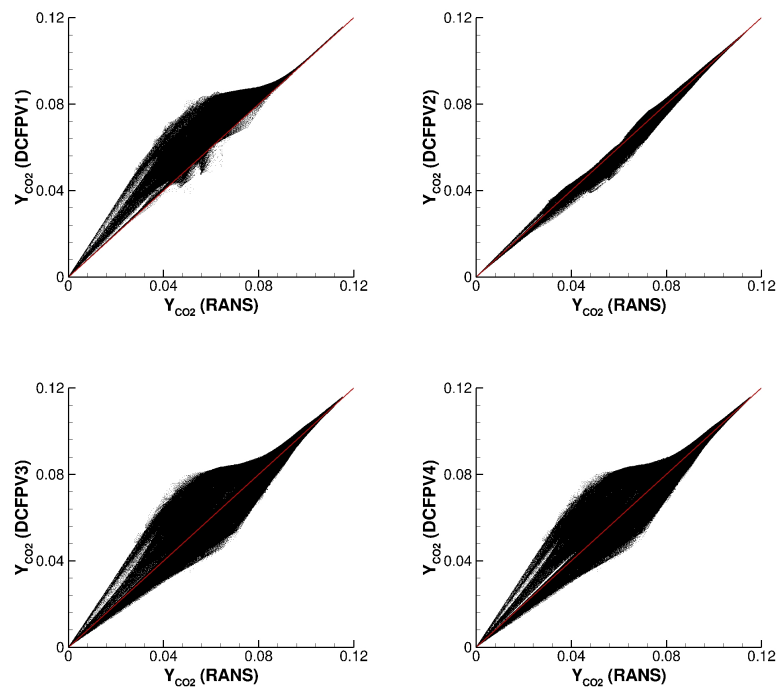


FIGURE 5.15: Scatter plots of  $Y_{CO_2}$  obtained using the APFM-RANS analysis method versus that from the baseline RANS simulations of the HDCR combustor for the full computational domain for cases DCFPV1-DCFPV4. The red line denotes a line with slope of one.

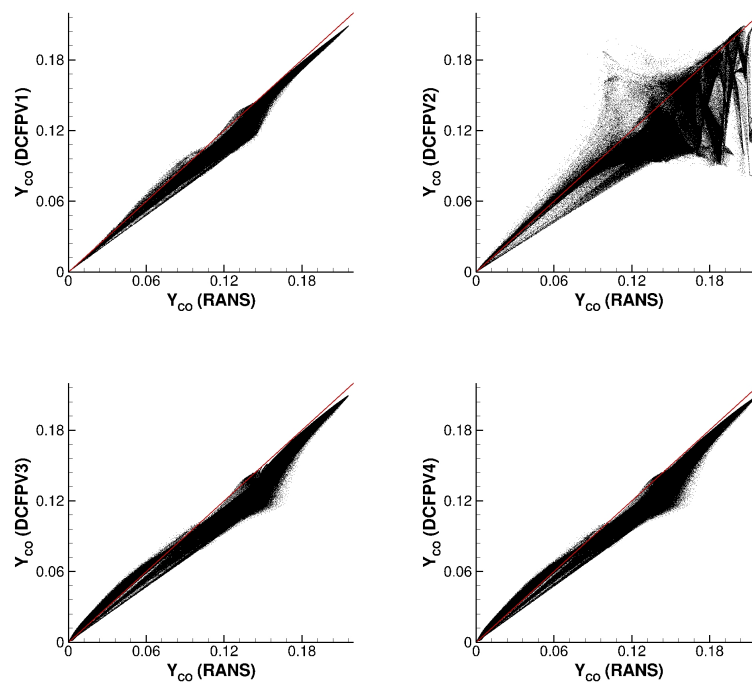


FIGURE 5.16: Scatter plots of  $Y_{CO}$  obtained using the APFM-RANS analysis method versus that from the baseline RANS simulations of the HDCR combustor for the full computational domain for cases DCFPV1-DCFPV4. The red line denotes a line with slope of one.

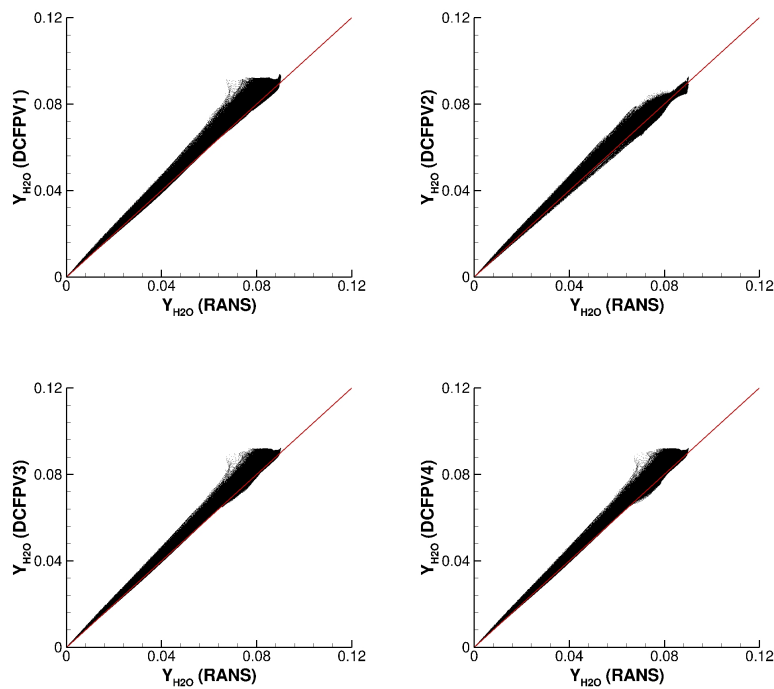


FIGURE 5.17: Scatter plots of  $Y_{H_2O}$  obtained using the APFM-RANS analysis method versus that from the baseline RANS simulations of the HDCR combustor for the full computational domain for cases DCFPV1-DCFPV4. The red line denotes a line with slope of one.

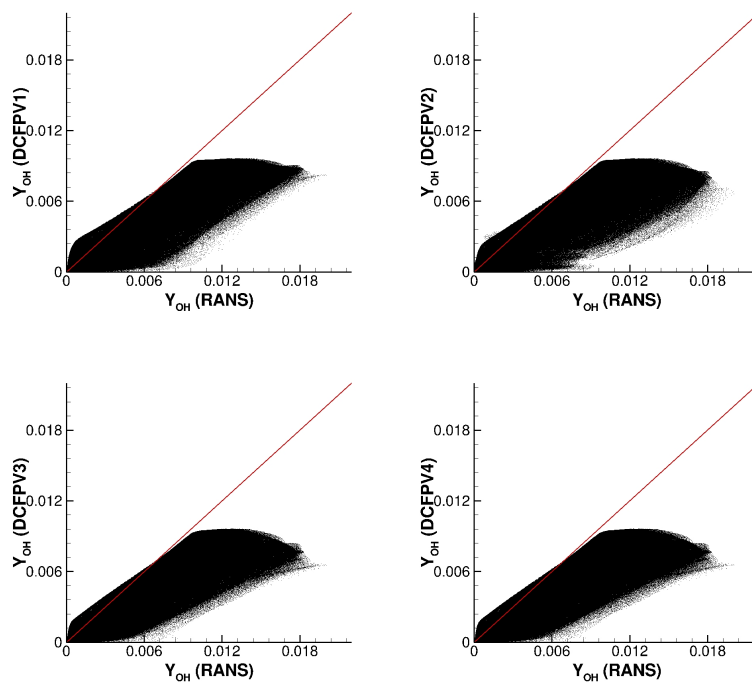


FIGURE 5.18: Scatter plots of  $Y_{OH}$  obtained using the APFM-RANS analysis method versus that from the baseline RANS simulations of the HDCR combustor for the full computational domain for cases DCFPV1-DCFPV4. The red line denotes a line with slope of one.

Based on the comparisons made using Figs. 5.4-5.18, several important observations regarding the choice of  $C$  and the benefits of using a CFPV model in place of an IFPV model were made for dual-mode operation of the HDCR combustor. These observations included:

1. When using an IFPV model, the form for  $C$  shown in Eq. (5.7) resulted in the minimal error in the reconstructed  $T$  field.
2. Including  $p$  as a parameterizing variable via the use of a CFPV model significantly reduced the sensitivity of the reconstructed  $T$  field to the detailed form chosen for  $C$ .
3. The detailed form of  $C$  affected each chemical species uniquely.
4. While using a CFPV model in place of the IFPV model resulted in marginal improvements in  $Y_{CO_2}$ ,  $Y_{CO}$ ,  $Y_{H_2O}$ , and  $Y_{OH}$ , the aggregate effect was an improved prediction for  $T$ .

A similar analysis is performed for the HDCR combustor in scram-mode operation in the following section.

### 5.2.1.2 Scram-Mode Operation

Similar to the approach taken for the dual-mode results shown in the previous section, line plots of  $T$ ,  $Y_{CO_2}$ ,  $Y_{CO}$ ,  $Y_{H_2O}$ , and  $Y_{OH}$  at selected streamwise locations along the injector centerline nearest to the combustor centerline are included for cases SIFPV1-SIFPV4 and cases SCFPV1-SCFPV4 in Figs. 5.19-5.23. The streamwise locations were selected to approximately span the flame regions as indicated by the chemical heat release and flame index in Figs. 3.8 and 4.2, respectively. For each of these figures, the S800A RANS solution (truth model) is shown for comparison. For both the IFPV and CFPV models, the FPV-modeled solutions generally show less agreement with the baseline RANS solution as compared to the dual-mode results. The line plots of  $T$ ,  $Y_{CO}$ , and  $Y_{H_2O}$  demonstrate relatively good agreement for nearly all cases, not including the results for  $Y_{CO}$  at stations 29.5 cm, 31.0 cm, 42.0 cm, and 43.5 cm for cases SIFPV2 and SCFPV2; the spikes in concentration at these planes are a sign of FPV model

parameterization non-uniqueness for  $Y_{CO}$ , as was seen also in Fig. 5.6 for dual-mode operation. The  $Y_{CO_2}$  and  $Y_{OH}$  fields exhibit weaker agreement with the baseline RANS solution for both the IFPV and CFPV models for all four  $C$  definitions. While the trending of these parameters is similar to that of the RANS solution, it is clear that the FPV models under-predict the production of  $Y_{OH}$  for both dual- and scram-mode operation of the HDCR.

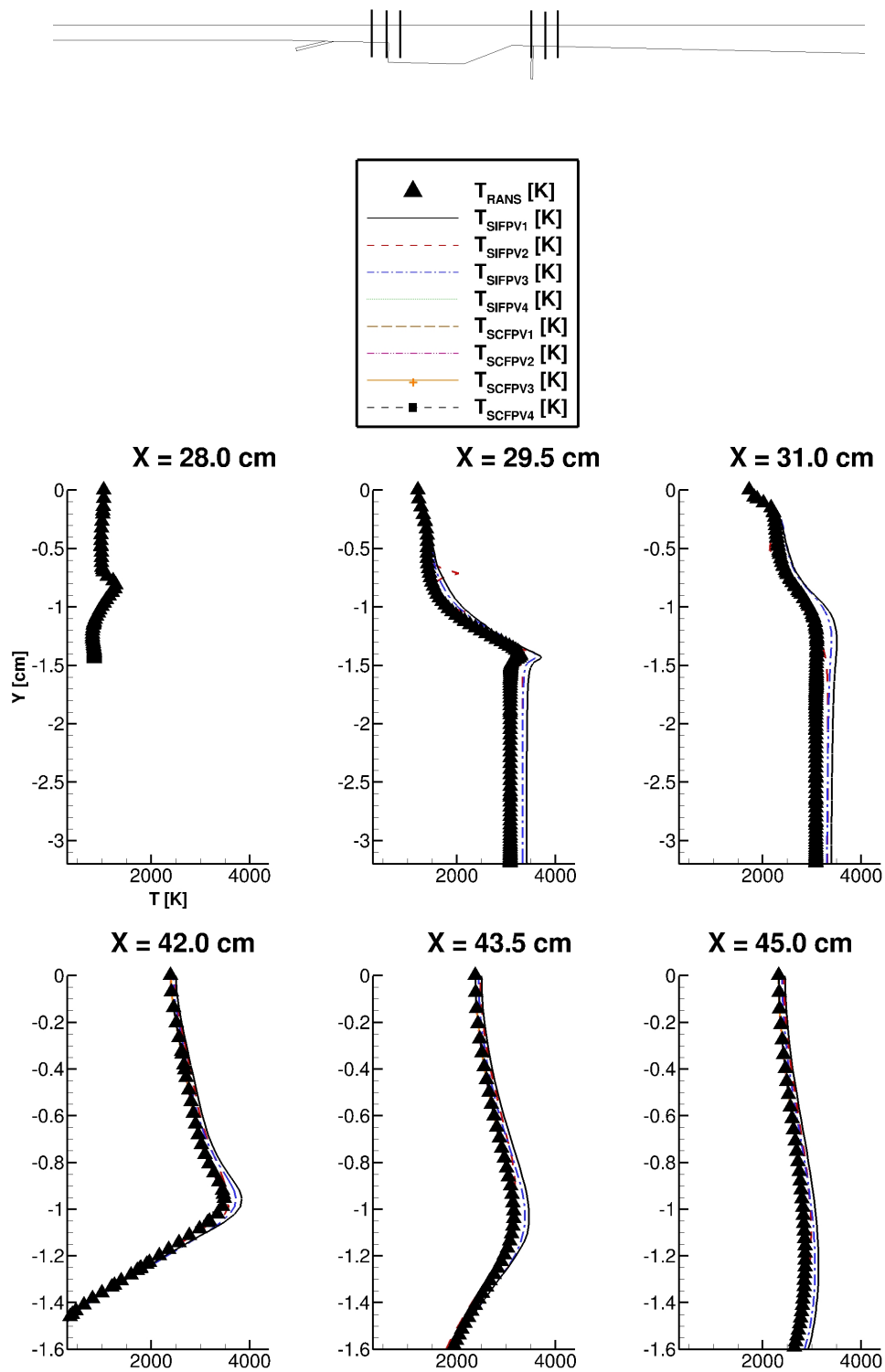


FIGURE 5.19: Line plots of  $Y$  [cm] versus  $T$  [K] obtained using the APFM-RANS analysis method and from the baseline RANS simulations of the HDCR combustor at several locations through the primary and secondary injector flames at the injector centerline nearest to the combustor centerline for cases corresponding to SIFPV1-SIFPV4 and SCFPV1-SCFPV4. Units on each subfigure are the same as those shown on the top-row, left-most subfigure.

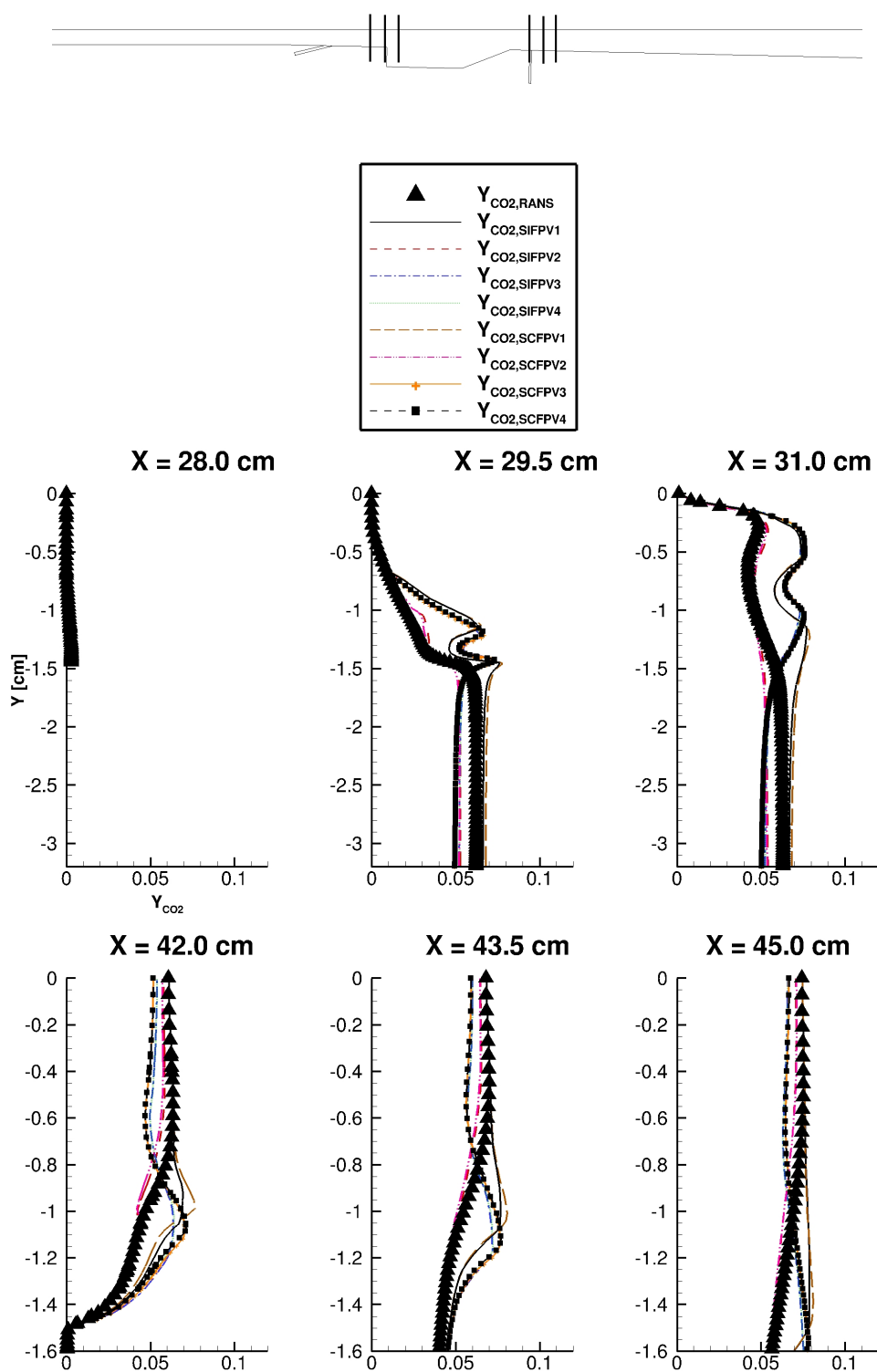


FIGURE 5.20: Line plots of  $Y$  [cm] versus  $Y_{CO_2}$  obtained using the APFM-RANS analysis method and from the baseline RANS simulations of the HDCR combustor at several locations through the primary and secondary injector flames at the injector centerline nearest to the combustor centerline for cases corresponding to SIFPV1-SIFPV4 and SCFPV1-SCFPV4. Units on each subfigure are the same as those shown on the top-row, left-most subfigure.

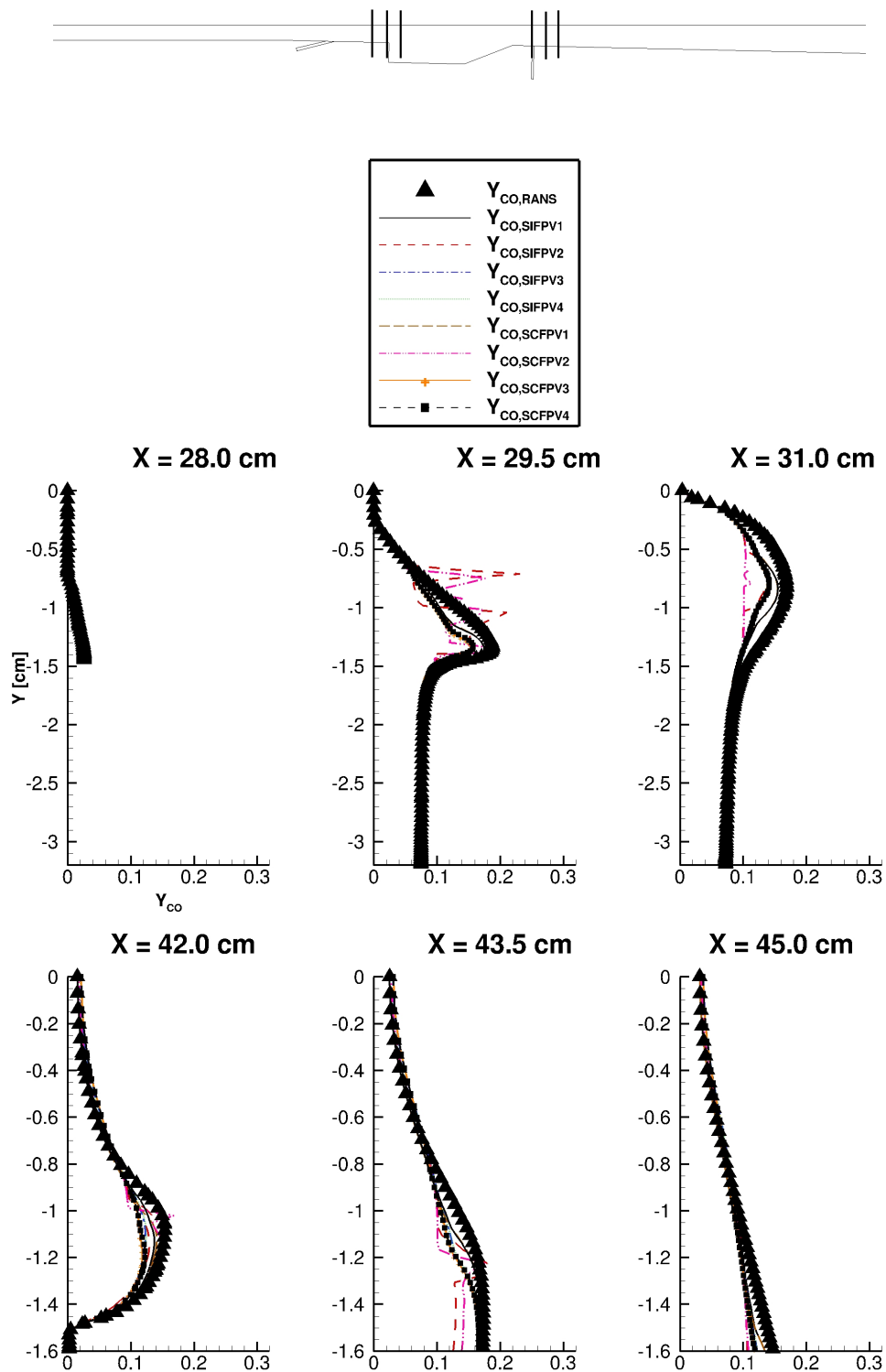


FIGURE 5.21: Line plots of  $Y$  [cm] versus  $Y_{CO}$  obtained using the APFM-RANS analysis method and from the baseline RANS simulations of the HDCR combustor at several locations through the primary and secondary injector flames at the injector centerline nearest to the combustor centerline for cases corresponding to SIFPV1-SIFPV4 and SCFPV1-SCFPV4. Units on each subfigure are the same as those shown on the top-row, left-most subfigure.

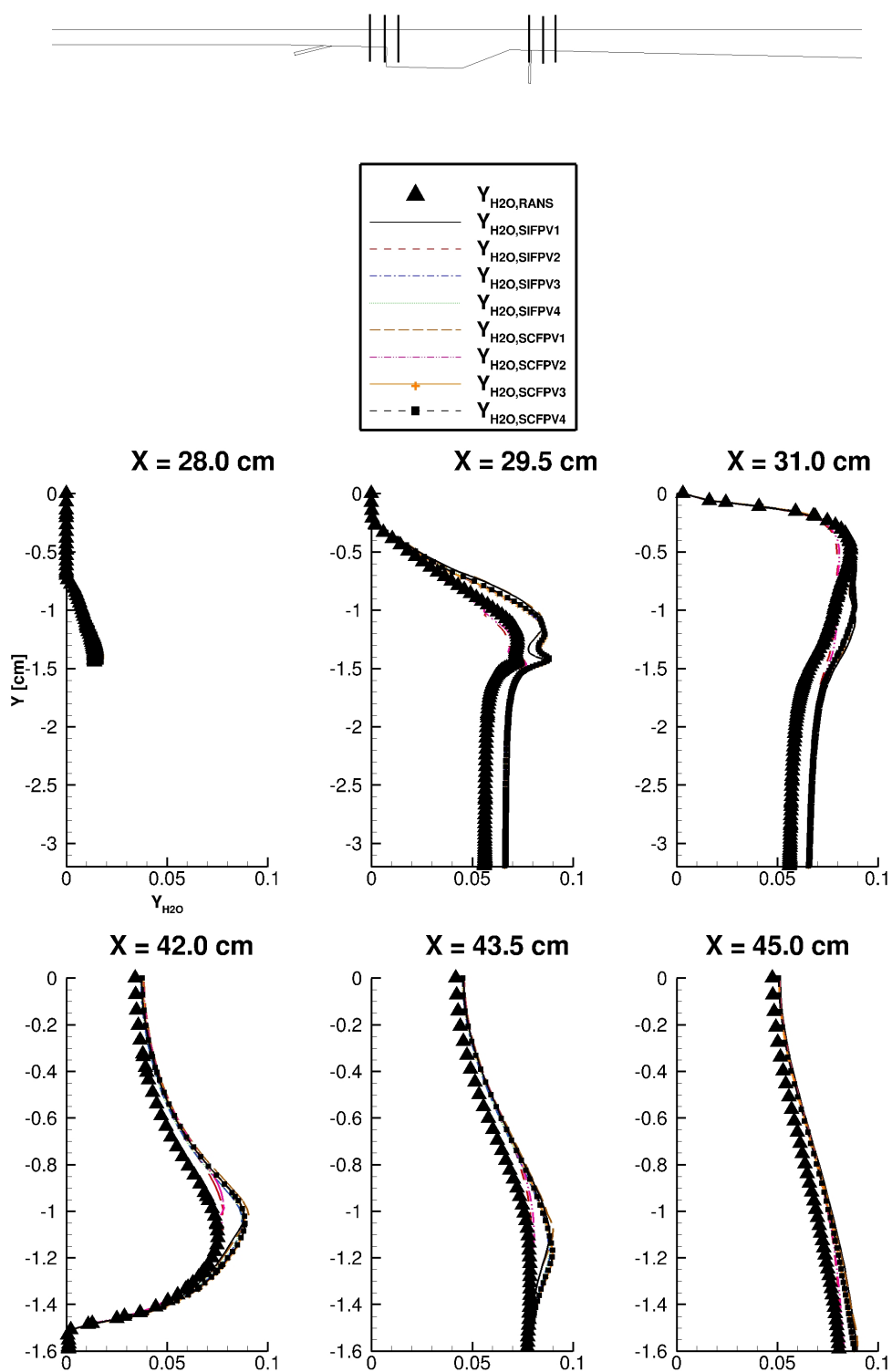


FIGURE 5.22: Line plots of  $Y$  [cm] versus  $Y_{H_2O}$  obtained using the APFM-RANS analysis method and from the baseline RANS simulations of the HDCR combustor at several locations through the primary and secondary injector flames at the injector centerline nearest to the combustor centerline for cases corresponding to SIFPV1-SIFPV4 and SCFPV1-SCFPV4. Units on each subfigure are the same as those shown on the top-row, left-most subfigure.

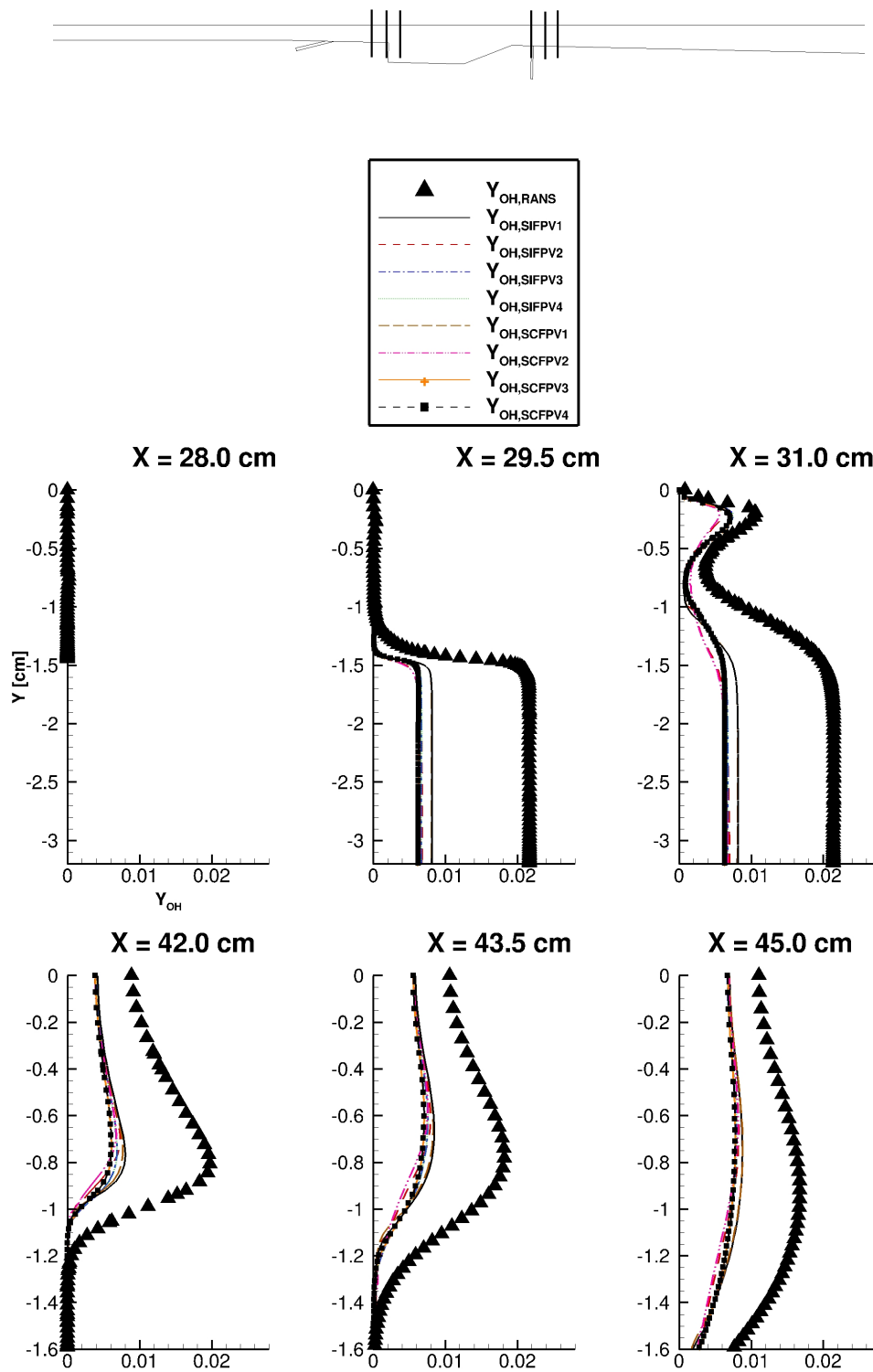


FIGURE 5.23: Line plots of  $Y$  [cm] versus  $Y_{OH}$  obtained using the APFM-RANS analysis method and from the baseline RANS simulations of the HDCR combustor at several locations through the primary and secondary injector flames at the injector centerline nearest to the combustor centerline for cases corresponding to SIFPV1-SIFPV4 and SCFPV1-SCFPV4. Units on each subfigure are the same as those shown on the top-row, left-most subfigure.

A more detailed comparison is made by scatter plotting FPV-modeled results against those of the baseline RANS case. These plots are shown for cases SIFPV1-SIFPV4 and cases SCFPV1-SCFPV4 in Figs. 5.24-5.28 and Figs. 5.29-5.33, respectively. In each of these figures, a solid red line of slope one is overlaid on the data as a marker for one-to-one agreement. Deviation from this solid red line indicates the extent of disagreement among the modeled data. Analyzing Figs. 5.24 and 5.29 suggests that for IFPV models, the detailed form of  $C$  is critical to recovering the  $T$  field, whereas for CFPV models, the  $T$  field is much less sensitive. Figure 5.24 shows that the scatter plot corresponding to SIFPV4 obtained using Eq. (5.7) results in a significantly more-accurate comparison than the other candidate definitions for  $C$ , whereas in Fig. 5.29, all four candidates for  $C$  result in similar scatter. These observations regarding  $T$  are identical to those made earlier for the dual-mode results.

Analyzing results for the selected species mass fractions in Figs. 5.25-5.28 and Figs. 5.30-5.33 suggests the chemical composition exhibits considerably less sensitivity to the inclusion of  $p$  as a parameterizing variable in the FPV model. Though, for both the IFPV and CFPV models, the chemical composition exhibits a similarly-high sensitivity to the detailed form of  $C$ . In Figs. 5.26 and 5.31, the non-uniqueness of the FPV manifold for  $Y_{CO}$  is clearly apparent in the scatter data. Much like the dual-mode cases of the previous section, the level of agreement for the four  $C$  candidates varies considerably from one species to the next. For example, in the case of  $Y_{CO_2}$  in Figs. 5.25 and 5.30, the results given by Eq. (5.5) in the top-row, right-most subfigure exhibit the best agreement with the baseline RANS solution; however, for  $Y_{CO}$  in Figs. 5.27 and 5.32 in the top-row, left-most subfigure, results given by Eq. (5.4) show the best agreement.

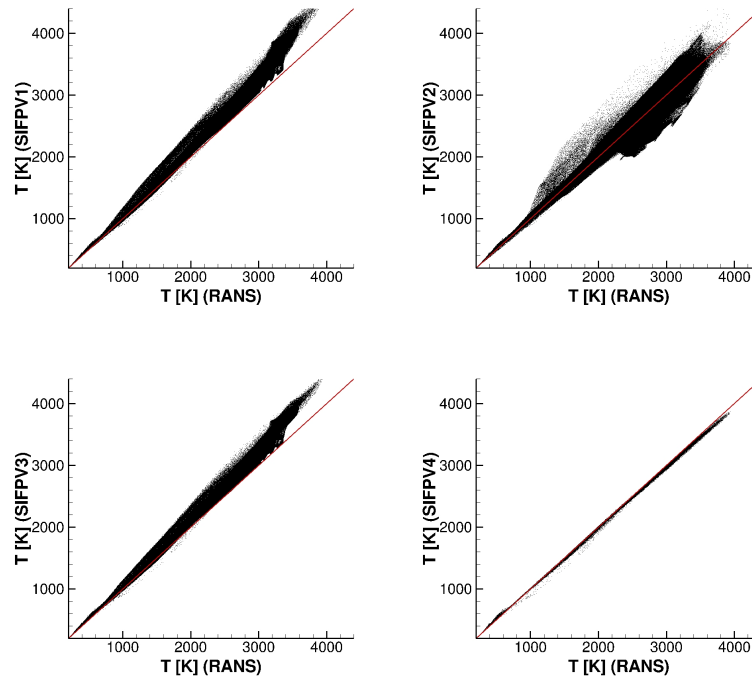


FIGURE 5.24: Scatter plots of the temperature,  $T$  [K], obtained using the APFM-RANS analysis method versus that from the baseline RANS simulations of the HDCR combustor for the full computational domain for cases SIFPV1-SIFPV4. The red line denotes a line with slope of one.

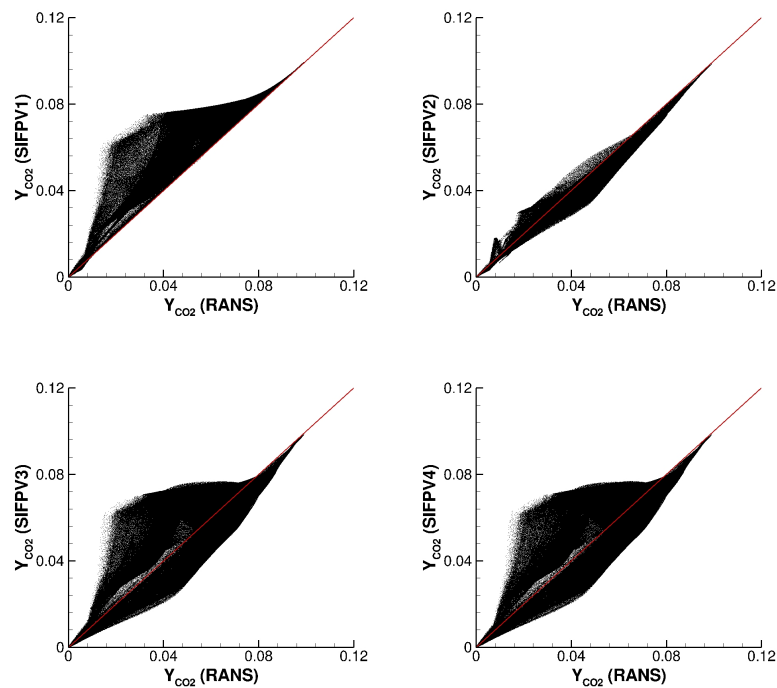


FIGURE 5.25: Scatter plots of  $Y_{CO_2}$  obtained using the APFM-RANS analysis method versus that from the baseline RANS simulations of the HDCR combustor for the full computational domain for cases SIFPV1-SIFPV4. The red line denotes a line with slope of one.

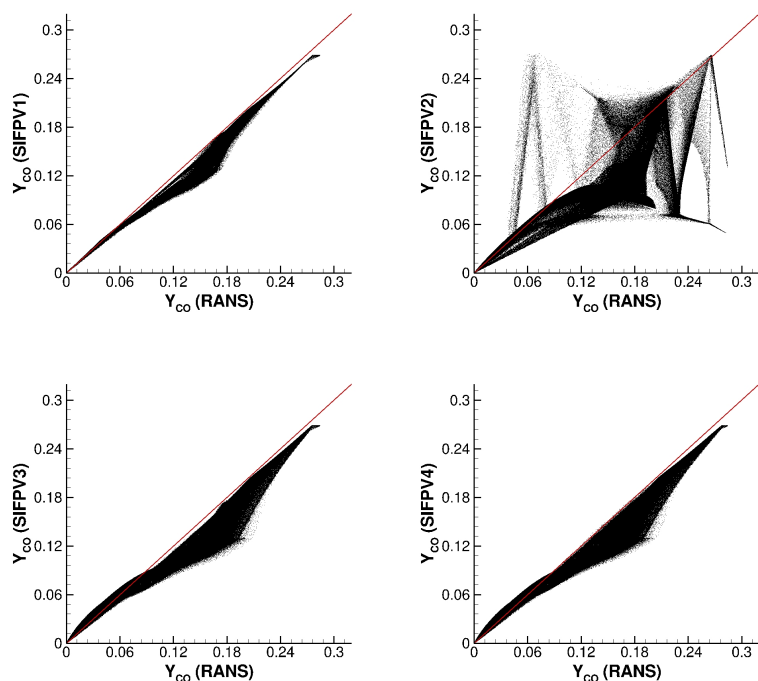


FIGURE 5.26: Scatter plots of  $Y_{CO}$  obtained using the APFM-RANS analysis method versus that from the baseline RANS simulations of the HDCR combustor for the full computational domain for cases SIFPV1-SIFPV4. The red line denotes a line with slope of one.

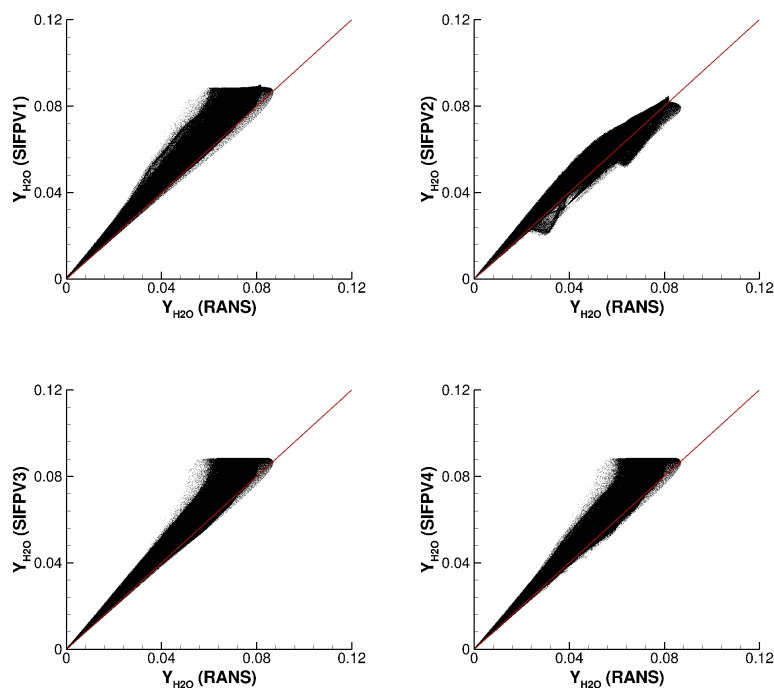


FIGURE 5.27: Scatter plots of  $Y_{H_2O}$  obtained using the APFM-RANS analysis method versus that from the baseline RANS simulations of the HDCR combustor for the full computational domain for cases SIFPV1-SIFPV4. The red line denotes a line with slope of one.

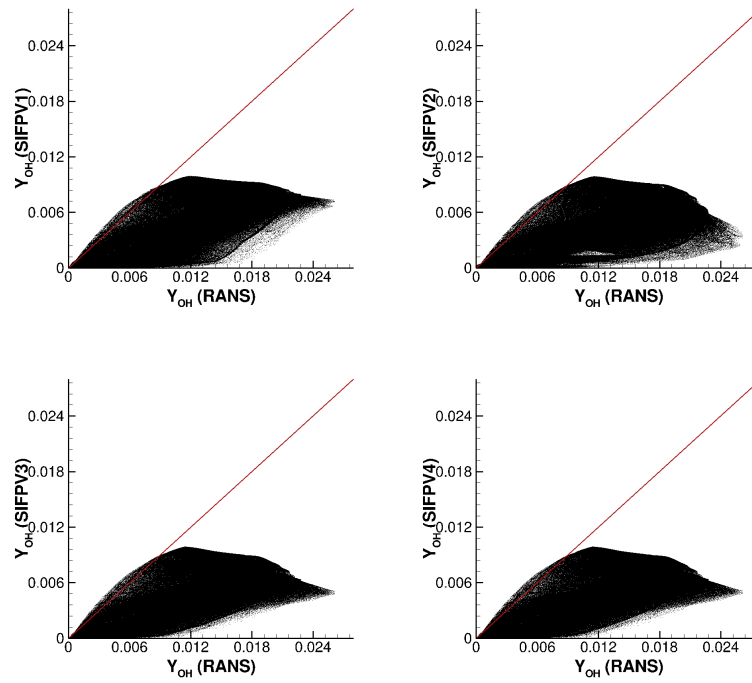


FIGURE 5.28: Scatter plots of the temperature,  $Y_{OH}$ , obtained using the APFM-RANS analysis method versus that from the baseline RANS simulations of the HDCR combustor for the full computational domain for cases SIFPV1-SIFPV4. The red line denotes a line with slope of one.

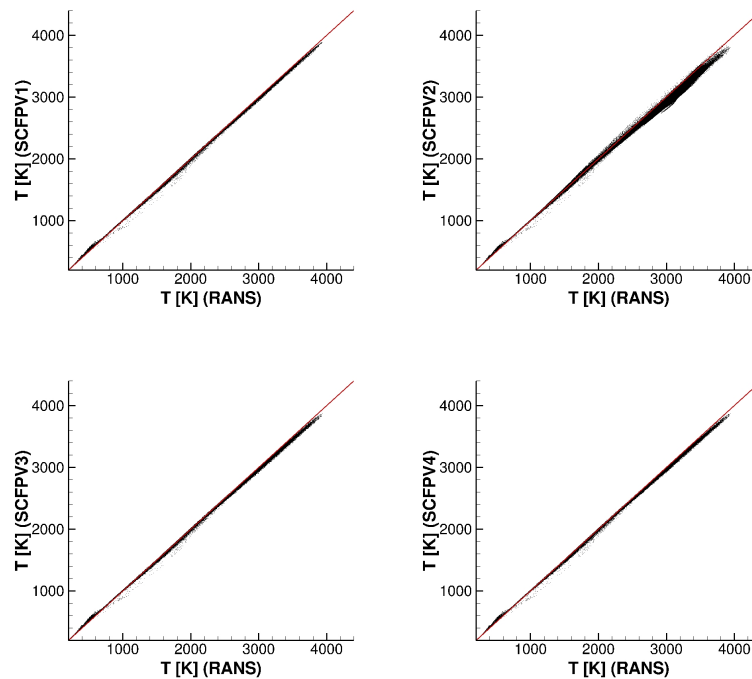


FIGURE 5.29: Scatter plots of  $T$  [K] obtained using the APFM-RANS analysis method versus that from the baseline RANS simulations of the HDCR combustor for the full computational domain for cases SCFPV1-SCFPV4. The red line denotes a line with slope of one.

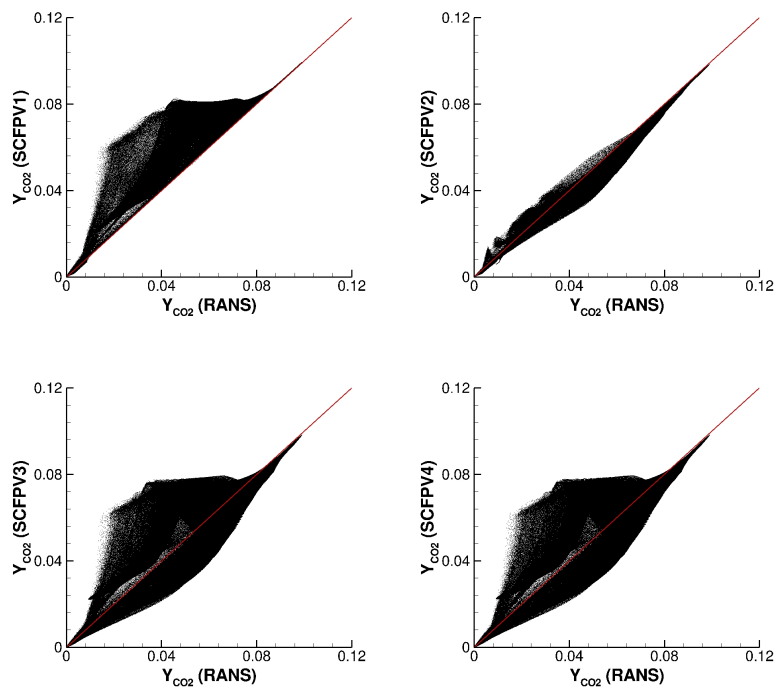


FIGURE 5.30: Scatter plots of  $Y_{CO_2}$  obtained using the APFM-RANS analysis method versus that from the baseline RANS simulations of the HDCR combustor for the full computational domain for cases SCFPV1-SCFPV4. The red line denotes a line with slope of one.

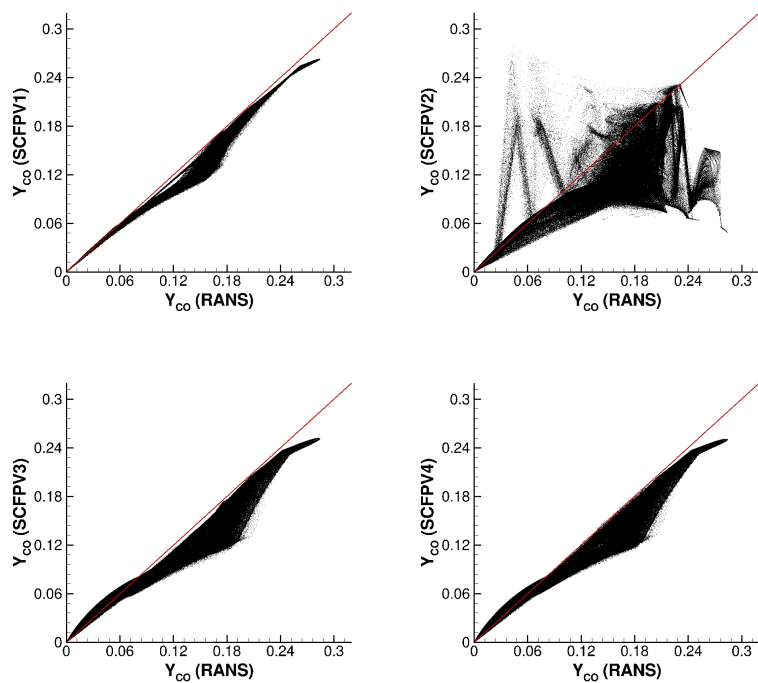


FIGURE 5.31: Scatter plots of  $Y_{CO}$  obtained using the APFM-RANS analysis method versus that from the baseline RANS simulations of the HDCR combustor for the full computational domain for cases SCFPV1-SCFPV4. The red line denotes a line with slope of one.

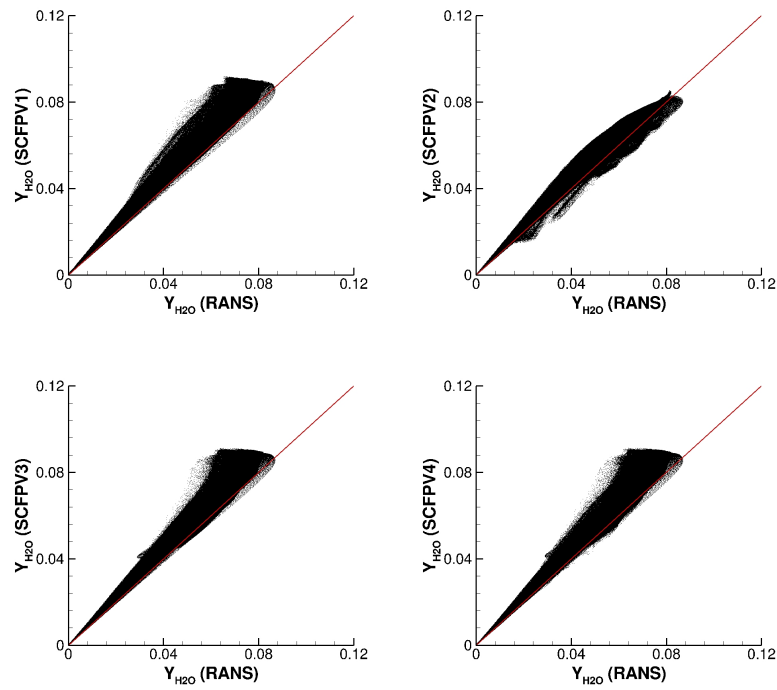


FIGURE 5.32: Scatter plots of  $Y_{H_2O}$  obtained using the APFM-RANS analysis method versus that from the baseline RANS simulations of the HDCR combustor for the full computational domain for cases SCFPV1-SCFPV4. The red line denotes a line with slope of one.

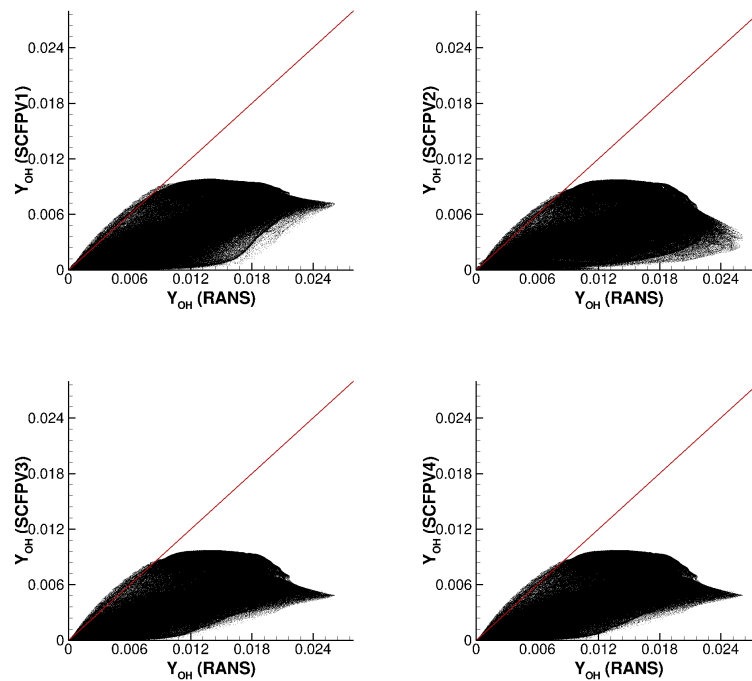


FIGURE 5.33: Scatter plots of  $Y_{OH}$  obtained using the APFM-RANS analysis method versus that from the baseline RANS simulations of the HDCR combustor for the full computational domain for cases SCFPV1-SCFPV4. The red line denotes a line with slope of one.

Based on the comparisons made using Figs. 5.19-5.33, the same important observations regarding the choice of  $C$  and the benefits of using a CFPV model in place of an IFPV model that were made for dual-mode operation of the HDCR hold true for scram-mode operation. These observations were described in section 5.2.1.1, so are not repeated here.

## 5.2.2 Progress Variable Production Models

Since the reaction rates used to model the combustion chemistry are strong nonlinear functions of pressure and temperature, the former are expected to be especially sensitive to any modeling errors in the latter. Unfortunately, the detailed variation in these properties is not known *a priori*; only after a simulation has been performed may the variation of  $p$  and  $T$  be obtained and sufficiently modeled for an accompanying flamelet table. Herein lies a fundamental problem with FPV models; the temperature values for fuel and oxidizer and background pressure needed to set the boundary conditions for the flamelet equations are not available and cannot be easily computed *a priori*. Further,  $\dot{\omega}_C$  is generally used directly from the flamelet table—meaning that the  $p$  and  $T$  used in the calculation of  $\dot{\omega}_C$  are those corresponding to the solution of the flamelet equations and not those of the local compressible flowfield. For high-speed, compressible, reacting flows, the difference between the temperature and pressure embedded in the flamelet table and that of the local flowfield are typically significantly different, and when this difference is considered without variation in  $p$  and the strong nonlinearity of  $\dot{\omega}_C$ , it is clear that for FPV models the tabulated  $\dot{\omega}_C$  contains considerable error. In this section, several possible methods for reducing this error in  $\dot{\omega}_C$  are evaluated.

To gauge the accuracy of the pressure-scaling approach,  $\dot{\omega}_C$  for cases DIFPV4 and SIFPV4 was recomputed using Eq. (2.40) and were compared to that of cases DCFPV4 and SCFPV4, respectively. These comparisons are shown in Figs. 5.34 and 5.35, respectively, which demonstrate the pressure-scaled  $\dot{\omega}_C$  agrees reasonably well with the results of cases DCFPV4 and SCFPV4, for which the flamelet solutions are explicitly solved at several pressure levels. The greater disagreement at higher values of  $\dot{\omega}_C$  seen in Fig. 5.34 may be a result of trimolecular reactions reflected in cases DCFPV4 but omitted from the pressure-scaling model with case DIFPV4. If this were true, using a higher exponent in Eq. (2.40) may help to reduce this discrepancy. Results for cases SIFPV4 and

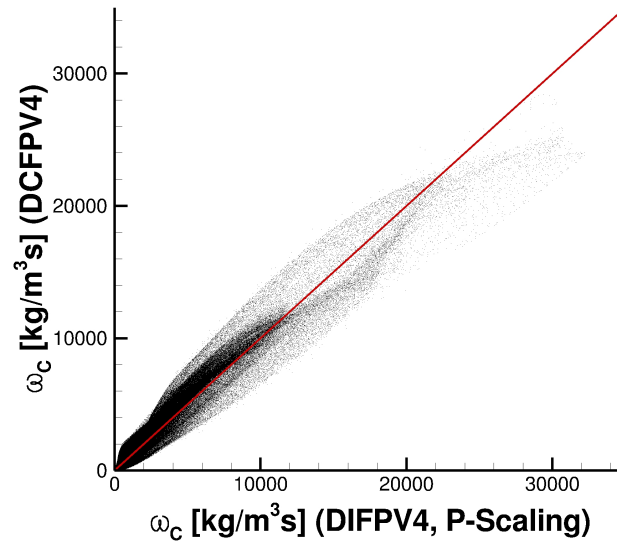


FIGURE 5.34: Scatter plot of  $\omega_C$  [kg/m<sup>3</sup>s] calculated using the APFM-RANS analysis method for case DIFPV4 with the pressure-scaling model in Eq. (2.40) as compared to that of case DCFPV4, for which  $\omega_C$  is parameterized explicitly by pressure. The red line denotes a line with slope of one.

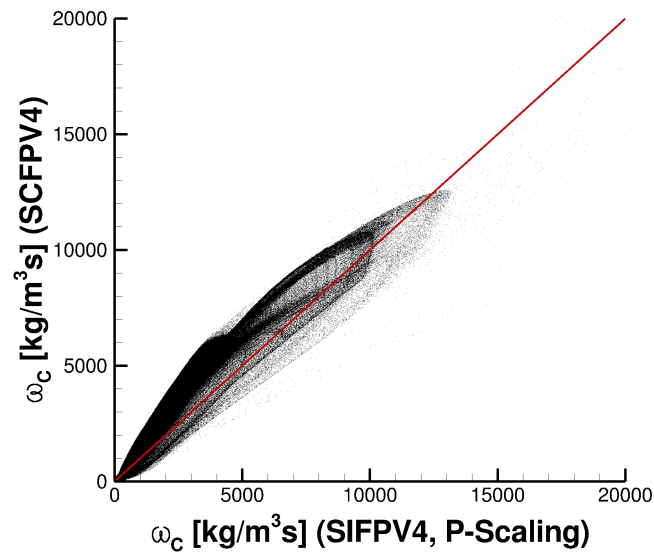


FIGURE 5.35: Scatter plot of  $\omega_C$  [kg/m<sup>3</sup>s] calculated using the APFM-RANS analysis method for case SIFPV4 with the pressure-scaling model in Eq. (2.40) as compared to that of case SCFPV4, for which  $\omega_C$  is parameterized explicitly by pressure. The red line denotes a line with slope of one.

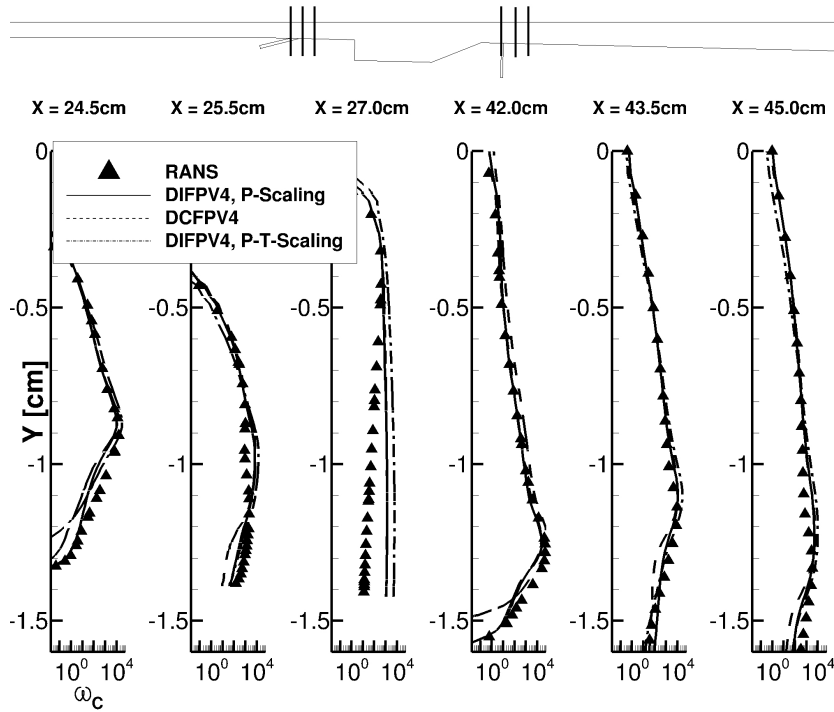


FIGURE 5.36: Line plot  $Y$  [cm] versus  $\dot{\omega}_C$  [ $\text{kg}/\text{m}^3\text{s}$ ] calculated using the APFM-RANS analysis method for case DIFPV4 with the use of Eq. (2.40), case DCFPV4, and case DIFPV4 with the use of Eq. (5.8) to baseline RANS data at selected locations for the primary and secondary injectors spanning the flame regions. Locations of the sampled data planes are shown on the combustor geometry cross-section.

SCFPV4 demonstrate more disagreement, where case SCFPV4 overpredicts  $\dot{\omega}_C$  slightly more. These results were also compared to the baseline RANS solution in flame regions around each injector in Fig. 5.36 for the dual-mode case, and comparisons of these results to those of the baseline RANS solution are shown for the entire combustor in Fig. 5.37. Note that a third scaling approach based on pressure and temperature is included in Fig. 5.36, which will be discussed later.

In Fig. 5.36, the results indicate that in flame regions both approaches agree similarly well with the baseline RANS data, thereby suggesting both approaches offer similarly accurate  $\dot{\omega}_C$  values. However, note that while the  $\dot{\omega}_C$  may agree reasonably well for both pressure-scaling approaches, pressure effects are not captured for any other table data using this approach. Specifically, the agreement with the RANS data for the  $Y_\alpha$ ,  $T$ , and  $\frac{\partial Y_\alpha}{\partial Z}$  are identical to that of the IFPV model results. Only by using pressure as a parameterizing variable in the flamelet table may the effects of pressure be reflected in these additional terms.

The Arrhenius-based temperature scaling approach shown previously in Eq. (2.45) was

also assessed. To do so, the original scaling was recast using the equation of state into independent pressure and temperature scalings, as shown below in Eq. (5.8)

$$\dot{\omega}_C = \underbrace{\left(\frac{p}{p_0}\right)^{a_p}}_{p\text{-scaling}} \underbrace{\left(\frac{T_0}{T}\right)^{a_p} \exp\left[-T_a\left(\frac{1}{T} - \frac{1}{T_0}\right)\right]}_{T\text{-scaling}} \dot{\omega}_{C_0} \quad (5.8)$$

where the pressure and temperature scalings are annotated and the pressure scaling is identical to that shown in Eq. (2.40). The modeled activation temperature,  $T_a$ , was set to 10,000 K to best fit the flamelet table data.

To demonstrate the performance of the  $\dot{\omega}_C$  corrections introduced in Chapter 2 for dual-mode HDCR operation, four FPV solutions are compared to the baseline RANS solution in Fig. 5.37. These solutions included: the results of case DIFPV4, the pressure-scaled results of case DIFPV4 using Eq. (2.40), the pressure-temperature-scaled results of case DIFPV4 using Eq. (5.8), and the temperature-scaled results of case DCFPV4 using Eq. (5.8). An identical comparison is made for the scram-mode cases in Fig. 5.38. These comparisons demonstrate the strong influence of both pressure and temperature corrections on the value of  $\dot{\omega}_C$ , and for the current study, both pressure- and temperature-scalings will be used to recover the  $\dot{\omega}_C$ . Similarly to Figs. 5.34 and 5.35, the difference between using scaling models with cases DIFPV4 and SIFPV4 versus using the temperature-scaling in Eq. (5.8) with cases DCFPV4 and SCFPV4, respectively, is small for  $\dot{\omega}_C$ ; however, note that the scaling models discussed here only apply to  $\dot{\omega}_C$  and that any pressure effects for the other flamelet table terms are neglected by using a scaling model.

### 5.2.3 FPV Model Coupling

In every FPV model implementation, the flamelet table and associated thermochemical state-space must be coupled to the governing transport equations. This coupling is generally performed using Eqs. (2.20), (2.28), and (2.35) and by retrieving  $Y_\alpha$  and  $\dot{\omega}_C$  from the flamelet table. In this work, however, alternative approaches for calculating the energy interdiffusion term in Eq. (5.1) are considered. Similar terms that require coupling exist in other forms of the energy equation, as well. Several approaches for calculating this term are considered in this section.

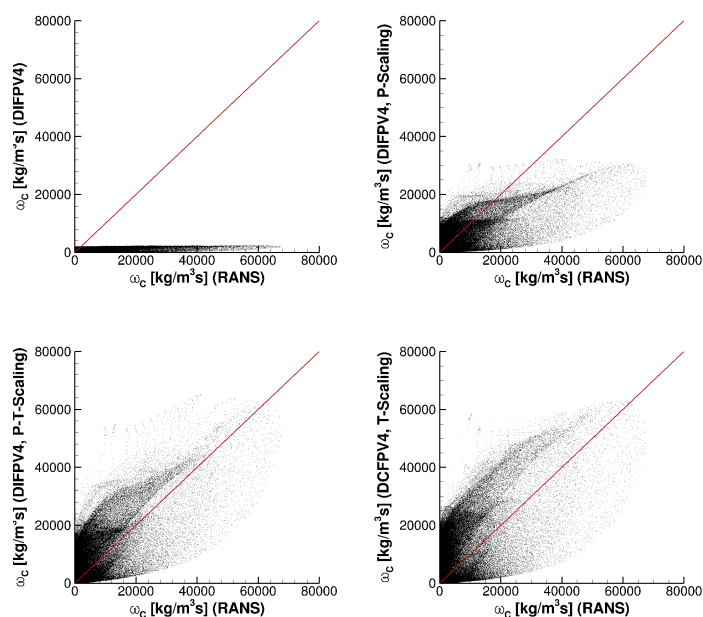


FIGURE 5.37: Scatter plot comparisons of APFM-RANS analysis results and the baseline RANS data for  $\omega_C$  [ $\text{kg}/\text{m}^3\text{s}$ ] for the entire computational domain for cases: (top-left) DIFPV4, (top-right) DIFPV4 with the pressure-scaling model shown in Eq. (2.40), (bottom-left) DIFPV4 with the pressure- and temperature-scaling models shown in of Eq. (5.8), and (bottom-right) DCFPV4 with the temperature-scaling model shown in Eq. (5.8).

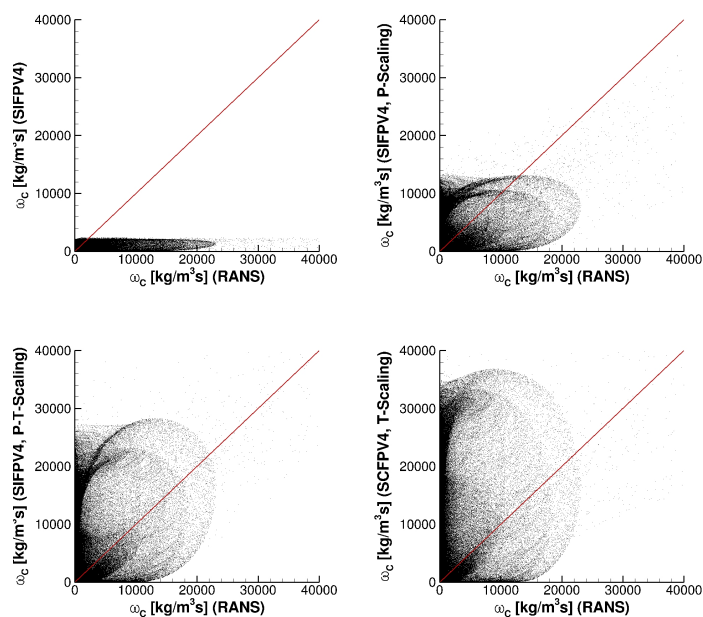


FIGURE 5.38: Scatter plot comparisons of APFM-RANS analysis results and the baseline RANS data for  $\omega_C$  [ $\text{kg}/\text{m}^3\text{s}$ ] for the entire computational domain for cases: (top-left) SIFPV4, (top-right) SIFPV4 with the pressure-scaling model shown in Eq. (2.40), (bottom-left) SIFPV4 with the pressure- and temperature-scaling models shown in of Eq. (5.8), and (bottom-right) SCFPV4 with the temperature-scaling model shown in Eq. (5.8).

Direct calculation of the energy interdiffusion term is straight forward when transport equations for  $Y_\alpha$  are solved. However, for FPV model implementations, data from the flamelet table are required to compute this term, since only transport equations for  $Z$  and  $C$  are solved. Equation (5.9) shows the energy interdiffusion term that appears on the right hand side of the total energy transport equation and several possible FPV-modeled formulations. Though the  $Y_\alpha$  could be taken directly from the flamelet table at runtime to calculate this term, this approach would require numerically differentiating  $Y_\alpha$  with respect to each space dimension within the solver, which would require significant computational resources. Alternatively, this term can be recast using the chain rule on the flamelet manifold parameterizing variables. Performing this decomposition would yield derivatives of  $Y_\alpha$  with respect to each of the manifold dimensions and would require the tabulation of each in the flamelet library. In order to maintain a reasonably-compact flamelet library, only contributions in  $Z$  space are considered for the current model, for which only  $\frac{\partial Y_\alpha}{\partial Z}$  requires storage. A third option for calculating this term is to simply tabulate the entire summation appearing on the right-hand-side of Eq. (5.9) and make it available directly from the flamelet solutions. The three choices for computing the energy interdiffusion term, denoted as  $\beta$ , are shown below in Eq. (5.9), where data retrieved from the flamelet table are colored red.

$$\begin{aligned} \frac{\partial}{\partial x_j} \left[ \rho \left( \frac{\mu}{S_c} + \frac{\mu_t}{S_{c_t}} \right) \sum_{\alpha=1}^N h_\alpha \frac{\partial Y_\alpha}{\partial x_j} \right] = \beta \\ = \begin{cases} \beta_i & \left[ \rho \left( \frac{\mu}{S_c} + \frac{\mu_t}{S_{c_t}} \right) \sum_{\alpha=1}^N h_\alpha \frac{\partial Y_\alpha}{\partial x_j} \right] \\ \beta_{ii} & \left[ \rho \left( \frac{\mu}{S_c} + \frac{\mu_t}{S_{c_t}} \right) \frac{\partial Z}{\partial x_j} \sum_{\alpha=1}^N h_\alpha \frac{\partial Y_\alpha}{\partial Z} \right] \\ \beta_{iii} & \left[ \rho \left( \frac{\mu}{S_c} + \frac{\mu_t}{S_{c_t}} \right) \frac{\partial Z}{\partial x_j} \sum_{\alpha=1}^N h_\alpha \frac{\partial Y_\alpha}{\partial Z} \right] \end{cases} \quad (5.9) \end{aligned}$$

Since option  $\beta_i$  requires  $3N$  numerical differentiations of  $Y_\alpha$  for a three-dimensional problem, this approach was ruled out on account of processing requirements. Options  $\beta_{ii}$  and  $\beta_{iii}$  differ only in their calculation of  $h_\alpha$  and their tabulation requirements. For  $\beta_{ii}$ , the transported temperature is used to calculate  $h_\alpha$ , and  $\frac{\partial Y_\alpha}{\partial Z}$  must be stored for all  $N$  species. Alternatively, for  $\beta_{iii}$ , the local flamelet temperature is used to compute  $h_\alpha$ , which then allows for the storage and retrieval of a single term from the table.

In order to determine whether the presumed increase in accuracy of  $\beta_{ii}$  outweighed the table consolidation permitted by  $\beta_{iii}$ , both of these calculations were performed using the APFM-RANS analysis method. Scatter plots of the two terms against the baseline

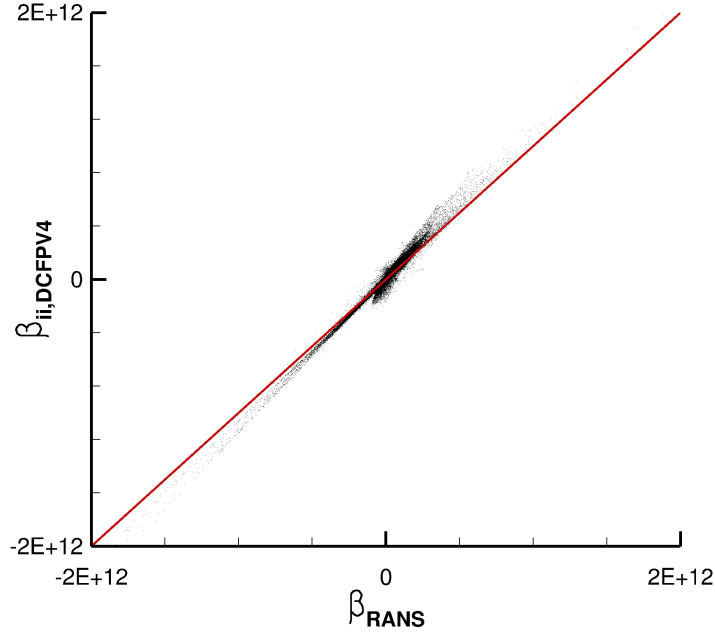


FIGURE 5.39: Scatter plot of energy interdiffusion using the  $\beta_{ii}$  formulation for case DCFPV4 compared to the baseline RANS data. The red line denotes a line with slope of one.

RANS data demonstrates the level of modeling error associated with both, as shown for cases DCFPV4 and SCFPV4 in Figs. 5.39 and 5.41, respectively, for  $\beta_{ii}$  and for cases DCFPV4 and SCFPV4 in Figs. 5.40 and 5.42, respectively, for  $\beta_{iii}$ . As seen by comparing these figures, the additional information required to calculate  $\beta_{ii}$  generally results in a more accurate prediction for the energy interdiffusion, as compared to using  $\beta_{iii}$ . In particular,  $\beta_{iii}$  diverges from the baseline RANS data substantially at large negative values for dual-mode operation, while  $\beta_{ii}$  for the same case closely tracks the baseline RANS data through the same region. For scram-mode operation,  $\beta_{iii}$  exhibits generally more variability as compared to the RANS data. The variability of  $\beta_{ii}$  around the red line with a slope of one appears to be less than that of  $\beta_{iii}$  for both dual-mode and scram-mode operation. Based on these observations, the  $\beta_{ii}$  formulation is chosen for the current analysis; however, for cases employing significantly larger reaction mechanisms for construction of the flamelet table, the error in using  $\beta_{iii}$  may be justifiable for the table consolidation offered by this term.

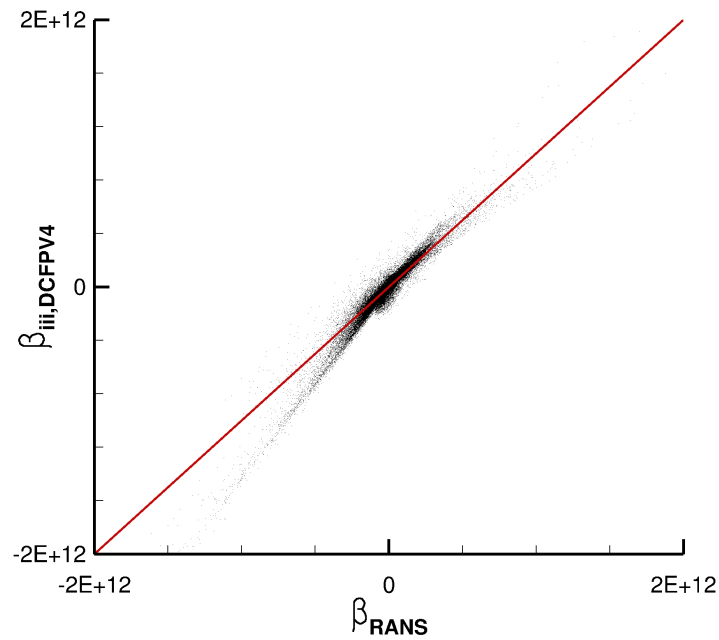


FIGURE 5.40: Scatter plot of energy interdiffusion using the  $\beta_{iii}$  formulation for case DCFPV4 compared to the baseline RANS data. The red line denotes a line with slope of one.

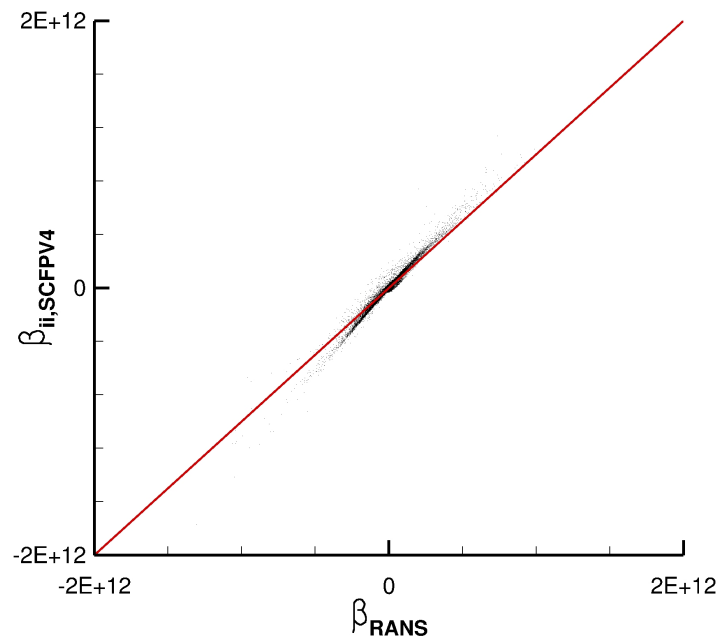


FIGURE 5.41: Scatter plot of energy interdiffusion using the  $\beta_{ii}$  formulation for case SCFPV4 compared to the baseline RANS data. The red line denotes a line with slope of one.

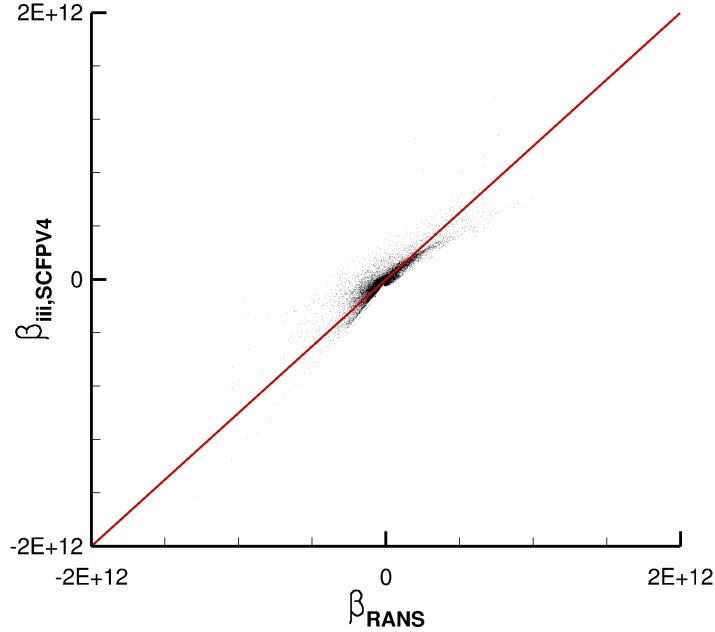


FIGURE 5.42: Scatter plot of energy interdiffusion using the  $\beta_{iii}$  formulation for case SCFPV4 compared to the baseline RANS data. The red line denotes a line with slope of one.

#### 5.2.4 CFPVX Model

The final objective of the current chapter was to demonstrate the validity of the proposed CFPVX model using the APFM-RANS analysis method. In this approach, the three-dimensional CFPV model is extended to include a fourth dimension that accounts for the effects of variability in flamelet oxidizer temperature,  $T_{ox}$ . Since a transport equation cannot be solved for  $T_{ox}$  easily, the table is mapped to the  $Z$ - $C$ - $p$ - $h$  four-dimensional state-space. This formulation is similar to previous attempts [86, 87] at including the effects of non-adiabatic heat transfer on the flamelet manifold through the inclusion of  $h$  as an additional dimension. The values of  $T_{ox}$  are obtained from the baseline RANS data and converted to a local value of the mixture enthalpy,  $h$ . APFM-RANS analyses for each of the four progress variable definitions shown in Eqs. (5.4)-(5.7) were performed in cases DCFPVX1-DCFPVX4 and SCFPVX1-SCFPVX4, for which analysis details are summarized in Table 5.1. However, based on the observations in preceding sections, only CFPVX results for cases DCFPVX4 and SCFPVX4 are presented in the current section and are compared to the respective baseline RANS data.

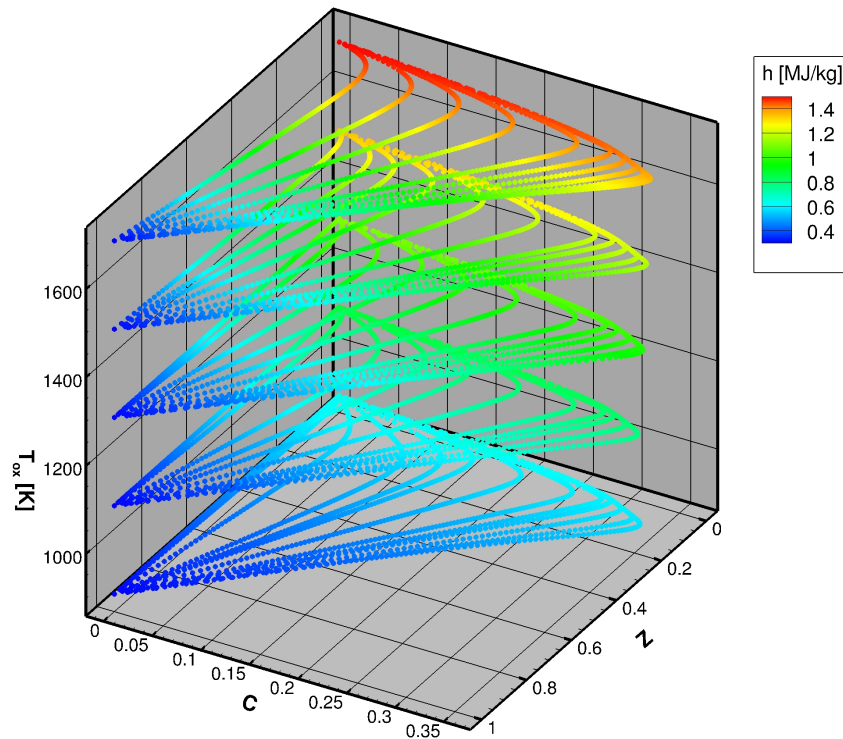


FIGURE 5.43: The flamelet manifold embedded in table FT3 presented in  $Z$ - $C$ - $T_{ox}$  space where points are colored by  $h$  to demonstrate the monotonic nature of the  $T_{ox}$ - $h$  mapping.

Figure 5.43 shows how the mixture enthalpy changes within the  $Z$ ,  $C$ ,  $T_{ox}$  flamelet manifold. The manifold data points are colored by  $h$ , which shows that the  $T_{ox}$ -to- $h$  mapping is reasonably monotonic across the entire manifold. There exists some small level of multivaluedness around stoichiometry and also in regions nearing  $Z = 1$  due to the pure fuel state.

Similar to section 5.2.1, results for the CFPVX model are presented in the form of line plots and scatter plots for several parameters of interest. Results for cases DIFPV4, DCFPV4, and DCFPVX4 are compared to the baseline D584A RANS data in section 5.2.4.1, and results for cases SIFPV4, SCFPV4, and SCFPVX4 are compared to the baseline S800A RANS data in section 5.2.4.2.

#### 5.2.4.1 Dual-Mode Operation

Line plots for  $T$ ,  $Y_{CO_2}$ ,  $Y_{H_2O}$ ,  $Y_{CO}$ , and  $Y_{OH}$  are included in Figs. 5.44-5.48. For each of these figures, comparisons are made to the baseline RANS data, as well as results of

cases DIFPV4 and DCFPV4, at a spanwise plane through the centerline of the injectors at several streamwise locations through the primary and secondary flames. While the temperature shows agreement with the baseline RANS data similar to that of cases DIFPV4 and DCFPV4, the results for  $Y_{CO_2}$ ,  $Y_{H_2O}$ ,  $Y_{CO}$ , and  $Y_{OH}$  show some improvement. Specifically, at most of the streamwise locations, the DCFPVX4 results more closely track the baseline RANS data, with the most significant improvement being for  $Y_{OH}$ . At each of the streamwise locations in Fig. 5.48, the DCFPVX4 results show considerable improvement over both the DIFPV4 and DCFPV4 cases, and these results are particularly promising due to the significant difficulty FPV models typically have predicting minor species concentrations. Inspecting the results for  $Y_{CO_2}$  and  $Y_{CO}$  suggests some minor multivaluedness of the DCFPVX4 manifold. The spikes in concentration for  $Y_{CO_2}$  at measurement locations 24 cm and 25.5 cm and for  $Y_{CO}$  at location 24 cm are a result of the slight multivaluedness of the  $Z$ - $C$ - $p$ - $h$  manifold mentioned previously. This problem is common to all FPV modeling approaches, since the manifold mappings typically used are generally not completely unique. Further work is necessary to parse the multivalued portions of the flamelet state-space and remove some of the flamelet solutions around the manifold overlap region to help alleviate this problem.

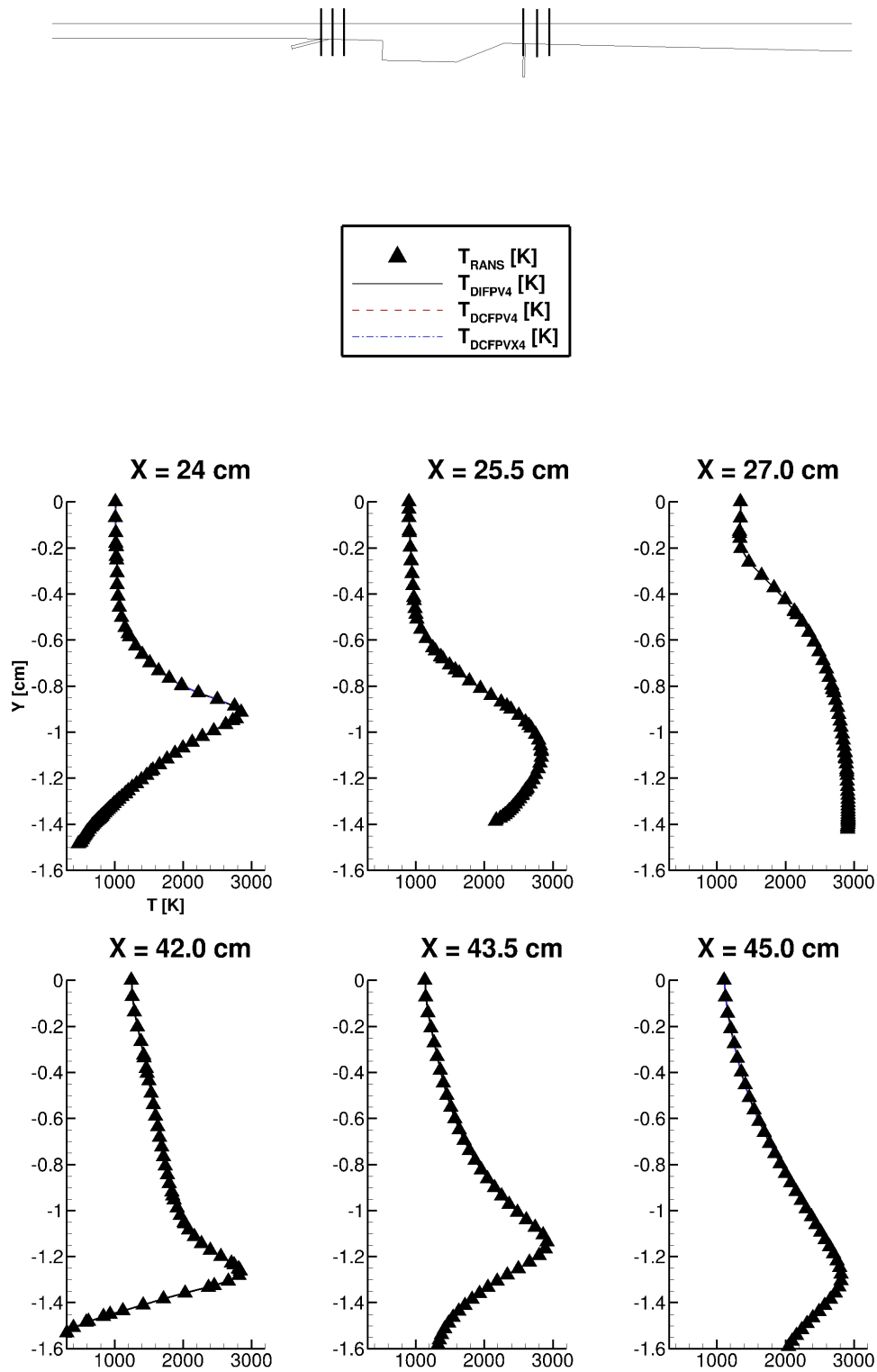


FIGURE 5.44: Line plots of  $Y$  [cm] versus  $T$  [K] obtained using the APFM-RANS analysis method and from the baseline RANS simulations of the HDCR combustor at several locations through the primary and secondary injector flames at the injector centerline nearest to the combustor centerline for cases corresponding to DIFPV4, DCFPV4, and DCFPVX4.

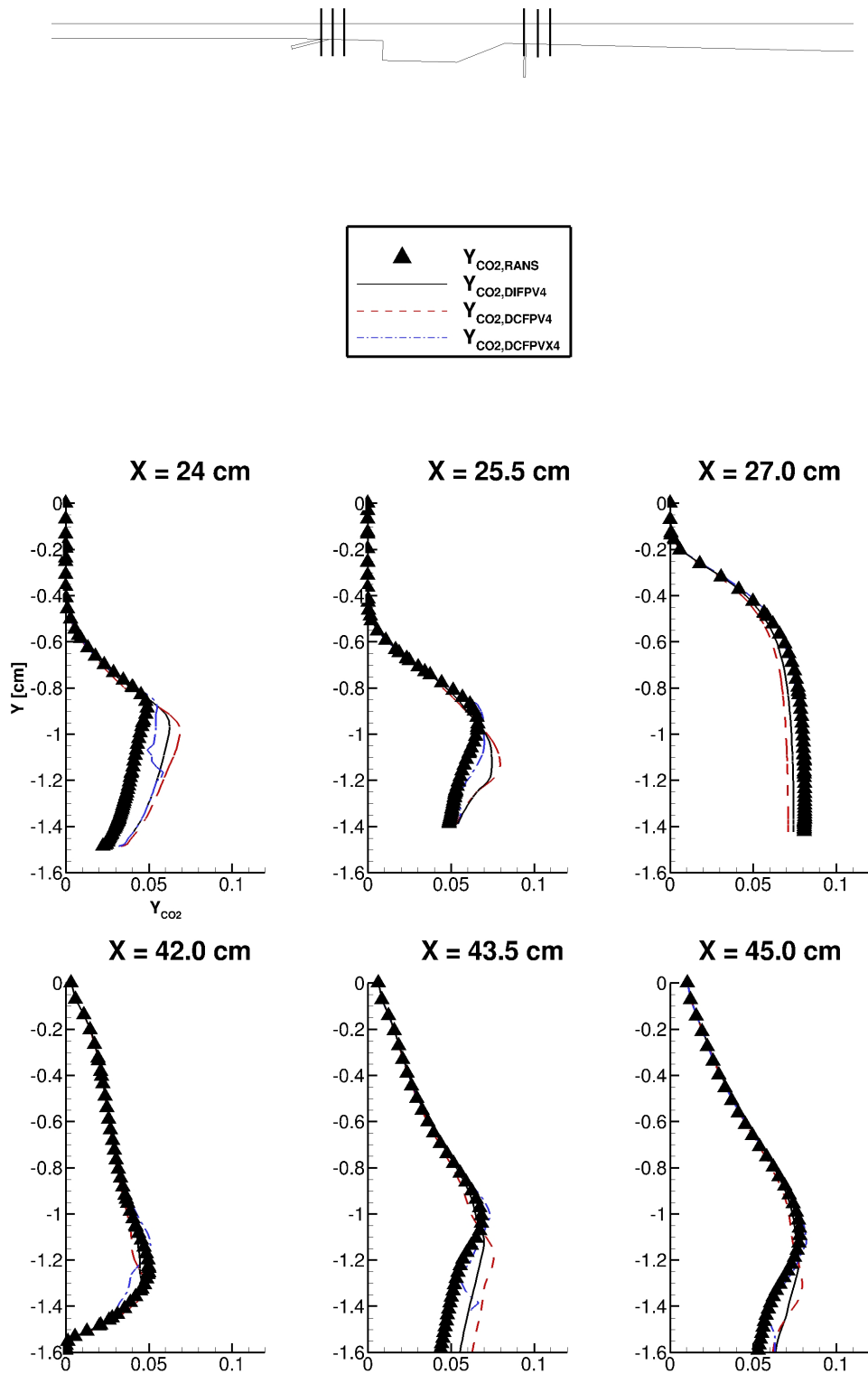


FIGURE 5.45: Line plots of  $Y$  [cm] versus  $Y_{CO_2}$  obtained using the APFM-RANS analysis method and from the baseline RANS simulations of the HDCR combustor at several locations through the primary and secondary injector flames at the injector centerline nearest to the combustor centerline for cases corresponding to DIFPV4, DCFPV4, and DCFPVX4.

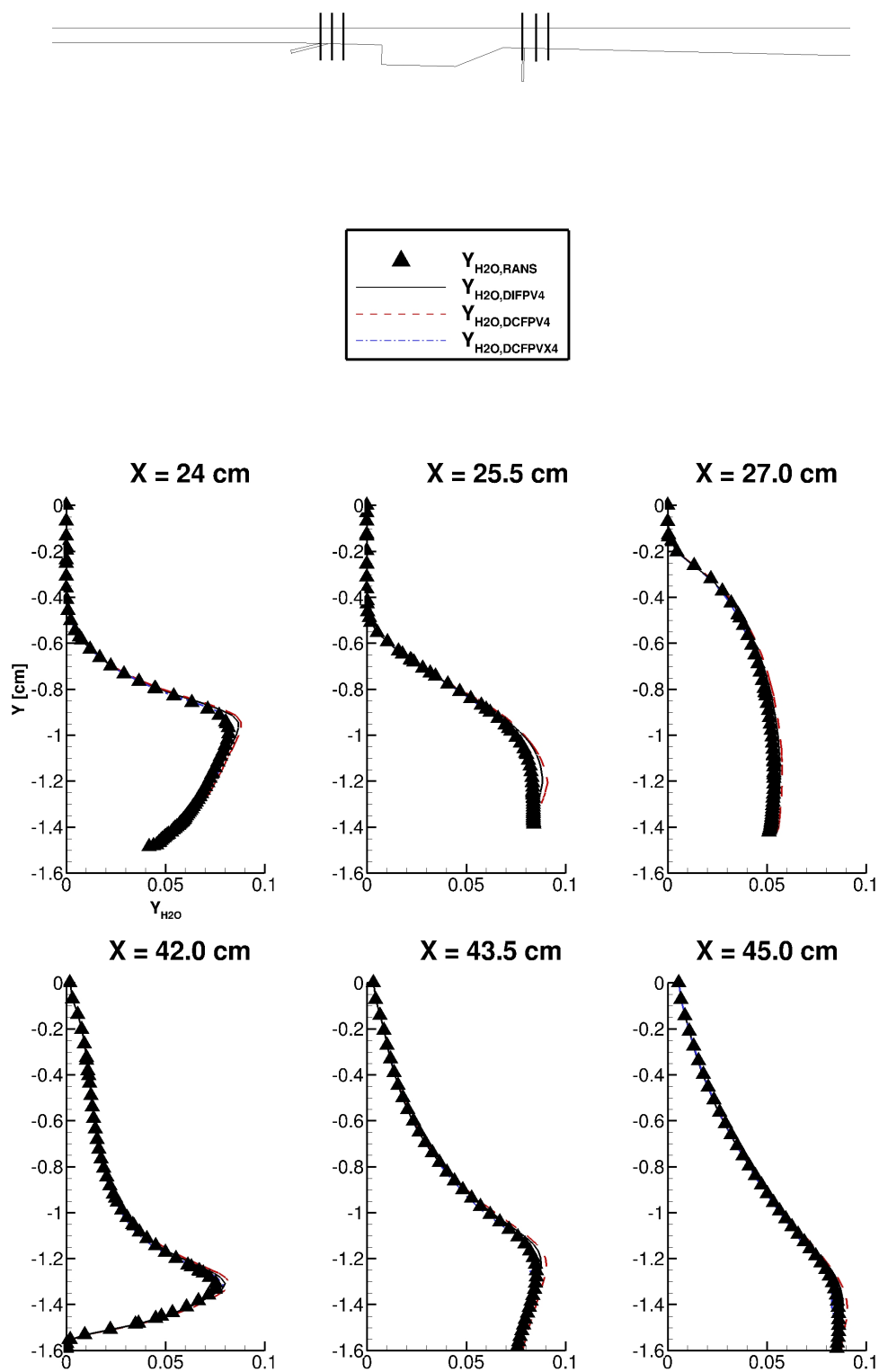


FIGURE 5.46: Line plots of  $Y$  [cm] versus  $Y_{H_2O}$  obtained using the APFM-RANS analysis method and from the baseline RANS simulations of the HDCR combustor at several locations through the primary and secondary injector flames at the injector centerline nearest to the combustor centerline for cases corresponding to DIFPV4, DCFPV4, and DCFPVX4.

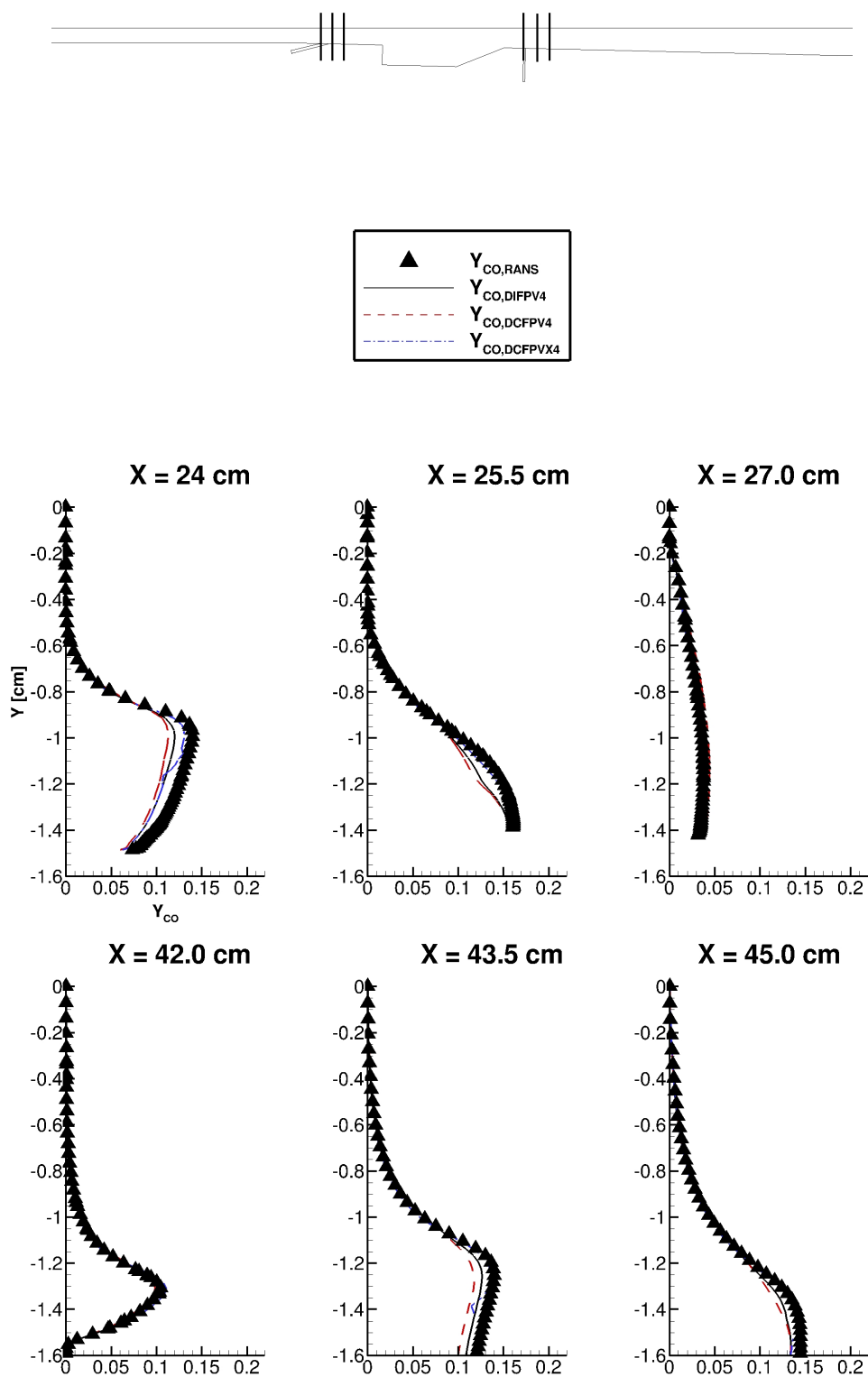


FIGURE 5.47: Line plots of  $Y$  [cm] versus  $Y_{CO}$  obtained using the APFM-RANS analysis method and from the baseline RANS simulations of the HDCR combustor at several locations through the primary and secondary injector flames at the injector centerline nearest to the combustor centerline for cases corresponding to DIFPV4, DCFPV4, and DCFPVX4.

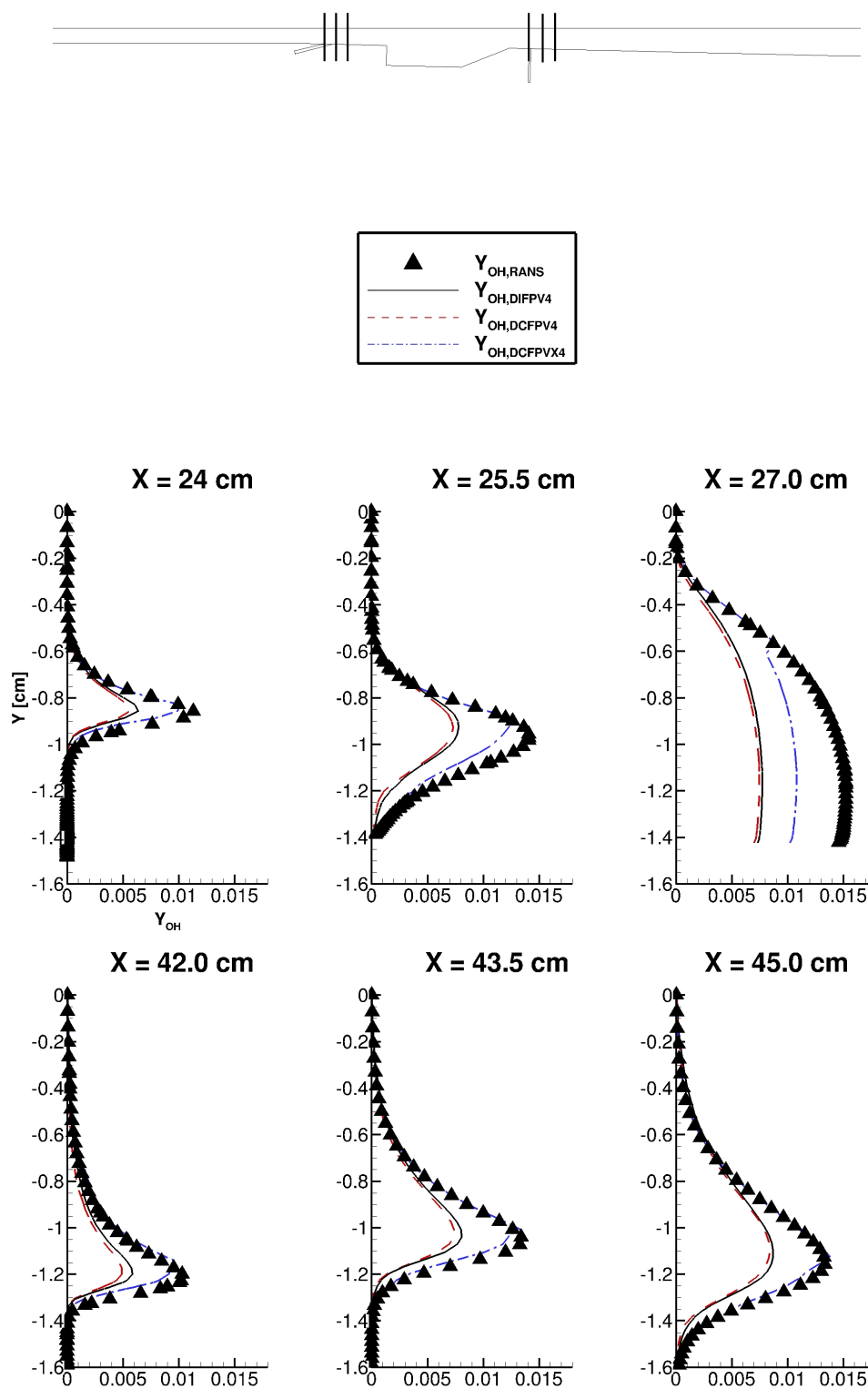


FIGURE 5.48: Line plots of  $Y$  [cm] versus  $Y_{OH}$  obtained using the APFM-RANS analysis method and from the baseline RANS simulations of the HDCR combustor at several locations through the primary and secondary injector flames at the injector centerline nearest to the combustor centerline for cases corresponding to DIFPV4, DCFPV4, and DCFPVX4.

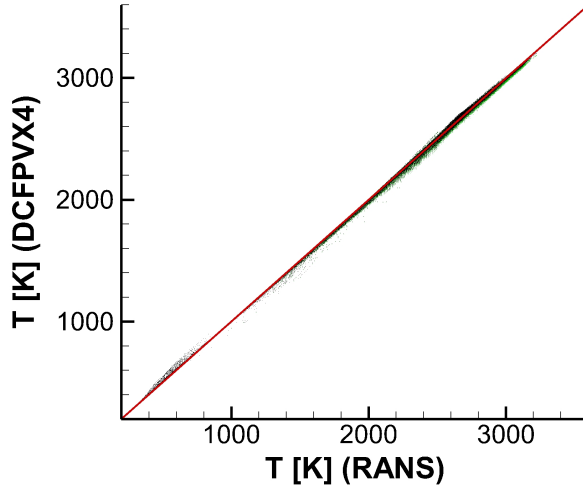


FIGURE 5.49: Scatter plots of  $T$  obtained using the APFM-RANS analysis method in black versus that from the baseline RANS simulations of the HDCR combustor for the full computational domain for case DCFPVX4. Results for case DCFPV4 are shown in green, and the red line denotes a line with slope of one.

Scatter plots of  $T$  versus the baseline RANS data are included in Fig. 5.49, and similar scatter plot comparisons to the baseline RANS data for  $Y_{CO_2}$ ,  $Y_{H_2O}$ ,  $Y_{CO}$ , and  $Y_{OH}$  are included in Fig. 5.50. These scatter plots show data for the entire HDCR combustor flowfield, similar to the figures shown previously for cases DIFPV1-DIFPV4 and DCFPV1-DCFPV4 in Figs. 5.9-5.13 and 5.14-5.18. However, for Figs. 5.49-5.50, the results for case DCFPV4 are also plotted in green to highlight the improvements made by the DCFPVX4 model. For temperature, little improvement can be seen owing mostly to the good agreement with the baseline RANS data for both the DCFPV4 and DCFPVX4 cases. Considerably more improvement, however, can be seen in the results for  $Y_{CO_2}$ ,  $Y_{H_2O}$ ,  $Y_{CO}$ , and  $Y_{OH}$ . In each case, the DCFPVX4 results, shown by black points, exhibit less dispersion around the red line than those of the DCFPV4 results. For  $Y_{OH}$ , the improvement appears most significant, as both the approximate slope of the data spread better matches that of the red line and the dispersion is lessened. The results for  $Y_{CO_2}$  also show a substantial improvement, while results for  $Y_{H_2O}$  and  $Y_{CO}$  show more modest improvements over the DCFPV4 results.

Additionally,  $\dot{\omega}_C$  was calculated for case DCFPVX4 and compared to the baseline RANS solution in Fig. 5.51, in which the temperature-scaling in Eq. (5.8) was used. Since case DCFPVX4 used FT3, for which pressure was a parameterizing variable, no

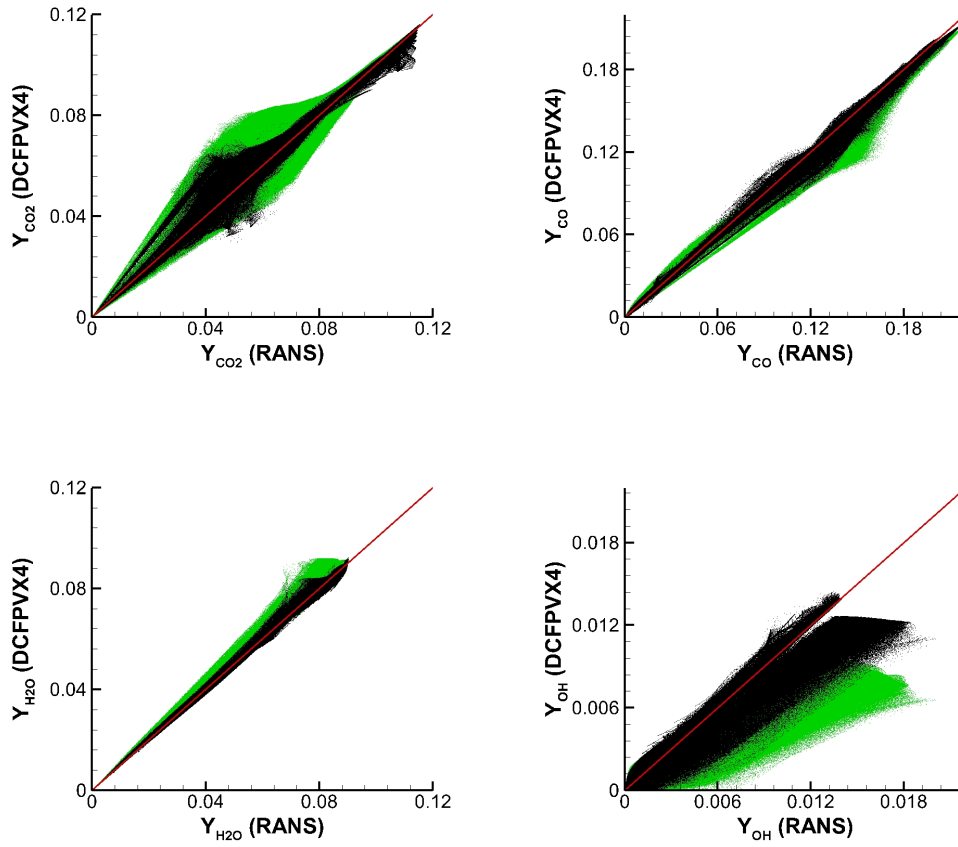


FIGURE 5.50: Scatter plots of  $Y_{CO_2}$ ,  $Y_{CO}$ ,  $Y_{H_2O}$ , and  $Y_{OH}$  obtained using the APFM-RANS analysis method in black versus that from the baseline RANS simulations of the HDCR combustor for the full computational domain for case DCFPVX4. Results for case DCFPV4 are shown in green, and the red line denotes a line with slope of one.

pressure-scaling was necessary to compute  $\dot{\omega}_C$ . Comparing Fig. 5.51 to the results for case DIFPV4 using Eq. (5.8) and to case DCFPV4 using the temperature scaling from Eq. (5.8) in Fig. 5.37 suggests a similar level of agreement in the prediction of  $\dot{\omega}_C$  for the CFPVX model. When considered with the results for  $T$ ,  $Y_{CO_2}$ ,  $Y_{H_2O}$ ,  $Y_{CO}$ , and  $Y_{OH}$ , the *a priori* performance of the CFPVX model suggests a modest improvement over the state-of-the-art IFPV and CFPV model formulations for the HDCR combustor in dual-mode operation.

#### 5.2.4.2 Scram-Mode Operation

Similar to the previous section, line plots for  $T$ ,  $Y_{CO_2}$ ,  $Y_{H_2O}$ ,  $Y_{CO}$ , and  $Y_{OH}$  are included in Figs. 5.52-5.56 for the scram-mode cases. For each of these figures, comparisons are made to the baseline RANS data, as well as results of cases SIFPV4 and SCFPV4, at

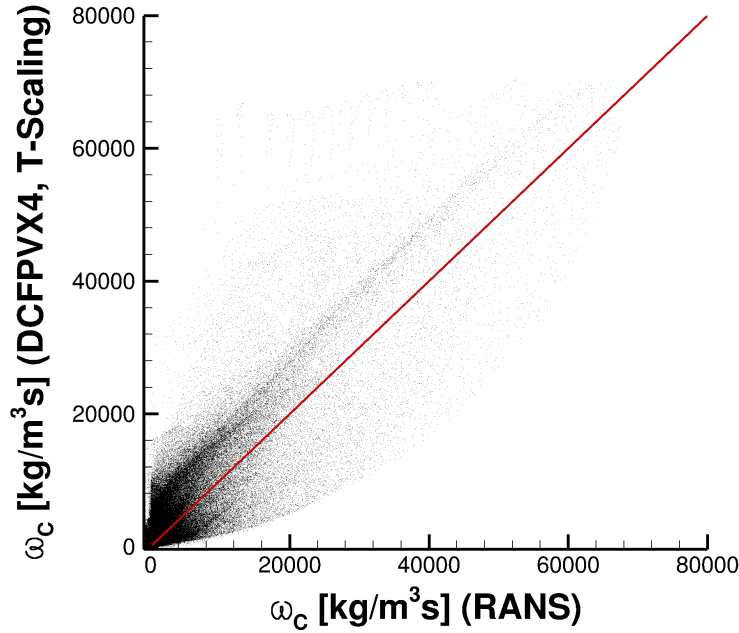


FIGURE 5.51: Scatter plot of  $\dot{\omega}_C$  [ $\text{kg}/\text{m}^3\text{s}$ ] obtained using the APFM-RANS analysis method for case DCFPVX4 versus that from the baseline RANS simulations of the HDCR combustor for the full computational domain. The temperature-scaling presented in Eq. (5.8) is used to correct the tabulated DCFPVX4  $\dot{\omega}_C$ .

a spanwise plane through the centerline of the injectors at several streamwise locations through the primary and secondary flames. While the temperature shows agreement with the baseline RANS data similar to that of cases SIFPV4 and SCFPV4, the results for  $Y_{CO_2}$ ,  $Y_{H_2O}$ , and  $Y_{CO}$  show a slight improvement. Results for  $Y_{OH}$  show a significant improvement. At each of the streamwise locations in Fig. 5.56, the SCFPVX4 results show considerable improvement over both the SIFPV4 and SCFPV4 cases; however, the agreement with the RANS data remains less-than-desired. Fortunately, the multivaluedness of the flamelet manifold discussed in section 5.2.4.1 is absent in these results, thereby suggesting the previous non-uniqueness of the manifold is of a considerably limited scope.

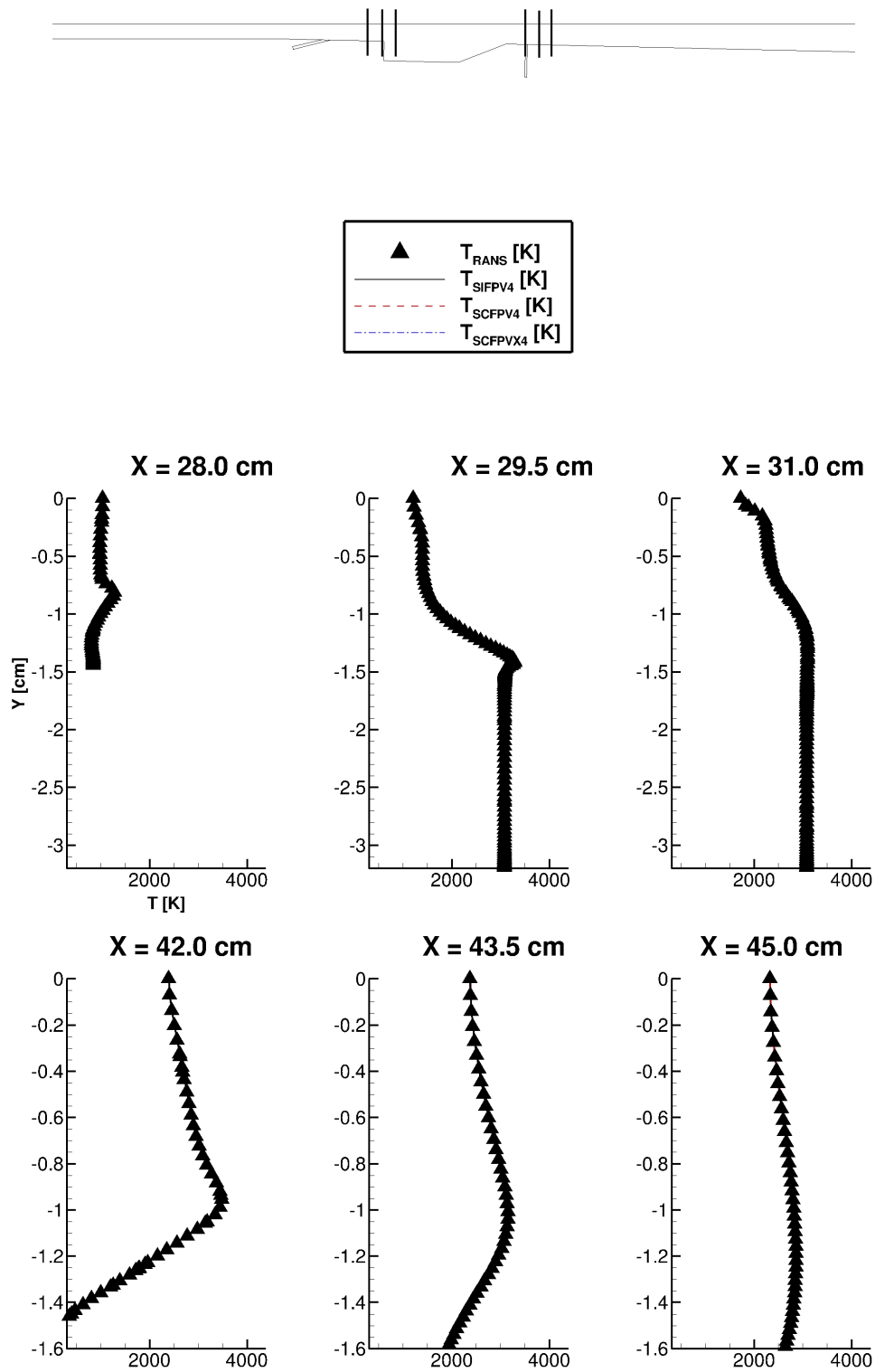


FIGURE 5.52: Line plots of  $Y$  [cm] versus  $T$  [K] obtained using the APFM-RANS analysis method and from the baseline RANS simulations of the HDCR combustor at several locations through the primary and secondary injector frames at the injector centerline nearest to the combustor centerline for cases corresponding to SIFPV4, SCFPV4, and SCFPVX4.

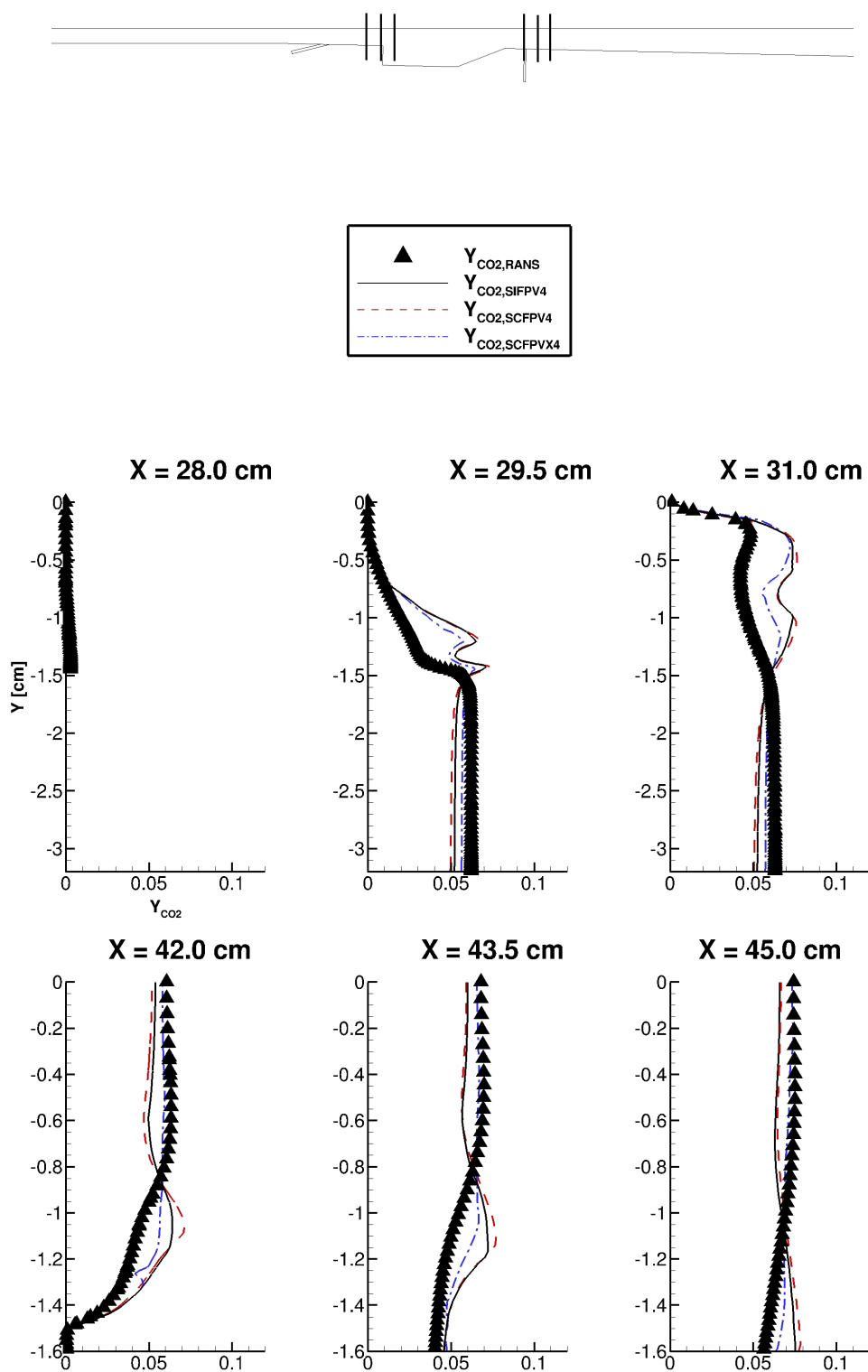


FIGURE 5.53: Line plots of  $Y$  [cm] versus  $Y_{CO_2}$  obtained using the APFM-RANS analysis method and from the baseline RANS simulations of the HDCR combustor at several locations through the primary and secondary injector frames at the injector centerline nearest to the combustor centerline for cases corresponding to SIFPV4, SCFPV4, and SCFPVX4.

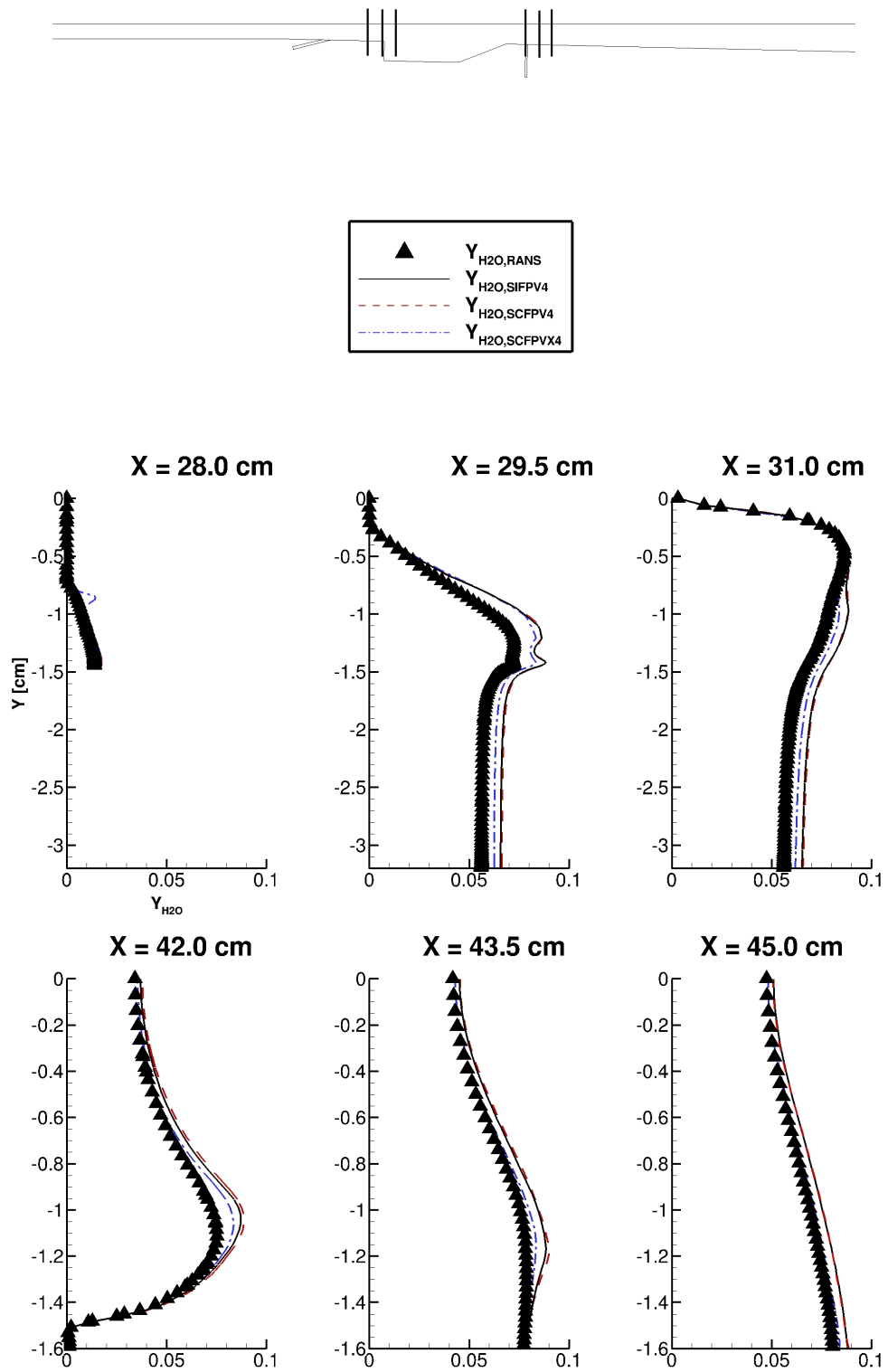


FIGURE 5.54: Line plots of  $Y$  [cm] versus  $Y_{H_2O}$  obtained using the APFM-RANS analysis method and from the baseline RANS simulations of the HDCR combustor at several locations through the primary and secondary injector frames at the injector centerline nearest to the combustor centerline for cases corresponding to SIFPV4, SCFPV4, and SCFPVX4.

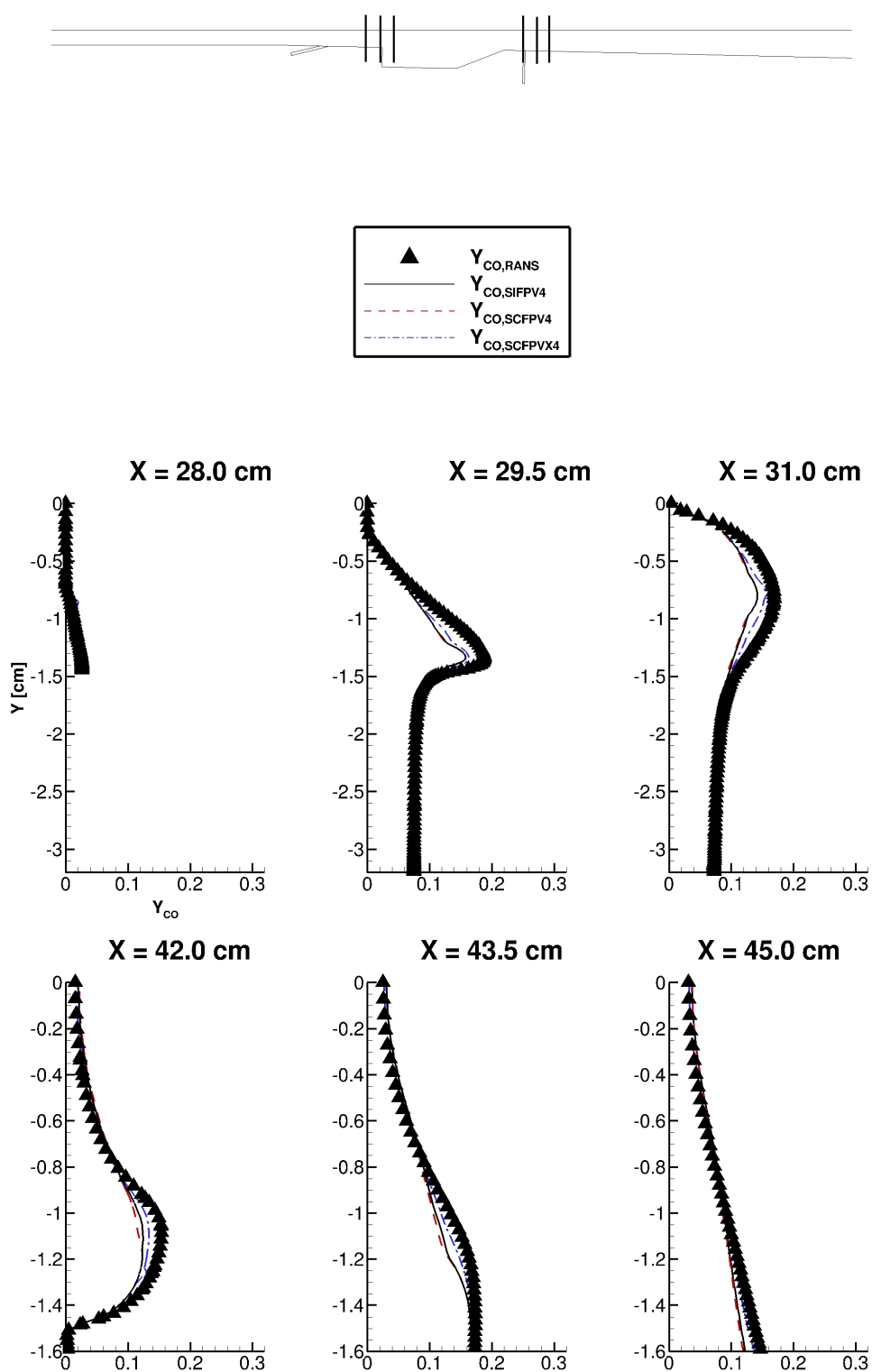


FIGURE 5.55: Line plots of  $Y$  [cm] versus  $Y_{CO}$  obtained using the APFM-RANS analysis method and from the baseline RANS simulations of the HDCR combustor at several locations through the primary and secondary injector frames at the injector centerline nearest to the combustor centerline for cases corresponding to SIFPV4, SCFPV4, and SCFPVX4.

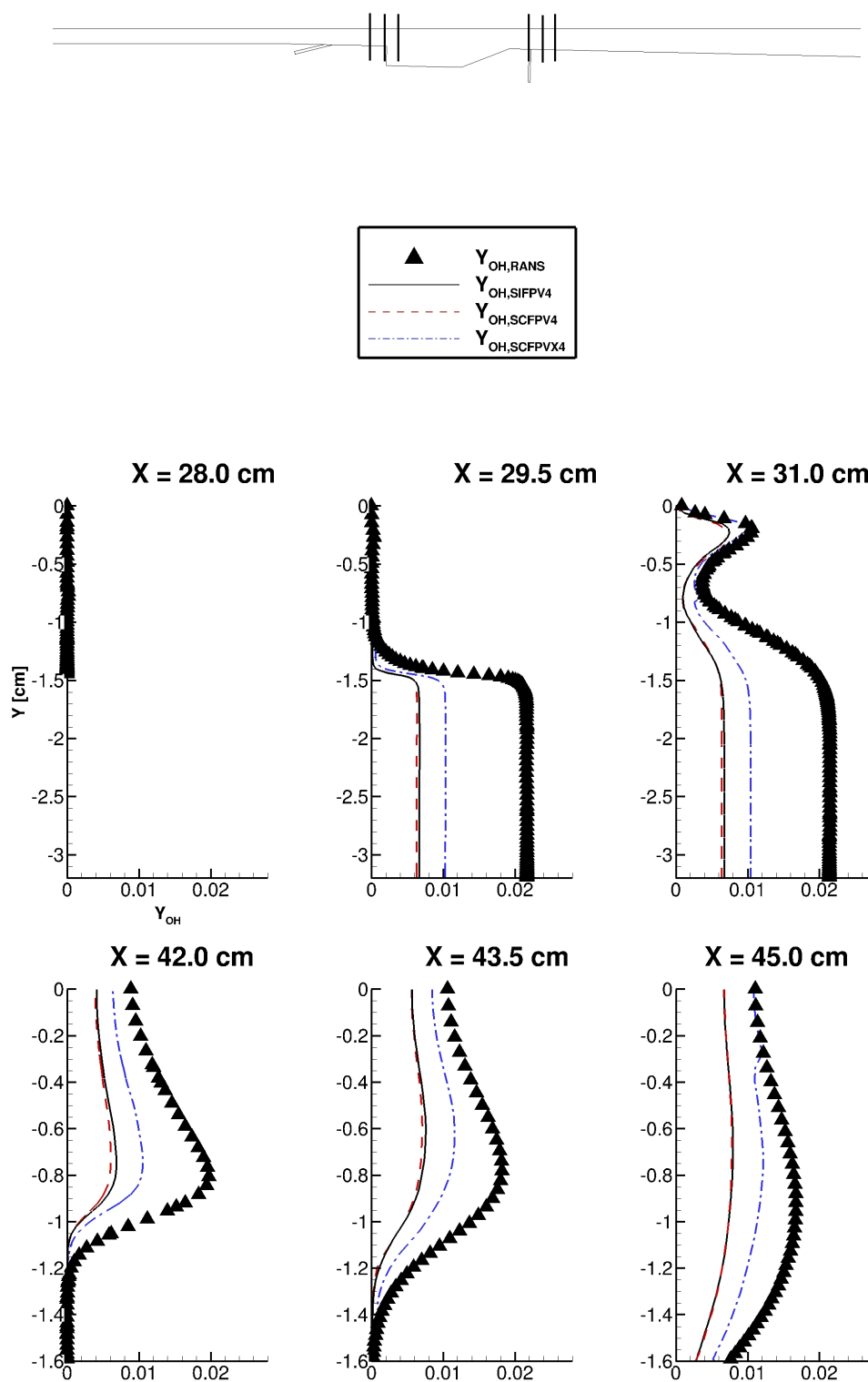


FIGURE 5.56: Line plots of  $Y$  [cm] versus  $Y_{OH}$  obtained using the APFM-RANS analysis method and from the baseline RANS simulations of the HDCR combustor at several locations through the primary and secondary injector frames at the injector centerline nearest to the combustor centerline for cases corresponding to SIFPV4, SCFPV4, and SCFPVX4.

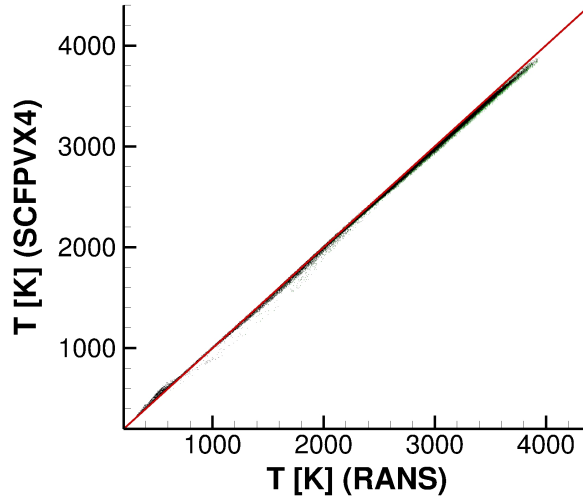


FIGURE 5.57: Scatter plots of  $T$  obtained using the APFM-RANS analysis method in black versus that from the baseline RANS simulations of the HDCR combustor for the full computational domain for case SCFPVX4. Results for case SCFPV4 are shown in green, and the red line denotes a line with slope of one.

Scatter plots of  $T$  versus the baseline RANS data are included in Fig. 5.57, and similar scatter plot comparisons to the baseline RANS data for  $Y_{CO_2}$ ,  $Y_{H_2O}$ ,  $Y_{CO}$ , and  $Y_{OH}$  are included in Fig. 5.58. These scatter plots show data for the entire HDCR combustor flowfield, similar to the figures shown previously for cases SIFPV1-SIFPV4 and SCFPV1-SCFPV4 in Figs. 5.24-5.28 and 5.29-5.33. However, for Figs. 5.57-5.58, the results for case SCFPV4 are also plotted in green to highlight the improvements made by the SCFPVX4 model. For temperature, little improvement can be seen owing mostly to the good agreement with the baseline RANS data for both the SCFPV4 and SCFPVX4 cases. Considerably more improvement, however, can be seen in the results for  $Y_{CO_2}$ ,  $Y_{H_2O}$ ,  $Y_{CO}$ , and  $Y_{OH}$ . In each case, the SCFPVX4 results, shown by black points, exhibit less dispersion around the red line than those of the SCFPV4 results.

Additionally,  $\dot{\omega}_C$  was calculated for case SCFPVX4 and compared to the baseline RANS solution in Fig. 5.59, in which the temperature-scaling in Eq. (5.8) was used. Since case SCFPVX4 used FT3, for which pressure was a parameterizing variable, no pressure-scaling was necessary to compute  $\dot{\omega}_C$ . Comparing Fig. 5.59 to the results for case SIFPV4 using Eq. (5.8) and to case SCFPV4 using the temperature scaling from Eq. (5.8) in Fig. 5.37 suggests a similar level of agreement in the prediction of  $\dot{\omega}_C$  for the CFPVX

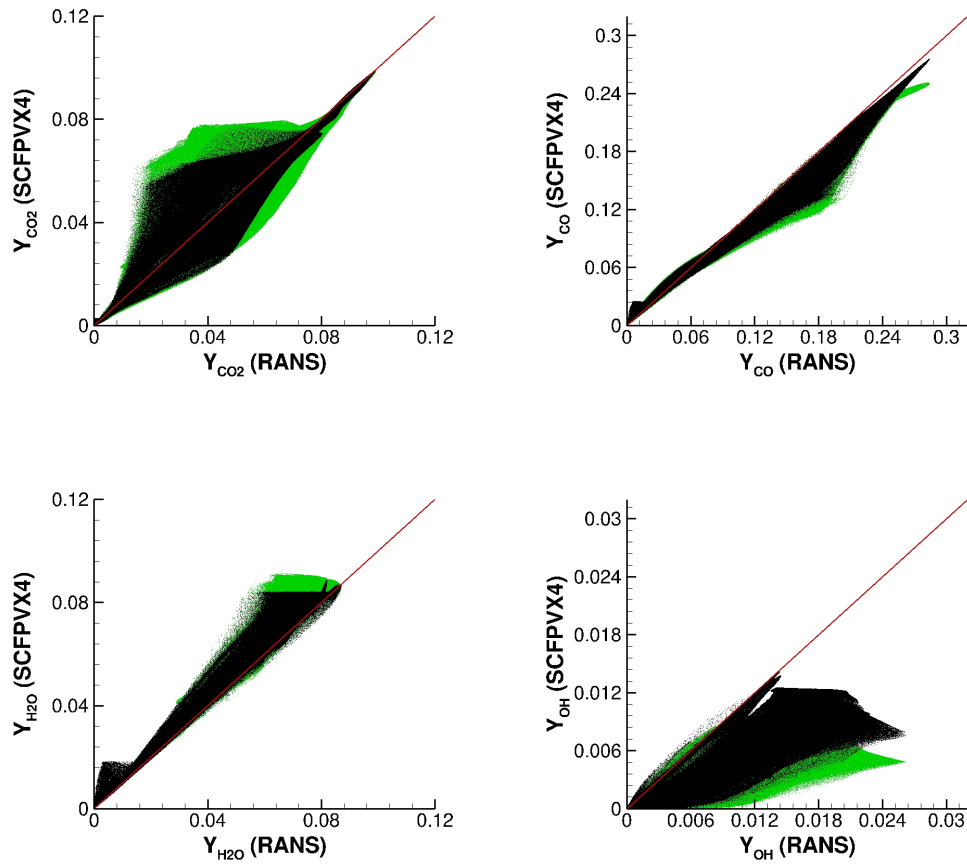


FIGURE 5.58: Scatter plots of  $Y_{CO_2}$ ,  $Y_{CO}$ ,  $Y_{H_2O}$ , and  $Y_{OH}$  obtained using the APFM-RANS analysis method in black versus that from the baseline RANS simulations of the HDCR combustor for the full computational domain for case SCFPVX4. Results for case SCFPV4 are shown in green, and the red line denotes a line with slope of one.

model. When considered with the results for  $T$ ,  $Y_{CO_2}$ ,  $Y_{H_2O}$ ,  $Y_{CO}$ , and  $Y_{OH}$ , the *a priori* performance of the CFPVX model suggests some improvement over the state-of-the-art IFPV and CFPV model formulations for the HDCR combustor both both dual- and scram-mode operation.

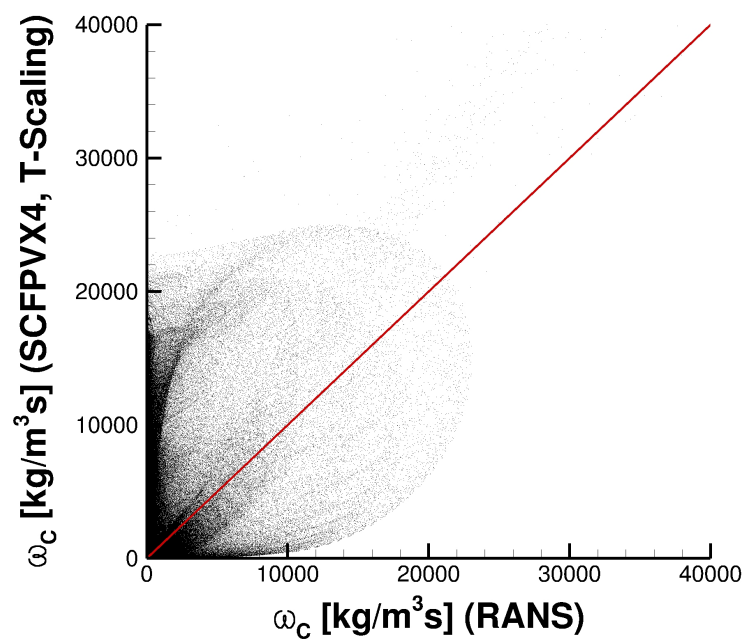


FIGURE 5.59: Scatter plot of  $\dot{\omega}_C$  [ $\text{kg}/\text{m}^3\text{s}$ ] obtained using the APFM-RANS analysis method for case SCFPVX4 versus that from the baseline RANS simulations of the HDCR combustor for the full computational domain. The temperature-scaling presented in Eq. (5.8) is used to correct the tabulated SCFPVX4  $\dot{\omega}_C$ .

## Chapter 6

# *A Posteriori* Model Assessment

While the results from Chapter 5 suggested modest improvements for the CFPVX model, the APFM-RANS analysis represents a *best case* assessment because the solutions are *a priori* formed using reconstructed manifold parameters directly from the baseline RANS solutions. In this context, the APFM-RANS analysis results demonstrated the *potential* theoretical improvements obtained by using the CFPVX model in place of other IFPV and CFPV models. Accordingly, *a posteriori* testing is required to demonstrate the *actual* improvement gained by using the CFPVX model for the simulation of high-speed, compressible, reacting flows like those within the HDCR dual-mode scramjet combustor.

The current chapter presents results of an *a posteriori* FPV model testing campaign for the HDCR combustor, for which IFPV, CFPV, and CFPVX models were implemented in the VULCAN-CFD solver, and cases DIFPV4, DCFPV4, DCFPVX4, SIFPV4, SCFPV4, and SCFPVX4 described previously in Chapter 5 and summarized in Table 5.1 were simulated by solving the full, three-dimensional, Favre-averaged Navier-Stokes equations subject to the FPV model implementation. Details of the FPV modeling implementation in VULCAN-CFD are included in section 6.1, where the complete set of governing equations are presented. VULCAN-CFD is then used to simulate the HDCR combustor using the IFPV, CFPV, and CFPVX models for both dual- and scram-mode operational conditions, and the results of these *a posteriori* simulations are presented in section 6.2, where results for a flight Mach number of 5.84 (baseline RANS case D584A) are presented in section 6.2.1 and for a flight Mach number of 8.00 (baseline RANS case S800A) in section 6.2.2.

## 6.1 FPV Model Implementation

The primary tasks in implementing an FPV modeling capability in VULCAN-CFD were modifying the existing set of governing equations to accommodate the FPV-modeled Favre-averaged RANS equations and developing the interface routines for VULCAN-CFD to access the tabulated flamelet data. Both of these tasks required modifications for the pre-processor, solver, and post-processor routines. The FPV-modeled governing equations solved by VULCAN-CFD are summarized in the current section.

The Favre-averaged RANS equations were presented previously in Chapter 2 for a mixture of thermally perfect gases in Eqs. (2.18)-(2.22). Following the results of Chapter 5, the complete system of FPV-modeled governing equations implemented in VULCAN-CFD is shown below in Eqs. (6.1)-(6.6)

$$\frac{\partial \bar{\rho}}{\partial t} + \frac{\partial \bar{\rho} \tilde{u}_j}{\partial x_j} = 0 \quad (6.1)$$

$$\begin{aligned} \frac{\partial \bar{\rho} \tilde{u}_i}{\partial t} + \frac{\partial \bar{\rho} \tilde{u}_i \tilde{u}_j}{\partial x_j} = & -\frac{\partial \bar{p}}{\partial x_i} \\ & + \frac{\partial}{\partial x_j} \left\{ (\mu + \mu_t) \left[ \left( \frac{\partial \tilde{u}_i}{\partial x_j} + \frac{\partial \tilde{u}_j}{\partial x_i} \right) - \frac{2}{3} \delta_{ij} \frac{\partial \tilde{u}_k}{\partial x_k} \right] - \frac{2}{3} \delta_{ij} \bar{\rho} \tilde{k} \right\} \end{aligned} \quad (6.2)$$

$$\begin{aligned} \frac{\partial \bar{\rho} \tilde{E}}{\partial t} + \frac{\partial \bar{\rho} \tilde{H} \tilde{u}_j}{\partial x_j} = & \frac{\partial}{\partial x_j} \left\{ \tilde{u}_i \left[ \mu \left( \frac{\partial \tilde{u}_i}{\partial x_j} + \frac{\partial \tilde{u}_j}{\partial x_i} \right) - \frac{2}{3} \delta_{ij} \mu \frac{\partial \tilde{u}_k}{\partial x_k} \right] \right\} \\ & + \frac{\partial}{\partial x_j} \left[ \left( \lambda + \frac{\mu_t c_p}{Pr_t} \right) \frac{\partial \tilde{T}}{\partial x_i} + \left( \frac{\mu}{Sc} + \frac{\mu_t}{Sc_t} \right) \sum_{\alpha} \tilde{h}_{\alpha} \frac{\partial \tilde{Z}}{\partial x_j} \frac{\partial \tilde{Y}_{\alpha}}{\partial \tilde{Z}} \right] \\ & + \frac{\partial}{\partial x_j} \left[ \left( \frac{\mu}{\sigma_k} + \frac{\mu_t}{\sigma_k} \right) \frac{\partial \tilde{k}}{\partial x_j} \right] \end{aligned} \quad (6.3)$$

$$\frac{\partial \bar{\rho} \tilde{Z}}{\partial t} + \frac{\partial \bar{\rho} \tilde{Z} \tilde{u}_j}{\partial x_j} = \frac{\partial}{\partial x_j} \left[ \left( \frac{\mu}{Sc} + \frac{\mu_t}{Sc_t} \right) \frac{\partial \tilde{Z}}{\partial x_j} \right] \quad (6.4)$$

$$\frac{\partial \bar{\rho} \tilde{C}}{\partial t} + \frac{\partial \bar{\rho} \tilde{C} \tilde{u}_j}{\partial x_j} = \frac{\partial}{\partial x_j} \left[ \left( \frac{\mu}{Sc} + \frac{\mu_t}{Sc_t} \right) \frac{\partial \tilde{C}}{\partial x_j} \right] + \bar{\omega}_C \quad (6.5)$$

$$\bar{p} = \bar{\rho} \tilde{T} R_u \sum_{\alpha} \frac{\tilde{Y}_{\alpha}}{MW_{\alpha}} \quad (6.6)$$

where the terms colored red are retrieved from a flamelet table at runtime. Equations (6.1), (6.2), (6.4), (6.5), and (6.6) were introduced previously in Eqs. (2.18), (2.19), (2.28), (2.35), and (2.22), respectively, and are repeated here with FPV model couplings highlighted in red to clarify the present discussion. Equation (6.3) follows from Eq. (2.20) subject to the energy interdiffusion modeling discussion presented in Chapter 5. The  $\bar{\omega}_C$  term is corrected using both pressure- and temperature-scalings shown earlier in Eq. (5.8) for IFPV applications and using only the temperature-scaling component also shown earlier in Eq. (5.8) for CFPV and CFPVX applications.

A schematic illustrating the application of an FPV model using VULCAN-CFD is included in Fig. 6.1. Using this approach, the use of *a priori* data for oxidizer temperature and static pressure are used in order to construct a suitable flamelet table for the flow-field under study, and for the current study, this data was computed using the baseline finite-rate RANS simulations. Additional details regarding the implementation of the governing equations and the FPV model architecture described in Fig. 6.1 are included in Appendix A.

## 6.2 Results

Several *a posteriori* simulations of the HDCR using the FPV models described in previous chapters were performed using VULCAN-CFD by solving Eqs. (6.1)-(6.6). The results of these simulations are presented in the current section. Based on the findings of Chapter 5, only cases DIFPV4, DCFPV4, DCFPVX4, SIFPV4, SCFPV4, and SCFPVX4 were performed using VULCAN-CFD. The results were post-processed similar to those of Chapter 5, albeit with additional comparisons to the available experimental data and additional contour comparisons. Whereas the results of the APFM-RANS analysis method posed a *best-case* comparison to the baseline RANS solutions, the *a posteriori* results of this section demonstrate the level of agreement attainable in practice.

All *a posteriori* calculations were performed using the same numerical approach described previously in Chapter 3 for the *a priori* baseline finite-rate RANS calculations. Though, since FPV modeling is not yet implemented for implicit methods, the current calculations utilized a five-stage, fourth-order Runge-Kutta scheme to integrate Eqs. (6.1)-(6.5). Additional work toward extending these models to the implicit DAF

routines is documented in Appendix B. Results for the dual-mode cases (DIFPV4, DCFPV4, and DCFPVX4) are included in section 6.2.1, and those for the scram-mode cases (SIFPV4, SCFPV4, and SCFPVX4) are included in section 6.2.2.

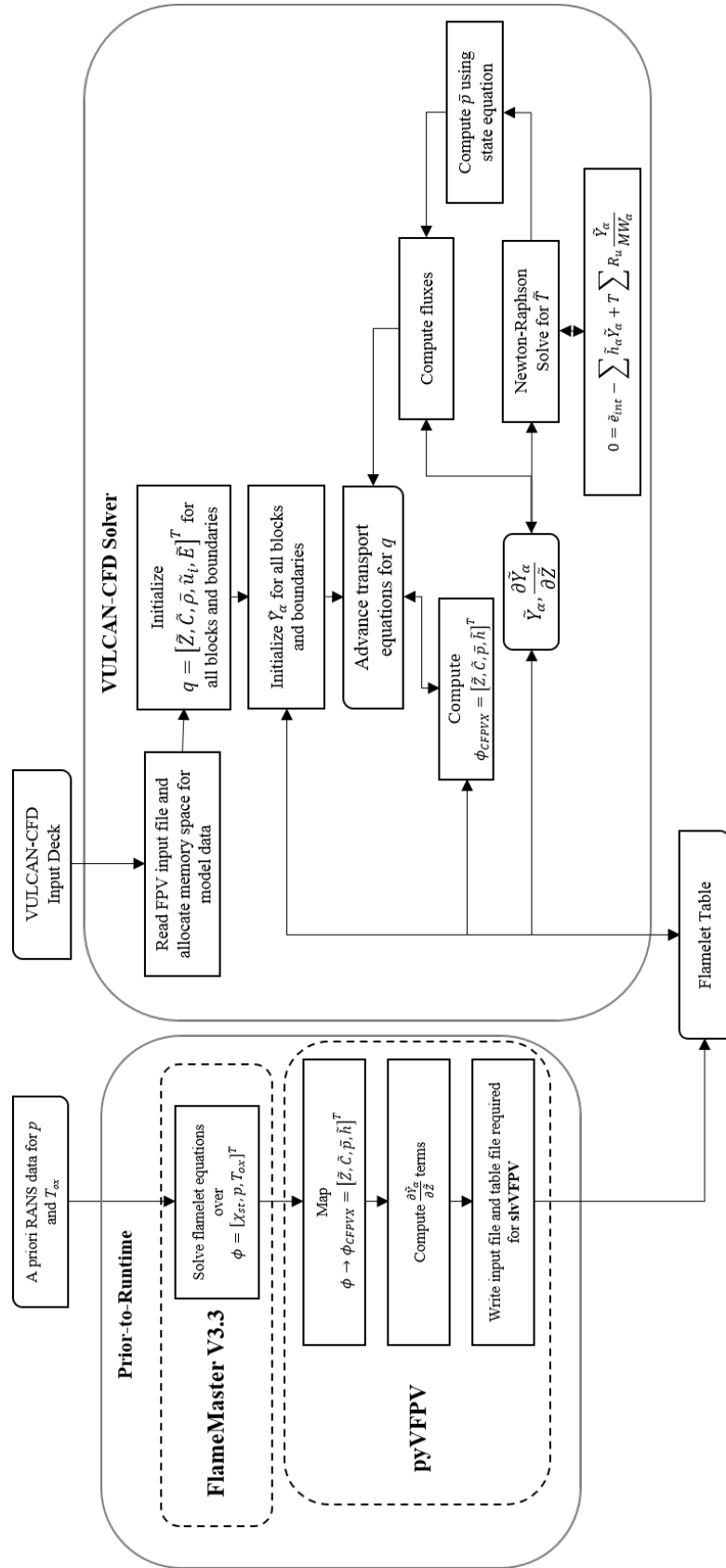


FIGURE 6.1: Flowchart depicting the application of FPV models using VULCAN-CFD.

### 6.2.1 Dual-Mode Operation

The *a posteriori* results for dual-mode operation of the HDCR combustor are presented foremost in comparison to the baseline RANS results for case D584A. An initial comparison is made using the centerline wall static pressure, with subsequent comparisons for  $\tilde{T}$ ,  $\tilde{Y}_{CO_2}$ ,  $\tilde{Y}_{CO}$ ,  $\tilde{Y}_{H_2O}$ , and  $\tilde{Y}_{OH}$  using both contour plots and line plots at the spanwise plane intersecting the first set of injectors off the combustor centerline. The line plot comparisons are made using a similar approach to those shown in Chapter 5 for several locations spanning the primary and secondary injector flames at the injector centerline nearest to the combustor centerline.

Comparisons of combustor centerline wall pressure are typically the focal benchmark for assessing CFD simulations of scramjet combustors in practice. Its ubiquity is largely due to the importance of predicting the location of the combustion-induced leading shock, in addition to the general availability and reliability of wall pressure experimental measurements. In Fig. 6.2, the centerline static wall pressure is compared for cases DIFPV4, DCFPV4, and DCFPVX4 to both the baseline dual-mode RANS case D584A and to the experimental data [58, 88]. The first important observation is that all three models predict the location of the leading compression shock ahead of the primary injectors well. Predicting the location of this leading shock is critical to ensuring proper isolator margin for the engine. The second important observation is that all three models predict the peak combustor pressure very well, with the IFPV and CFPV models showing slightly better predictions. However, the IFPV and CFPV models underpredict the pressure drop just downstream of the secondary injectors, whereas the CFPVX model compares favorably to the baseline RANS solution through this region.

Contour plots for cases DIFPV4, DCFPV4, and DCFPVX4 are shown with the corresponding RANS contour plot for  $\tilde{T}$ ,  $\tilde{Y}_{CO_2}$ ,  $\tilde{Y}_{CO}$ ,  $\tilde{Y}_{H_2O}$ , and  $\tilde{Y}_{OH}$  in Figs. 6.3-6.7, respectively, and these plots serve to highlight the general agreement for each case. Generally, results for all metrics qualitatively resemble the baseline RANS solution. For each case, thin flame regions reside near the primary and secondary injectors, and the species mass fraction distributions largely agree with those of the RANS solution. For each of the FPV cases, the major flow features are captured; although, differences among the FPV results can be seen, such as in Fig. 6.7, where the IFPV and CFPV models appear to

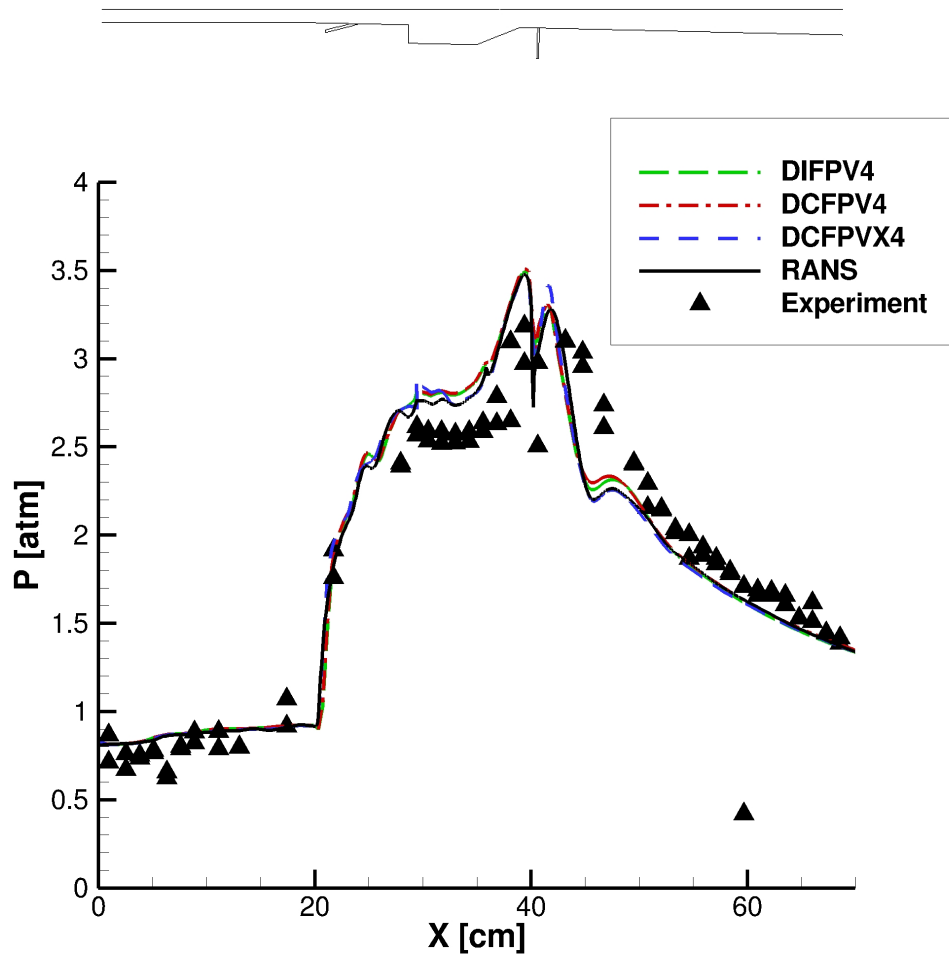


FIGURE 6.2: Comparisons of streamwise ( $x$  [cm]) wall static pressure ( $p$  [atm]) data at the HDCR combustor centerline for FPV simulation cases DIFPV4, DCFPV4, and DCFPVX4 computed using VULCAN-CFD. The baseline dual-mode RANS case D584A and experimental data are also plotted.

considerably underpredict the  $\tilde{Y}_{OH}$  across the entire flowfield as compared to the CFPVX model and in Fig. 6.4 where the IFPV and CFPV models appear to overpredict  $\tilde{Y}_{CO_2}$ . Some variation in agreement for the prediction of the  $\tilde{T}$  fields can also be seen in Fig. 6.3, where the CFPVX model appears to better match the  $\tilde{T}$  distributions around the primary and secondary injectors.

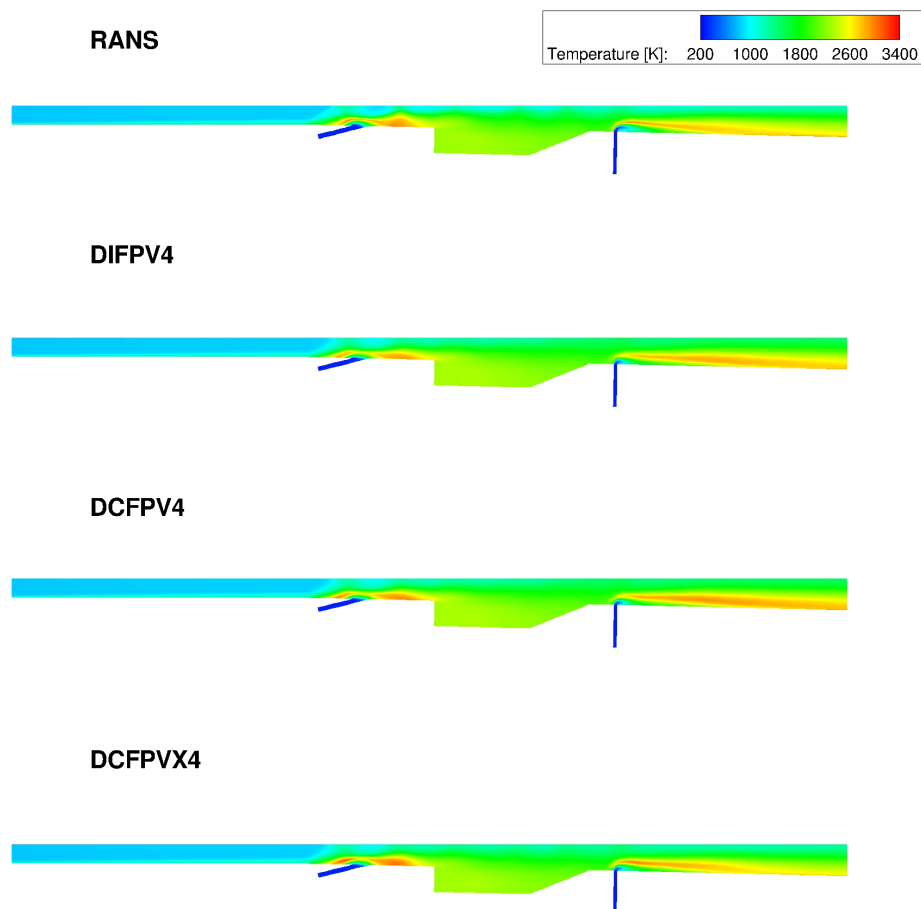


FIGURE 6.3: Contours of  $\tilde{T}$  [K] obtained by solving Eqs. (6.1)-(6.6) using VULCAN-CFD for the HDCR combustor at the injector centerline nearest to the combustor centerline for cases DIFPV4, DCFPV4, and DCFPVX4 and compared to the baseline dual-mode RANS case D584A.

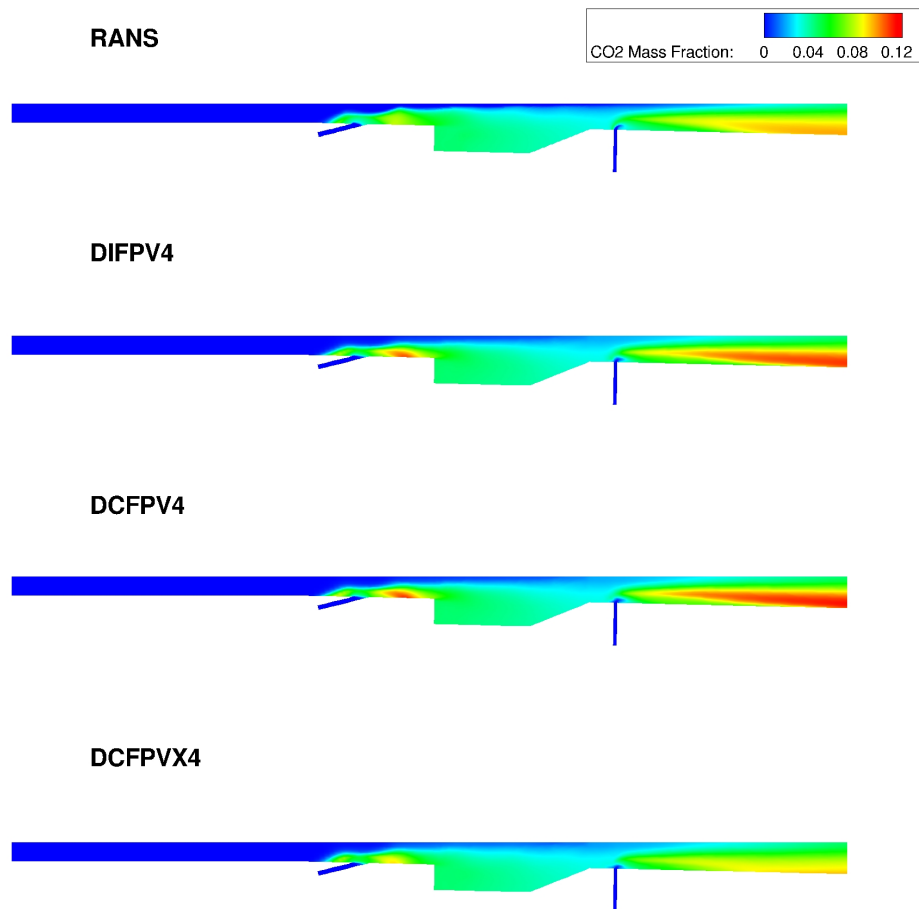


FIGURE 6.4: Contours of  $\tilde{Y}_{CO_2}$  obtained by solving Eqs. (6.1)-(6.6) using VULCAN-CFD for the HDCR combustor at the injector centerline nearest to the combustor centerline for cases DIFPV4, DCFPV4, and DCFPVX4 and compared to the baseline dual-mode RANS case D584A.

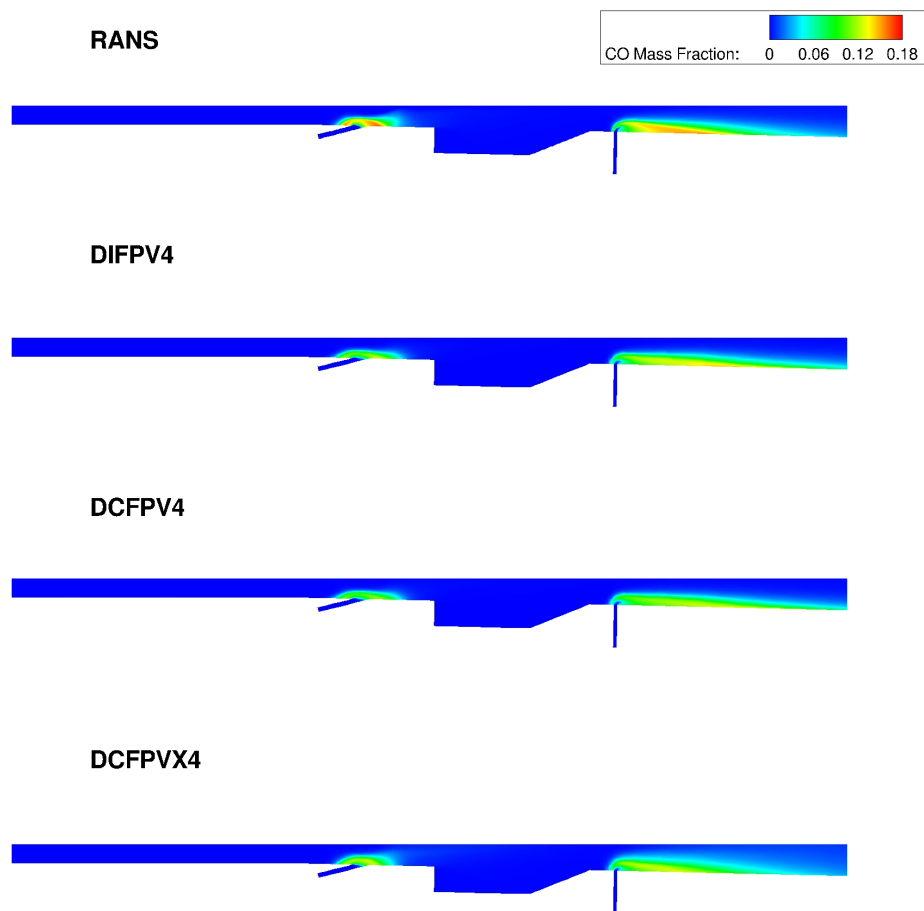


FIGURE 6.5: Contours of  $\tilde{Y}_{CO}$  obtained by solving Eqs. (6.1)-(6.6) using VULCAN-CFD for the HDCR combustor at the injector centerline nearest to the combustor centerline for cases DIFPV4, DCFPV4, and DCFPVX4 and compared to the baseline dual-mode RANS case D584A.

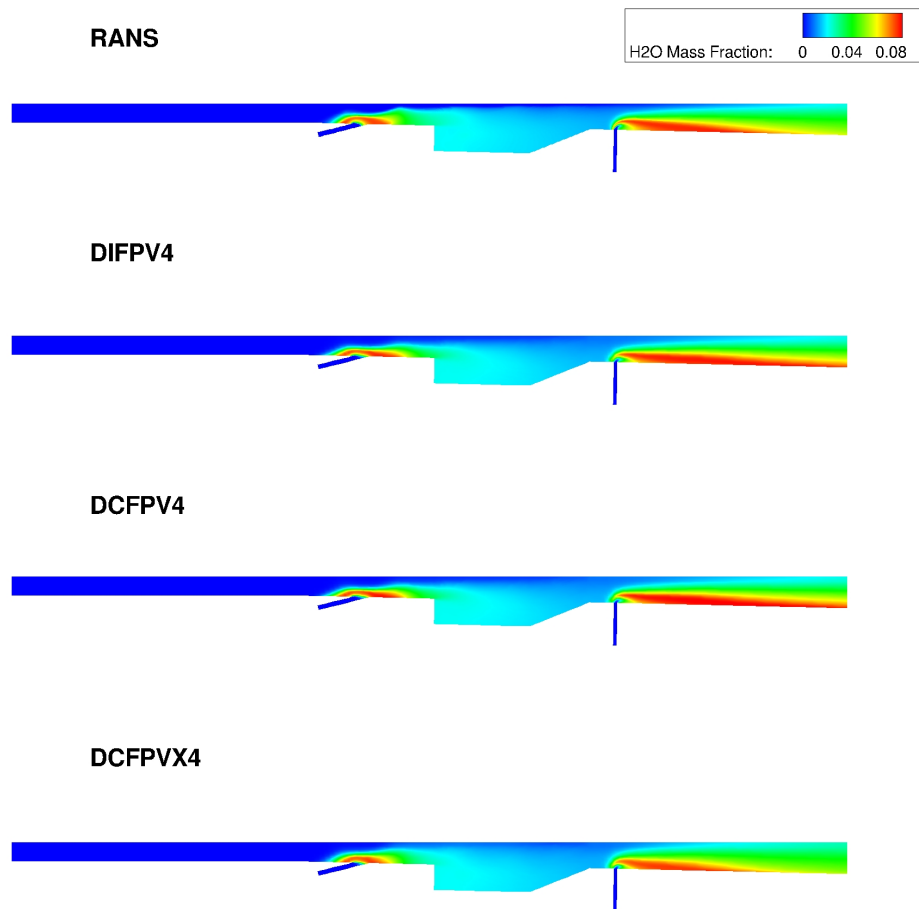


FIGURE 6.6: Contours of  $\tilde{Y}_{H_2O}$  obtained by solving Eqs. (6.1)-(6.6) using VULCAN-CFD for the HDCR combustor at the injector centerline nearest to the combustor centerline for cases DIFPV4, DCFPV4, and DCFPVX4 and compared to the baseline dual-mode RANS case D584A.

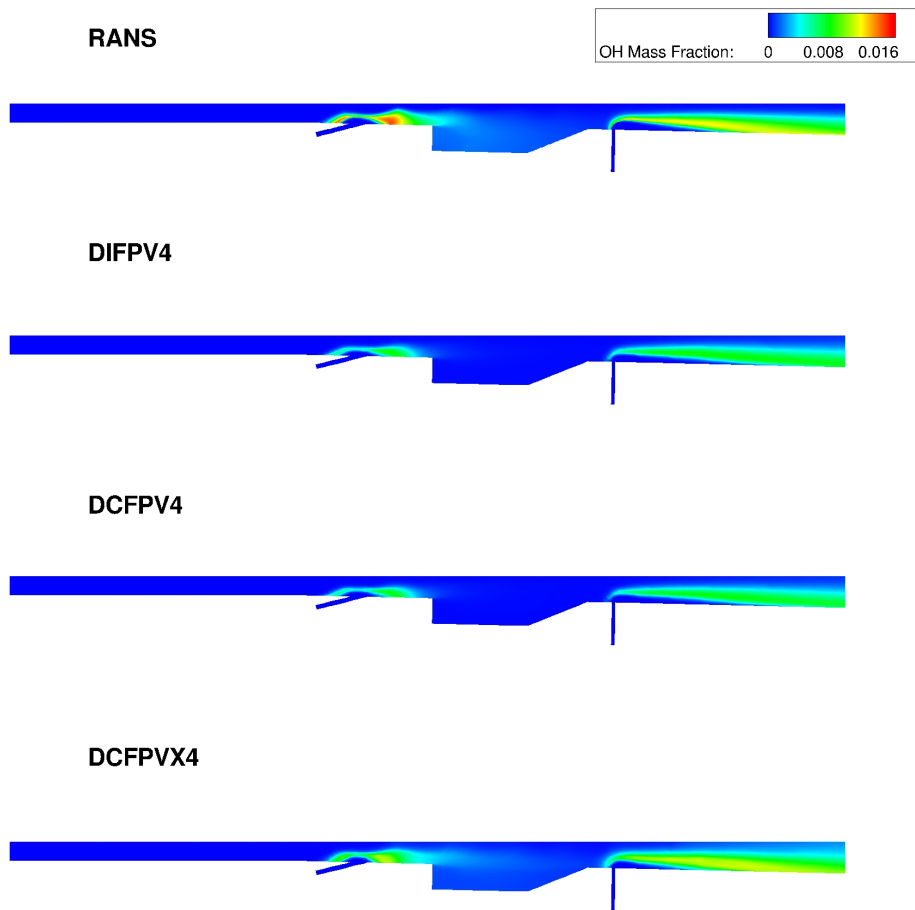


FIGURE 6.7: Contours of  $\tilde{Y}_{OH}$  obtained by solving Eqs. (6.1)-(6.6) using VULCAN-CFD for the HDCR combustor at the injector centerline nearest to the combustor centerline for cases DIFPV4, DCFPV4, and DCFPVX4 and compared to the baseline dual-mode RANS case D584A.

Quantitative comparisons are made in Figs. 6.8-6.12, where results for  $\tilde{T}$ ,  $\tilde{Y}_{CO_2}$ ,  $\tilde{Y}_{CO}$ ,  $\tilde{Y}_{H_2O}$ , and  $\tilde{Y}_{OH}$  are shown, respectively, using line plots at several planes through the primary and secondary injectors at the centerline plane intersecting the first set of injectors off the combustor centerline. Agreement with the baseline RANS data for all metrics approached that of the APFM-RANS analysis, and generally, the *a posteriori* results agree well with the baseline RANS solution. For each metric, the CFPVX model demonstrates generally better agreement with the RANS solution for the primary injector flames, whereas for the secondary injector flames, all three models provide a similar level of agreement.

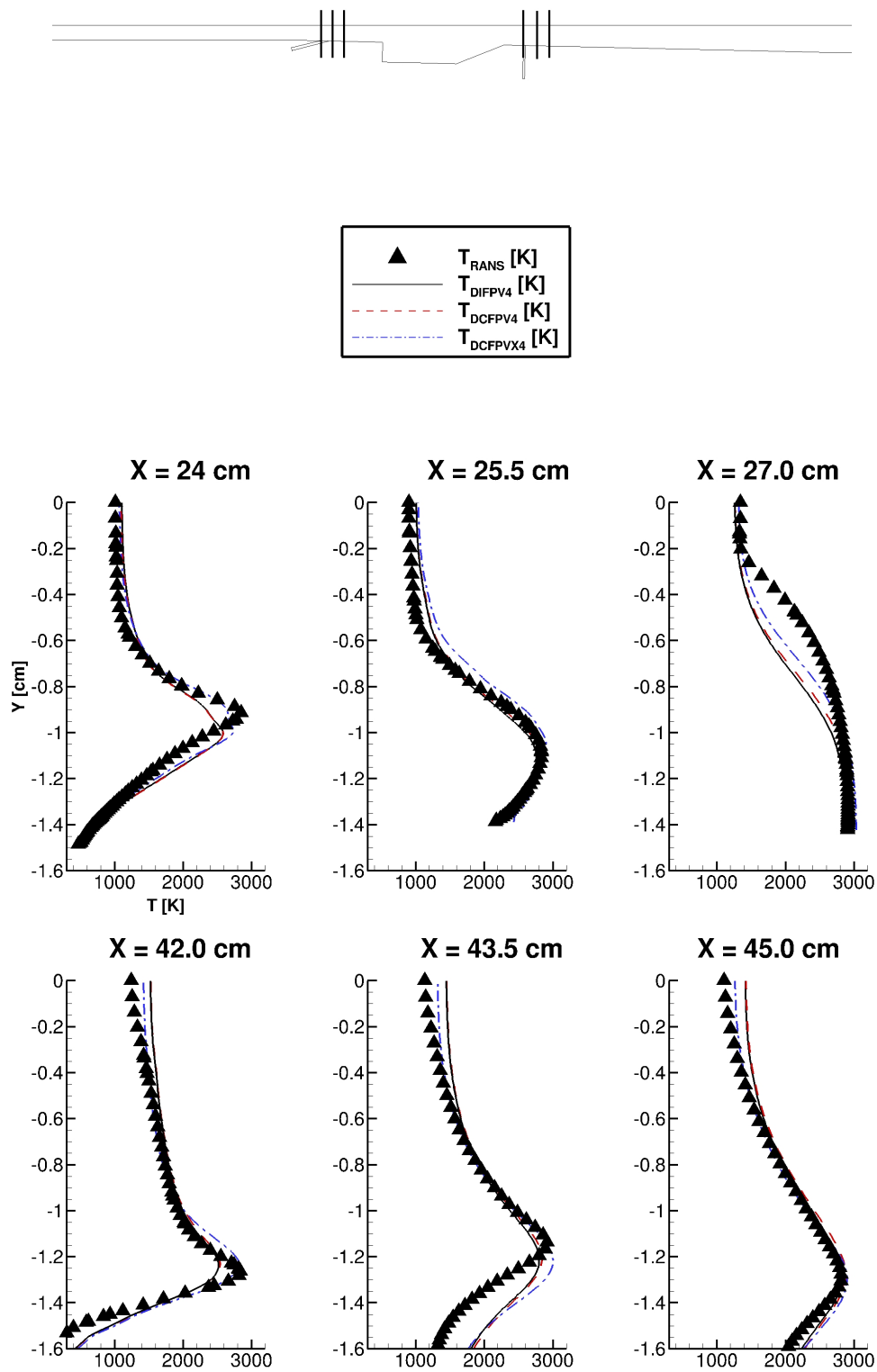


FIGURE 6.8: Line plots of  $Y$  [cm] versus  $\tilde{T}$  [K] obtained by solving Eqs. (6.1)-(6.6) using VULCAN-CFD for the HDCR combustor at several locations through the primary and secondary injector flames at the injector centerline nearest to the combustor centerline for cases DIFPV4, DCFV4, and DCFVX4 and compared to the baseline dual-mode RANS case D584A.

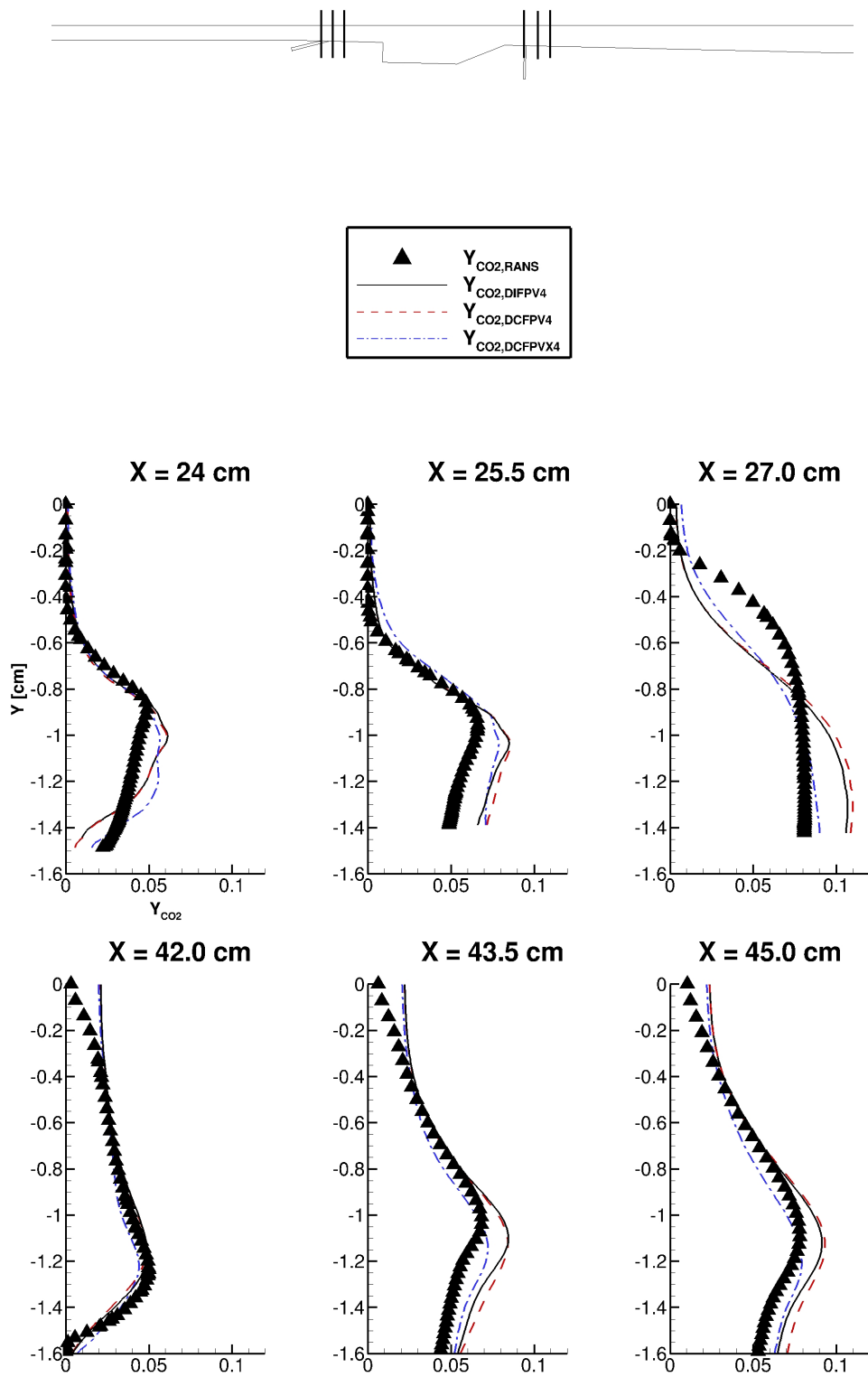


FIGURE 6.9: Line plots of  $Y$  [cm] versus  $\tilde{Y}_{CO_2}$  obtained by solving Eqs. (6.1)-(6.6) using VULCAN-CFD for the HDCR combustor at several locations through the primary and secondary injector flames at the injector centerline nearest to the combustor centerline for cases DIFPV4, DCFPV4, and DCFPVX4 and compared to the baseline dual-mode RANS case D584A.

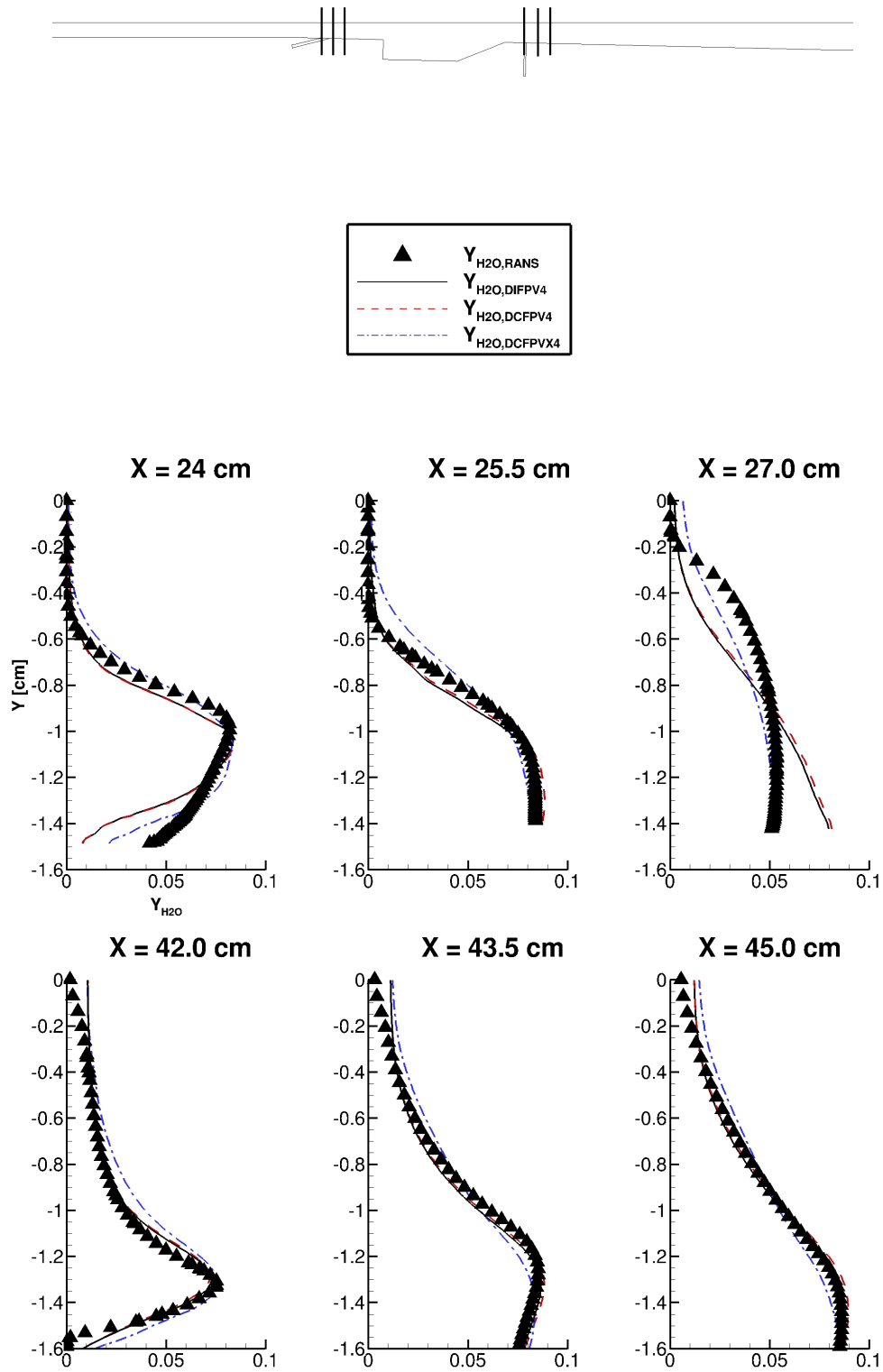


FIGURE 6.10: Line plots of  $Y$  [cm] versus  $\tilde{Y}_{H_2O}$  obtained by solving Eqs. (6.1)-(6.6) using VULCAN-CFD for the HDCR combustor at several locations through the primary and secondary injector flames at the injector centerline nearest to the combustor centerline for cases DIFPV4, DCFPV4, and DCFPVX4 and compared to the baseline dual-mode RANS case D584A.

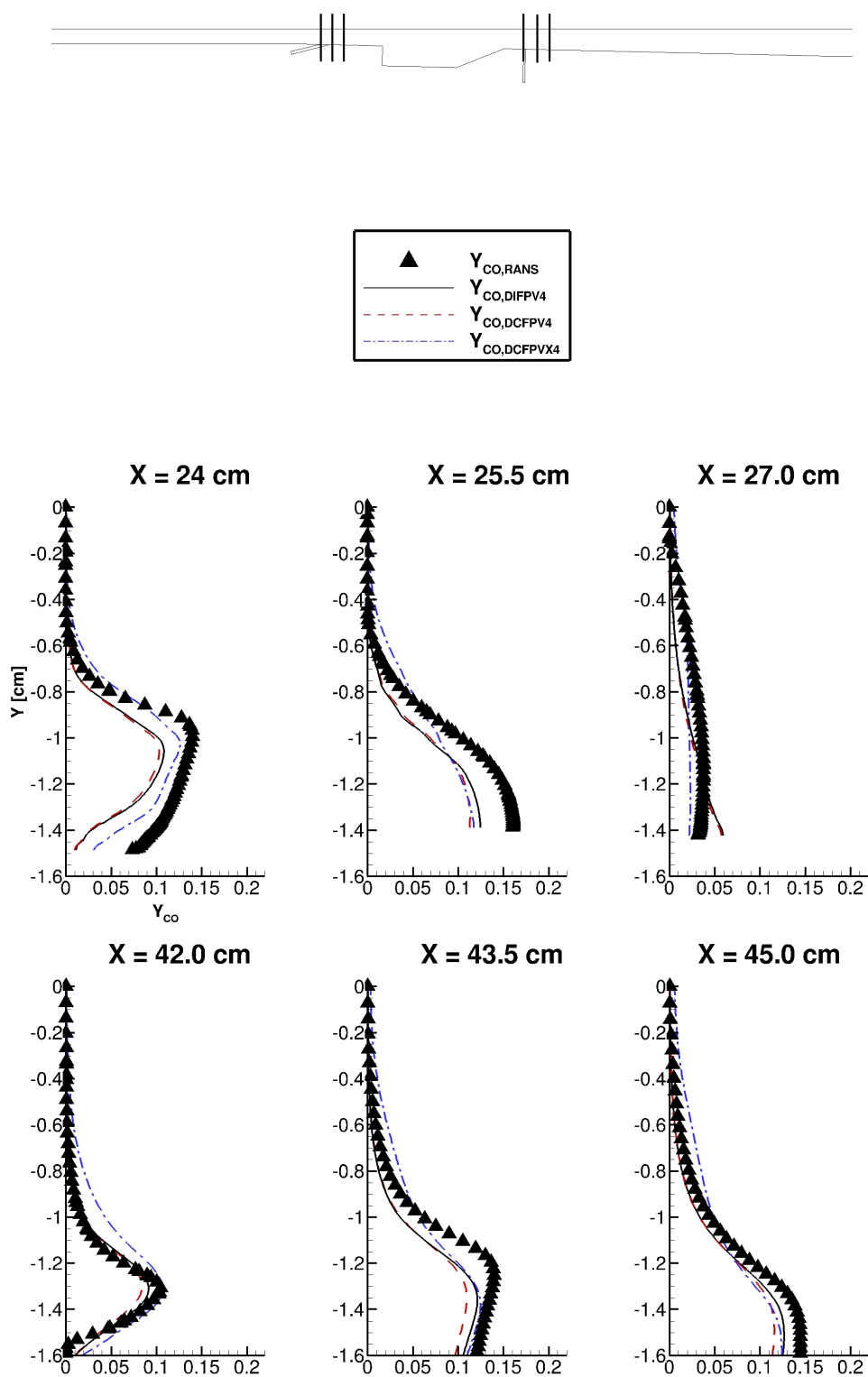


FIGURE 6.11: Line plots of  $Y$  [cm] versus  $\tilde{Y}_{CO}$  obtained by solving Eqs. (6.1)-(6.6) using VULCAN-CFD for the HDCR combustor at several locations through the primary and secondary injector flames at the injector centerline nearest to the combustor centerline for cases DIFPV4, DCFPV4, and DCFPVX4 and compared to the baseline dual-mode RANS case D584A.

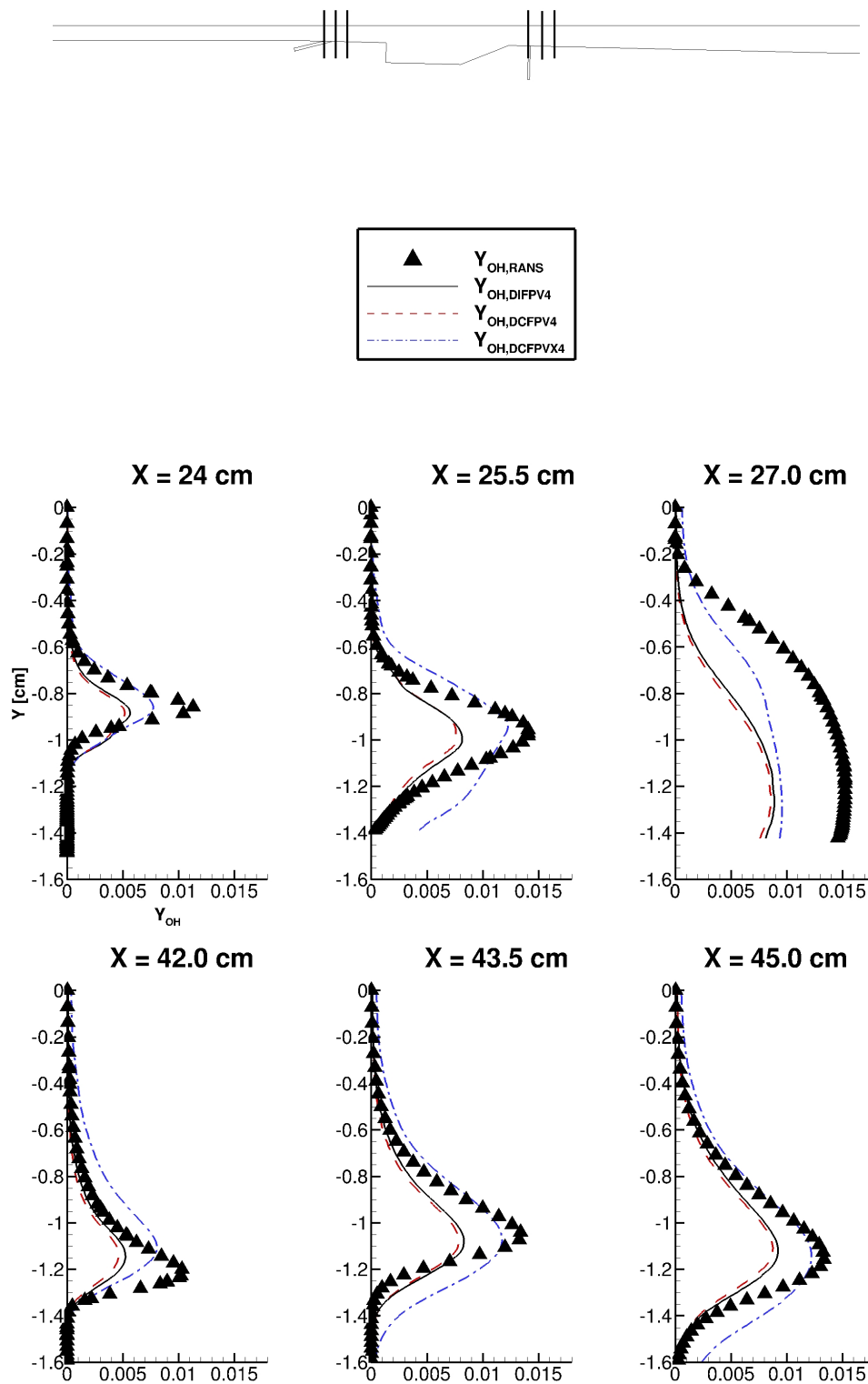


FIGURE 6.12: Line plots of  $Y$  [cm] versus  $\tilde{Y}_{OH}$  obtained by solving Eqs. (6.1)-(6.6) using VULCAN-CFD for the HDCR combustor at several locations through the primary and secondary injector flames at the injector centerline nearest to the combustor centerline for cases DIFPV4, DCFPV4, and DCFPVX4 and compared to the baseline dual-mode RANS case D584A.

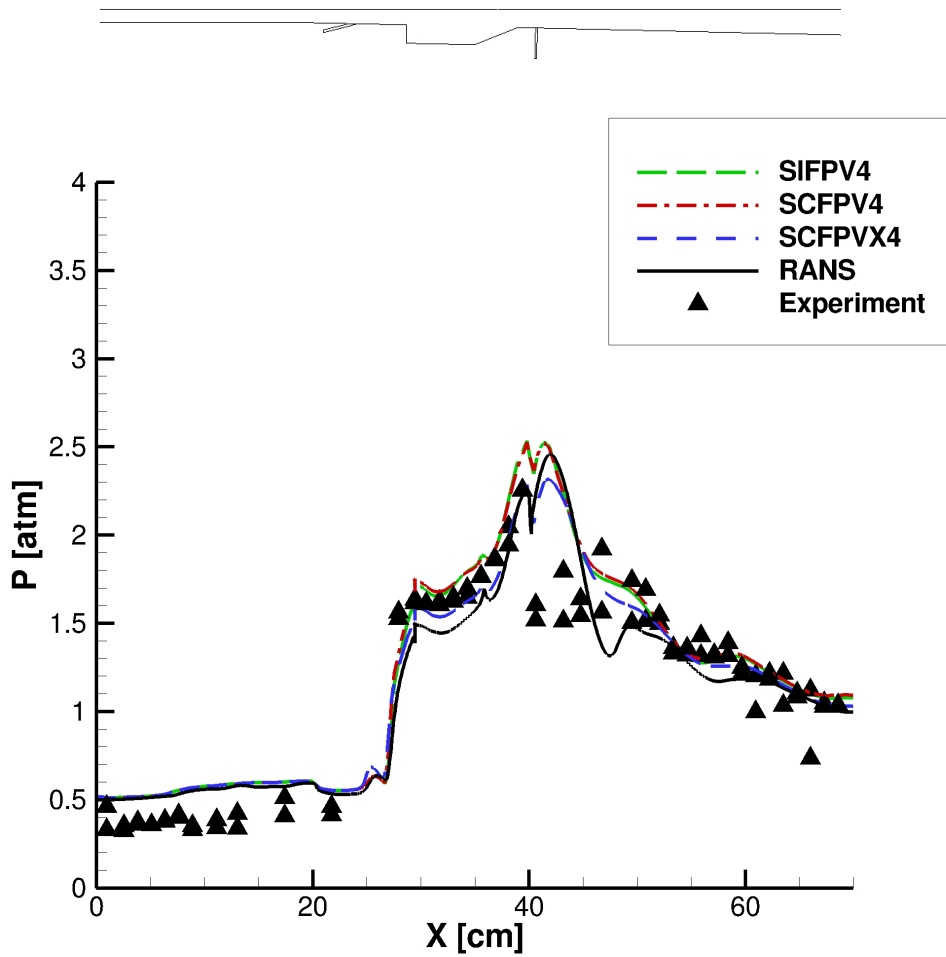


FIGURE 6.13: Comparisons of streamwise ( $x$  [cm]) wall static pressure ( $p$  [atm]) data at the HDCR combustor centerline for FPV simulation cases SIFPV4, SCFPV4, and SCFPVX4 computed using VULCAN-CFD. The baseline scram-mode RANS case S800A and experimental data are also plotted.

### 6.2.2 Scram-Mode Operation

Presentation of the *a posteriori* results for scram-mode operation of the HDCR combustor follows the same format as for the dual-mode results presented in the previous section. An initial comparison is made using the centerline wall static pressure, and subsequent comparisons are made using  $\tilde{T}$ ,  $\tilde{Y}_{CO_2}$ ,  $\tilde{Y}_{CO}$ ,  $\tilde{Y}_{H_2O}$ , and  $\tilde{Y}_{OH}$  in the form of both contour and line plots. All contour and line plots are shown for the spanwise centerline injector plane nearest to the combustor centerline, where line plots are shown for locations spanning the primary and secondary injector flames.

For the same reasons described in the previous section, comparisons of the centerline wall static pressure are shown first for the scram-mode cases. In Fig. 6.13, the centerline

static wall pressure is compared for cases SIFPV4, SCFPV4, and SCFPVX4 to both the baseline scram-mode RANS case S800A and to the experimental data [58, 88]. The first important observation is that all three models predict the location of the leading compression shock ahead of the primary injectors well. Predicting the location of this leading shock is critical to ensuring proper isolator margin for the engine. The second important observation is that the IFPV and CFPV models overpredict the peak combustor pressure and generally mispredict the pressure downstream of the leading shock. On the other hand, the CFPVX model slightly underpredicts the peak combustor pressure but provides better predictions of the pressure overall downstream of the leading shock.

Contour plots for cases SIFPV4, SCFPV4, and SCFPVX4 are shown with the corresponding RANS contour plot for  $\tilde{T}$ ,  $\tilde{Y}_{CO_2}$ ,  $\tilde{Y}_{CO}$ ,  $\tilde{Y}_{H_2O}$ , and  $\tilde{Y}_{OH}$  in Figs. 6.14-6.18, respectively, and these plots serve to highlight the general agreement for each case. Generally, results for all metrics qualitatively resemble the baseline RANS solution. For each case, the primary flame resides near the cavity step corner, immediately behind the leading compression shock, and the secondary flame forms a thin flame region near the secondary injector orifices. The SCFPVX4 results demonstrate moderately better agreement with the RANS results than those of cases SIFPV4 and SCFPV4 for each of the comparisons metrics, while all three models overpredict the temperatures within the cavity region.

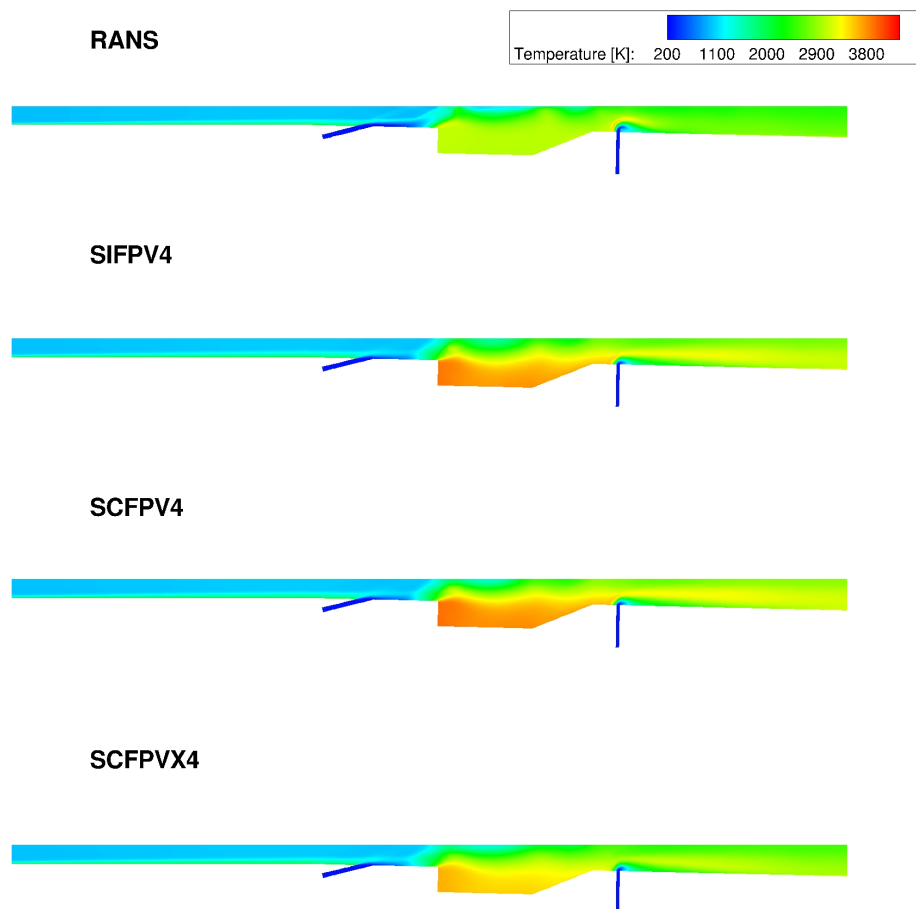


FIGURE 6.14: Contours of  $\tilde{T}$  [K] obtained by solving Eqs. (6.1)-(6.6) using VULCAN-CFD for the HDCR combustor at the injector centerline nearest to the combustor centerline for cases SIFPV4, SCFPV4, and SCFPVX4 and compared to the baseline scram-mode RANS case S800A.

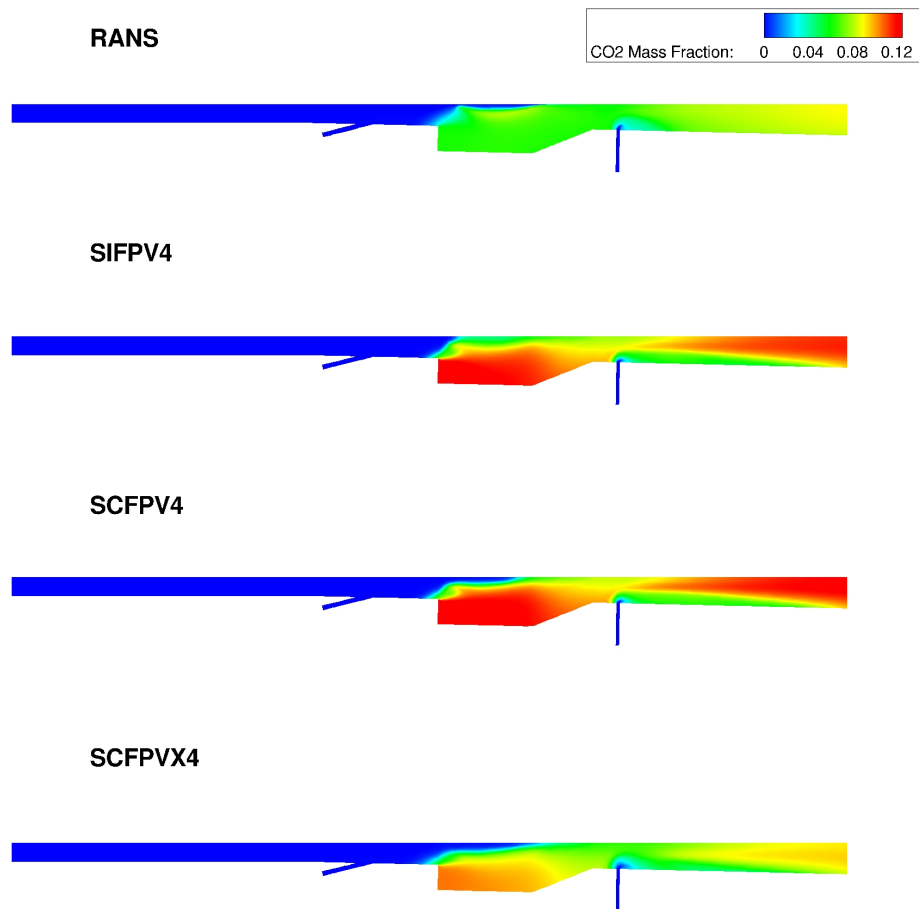


FIGURE 6.15: Contours of  $\tilde{Y}_{CO_2}$  obtained by solving Eqs. (6.1)-(6.6) using VULCAN-CFD for the HDCR combustor at the injector centerline nearest to the combustor centerline for cases SIFPV4, SCFPV4, and SCFPVX4 and compared to the baseline scram-mode RANS case S800A.

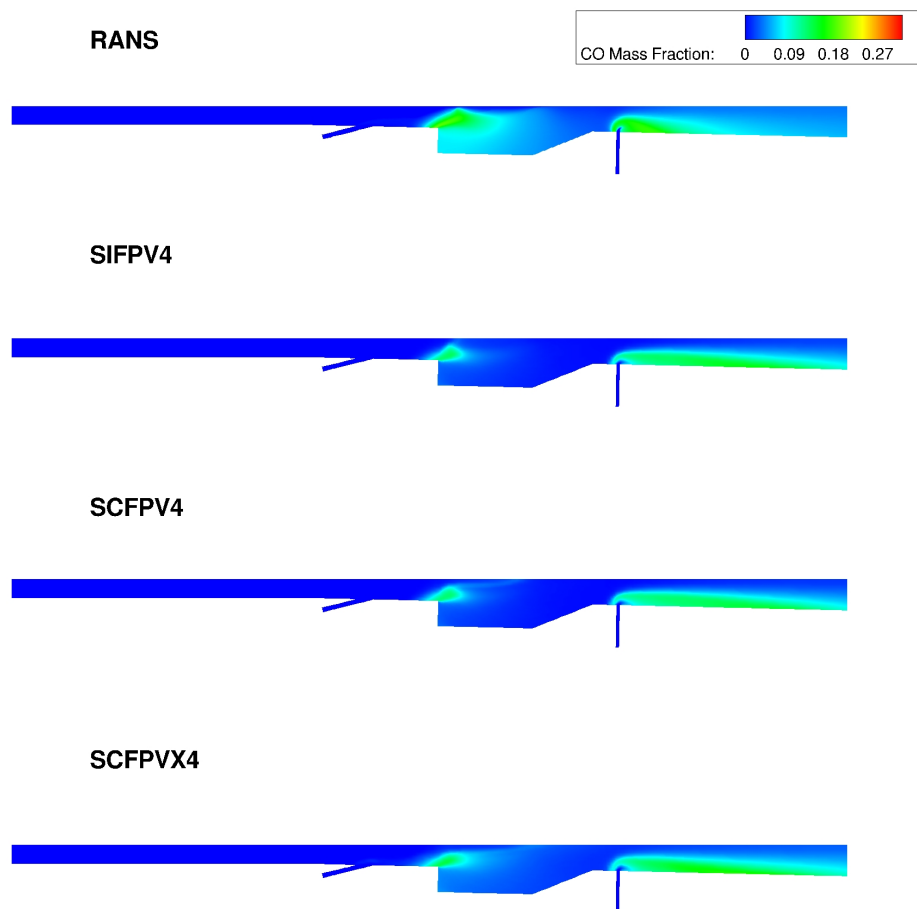


FIGURE 6.16: Contours of  $\tilde{Y}_{CO}$  obtained by solving Eqs. (6.1)-(6.6) using VULCAN-CFD for the HDCR combustor at the injector centerline nearest to the combustor centerline for cases SIFPV4, SCFPV4, and SCFPVX4 and compared to the baseline scram-mode RANS case S800A.

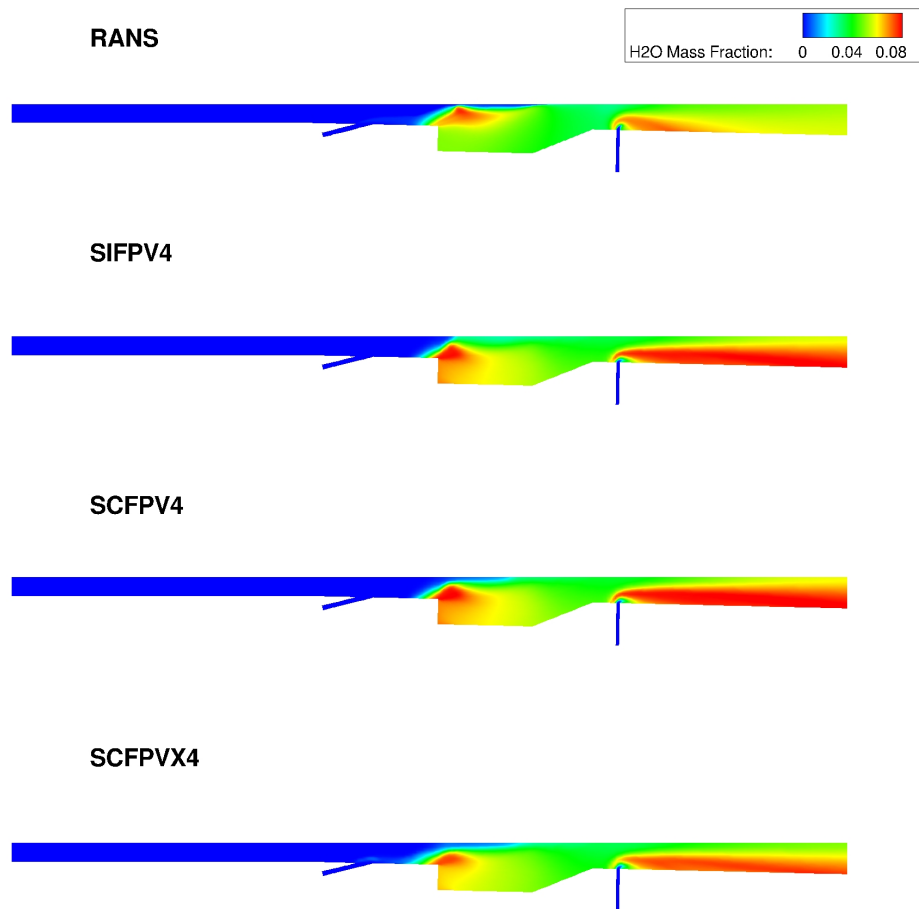


FIGURE 6.17: Contours of  $\tilde{Y}_{H_2O}$  obtained by solving Eqs. (6.1)-(6.6) using VULCAN-CFD for the HDCR combustor at the injector centerline nearest to the combustor centerline for cases SIFPV4, SCFPV4, and SCFPVX4 and compared to the baseline scram-mode RANS case S800A.

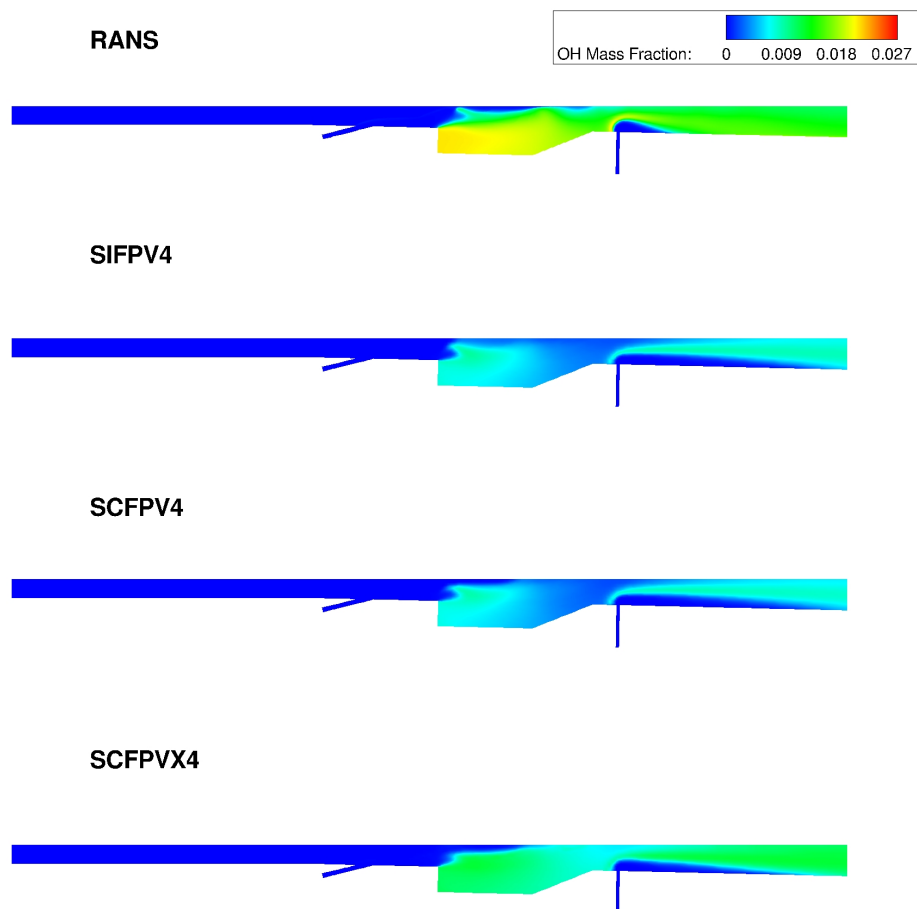


FIGURE 6.18: Contours of  $\tilde{Y}_{OH}$  obtained by solving Eqs. (6.1)-(6.6) using VULCAN-CFD for the HDCR combustor at the injector centerline nearest to the combustor centerline for cases SIFPV4, SCFPV4, and SCFPVX4 and compared to the baseline scram-mode RANS case S800A.

Line plot comparisons are included in Figs. 6.19-6.23, where results for  $\tilde{T}$ ,  $\tilde{Y}_{CO_2}$ ,  $\tilde{Y}_{CO}$ ,  $\tilde{Y}_{H_2O}$ , and  $\tilde{Y}_{OH}$  are shown at several planes through the primary and secondary injectors at the centerline plane intersecting the first set of injectors off the combustor centerline. As was also seen for the dual-mode results in the previous section, agreement with the baseline RANS data for all metrics was less than for the APFM-RANS analysis, as the *a priori* results were *best-case* comparisons. Generally, though, the *a posteriori* results agree reasonably well with the baseline RANS solution. All three FPV models show similar levels of agreement with the baseline RANS solution, while the CFPVX model does yield a moderate benefit for each comparison metric. This general benefit was also seen as an aggregate improvement over the IFPV and CFPV models in Fig. 6.13 for the centerline wall static pressure.

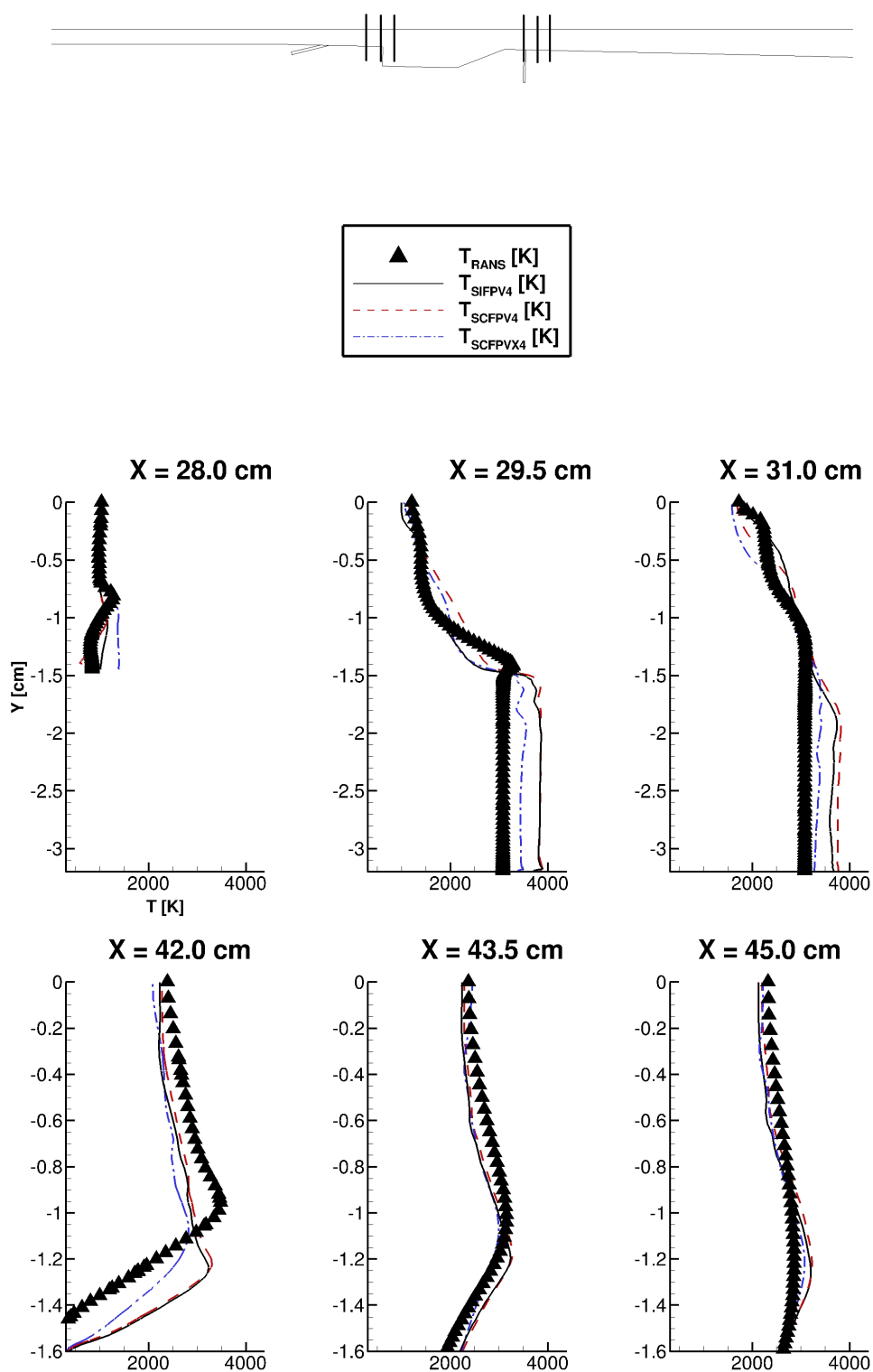


FIGURE 6.19: Line plots of  $Y$  [cm] versus  $\tilde{T}$  [K] obtained by solving Eqs. (6.1)-(6.6) using VULCAN-CFD for the HDCR combustor at several locations through the primary and secondary injector flames at the injector centerline nearest to the combustor centerline for cases SIFPV4, SCFPV4, and SCFPVX4 and compared to the baseline scram-mode RANS case S800A.

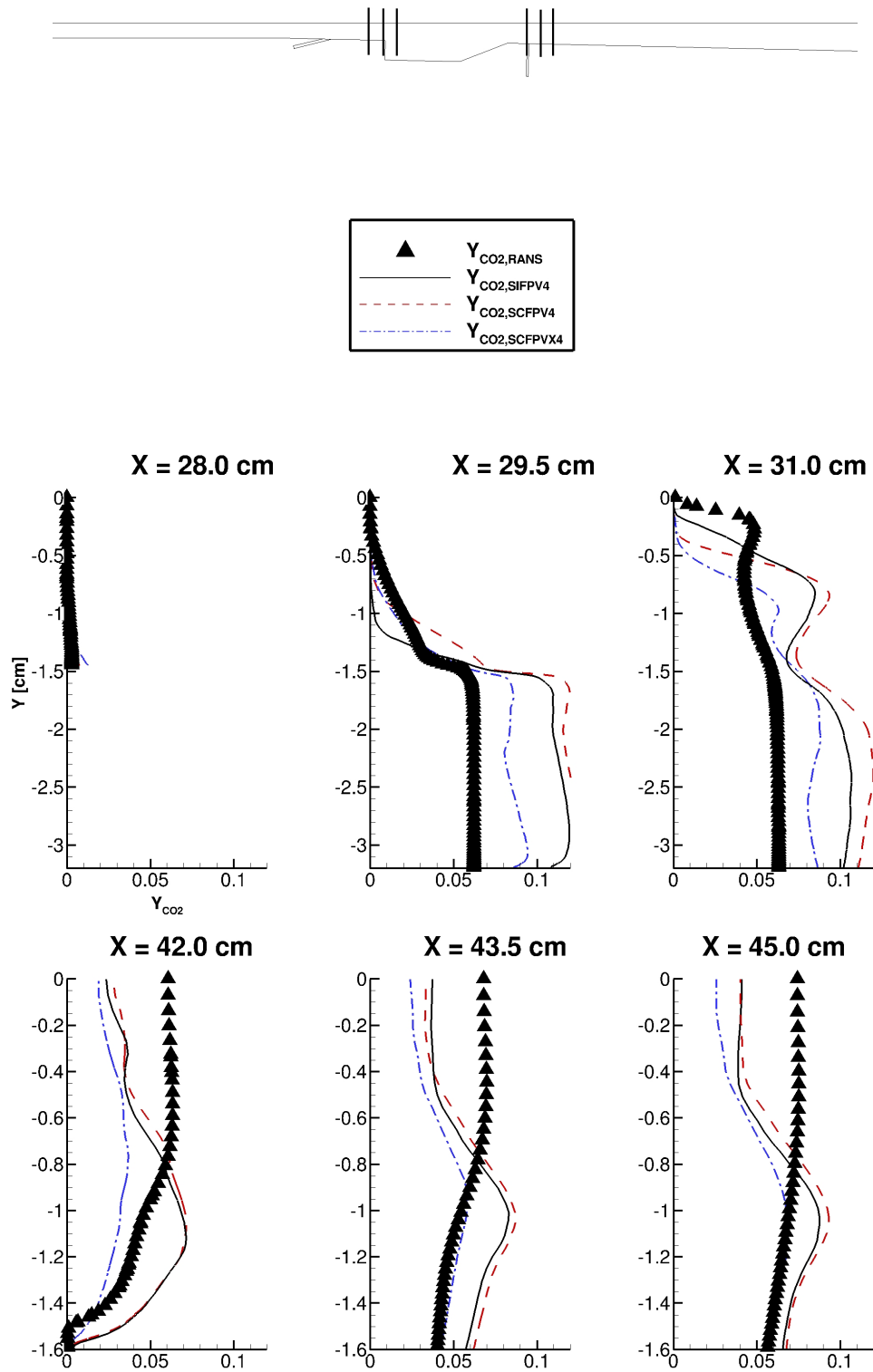


FIGURE 6.20: Line plots of  $Y$  [cm] versus  $\tilde{Y}_{CO_2}$  obtained by solving Eqs. (6.1)-(6.6) using VULCAN-CFD for the HDCR combustor at several locations through the primary and secondary injector flames at the injector centerline nearest to the combustor centerline for cases SIFPV4, SCFPV4, and SCFPVX4 and compared to the baseline scram-mode RANS case S800A.

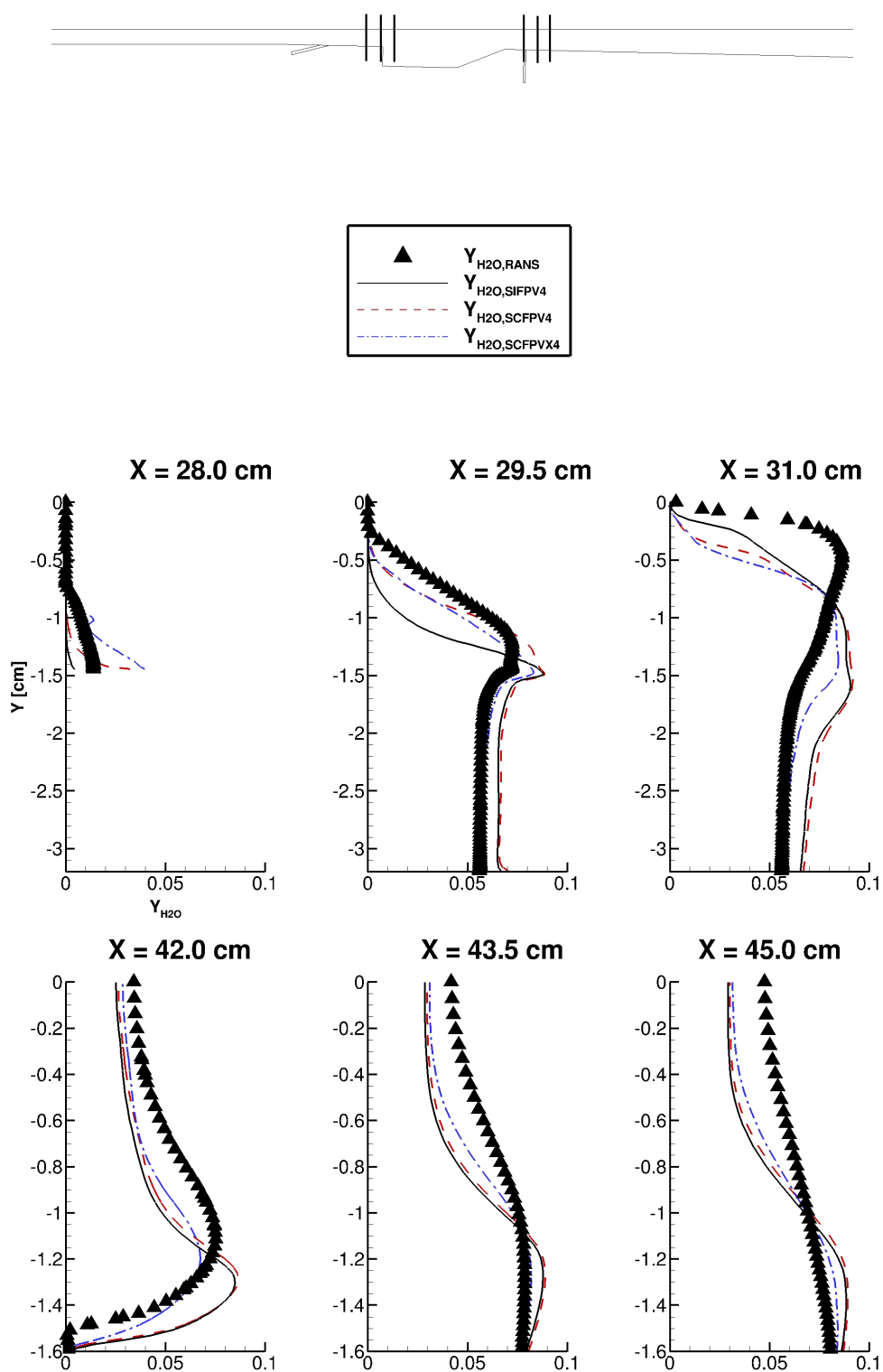


FIGURE 6.21: Line plots of  $Y$  [cm] versus  $\tilde{Y}_{H_2O}$  obtained by solving Eqs. (6.1)-(6.6) using VULCAN-CFD for the HDCR combustor at several locations through the primary and secondary injector flames at the injector centerline nearest to the combustor centerline for cases SIFPV4, SCFPV4, and SCFPVX4 and compared to the baseline scram-mode RANS case S800A.

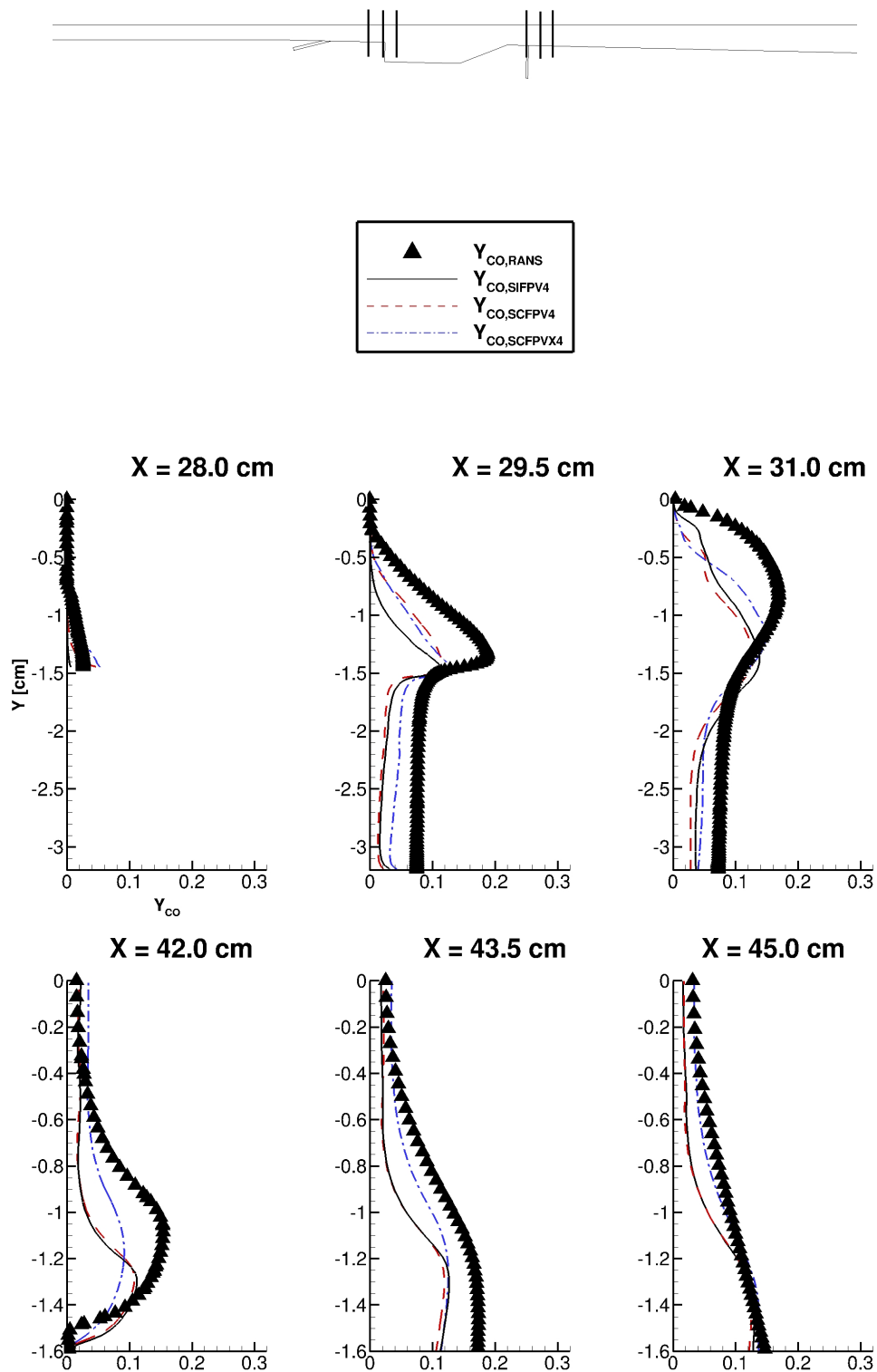


FIGURE 6.22: Line plots of  $Y$  [cm] versus  $\tilde{Y}_{CO}$  obtained by solving Eqs. (6.1)-(6.6) using VULCAN-CFD for the HDCR combustor at several locations through the primary and secondary injector frames at the injector centerline nearest to the combustor centerline for cases SIFPV4, SCFPV4, and SCFPVX4 and compared to the baseline scram-mode RANS case S800A.

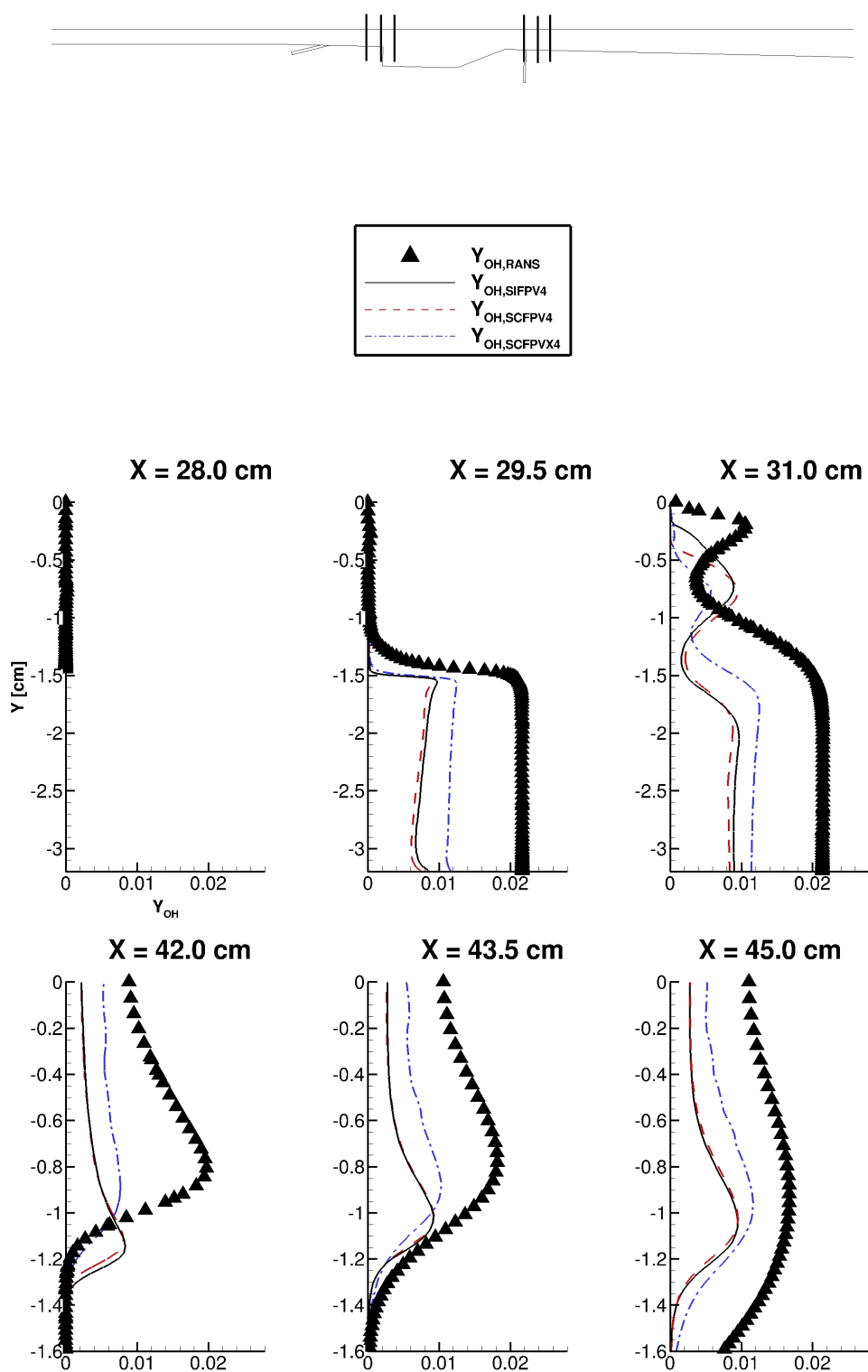


FIGURE 6.23: Line plots of  $Y$  [cm] versus  $\tilde{Y}_{OH}$  obtained by solving Eqs. (6.1)-(6.6) using VULCAN-CFD for the HDCR combustor at several locations through the primary and secondary injector frames at the injector centerline nearest to the combustor centerline for cases SIFPV4, SCFPV4, and SCFPVX4 and compared to the baseline scram-mode RANS case S800A.

### 6.2.3 FPV Model Performance

The primary objective for pursuing a compressible FPV model formulation is to realize the savings in computational cost offered by such an approach. Accordingly, significant work was focused on designing the current VULCAN-CFD FPV model implementation for minimal runtime. These efforts resulted in an efficient FPV model implementation, and a performance comparison to the baseline RANS simulations was performed to demonstrate the advantage of using the FPV approach.

TABLE 6.1: Summary of FPV model performance (IFPV, CFPV, and CFPVX) comparisons to both reacting and non-reacting baseline finite-rate RANS simulations (Reacting Baseline and Non-Reacting Baseline) for VULCAN-CFD. Cost is shown in units of seconds per iteration per CPU [s/it/CPU], and Cost Benefit is shown in percentage points [%] less than the Reacting Baseline case.

Model	Cost [s/it/CPU]	Normalized Cost	Cost Benefit [%]
IFPV	0.5915	0.1985	80.14
CFPV	0.5931	0.1990	80.09
CFPVX	0.5980	0.2006	79.93
Reacting Baseline	2.9798	1.0000	0.00
Non-Reacting Baseline	0.6115	0.2052	N/A

Runtime performance for each of the FPV models implemented in VULCAN-CFD was compared to both reacting and non-reacting baseline RANS simulations for which a finite-rate kinetics reaction mechanism was used with VULCAN-CFD to solve Eqs. (2.18)-(2.22). The only difference between the cases used for the current analysis was the choice of combustion model. The computational cost was first computed in units of seconds per iteration per central processor unit (CPU) for each case and subsequently normalized using the baseline RANS value. These results are summarized in Table 6.1. As expected, the FPV models were all significantly faster than the baseline, finite-rate kinetics approach. In fact, the IFPV, CFPV, and CFPVX models reduced the reacting baseline case runtimes by 80.14%, 80.09%, and 79.93%, respectively, and all three FPV models were also slightly less expensive than the non-reacting baseline RANS case. These figures also do not take into account any added benefit of using greater CFL numbers due to the reduced numerical stiffness of the governing equations, since the CFL was fixed for all cases shown here to 1.0. By using CFL numbers higher than 1.0, the performance advantage of the FPV models would be even greater than those shown in Table 6.1.



# Chapter 7

## Conclusion

The current chapter begins by summarizing the important findings for Chapters 3-6 in section 7.1. Next, a brief summary of the major research contributions and related publications resulting from this dissertation is included in section 7.2. Finally, a discussion of future research plans is included in section 7.3.

### 7.1 Concluding Discussion

After discussing the major problems facing the design and analysis of dual-mode scram-jet combustors in Chapter 1 and the physics required to understand how researchers can use FPV models with the Favre-averaged RANS equations to simulate these combustors in Chapter 2, several simulations of the HDCR were presented in Chapter 3 using VULCAN-CFD with a finite-rate kinetics chemical reaction mechanism for the combustion of a JP-7 fuel surrogate. Simulations were performed at flight Mach numbers of 5.84 and 8.00 corresponding to dual-mode and scram-mode combustor operation, respectively. Cases utilizing adiabatic and isothermal walls were performed, and the results were compared to experimental data for the centerline static wall pressure. All four cases agreed well with the experimental data; however, cases utilizing adiabatic walls yielded better agreement and were therefore chosen as the baseline solutions for further study.

Further confirmation that the combustor's operational mode was predicted required analyzing contours of Mach number and chemical heat release. The Mach number contours

indicated the leading combustion-induced shock resided upstream of the primary injectors for case D584A, while the same leading shock was found downstream of the primary injectors for case S800A. As a result, both the primary and secondary injector flames for case D584A resided in largely subsonic regions, whereas those for case S800A resided primarily in supersonic regions. These observations were consistent with the assumed operational modes of the combustor. Inspection of chemical heat release contours further demonstrated that the majority of heat release for case D584A took place in regions of subsonic flow, whereas heat release for case S800A was predominantly within regions of supersonic flow for the primary injector flames.

In Chapter 4, an *a priori* analysis of the HIFiRE ground experiment combustor was performed to determine the validity of fundamental flamelet-model assumptions. The baseline RANS solutions described in Chapter 3 were used to reconstruct the mixture fraction using Bilger's definition. The flames were then characterized using a flame-weighted Takeno index and combustion regime diagrams, which suggested that for dual-mode engine operation, combustion occurred at relatively high Damköhler numbers ( $Da \gg 1$ ) and in a non-premixed mode. These results also suggested that for scram-mode engine operation, the primary injector flames exhibited mixed combustion modes, in which significant heat release was found in regions of both non-premixed and premixed conditions and at both moderate ( $Da = 1$ ) and high ( $Da \gg 1$ ) Damköhler numbers. Detailed analysis of the premixed combustion data suggested thin and broken reaction zones, as evidenced by Borghi combustion regime diagrams. These findings suggested that a hybrid non-premixed/premixed flamelet-model may be necessary to adequately model the flames for scram-mode engine operation.

Compressibility and heat losses were found to have a significant effect on the combustion for the HDCR, thereby suggesting that a suitable flamelet manifold must be parameterized by pressure and enthalpy. An analysis of the temperature and pressure at theoretical flamelet boundaries further supported the necessity of including pressure and enthalpy as manifold dimensions and suggested that the standard practice of using a single set of flamelet boundary conditions is a gross approximation. PDFs of fuel and oxidizer temperature and pressure were shown for cases D584A and S800A, which were also used in the subsequent construction of flamelet manifolds in Chapters 5 and 6.

In an effort to assess state-of-the-art FPV model formulations for application to a dual-mode scramjet combustor, a detailed *a priori* study was performed in Chapter 5. The baseline, finite-rate, RANS solutions described in Chapters 3 and 4 served as the truth solution for model comparison. The APFM-RANS analysis method was developed and used for assessing the IFPV, CFPV, and CFPVX models. The data obtained using the APFM-RANS analysis method provided the best-case performance of the FPV models. IFPV and CFPV models were used along with several candidate progress variables, for which a trade study was performed. Based on comparisons of  $T$ ,  $Y_{CO_2}$ ,  $Y_{H_2O}$ ,  $Y_{CO}$ , and  $Y_{OH}$ , four definitions for  $C$  commonly used in the literature were compared, and the most representative  $C$  for the current application was found to be  $C = Y_{CO_2} + Y_{H_2O} + Y_{CO} + Y_{H_2}$ .

Using the APFM-RANS analysis method, models used for calculating  $\dot{\omega}_C$  were also assessed. Pressure and temperature scaling techniques, as well as using pressure as an independent parameterizing variable for the flamelet table, were tested. Results suggested that both pressure and temperature effects must be properly accounted for when calculating  $\dot{\omega}_C$ . The necessity of such an approach is due primarily to the strongly non-linear nature of the  $\dot{\omega}_C$  term and the significant difference between the local flowfield temperature computed using the transported total energy and the temperature native to the flamelet solutions.

In addition to  $\dot{\omega}_C$ , the energy interdiffusion term in the total energy transport equation was investigated, as this term serves as an additional coupling to the thermochemical state-space embedded in the flamelet table. Several methods of tabulating and calculating this term were presented and evaluated. Results suggested using a chain rule decomposition of  $\frac{\partial Y_\alpha}{\partial x_j}$  and tabulating only  $\frac{\partial Y_\alpha}{\partial Z}$  may be a reasonable model for calculating the energy interdiffusion term.

Finally, a CFPV model was proposed that included the effects of flamelet boundary conditions, which were shown previously to strongly vary across the combustor. The CFPVX model extended earlier CFPV model formulations by using  $T_{ox}$  to parameterize the flamelet solution space, in addition to using pressure as an explicit parameterizing variable. These developments led to a four-dimensional, compressible, FPV model. APFM-RANS analysis results using the CFPVX model were compared to both IFPV and CFPV model results. These comparisons demonstrated an improved agreement

with the baseline RANS solution for  $T$ ,  $Y_{CO_2}$ ,  $Y_{H_2O}$ ,  $Y_{CO}$ , and  $Y_{OH}$ . When corrected for temperature,  $\dot{\omega}_C$  also showed good agreement with the baseline RANS solution.

Following onto the extensive *a priori* analysis of the HDCR in Chapters 3 and 4 and the APFM-RANS assessment of FPV models in Chapter 5, a *posteriori* assessment of FPV modeling for the HDCR scramjet combustor was presented in Chapter 6. An FPV modeling capability was implemented in the VULCAN-CFD code, and a *posteriori* simulations of dual-mode cases DIFPV4, DCFPV4, and DCFPVX4 and scram-mode cases SIFPV4, SCFPV4, and SCFPVX4 were performed using VULCAN-CFD to validate the observations found in Chapter 5 using the APFM-RANS analysis method. Results for these cases were first compared using centerline wall static pressure to the baseline RANS solutions and experimental data. For every FPV model for both dual- and scram-mode operation, the location of the leading combustion-induced pressure rise was predicted well, and all three FPV models predicted the peak pressure rise reasonably well. These observations suggested that each FPV model provided a reasonable prediction for the aggregate chemical heat release due to combustion. For both dual- and scram-mode operation, the CFPVX model provided better general predictions of the pressure downstream of the leading shock. Results were also compared to the baseline RANS solutions using contour and line plots. For dual-mode operation, results for all FPV cases showed similar agreement with the baseline RANS solution, with results for the CFPVX model showing a slight improvement over the IFPV and CFPV models for several comparison metrics. For scram-mode operation, similar agreement with the baseline RANS solution was found, and the CFPVX model demonstrated even greater benefit as compared to the IFPV and CFPV models. These results suggested that while the IFPV, CFPV, and CFPVX models are approximately equally suitable for dual-mode application, scram-mode applications benefit moderately with the use of the CFPVX model. The differences between the *a posteriori* results and those of the earlier *a priori* study suggested additional improvement may be achieved.

Performance comparisons to the baseline finite-rate RANS approach demonstrated the computational efficiency realized by the FPV models implemented in VULCAN-CFD. The IFPV, CFPV, and CFPVX models required 80.14%, 80.09%, and 79.93% less computational resources, respectively, than the baseline reacting case, and all three FPV models required less computational resources than the baseline non-reacting case.

In summary, the primary objective of the current dissertation was to assess flamelet-based turbulent combustion modeling approaches for application to dual-mode scramjet combustors of engineering complexity. Through studying the HDCR combustor, several commonly-used FPV model formulations were shown to be improved by using a new model formulation including explicit pressure and oxidizer temperature effects. While *a priori* testing showed a modest advantage to using the CFPVX model, *a posteriori* testing suggested a somewhat smaller benefit; however, improved model corrections for  $\dot{\omega}_C$  and the energy interdiffusion term may hone the benefit of the CFPVX model in *a posteriori* applications. Further, the FPV models implemented in VULCAN-CFD were shown to run 5 times faster than using a comparable finite-rate reaction mechanism for the baseline RANS simulations, thereby confirming the considerable utility of such a modeling approach for flowfields typical of dual-mode scramjet combustors.

## 7.2 Contributions Summary

The research presented in the current dissertation yielded several important contributions to the understanding and modeling of dual-mode scramjet combustor flowfields using flamelet-based modeling approaches. These contributions included:

1. compressible (Favre-averaged) RANS simulations of the HDCR combustor at dual- and scram-mode operational test points including finite-rate effects;
2. *a priori* analysis and characterization of the HDCR combustor's flames and flow-field;
3. development and application of the APFM-RANS analysis method;
4. development of the CFPVX model for high-speed, compressible, turbulent combustion simulations;
5. implementation of FPV modeling in VULCAN-CFD; and
6. *a posteriori* assessment of compressible FPV models using VULCAN-CFD for the HDCR combustor.

Research performed by the author as a PhD candidate has been reported via numerous venues resulting in nine publications—one of which earning the 2015 AIAA Best

Paper Award by the High Speed Air Breathing Propulsion Technical Committee [74]. Additional publications as a result of the current dissertation research include several conference papers [89–91], as well as a student research conference paper [92], among numerous other presentations and seminars at NASA Langley Research Center, the National Institute of Aerospace, and Sandia National Laboratories. The author plans to submit Chapters 3–6 for journal publication following the defense of this work.

While not discussed as part of the current work, the author also had the privilege to collaborate on development and advancements of hybrid LES/RANS methods for supersonic cavities and cavity-based scramjet combustors during his PhD candidacy. These additional efforts resulted in several publications, including the 2012 AIAA Best Paper Award by the AIAA High Speed Air Breathing Propulsion Technical Committee [93], a peer-reviewed conference article [94], a conference paper [95], and a student research conference paper [96].

The author also served as the Principal Investigator (PI) for four supercomputing awards on the NASA Advanced Supercomputing (NAS) division Pleiades cluster [76] totaling more than 3.5 million processor hours. These awards were used to perform the computations presented in Chapters 3 and 6, as well as to support the aforementioned LES/RANS studies.

### 7.3 Future Research Plans

Several follow-on research plans based on the findings of this dissertation were identified and are discussed here. The primary effort moving forward is further development and application of the CFPVX model. The primary issues identified in Chapter 6 included the models used for  $\bar{\omega}_C$  and for the energy interdiffusion term,  $\beta$ . Alternative approaches identified for computing  $\bar{\omega}_C$  include computing it directly using a reaction mechanism with the FPV-mapped  $\tilde{Y}_\alpha$  and local  $\tilde{T}$  and  $\bar{p}$  or by including an additional correction scaling for composition similar in purpose to those for  $\tilde{T}$  and  $\bar{p}$ . Additionally, several alternative models for the energy interdiffusion term have been identified, including incorporating additional FPV dimension effects in the correction (e.g. including  $\frac{\partial \tilde{Y}_\alpha}{\partial \tilde{C}}$  contributions with the present  $\frac{\partial \tilde{Y}_\alpha}{\partial \tilde{Z}}$ ) or computing the  $\frac{\partial \tilde{Y}_\alpha}{\partial x_j}$  terms directly after updating the FPV-mapped  $\tilde{Y}_\alpha$ .

FPV models are implemented in VULCAN-CFD for both RANS and hybrid LES/RANS applications in their current form, and the author would foremost like to pursue hybrid LES/RANS applications using FPV modeling for the HDCR combustor. With these additional simulations, the unsteady nature of the dual-mode transition process may be studied, and the effects of turbulence on the flowfield and combustion will be illuminated through the natural-resolution of substantial turbulent structure. This additional resolved turbulence may help to yield additional understanding of the key phenomena governing the HDCR combustor's operation. The primary hurdle to this effort will be computational cost, as earlier attempts at hybrid LES/RANS of the HDCR combustor proved unaffordable using the same finite-rate chemical reaction mechanism employed for the baseline RANS calculations in Chapter 3. However, with the promising performance figures reported in section 6.2.3, the author anticipates the savings gained by using the FPV models will help to make these LES/RANS simulations feasible.

Additionally, the author would like to extend the FPV models presented here to include some form of turbulence-chemistry-interaction (TCI) modeling. Since, the observations presented in this work were made independently of any TCI modeling, it would be prudent to perform this same analysis with the inclusion of a TCI model. The present analysis omitted TCI effects in order to isolate modeling error to that of the FPV model implementation, specifically; however, numerous prior research efforts have suggested the importance of TCI modeling for turbulent combustion [97–102]. A first step at incorporating TCI effects will be through the use of a presumed-PDF approach [103], wherein which the mixture fraction variance will be included in the FPV modeling framework and an additional transport equation for mixture fraction variance will be added to VULCAN-CFD.



# Appendix A

## Documentation for VULCAN-CFD with FPV Modeling

While some details regarding the implementation of FPV modeling in VULCAN-CFD were included in Chapter 6, much was missing for the interested VULCAN-CFD user. Additional information pertaining to the specific implementation architecture for the VULCAN-CFD solver routines, as well as for the implementation in the pre- and post-processor routines, is presented here. Details regarding newly-available input deck flags are also presented. The user should consult the source code for any additional information not found here.

### A.1 Implementation Architecture

Implementation of FPV modeling in VULCAN-CFD required modifications to the pre-processor, solver, and post-processor routines, in addition to the development of flamelet table generation scripts and interface routines. The modifications to the VULCAN-CFD solver routines are described briefly in the current section, and details regarding modifications to the pre- and post-processor routines are described in subsequent sections. A sample input deck used to perform a VULCAN-CFD simulation using an FPV model is

included at the end of the current appendix in order to highlight new options available to the user.

The first major modification to VULCAN-CFD involved augmenting the solver equation controller array, *ngov*, which was modified internally so that memory allocations are made for  $\bar{\rho}$ ,  $\tilde{u}_i$ ,  $\tilde{E}$ ,  $\tilde{Z}$ , and  $\tilde{C}$  transport equations after finding a user-specified FPV model flag in the input deck. For this purpose, VULCAN-CFD's native reactive scalar equation form was used for  $\tilde{Z}$  and  $\tilde{C}$ , where the production rate of  $\tilde{Z}$  is identically zero and  $\bar{\omega}_C$  is retrieved using the *wdotfpv* subroutine in the *slvVFPV* Fortran 90 module. Advancing Eqs. (6.3) and (6.6) required  $\tilde{Y}_\alpha$  and  $\frac{\partial \tilde{Y}_\alpha}{\partial \tilde{Z}}$  terms for each chemical species,  $\alpha$ , comprising the reaction mechanism used to construct the flamelet table. These parameters were required to compute the energy interdiffusion term in Eq. (6.3), the mixture gas constant in Eq. (6.6), the Newton-Raphson iteration on Eq. (5.2) for computing  $\tilde{T}$ , and calculation of all mixture-based thermodynamic parameters.

Extensibility was of a primary focus for FPV model implementation. The philosophy taken, therefore, was one of maintaining as much of VULCAN-CFD's infrastructure intact as possible. One of the fundamental modifications required for VULCAN-CFD was the treatment of the thermodynamic terms. Since, thermodynamic quantities like enthalpy, internal energy, entropy, specific heat at constant pressure, and specific heat at constant volume are all both composition and temperature dependent, composition data is required at numerous locations throughout the code. In its native form, VULCAN-CFD stores all transported variables globally in the  $\vec{q}$  vector structure, including all  $\tilde{Y}_\alpha$ . Since  $\vec{q}$  is globally available, composition-dependent thermodynamic calculations are easy to perform anywhere within the source using the user-supplied database of NASA polynomial coefficients and the local static temperature. However, by modifying VULCAN-CFD to solve Eqs. (6.4)-(6.5) in place of Eq. (2.21),  $\vec{q}$  no longer contains  $\tilde{Y}_\alpha$ . Instead,  $\vec{q}$  contains  $\tilde{Z}$  and  $\tilde{C}$  in their place, for which composition is implicitly mapped using the FPV model. The most direct solution to this problem would have been to query the FPV table for every calculation requiring composition data; however, this would have resulted in an enormous number of redundant table queries, which would have counteracted any efficiencies gained by using the FPV model over more expensive approaches.

Instead, the current version of VULCAN-CFD was modified so that when an FPV model

is invoked, global memory space is allocated for  $\tilde{Y}_\alpha$  separate from  $\vec{q}$ . Specifically, a global vector,  $\vec{q}_{smf}$ , is preallocated and used to store the  $\tilde{Y}_\alpha$  retrieved from the flamelet table using  $\phi_{FPV}$  as computed by the solver at each integration step. By allocating  $\vec{q}_{smf}$  globally, VULCAN-CFD may utilize the same thermodynamics subroutines and database infrastructure as before with only minor modifications regardless of the chosen combustion model. The total increased cost of this approach is marginal since  $\vec{q}_{smf}$  only needs to be updated once at each solver step. Since  $\vec{q}_{smf}$  is passed in a similar manner as  $\vec{q}$  through the call structure, this new approach leverages completely the existing Message Passing Interface (MPI) implementation.

In order to use an FPV model with VULCAN-CFD, the solver (and pre- and post-processors) must find two additional files in the working directory: one file containing input data used by VULCAN-CFD to interpret the flamelet table; and one file containing the raw flamelet table data. The FPV model pre-processing package, *pyVFPV*, is used in conjunction with FlameMaster V3.3 to build these files, and once they are constructed for a given table, the input file and table file may be used with any future VULCAN-CFD simulation simply by invoking the FPV chemistry model and placing the two files in the working directory. Compiling the *slvVFPV* Fortran 90 module with VULCAN-CFD provides all the FPV table processing and interfacing subroutines required for use, including a subroutine to construct a uniformly-spaced flamelet table, binomial search routines, index-based search routines, table data retrieval processing subroutines, and others. VULCAN-CFD's Makefile, scripting system, and utilities were modified to accommodate compilation with this additional module.

Since VULCAN-CFD is such an extensive code, at nearly 400,000 lines of source code, the implementation of FPV models was necessarily limited for the current work to a subset of available boundary conditions and numerical routines. Supported solver routines include the Runge-Kutta integration routines with both local and explicit time-stepping while employing the low diffusion flux splitting scheme (LDFSS) [60] with a MUSCL flux reconstruction. While this solution architecture is robust, extension of the FPV modeling to additional integration and flux splitting schemes is ongoing. Work toward implementing FPV modeling for use with the DAF routines is included in Appendix B, where the flux Jacobian transformation matrices for the system of equations shown in Eqs. (6.1)-(6.5) are derived. These matrices are necessary to derive the eigenvector matrices for the flux Jacobian, which are required by the DAF formulation currently

available in VULCAN-CFD. Additionally, FPV modeling is currently supported by all of VULCAN-CFD's turbulence models and transport property models, as these are largely independent of the chosen combustion model.

## A.2 FPV Model Configuration

In order to use FPV models with VULCAN-CFD, the user must first use *pyVFPV* and FlameMaster V3.3 to construct the *ft\_inp.csv* and *ft\_vulc.csv* files containing VULCAN-CFD-specific flamelet table interface and manifold data, respectively. These two files are the only two external data files necessary for application of an FPV model using VULCAN-CFD. In fact, the current implementation uses data from these files to determine the appropriate FPV model (IFPV, CFPV, vs CFPVX and respective  $\bar{\omega}_C$  correction), without additional user specification, as well, based on the number of pressure levels embedded in the manifold.

Instructing VULCAN-CFD to use an FPV model requires setting the CHEMISTRY MODEL flag to 5.0. Additionally, the user must set the NO. OF CHEMICAL SPECIES flag to the number of transported mixture fractions,  $\tilde{Z}$ , and progress variables,  $\tilde{C}$ . Since a single  $\tilde{Z}$  and  $\tilde{C}$  are supported by the current version, this input should be set to 2.0. Appropriate reference values should be provided (for example, 0.0 and 0.1), and the NO. OF CHEMICAL REACTIONS flag must be set to 0.0. The user must also set the NO. OF MAPPED SPECIES flag to the number of unique species tabulated in the flamelet table; this input is only required for FPV model use. On the line following this designation, the user must specify the location of a VULCAN-CFD compatible thermodynamics database, followed by reference values for each of the mapped species. VULCAN-CFD uses this data to allocate memory for  $\vec{q}_{smf}$  and for thermodynamic calculations. The *mapped species* are those to which the transported tracking scalars *map* within the provided flamelet table.

If the user wishes to use an FPV model for mixing calculations, the BURNING flag can be set to 0.0, which limits the solver to retrieving solutions only from the mixing solutions within the supplied flamelet table (where  $\tilde{C} = 0.0$ ). By default, the BURNING flag is set to 1.0, which allows VULCAN-CFD to retrieve solutions from the entirety of the tabulated solutions. The user must also set the  $a_p$  and  $T_a$  model constants

required for the pressure- and temperature-scaling correction models for  $\bar{\omega}_C$  described in Chapter 5 by using the MODEL CONSTANT AP and MODEL CONSTANT TA flags, respectively. The input value for MODEL CONSTANT TA must have units of Kelvin, and the MODEL CONSTANT AP parameter is nondimensional.

FPV modeling was implemented and used for boundary condition routines listed in Table A.1. While there likely exists other native boundary condition models for which the FPV implementation will work without further development, the boundary conditions cited in Table A.1 have been specifically adapted for the current work.

TABLE A.1: Summary of VULCAN-CFD boundary conditions for which FPV models are supported.

Keyword	Description
AWALL	No slip adiabatic wall
AWALLM	No slip adiabatic wall using wall functions
EXTRAP	Supersonic outflow extrapolation (zeroth order)
FIXED	Supersonic inflow with fixed conditions
IWALL	No slip isothermal wall
IWALLM	Isothermal wall using wall functions
SUBMDOTI	Subsonic inflow with mass flux held constant

### A.3 Solution Post-Processing

The user has several options for post-processing the flowfield using the PLOT FUNCTION command. Options implemented for use specifically with FPV models include MAPPED SMF and MAPPED PROD flags, which signal the output of the mapped species mass fractions,  $\tilde{Y}_\alpha$ , and production rates,  $\bar{\omega}_\alpha$ , respectively. The user can choose to output these parameters for any subset of the mapped chemical species by listing the requested species names on the line following these flags. This format is similar to VULCAN-CFD's native MASS FRACTION and PRODUCTION RATE plotting functions, which can also be used for FPV model applications to output  $\tilde{Z}$  and  $\tilde{C}$  or  $\bar{\omega}_Z$  and  $\bar{\omega}_C$ , respectively. Note that by definition  $\bar{\omega}_Z$  is identically zero.

The user can also choose to output VULCAN-CFD's native HEAT RELEASE plotting function. Note however that when an FPV model is used, the HEAT RELEASE calculation uses mapped  $\bar{\omega}_\alpha$  from the flamelet table with Eq. (A.1). Currently, no  $\bar{p}$  or  $\tilde{T}$

corrections are applied to these terms, so the results should be used judiciously, based on the discussion in Chapter 2 regarding the necessity of  $\bar{\omega}_C$  correction models.

$$\dot{Q} \equiv \sum_{\alpha} \Delta H_{f,\alpha}^o \bar{\omega}_{\alpha} \quad (\text{A.1})$$

## A.4 Example Input Deck

An example VULCAN-CFD input deck invoking an FPV model and using the model-specific configuration flags described in the previous two sections is included here. The boundary condition and cut condition configuration lines have been clipped here for clarity.

```

$*****$
$*****Vulcan Input File*****$
$*****$
$----- Parallel processing control data -----$
PROCESSORS          208.0
MESSAGE MODE        1.0 (message passing strategy: 0=std, 1=buf)
$----- Grid file data -----$
THREED              (threed, axisym, twod)
GRID FORMAT         4.0 (1=sb fmt, 2=sb unf, 3=mb fmt, 4=mb unf)
GRID                0.0 (0=plot3d->3-D or plot2d->2-D/axi, 1=plot3d->all)
    vulcan_split.grd
GRID SCALING FACTOR 1.0 (multiplication factor to convert grid to meters)
$----- Output file data -----$
RESTART IN          (input restart file name to follow)
    ./RESTART_split/restart
RESTART OUT         2000.0 (output restart file name to follow)
    ./RESTART_split/restart
WARNING MESSAGES    3.0 (0=off, 1=wf warn, 2=temp warn, 3=real warn, 4=all)
$----- Post-Processing control -----$
PLOT ON             4.0 (1=sb fmt, 2=sb unf, 3=mb fmt, 4=mb unf)
32 BIT BINARY       (write plot files as 32 or 64 bit binary)
PLOT NODES          (create PLOT3D files with data averaged to nodes)
PLOT FUNCTION       21.0 (create PLOT3D function file with these variables)
    DENSITY
    VELOCITY
    PRESSURE
    TEMPERATURE
    MACH NO.

```

```

TOTAL TEMP.
TOTAL PRESS.
GAMMA
TOTAL DENS.
TOTAL ENTH.
ENTHALPY
TURB. K.E.
OMEGA
LAM. VIS.
EDDY VIS. RATIO
MASS FRACTION
2
Z CPG
PRODUCTION RATE
2
Z CPG
HEAT RELEASE
MAPPED SMF
22
H2 H O O2 OH H2O HO2 H2O2 CH3 CH4 CO CO2 CH2O C2H2 C2H4 C2H6
HCCO CH2CO CH3CHO aC3H5 C3H6 N2
MAPPED PROD
22
H2 H O O2 OH H2O HO2 H2O2 CH3 CH4 CO CO2 CH2O C2H2 C2H4 C2H6
HCCO CH2CO CH3CHO aC3H5 C3H6 N2
WALL DISTANCE
$----- Equation set -----$
GLOBAL VISCOUS          (solve N-S equations using global algorithn)
$----- Thermodynamic model data -----$
GAS/THERMO MODEL      1.0 (0=calorically perfect, 1=thermally perfect)
$----- Chemistry model data -----$
CHEMISTRY MODEL      5.0 (0=frozen, 1=finite rate, 3=CARM, 4=CARM w/ISAT, 5=FPV)
BURNING                1.0
MODEL CONSTANT AP     2.0
MODEL CONSTANT TA     10000.0
EXPLICIT CHEMISTRY    0.0 (1=analytic jacobian, 2=numerical jacobian)
$----- Transport model data -----$
VISCOSITY MODEL       1.0 (n/a=power law, 1=Sutherland law)
CONDUCTIVITY MODEL    1.0 (0=Prandtl no., 1=Wassilej law)
SPEC. DIFF. MODEL     0.0 (0=Fickian law)
UNIV. GAS CONST.     8314.34
$----- Chemical species information -----$
NO. OF CHEMICAL SPECIES  2.0
Z CPG

```

```

0.0 0.001
NO. OF CHEMICAL REACTIONS 0.0
NO. OF MAPPED SPECIES 22.0
  ../gas_mod.Lewis_2_ckl_fr
H2 H O O2 OH H2O HO2 H2O2 CH3 CH4 CO C02 CH2O C2H2 C2H4 C2H6
HCCO CH2CO CH3CHO aC3H5 C3H6 N2
$----- Reference Condition Data -----$
ANGLE REF. FRAME 0.0 (0=alpha in xy plane, 1=alpha in xz plane)
ALPHA 0.0 (angle of attack measured in degrees)
NONDIM 2.0 (1=static conditions, 2=total conditions)
MACH NO. 2.51
TOTAL PRESS. 1480304.39
TOTAL TEMP. 1700.04
LAM. PRANDTL NO. 0.72
LAM. SCHMIDT NO. 0.22
TURB. PRANDTL NO. 0.89
TURB. SCHMIDT NO. 0.325
$----- Turbulence Model Data -----$
TURB. MODEL (laminar, spalart, menter, menter-sst, k-eps, k-w, low Re k-w)
  MENTER
TURB. INTENSITY 1.0e-02
TURB. VISC. RATIO 1.0e-01
BOUSSINESQ REY. STRESS 0.0
DURBIN REALIZABILITY 1.0
$----- Boundary and Cut Control -----$
BLOCKS 603.0 (no. of blocks)
FLOWBCS 769.0 (no. of boundary conditions to be specified)
  BCGROUPS 10.0 (no. of boundary condition groups)
  BCOBJECTS 0.0 (no. of boundary condition objects)
CUTBCS 1439.0 (no. of C(0) conectivity conditions to be specified)
PATCHBCS 0.0 (no. of non-C(0) conectivity conditions to be specified)
BLOCK CONFIG. 1.0 (no. of lines of block configurations input)
BLK I-VISC J-VISC K-VISC (N, T, or F) TURB REAC PLOT REGION
  0 F F F Y Y Y 1
$***** Region 1 Control *****$
SOLVER LDFSS KAPPA LIMITER LIMITER COEFFICIENT ENT FIX (U) ENT FIX (U+a)
  E/A 3 3 3 2 2 2 2.000 2.000 2.000 0.0 0.0 0.0 0.0 0.0 0.0
FMGLVLS NITSC NITSM NITSF 1ST-ORDER LEVELS REL RES ABS RES
  1 04000 000000 -6.0 -8.0
M.G. CYCLE COARSE GRIDS DQ SMOOTH DQ COEFF DAMP MEAN DAMP TURB
  I 0 0.25 +0.25 0.5 0.25
TURB CONVECTION DT RATIO NON EQUIL POINT IMP COMP MODEL CG WALL BC
  2ND 1.0 25.0 Y N WMF
SCHEME TIME-STEP IT-STATS MIN-CFL VAR-CFL CFL-VALUES VISC-DT IMP-BC REG-REST

```

```

R-K   LOCAL   10   0.1   N     3     Y     N     Y
  1  4000  8000
0.1  1.0   2.0

!***** End of general control data *****!
GROUP  NAME      TYPE      OPTION
      inflow    SUBMDOTI  PHYSICAL
Z      CPG   Rho    Uvel  Vvel  Wvel  T_tot  Tint  Murat
0.0  0.0  2.709  50.0  0.0  0.0  1700.0  0.01  0.001
      symmetry  SYMM      PHYSICAL
      outflow   EXTRAP   PHYSICAL
      noz_swall AWALLM   PHYSICAL
      noz_wall  AWALLM   PHYSICAL
      iso_wall  AWALLM   PHYSICAL
      comb_wall AWALLM   PHYSICAL
      inj_wall  AWALLM   PHYSICAL
      fuel1     SUBMDOTI  PHYSICAL
Z      CPG   Rho    Uvel  Vvel  Wvel  Temp  Tint  Murat
1.0  0.0  0.62297  0.0  300.0  0.0  299.5  0.01  0.10
      fuel2     SUBMDOTI  PHYSICAL
Z      CPG   Rho    Uvel  Vvel  Wvel  Temp  Tint  Murat
1.0  0.0  3.75809  0.0  300.0  0.0  299.7  0.01  0.10
BC  NAME  BLK  FACE  PLACE  IND1  BEG  END  IND2  BEG  END  IN-ORD
inflow  1  I  MIN  J  MIN  MAX  K  MIN  MAX  0
noz_wall 1  J  MIN  K  MIN  MAX  I  MIN  MAX  0
symmetry 1  K  MIN  I  MIN  MAX  J  MIN  MAX  0
inflow  2  I  MIN  J  MIN  MAX  K  MIN  MAX  0
:
CUT-INT 600  J  MAX  K  MIN  MAX  I  MIN  MAX  0
CUT-INT 601  J  MIN  K  MIN  MAX  I  MIN  MAX  0
CUT-INT 602  J  MAX  K  MIN  MAX  I  MIN  MAX  0
CUT-INT 603  J  MIN  K  MIN  MAX  I  MIN  MAX  0

```



## Appendix B

# Flux Jacobian Transformation Matrices for FPV Models

Implementation of a compressible FPV model in the VULCAN-CFD code for use with the DAF integration option requires fundamental modifications to the DAF subroutines. The existing DAF implementation supports the calculation of convective fluxes based on the assumption that the governing transport equations include reactive scalar transport equations for each of the species mass fractions comprising the assumed thermally-perfect mixture. This assumption fails, however, in the case of an FPV model as transport equations for the constituent species are no longer solved for explicitly. The first step in implementing FPV models for use with VULCAN-CFD's DAF option is deriving the relevant diagonalized flux Jacobian transformation matrices that may then be used to derive the flux Jacobian eigenvector matrices. This appendix presents the derivation of the transformation matrices required for subsequent derivation of eigenvector matrices required for low-level DAF implementation.

The first section presents the general governing equations for a mixture of thermally-perfect gases subject to an FPV model, and the second section presents the derivation of the FPV-modeled diagonalized flux Jacobian transformation matrices necessary for the implementation of FPV models for DAF in VULCAN-CFD.

## B.1 General System of Governing Equations

The equations governing the transport of mass, momentum, energy, and chemical species derived in Chapter 2 may be written in conservative form, as shown below in Eq. (B.1),

$$\frac{\partial \vec{q}}{\partial t} + \frac{\partial \vec{f}_I}{\partial x} + \frac{\partial \vec{g}_I}{\partial y} + \frac{\partial \vec{h}_I}{\partial z} = \vec{S} \quad (\text{B.1})$$

where  $\vec{q}$  is the vector of conserved variables, and  $\vec{f}_I$ ,  $\vec{g}_I$ , and  $\vec{h}_I$  are the fluxes in the  $x$ ,  $y$ , and  $z$  coordinate directions, respectively.  $\vec{S}$  is a source vector. Each of the flux vectors is comprised of inviscid and viscous contributions, and only the inviscid components are considered here, as the viscous components and source terms are independent of the convective fluxes. The existing vector of conserved variables solved by VULCAN-CFD is shown in Eq. (B.2), without consideration of turbulence model equations, and the inviscid components of  $\vec{f}_I$ ,  $\vec{g}_I$ , and  $\vec{h}_I$  are shown in Eqs. (B.3)-(B.5).

$$\vec{q} = \begin{bmatrix} \rho \\ \rho u \\ \rho v \\ \rho w \\ \rho E \\ \rho Y_1 \\ \vdots \\ \rho Y_\alpha \\ \vdots \\ \rho Y_N \end{bmatrix} \quad (\text{B.2})$$

$$\vec{f}_I = \begin{bmatrix} \rho u \\ \rho u^2 + P \\ \rho uv \\ \rho uw \\ \rho uH \\ \rho uY_1 \\ \vdots \\ \rho uY_\alpha \\ \vdots \\ \rho uY_N \end{bmatrix} \quad (\text{B.3})$$

$$\vec{g}_I = \begin{bmatrix} \rho v \\ \rho uv \\ \rho \rho v^2 + P \\ \rho \rho uv \\ \rho u H \\ \rho u Y_1 \\ \vdots \\ \rho u Y_\alpha \\ \vdots \\ \rho u Y_N \end{bmatrix} \quad (\text{B.4})$$

$$\vec{h}_I = \begin{bmatrix} \rho w \\ \rho ww \\ \rho vw \\ \rho w^2 + P \\ \rho u H \\ \rho u Y_1 \\ \vdots \\ \rho u Y_\alpha \\ \vdots \\ \rho u Y_N \end{bmatrix} \quad (\text{B.5})$$

As is typically done, this system of equations is transformed to a generalized coordinate system via Eq. (B.6), and the generalized system of equations is written as shown in Eq. (B.7).

$$\begin{aligned} \tau &= t \\ \xi &= \xi(x, y, z) \\ \eta &= \eta(x, y, z) \\ \zeta &= \zeta(x, y, z) \end{aligned} \quad (\text{B.6})$$

$$\frac{\partial \vec{Q}}{\partial \tau} + \frac{\partial \vec{F}_I}{\partial \xi} + \frac{\partial \vec{G}_I}{\partial \eta} + \frac{\partial \vec{H}_I}{\partial \zeta} = 0 \quad (\text{B.7})$$

The new state and flux vectors are then written using the Jacobian,  $J$ , according to Eqs. (B.8)-(B.11).

$$\vec{Q} = \frac{\vec{q}}{J} \quad (\text{B.8})$$

$$\vec{F}_I = \frac{\xi_x}{J} \vec{f}_I + \frac{\xi_y}{J} \vec{g}_I + \frac{\xi_z}{J} \vec{h}_I \quad (\text{B.9})$$

$$\vec{G}_I = \frac{\eta_x}{J} \vec{f}_I + \frac{\eta_y}{J} \vec{g}_I + \frac{\eta_z}{J} \vec{h}_I \quad (\text{B.10})$$

$$\vec{H}_I = \frac{\zeta_x}{J} \vec{f}_I + \frac{\zeta_y}{J} \vec{g}_I + \frac{\zeta_z}{J} \vec{h}_I \quad (\text{B.11})$$

These flux vectors can be written more generally, as shown in Eq. (B.12),

$$\vec{K} = \frac{k_x}{J} \vec{f}_I + \frac{k_y}{J} \vec{g}_I + \frac{k_z}{J} \vec{h}_I \quad (\text{B.12})$$

where  $k$  takes on one of  $\xi$ ,  $\eta$ , or  $\zeta$  for  $\vec{F}_I$ ,  $\vec{G}_I$ , or  $\vec{H}_I$ , respectively.

These equations may be written in a non-conservative form, as shown in Eq. (B.13). In this construct, matrices  $A$ ,  $B$ , and  $C$  are referred to as the flux Jacobians for the  $\xi$ ,  $\eta$ , and  $\zeta$  directions, respectively, and are defined according to Eqs. (B.14)-(B.16).

$$\frac{\partial \vec{Q}}{\partial \tau} + A \frac{\partial \vec{Q}}{\partial \xi} + B \frac{\partial \vec{Q}}{\partial \eta} + C \frac{\partial \vec{Q}}{\partial \zeta} = 0 \quad (\text{B.13})$$

$$A = \frac{\partial \vec{F}_I}{\partial \vec{Q}} \quad (\text{B.14})$$

$$B = \frac{\partial \vec{G}_I}{\partial \vec{Q}} \quad (\text{B.15})$$

$$C = \frac{\partial \vec{H}_I}{\partial \vec{Q}} \quad (\text{B.16})$$

The flux Jacobians may also be written in a more generalized form, as shown below in Eq. (B.17).

$$D = \frac{\partial \vec{K}}{\partial \vec{Q}} \quad (\text{B.17})$$

Handling this matrix can be rather cumbersome, and as is done in the DAF algorithm, it is diagonalized using similarity as

$$D = M d M^{-1} \quad (\text{B.18})$$

such that we can write

$$d = M^{-1} d M \quad (\text{B.19})$$

where

$$M = \frac{\partial \vec{q}}{\partial \vec{q}^*} \quad (\text{B.20})$$

and  $\vec{q}^*$  describes the system of primitive variables, which are shown in Eq. (B.21).

$$\vec{q}^* = \begin{bmatrix} \rho \\ u \\ v \\ w \\ P \\ Y_1 \\ \vdots \\ Y_\alpha \\ \vdots \\ Y_N \end{bmatrix} \quad (\text{B.21})$$

In this context,  $M$  and  $M^{-1}$  represent transformation matrices, which are required for the DAF algorithm. These matrices are derived in explicit form for the CFPV modeling framework in the following section.

## B.2 FPV Model Transformation Matrices

Since the species mass fractions,  $Y_\alpha$ , are not explicitly solved for within the FPV framework, the vector of conserved variables requiring solution by VULCAN-CFD must be modified to include the transported FPV variables and is shown in Eq. (B.22). The primitive variables vector is shown in Eq. (B.23).

$$\vec{q} = \begin{bmatrix} \rho \\ \rho u \\ \rho v \\ \rho w \\ \rho E \\ \rho Z \\ \rho C \end{bmatrix} \quad (\text{B.22})$$



$\vec{q}$  vector may be rewritten using the elements of  $\vec{q}^*$  according to Eq. (B.26) below.

$$\vec{q} = \begin{bmatrix} \rho \\ \rho u \\ \rho v \\ \rho w \\ \rho E \\ \rho Z \\ \rho C \end{bmatrix} = \begin{bmatrix} q_1^* \\ q_1^* q_2^* \\ q_1^* q_3^* \\ q_1^* q_4^* \\ q_1^* \left[ e + \frac{1}{2} (q_2^{*2} + q_3^{*2} + q_4^{*2}) \right] \\ q_1^* q_6^* \\ q_1^* q_7^* \end{bmatrix} \quad (\text{B.26})$$

We can then take each of the derivatives required according to Eq. (B.20). Proceeding element-by-element, the first derivatives are those corresponding to  $\vec{q}(1)$  and are shown below in Eqs. (B.27)-(B.33).

$$\frac{\partial q_1}{\partial q_1^*} = 1 \quad (\text{B.27})$$

$$\frac{\partial q_1}{\partial q_2^*} = 0 \quad (\text{B.28})$$

$$\frac{\partial q_1}{\partial q_3^*} = 0 \quad (\text{B.29})$$

$$\frac{\partial q_1}{\partial q_4^*} = 0 \quad (\text{B.30})$$

$$\frac{\partial q_1}{\partial q_5^*} = 0 \quad (\text{B.31})$$

$$\frac{\partial q_1}{\partial q_6^*} = 0 \quad (\text{B.32})$$

$$\frac{\partial q_1}{\partial q_7^*} = 0 \quad (\text{B.33})$$

The derivatives corresponding to  $\vec{q}(2)$  are shown below in Eqs. (B.34)-(B.40).

$$\frac{\partial q_2}{\partial q_1^*} = u \quad (\text{B.34})$$

$$\frac{\partial q_2}{\partial q_2^*} = \rho \quad (\text{B.35})$$

$$\frac{\partial q_2}{\partial q_3^*} = 0 \quad (\text{B.36})$$

$$\frac{\partial q_2}{\partial q_4^*} = 0 \quad (\text{B.37})$$

$$\frac{\partial q_2}{\partial q_5^*} = 0 \quad (\text{B.38})$$

$$\frac{\partial q_2}{\partial q_6^*} = 0 \quad (\text{B.39})$$

$$\frac{\partial q_2}{\partial q_7^*} = 0 \quad (\text{B.40})$$

The derivatives corresponding to  $\vec{q}(3)$  are shown below in Eqs. (B.41)-(B.47).

$$\frac{\partial q_3}{\partial q_1^*} = v \quad (\text{B.41})$$

$$\frac{\partial q_3}{\partial q_2^*} = 0 \quad (\text{B.42})$$

$$\frac{\partial q_3}{\partial q_3^*} = \rho \quad (\text{B.43})$$

$$\frac{\partial q_3}{\partial q_4^*} = 0 \quad (\text{B.44})$$

$$\frac{\partial q_3}{\partial q_5^*} = 0 \quad (\text{B.45})$$

$$\frac{\partial q_3}{\partial q_6^*} = 0 \quad (\text{B.46})$$

$$\frac{\partial q_3}{\partial q_7^*} = 0 \quad (\text{B.47})$$

The derivatives corresponding to  $\vec{q}(4)$  are shown below in Eqs. (B.48)-(B.54).

$$\frac{\partial q_4}{\partial q_1^*} = w \quad (\text{B.48})$$

$$\frac{\partial q_4}{\partial q_2^*} = 0 \quad (\text{B.49})$$

$$\frac{\partial q_4}{\partial q_3^*} = 0 \quad (\text{B.50})$$

$$\frac{\partial q_4}{\partial q_4^*} = \rho \quad (\text{B.51})$$

$$\frac{\partial q_4}{\partial q_5^*} = 0 \quad (\text{B.52})$$

$$\frac{\partial q_4}{\partial q_6^*} = 0 \quad (\text{B.53})$$

$$\frac{\partial q_4}{\partial q_7^*} = 0 \quad (\text{B.54})$$

The derivatives corresponding to  $\vec{q}(5)$  are shown below in Eqs. (B.55)-(B.61).

$$\frac{\partial q_5}{\partial q_1^*} = E + \rho \frac{\partial E}{\partial \rho} = E + \rho \frac{\partial e}{\partial \rho} \quad (\text{B.55})$$

$$\frac{\partial q_5}{\partial q_2^*} = \rho u \quad (\text{B.56})$$

$$\frac{\partial q_5}{\partial q_3^*} = \rho v \quad (\text{B.57})$$

$$\frac{\partial q_5}{\partial q_4^*} = \rho w \quad (\text{B.58})$$

$$\frac{\partial q_5}{\partial q_5^*} = E \frac{\partial \rho}{\partial P} + \rho \frac{\partial E}{\partial P} = \rho \frac{\partial e}{\partial P} \quad (\text{B.59})$$

$$\frac{\partial q_5}{\partial q_6^*} = E \frac{\partial \rho}{\partial Z} + \rho \frac{\partial E}{\partial Z} = \rho \frac{\partial e}{\partial Z} \quad (\text{B.60})$$

$$\frac{\partial q_5}{\partial q_7^*} = E \frac{\partial \rho}{\partial C} + \rho \frac{\partial E}{\partial C} = \rho \frac{\partial e}{\partial C} \quad (\text{B.61})$$

The derivatives corresponding to  $\vec{q}(6)$  are shown below in Eqs. (B.62)-(B.68).

$$\frac{\partial q_6}{\partial q_1^*} = Z + \rho \frac{\partial Z}{\partial \rho} = Z \quad (\text{B.62})$$

$$\frac{\partial q_6}{\partial q_2^*} = u \frac{\partial \rho}{\partial Z} = 0 \quad (\text{B.63})$$

$$\frac{\partial q_6}{\partial q_3^*} = v \frac{\partial \rho}{\partial Z} = 0 \quad (\text{B.64})$$

$$\frac{\partial q_6}{\partial q_4^*} = w \frac{\partial \rho}{\partial Z} = 0 \quad (\text{B.65})$$

$$\frac{\partial q_6}{\partial q_5^*} = \rho \frac{\partial Z}{\partial P} + Z \frac{\partial \rho}{\partial P} = 0 \quad (\text{B.66})$$

$$\frac{\partial q_6}{\partial q_6^*} = \rho \quad (\text{B.67})$$

$$\frac{\partial q_6}{\partial q_7^*} = C \frac{\partial \rho}{\partial Z} + \rho \frac{\partial C}{\partial Z} = 0 \quad (\text{B.68})$$

The derivatives corresponding to  $\vec{q}(7)$  are shown below in Eqs. (B.69)-(B.75).

$$\frac{\partial q_7}{\partial q_1^*} = C + \rho \frac{\partial C}{\partial \rho} = C \quad (\text{B.69})$$

$$\frac{\partial q_7}{\partial q_2^*} = u \frac{\partial \rho}{\partial C} = 0 \quad (\text{B.70})$$

$$\frac{\partial q_7}{\partial q_3^*} = v \frac{\partial \rho}{\partial C} = 0 \quad (\text{B.71})$$

$$\frac{\partial q_7}{\partial q_4^*} = w \frac{\partial \rho}{\partial C} = 0 \quad (\text{B.72})$$

$$\frac{\partial q_7}{\partial q_5^*} = E \frac{\partial \rho}{\partial P} + \rho \frac{\partial E}{\partial P} = 0 \quad (\text{B.73})$$

$$\frac{\partial q_7}{\partial q_6^*} = C \frac{\partial \rho}{\partial Z} + \rho \frac{\partial C}{\partial Z} = 0 \quad (\text{B.74})$$

$$\frac{\partial q_7}{\partial q_7^*} = \rho \quad (\text{B.75})$$

Finally, assembling the results of Eqs. (B.27)-(B.75) results in the general form of matrix  $M$ , as shown below in Eq. (B.76), and inverting this matrix yields  $M^{-1}$ , as shown below in Eq. (B.77).

$$M = \begin{bmatrix} 1 & 0 & 0 & 0 \\ u & \rho & 0 & 0 \\ v & 0 & \rho & 0 \\ w & 0 & 0 & \rho & \dots \\ (E + \rho \frac{\partial e}{\partial \rho}) & \rho u & \rho v & \rho w \\ Z & 0 & 0 & 0 \\ C & 0 & 0 & 0 \\ 0 & 0 & 0 \\ 0 & 0 & 0 \\ 0 & 0 & 0 \\ \dots & 0 & 0 & 0 \\ \rho \frac{\partial e}{\partial P} & \rho \frac{\partial e}{\partial Z} & \rho \frac{\partial e}{\partial C} \\ 0 & \rho & 0 \\ 0 & 0 & \rho \end{bmatrix} \quad (\text{B.76})$$

$$M^{-1} = \begin{bmatrix} 1 & 0 & 0 & 0 \\ -\frac{u}{\rho} & \frac{1}{\rho} & 0 & 0 \\ -\frac{v}{\rho} & 0 & \frac{1}{\rho} & 0 \\ -\frac{w}{\rho} & 0 & 0 & \frac{1}{\rho} & \dots \\ \rho(u^2 + v^2 + w^2 - E - \rho \frac{e}{\rho} + Z \frac{\partial e}{\partial Z} + C \frac{\partial e}{\partial C}) & -\frac{u}{\rho \frac{\partial e}{\partial P}} & -\frac{v}{\rho \frac{\partial e}{\partial P}} & -\frac{w}{\rho \frac{\partial e}{\partial P}} \\ -\frac{Z}{\rho} & 0 & 0 & 0 \\ -\frac{C}{\rho} & 0 & 0 & 0 \\ 0 & 0 & 0 \\ 0 & 0 & 0 \\ 0 & 0 & 0 \\ \dots & 0 & 0 & 0 \\ \frac{1}{\rho \frac{\partial e}{\partial P}} & -\frac{\frac{\partial e}{\partial Z}}{\rho \frac{\partial e}{\partial P}} & -\frac{\frac{\partial e}{\partial C}}{\rho \frac{\partial e}{\partial P}} \\ 0 & \frac{1}{\rho} & 0 \\ 0 & 0 & \frac{1}{\rho} \end{bmatrix} \quad (\text{B.77})$$

We can recast these matrices in calculable quantities by first assuming that the thermofluid system represented by the state vector  $\vec{q}$  abides by the assumption of a mixture of a thermally perfect gases, from which it follows that

$$e = e(T, Y_\alpha) = \sum_{\alpha} e_{\alpha}(T) Y_{\alpha} \quad (\text{B.78})$$

and

$$de = C_v dT + \sum_{\alpha} e_{\alpha} dY_{\alpha} \quad (\text{B.79})$$

Further observing the equation of state for a mixture of thermally perfect gases

$$p = \rho T \sum_{\alpha} R_{\alpha} Y_{\alpha} \quad (\text{B.80})$$

one can differentiate to find

$$dT = \frac{1}{\rho R} \left( dP - \frac{P}{\rho} d\rho - \frac{P}{R} \sum_{\alpha} R_{\alpha} dY_{\alpha} \right) \quad (\text{B.81})$$

Substituting Eq. (B.81) into Eq. (B.79), one can write

$$de = \frac{C_v}{\rho R} \left( dP - \frac{P}{\rho} d\rho - \frac{P}{R} \sum_{\alpha} R_{\alpha} dY_{\alpha} \right) + \sum_{\alpha} e_{\alpha} dY_{\alpha} \quad (\text{B.82})$$

Since for a mixture of thermally perfect gases,

$$R = C_v (\gamma - 1) \quad (\text{B.83})$$

we then find

$$\frac{\partial e}{\partial \rho} = -\frac{P}{\rho^2 (\gamma - 1)} \quad (\text{B.84})$$

and

$$\frac{\partial e}{\partial P} = \frac{1}{\rho (\gamma - 1)} \quad (\text{B.85})$$

We can further use the definition of internal energy in Eq. (B.78) to formulate analytic expressions for the derivatives of  $e$  with respect to  $Z$  and  $C$ , according to

$$\frac{\partial e}{\partial Z} = \frac{\partial \sum_{\alpha} e_{\alpha} Y_{\alpha}}{\partial Z} = \sum_{\alpha} \frac{\partial e_{\alpha} Y_{\alpha}}{\partial Z} = \sum_{\alpha} \left( Y_{\alpha} \frac{\partial e_{\alpha}}{\partial Z} + e_{\alpha} \frac{\partial Y_{\alpha}}{\partial Z} \right) = \sum_{\alpha} e_{\alpha} \frac{\partial Y_{\alpha}}{\partial Z} \quad (\text{B.86})$$

for which  $e_{\alpha}$  may be found using the NASA polynomials (and noting that  $e_{\alpha} = h_{\alpha} - R_{\alpha} T$ ) with the local  $T$  and for which  $\frac{\partial Y_{\alpha}}{\partial Z}$  is a tabulated quantity from the flamelet solution manifold. Similarly for  $C$ ,

$$\frac{\partial e}{\partial C} = \sum_{\alpha} e_{\alpha} \frac{\partial Y_{\alpha}}{\partial C} \quad (\text{B.87})$$

where  $\frac{\partial Y_\alpha}{\partial C}$  may also be easily tabulated with the flamelet solution manifold.

Thus,  $M$  and  $M^{-1}$  take on the more discernible forms shown below in Eqs. (B.88) and (B.89).

$$M = \begin{bmatrix} 1 & 0 & 0 & 0 \\ u & \rho & 0 & 0 \\ v & 0 & \rho & 0 \\ w & 0 & 0 & \rho & \dots \\ (E - \frac{P}{\rho(\gamma-1)}) & \rho u & \rho v & \rho w \\ Z & 0 & 0 & 0 \\ C & 0 & 0 & 0 \\ \dots & 0 & 0 & 0 & 0 \\ \frac{1}{(\gamma-1)} & \rho \sum_\alpha e_\alpha \frac{\partial Y_\alpha}{\partial Z} & \rho \sum_\alpha e_\alpha \frac{\partial Y_\alpha}{\partial C} \\ 0 & \rho & 0 \\ 0 & 0 & \rho \end{bmatrix} \quad (\text{B.88})$$

$$M^{-1} = \begin{bmatrix} 1 & 0 \\ -\frac{u}{\rho} & \frac{1}{\rho} \\ -\frac{v}{\rho} & 0 \\ -\frac{w}{\rho} & 0 & \dots \\ \rho \left[ (V^2) - E + \frac{P}{\rho(\gamma-1)} + Z \left( \sum_\alpha e_\alpha \frac{\partial Y_\alpha}{\partial Z} \right) + C \left( \sum_\alpha e_\alpha \frac{\partial Y_\alpha}{\partial C} \right) \right] & -u(\gamma-1) \\ -\frac{Z}{\rho} & 0 \\ -\frac{C}{\rho} & 0 \\ \dots & 0 & 0 & 0 & 0 \\ 0 & 0 & 0 & 0 & 0 \\ \frac{1}{\rho} & 0 & 0 & 0 & 0 \\ 0 & \frac{1}{\rho} & 0 & 0 & 0 \\ -v(\gamma-1) & -w(\gamma-1) & (\gamma-1) & -(\gamma-1) \left( \sum_\alpha e_\alpha \frac{\partial Y_\alpha}{\partial Z} \right) & -(\gamma-1) \left( \sum_\alpha e_\alpha \frac{\partial Y_\alpha}{\partial C} \right) \\ 0 & 0 & 0 & \frac{1}{\rho} & 0 \\ 0 & 0 & 0 & 0 & \frac{1}{\rho} \end{bmatrix} \quad (\text{B.89})$$

These final forms of the transformation matrices may then be used to derive the eigenvector matrices required for implementation of FPV models in the VULCAN-CFD DAF subroutines, which is an ongoing research effort.

# Bibliography

- [1] McClinton, C.R., Rausch, V.L., Nguyen, L.T., and Sitz, J.R., “Preliminary X-43 Flight Test Results,” *Acta Astronautica*, **57**(2):266–276, 2005.
- [2] McClinton, C.R., “X-43 Scramjet Power Breaks the Hypersonic Barrier: Dryden Lectureship in Research for 2006,” in *44th AIAA Aerospace Sciences Meeting and Exhibit*, Reno, NV, 2006.
- [3] Hass, N.E., Smart, M.K., and Paull, A., “Flight Data Analysis of HyShot 2,” in *AIAA/CIRA 13th International Space Planes and Hypersonics Systems and Technologies*, Capua, Italy, 2005.
- [4] Smart, M.K., Hass, N.E., and Paull, A., “Flight Data Analysis of the HyShot 2 Scramjet Flight Experiment,” *AIAA J.*, **44**(2):2366–2375, 2006.
- [5] Dolvin, D., “Hypersonic International Flight Research and Experimentation (HIFiRE),” in *15th AIAA International Space Planes and Hypersonic Systems and Technologies Conference*, Reno, NV, 2008.
- [6] Jackson, K.R., Gruber, M.R., and Barhorst, T.F., “The HIFiRE Flight 2 Experiment: An Overview and Status Update,” in *45th AIAA/ASME/SAE/ASEE Joint Propulsion Conference and Exhibit*, Denver, CO, 2009.
- [7] Montgomery, C.J., Zhao, W., Tam, C., Eklund, D.R., and Chen, J.Y., “CFD Simulations of a 3-D Scramjet Flameholder using Reduced Chemical Kinetic Mechanisms,” *AIAA/ASME/SAE/ASEE Joint Propulsion Conference & Exhibit*, 2004.
- [8] Fureby, C., Chapius, M., Fedina, E., and Karl, S., “CFD Analysis of the HyShot II Scramjet Combustor,” *Proc. Combust. Inst.*, **33**(2):2399–2405, 2011.
- [9] Edwards, J.R., Potturi, A., and Fulton, J.A., “Large-Eddy/Reynolds-Averaged Navier-Stokes Simulations of Scramjet Combustor Flowfields,” *AIAA/ASME/SAE/ASEE Joint Propulsion Conference & Exhibit*, 2012.

- [10] Fulton, J.A., Edwards, J.R., Goyne, C.P., McDaniel, J.C., and Rockwell, R.D., “Numerical Simulation of Flow in a Dual-Mode Scramjet Combustor,” in *41st AIAA Fluid Dynamics Conference and Exhibit*, Honolulu, HI, 2011.
- [11] Baurle, R.A. and Eklund, D.R., “Analysis of Dual-Mode Hydrocarbon Scramjet Operation at Mach 4-6.5,” *J. Propul. Power.*, **18**(5), 2002.
- [12] Gokulakrishnan, P., Pal, S., Klassen, M.S., Hamer, A.J., Roby, R.J., Kozaka, O., and Menon, S., “Supersonic Combustion Simulation of Cavity-Stabilized Hydrocarbon Flames using Ethylene Reduced Kinetic Mechanism,” *AIAA/ASME/SAE/ASEE Joint Propulsion Conference & Exhibit*, 2006.
- [13] Ramesh, K., R., E.J., Chelliah, H.K., Goyne, C.P., McDaniel, J.C., Rockwell, R., Kirk, J., Cutler, A., and Danehy, P., “Large Eddy Simulation of High-Speed, Premixed Ethylene Combustion,” *AIAA SciTech Conference*, 2015.
- [14] Magnussen, B.F. and Hjertager, B.W., “On the Structure of Turbulence and a Generalized Eddy Dissipation Concept for Chemical Reaction in Turbulent Flow,” in *19th AIAA Aerospace Science Meeting*, AIAA, St. Louis, MO, 1981.
- [15] Cook, A.W. and Riley, J.J., “Subgrid-Scale Modeling for Turbulent Reacting Flows,” *Combust. Flame*, **112**(4):593–606, 1998.
- [16] Storch, A., Bynum, M., Liu, J., and Gruber, M., “Combustor Operability and Performance Verification for HIFiRE Flight 2,” in *17th AIAA International Space Planes and Hypersonic Systems and Technologies Conference*, San Francisco, CA, 2011.
- [17] Hitch, B.D. and Lynch, E.D., “Use of Reduced, Accurate Ethylene Combustion Mechanisms for a Hydrocarbon-Fueled Ramjet Simulation,” in *45th AIAA Joint Propulsion Conference & Exhibit*, Denver, CO, 2009.
- [18] Wan, T., Chen, L., Wang, J., Fan, X., and Chang, X., “Computational Study of Supersonic Combustion Using Three Kerosene Reaction Mechanism Models,” in *Proceedings of the 13th Asian Congress of Fluid Mechanics*, Dhaka, Bangladesh, 2010.
- [19] Bermejo-Moreno, I., L.J.B.J. and Vicquelin, R., “Wall-Modeled Large-Eddy Simulations of the HIFiRE-2 Scramjet,” in *Annual Research Briefs*, Center for Turbulence Research, Stanford University, Stanford, CA, 2013.
- [20] Saghafian, A., Terrapon, V.E., and Pitsch, H., “An Efficient Flamelet-Based Combustion Model for Compressible Flows,” *Combust. Flame*, **162**, 2014.

- [21] Terrapon, V.E., Pecnik, R., Ham, F., and Pitsch, H., “Full-System RANS of the HyShot II Scramjet Part 2: Reactive Cases,” in *Annual Research Briefs*, Center for Turbulence Research, Stanford University, Stanford, CA, 2010.
- [22] Saghafian, A., Terrapon, V., Ham, F., and Pitsch, H., “An Efficient Flamelet-based Combustion Model for Supersonic Flows,” in *AIAA International Space Planes and Hypersonic Systems and Technologies Conference, 17th*, AIAA, San Francisco, CA, 2011.
- [23] Pecnik, R., Terrapon, V., Ham, F., Iaccarino, G., and Pitsch, H., “Reynolds-Averaged Navier-Stokes Simulations of the HyShot II Scramjet,” *AIAA J.*, **50**:1717–1732, 2012.
- [24] Saghafian, A., Shunn, L., Philips, D.A., and Ham, F., “Large Eddy Simulations of the HIFiRE Scramjet Using a Compressible Flamelet/Progress Variable Approach,” in *Proc. Combust. Inst.*, **35**, 2015.
- [25] “Viscous Upwind ALgorithm for Complex Flow ANalysis (VULCAN),” <http://vulcan-cfd.larc.nasa.gov>, 2014.
- [26] Pierce, C.D., *Progress-Variable Approach for Large Eddy Simulation of Turbulent Combustion*, Ph.D. thesis, Stanford University, 2001.
- [27] Peters, N., “Laminar Diffusion Flamelet Models in Non-Premixed Turbulent Combustion,” *Prog. Energy Combust. Sci.*, **10**(3):319–339, 1984.
- [28] Peters, N., “Laminar Flamelet Concepts in Turbulent Combustion,” *Proc. Combust. Inst.*, **21**:1231–1250, 1986.
- [29] Pierce, C. and Moin, P., “Progress-Variable Approach for Large-Eddy Simulation of Non-Premixed Turbulent Combustion,” *J. Fluid Mech.*, **504**:73–97, 2004.
- [30] Guy, R.W., Rogers, R.C., Puster, R.L., Rock, K.E., and Diskin, G.S., “The NASA Langley Scramjet Test Complex,” in *32nd ASME, SAE, and ASEE, Joint Propulsion Conference and Exhibit*, Lake Buena Vista, FL, 1996.
- [31] Roffe, G., Bakos, R., Erdos, J., and Swartwout, W., “The Propulsion Test Complex at GASL,” in *XIII International Symposium on Air Breathing Engines*, 1997.
- [32] Foelsche, R.O., Beckel, S.A., Betti, A.A., Wurst, G.T., Charletta, R.A., and Bakos, R.J., “Flight Results From a Program to Develop a Free-Flight Atmospheric Scramjet Test Technique,” in *14th AIAA/AHI Space Planes and Hypersonic Systems and Technologies Conference*, 2006.

- [33] Hank, J.M., Murphy, J.S., and Mutzman, R.C., "The X-51A Scramjet Engine Flight Demonstration Program," in *15th AIAA International Space Planes and Hypersonic Systems and Technologies Conference*, Dayton, OH, 2008.
- [34] Ferlemann, P.G., "Forebody and Inlet Design for the HIFiRE 2 Flight Test," in *JANNAF Airbreathing Propulsion Subcommittee Meeting*, Boston, MASS, 2008.
- [35] Cuda, V. and Hass, N.E., "Heat Flux and Wall Temperature Estimates for the NASA Langley HIFiRE Direct Connect Rig," in *JANNAF 43rd CS/31st APS/25th PSHS Joint Subcommittee Meeting*, La Jolla, CA, 2009.
- [36] McDaniel, J.C., Chelliah, H.K., Goyne, C.P., Edwards, J.R., Givi, P., and Cutler, A.D., "US National Center for Hypersonic Combined Cycle Propulsion: an overview," in *16th AIAA/DLR/DGLR International Space Planes and Hypersonic Systems and Technologies Conference*, 2009.
- [37] McBride, B.J., Gordon, S., and Reno, M.A., "Coefficients for Calculating Thermodynamic and Transport Properties of Individual Species," NASA Technical Memorandum 4513, NASA, Cleveland, OH, 1993.
- [38] Kuo, K.K., *Principles of Combustion*, John Wiley, Hoboken, N.J., 2nd ed., 2005.
- [39] Poinso, T. and Veynante, D., *Theoretical and Numerical Combustion*, R.T. Edwards, Inc., Philadelphia, PA, 2nd ed., 2005.
- [40] Sutherland, W., "The Viscosity of Gases and Molecular Force," *Philosophical Magazine*, **5**, 1893.
- [41] Dorrance, W.H., *Viscous Hypersonic Flow*, McGraw Hill, 1962.
- [42] Baurle, R.A., "Modeling of High Speed Reacting Flows: Established Practices and Future Challenges," in *42nd AIAA Aerospace Sciences Meeting and Exhibit*, AIAA-2004-267, AIAA, Reno, NV, 2004.
- [43] Menter, F.R., "Two-Equation Eddy-Viscosity Turbulence Models for Engineering Applications," *AIAA J.*, **32**(8):1598–1605, 1994.
- [44] van Oijen, J.A., *Flamelet-Generated Manifolds: Development and Application to Premixed Laminar Flames*, Ph.D. thesis, Eindhoven Technical University, Eindhoven, Netherlands, 2002.
- [45] Bilger, R.W., Starner, S.H., and Kee, R.J., "On Reduced Mechanisms for Methane-Air Combustion in Nonpremixed Flames," *Combust. Flame*, **80**:135–149, 1990.

- [46] Kim, J.S. and Williams, F.A., “Structures of Flow and Mixture-Fraction Fields for Counterflow Diffusion Flames with Small Stoichiometric Mixture Fractions,” *SIAM J. Appl. Math.*, (53), 1993.
- [47] van Oijen, J. and de Goey, L., “Modeling of Complex Premixed Burner Systems by Using Flamelet-Generated Manifolds,” *Combust. Theor. Model.*, **6**:463–478, 2002.
- [48] Nguyen, P.D., Vervisch, L., Subramanian, V., and Domingo, P., “Multidimensional Flamelet-Generated Manifolds for Partially Premixed Combustion,” *Combust. Flame*, **157**(1):43–61, 2010.
- [49] Sadasivuni, S. K., M.W. and Ibrahim, S.S., “Validation of Unsteady Flamelet/Progress Variable Methodology for Nonpremixed Turbulent Partially Premixed Flames,” in *Proc. of the European Comb. Meeting*, 2009.
- [50] de Swart, J., Bastiaans, R., van Oijen, J., de Goey, L., and Cant, R., “Inclusion of Preferential Diffusion in Simulations of Premixed Combustion of Hydrogen/Methane Mixtures with Flamelet Generated Manifolds,” *Flow Turbul. Combust.*, **85**:473–511, 2010. 10.1007/s10494-010-9279-y.
- [51] Michel, J.B., Colin, O., and Veynante, D., “Modeling Ignition and Chemical Structure of Partially Premixed Turbulent Flames using Tabulated Chemistry,” *Combust. Flame*, **152**(1-2):80 – 99, 2008.
- [52] Michel, J.B., Colin, O., Angelberger, C., and Veynante, D., “Using the Tabulated Diffusion Flamelet Model ADF-PCM to Simulate a Lifted Methane-Air Jet Flame,” *Combust. Flame*, **156**(7):1318 – 1331, 2009.
- [53] Knudsen, E. and Pitsch, H., “A General Flamelet Transformation Useful for Distinguishing Between Premixed and Non-Premixed Modes of Combustion,” *Combust. Flame*, **156**(3):678 – 696, 2009.
- [54] Pitsch, H. and Ihme, M., “An Unsteady/Flamelet Progress Variable Method for LES of Nonpremixed Turbulent Combustion,” in *AIAA Aerospace Sciences Meeting and Exhibit*, Reno, NV, 2005.
- [55] Terrapon, V.E., Ham, F., Pecnik, R., and Pitsch, H., “A Flamelet-Based Model for Supersonic Combustion,” in *Annual Research Briefs*, Center for Turbulence Research, Stanford University, Stanford, CA, 2009.
- [56] Oevermann, M., “Numerical Investigation of Turbulent Hydrogen Combustion in a SCRAMJET using Flamelet Modeling,” *Aerosp. Sci. Technol.*, **4**(7):463–480, 2000.

- [57] Bekdemir, C., Somers, L.M.T., and de Goey, L.P.H., “Modeling Diesel Engine Combustion Using Pressure Dependent Flamelet Generated Manifolds,” *Proc. Combust. Inst.*, **33**(2):2887–2894, 2011.
- [58] Cabell, K., Hass, N.E., Storch, A., and Gruber, M., “HIFiRE Direct-Connect Rig (HDCR) Phase I Scramjet Test Results from the NASA Langley Arc-Heated Scramjet Test Facility,” in *17th AIAA International Space Planes and Hypersonic Systems and Technologies Conference*, San Francisco, CA, 2011.
- [59] Wilcox, D.C., “Wall Matching, a Rational Alternative to Wall Functions,” in *27th Aerospace Sciences Meeting*, Reno, NV, 1989.
- [60] Edwards, J.R., “A Low-Diffusion Flux-Splitting Scheme for Navier-Stokes Calculations,” *Comput. Fluids.*, **26**(6):635–659, 1997.
- [61] Pulliam, T.H. and Chaussee, D.S., “A Diagonal Form of an Implicit Approximate-Factorization Algorithm,” *J. Comput. Phys.*, **39**(2):347–363, 1981.
- [62] Luo, Z., Yoo, C.S., Richardson, E.S., Chen, J.H., Law, C.K., and Lu, T.F., “Chemical Explosive Mode Analysis for a Turbulent Lifted Ethylene Jet Flame in Highly-Heated Coflow,” *Combust. Flame*, **159**(1):265–274, 2012.
- [63] Borghi, R., “On the Structure of Turbulent Premixed Flames,” *Recent Advances in Aeronautical Science*, pp. 117–138, 1984.
- [64] Lacaze, G., Richardson, E., and Poinso, T., “Large Eddy Simulation of Spark Ignition in a Turbulent Methane Jet,” *Combust. Flame*, **156**:1993–2009, 2009.
- [65] Yamashita, H., Shimada, M., and Takeno, T., “A Numerical Study on Flame Stability at the Transition Point of Jet Diffusion Flames,” *Proc. Combust. Inst.*, **26**:27–34, 1996.
- [66] Savard, B. and Blanquart, G., “An A Priori Model for the Effective Species Lewis Numbers in Premixed Turbulent Flames,” *Combust. Flame*, **161**(6):1547–1557, 2014.
- [67] Bekdemir, C., Somers, L., and de Goey, L., “Modeling Diesel Engine Combustion using Pressure Dependent Flamelet Generated Manifolds,” *Proc. Combust. Inst.*, **33**(2):2887 – 2894, 2011.
- [68] Larsson, J., Vicquelin, R., and Bermejo-Moreno, I., “Large Eddy Simulations of the HyShot II Scramjet,” in *Annual Research Briefs*, Center for Turbulence Research, Stanford University, Stanford, CA, 2011.

- [69] Sozer, E., Hassan, E., Yun, S., Thakur, S., Wright, J., Ihme, M., and Shyy, W., “Turbulence-Chemistry Interaction and Heat Transfer Modeling of H<sub>2</sub>/O<sub>2</sub> Gaseous Injector Flows,” in *48th AIAA Aerospace Sciences Meeting and Exhibit*, Orlando, FL, 2010.
- [70] Lee, D.J., Ihme, M., Thakur, S., and Shyy, W., “LES of a Gaseous H<sub>2</sub>/O<sub>2</sub> Rocket Injector: Wall Heat Transfer Modeling,” in *13th International Conference on Numerical Combustion*, Corfu, Greece, 2011.
- [71] Wu, H. and Ihme, M., “Modeling of Unsteady Heat Transfer in Flame-Wall Interaction,” in *66th Division of Fluid Dynamics Meeting of the American Physical Society*, Pittsburgh, PA, 2013.
- [72] Barths, H., Hasse, C., Bikas, G., and Peters, N., “Simulation of Combustion in Direct Injection Diesel Engines Using an Eulerian Particle Flamelet Model,” *Proc. Combust. Inst.*, **28**(1):1161–1167, 2000.
- [73] Felsch, C., Gauding, M., Hasse, C., Vogel, S., and Peters, N., “An Extended Flamelet Model for Multiple Injections in DI Diesel Engines,” *Proc. Combust. Inst.*, **32**(1):2775–2783, 2009.
- [74] Quinlan, J.R., McDaniel, J.C., Drozda, T.G., Lacaze, G., and Oefelein, J., “A Priori Analysis of Flamelet-Based Modeling for a Dual-Mode Scramjet Combustor,” in *50th AIAA Joint Propulsion Conference*, AIAA, Cleveland, OH, 2014.
- [75] Pitsch, H., “FlameMaster: A C++ Computer Program for 0D Combustion and 1D Laminar Flame Calculations,” <http://www.stanford.edu/hpitsch/>, 1998.
- [76] “NASA Advanced Supercomputing (NAS) Division,” <http://www.nas.nasa.gov/>, 2015.
- [77] Ihme, M., Shunn, L., and Zhang, J., “Regularization of Reaction Progress Variable for Application to Flamelet-Based Combustion Models,” *J. Comput. Phys.*, **231**:7715–7721, 2012.
- [78] Niu, Y., Vervisch, L., and Tao, P., “An Optimization-Based Approach to Detailed Chemistry Tabulation: Automated Progress Variable Definition,” *Combust. Flame*, **160**(1):776–785, 2013.
- [79] Fiorina, B., Baron, R., Gicquel, O., Thevenin, D., Carpentier, S., and Darabiha, N., “Modelling Non-Adiabatic Partially Premixed Flames Using Flame-Prolongation of ILDM,” *Combust. Theor. Model.*, **7**:449–470, 2003.

- [80] Fiorina, B., Gicquel, O., Vervisch, L., Carpentier, S., and Darabiha, N., “Approximating the Chemical Structure of Partially Premixed and Diffusion Counterflow Flames Using FPI Flamelet Tabulation,” *Combust. Flame*, **140**:147–160, 2005.
- [81] Fiorina, B., Gicquel, O., Vervisch, L., Carpentier, S., and Darabiha, N., “Premixed Turbulent Combustion Modeling Using Tabulated Detailed Chemistry and PDF,” *Proc. Combust. Inst.*, **30**:867–874, 2005.
- [82] Baburic, M., *Numerically Efficient Modelling of Turbulent Non-Premixed Flames*, Ph.D. thesis, University of Zagreb, 2005.
- [83] Perkovic, L., Baburic, M., Priesching, P., and Duic, N., “CFD Simulation of Methane Jet Burner,” in *Proc. of the European Comb. Meeting*, 2009.
- [84] Ihme, M. and Pitsch, H., “Prediction of Extinction and Reignition in Non-Premixed Turbulent Flames Using a Flamelet/Progress Variable Model. 1. A Priori Study and Presumed PDF Closure,” *Combust. Flame*, **155**:70–89, 2008.
- [85] Ihme, M. and Pitsch, H., “Prediction of Extinction and Reignition in Non-Premixed Turbulent Flames Using a Flamelet/Progress Variable Model. 2. A Posteriori Study with Application to Sandia Flames D and E,” *Combust. Flame*, **155**:90–107, 2008.
- [86] Hergart, C., Barths, H., and Peters, N., “Using Representative Interactive Flamelets in Three-Dimensional Modelling of the Diesel Combustion Process including Effects of Heat Transfer,” in *Proceedings of the Multidimensional Engine Modeling User’s Group Meeting*, 2000.
- [87] Wu, H. and Ihme, M., “Modeling of Unsteady Heat Transfer in Flame-Wall Interaction,” in *66th Division of Fluid Dynamics Meeting of the American Physical Society*, Pittsburgh, PA, 2013.
- [88] Hass, N., Cabell, K., and Storch, A., “HIFiRE Direct-Connect Rig (HDCR) Phase I Ground Test Results from the NASA Langley Arc-Heated Scramjet Test Facility,” in *JANNAF*, 2010.
- [89] Drozda, T.G., Quinlan, J.R., Piscuineri, P.H., and Yilmax, S.L., “Progress Toward Affordable High Fidelity Combustion Simulations for High-Speed Flows in Complex Geometries,” *48th AIAA/ASME/SAE/ASEE Joint Propulsion Conference & Exhibit*, 2012.
- [90] Quinlan, J., McDaniel, J.C., Drozda, T., Lacaze, G., and Oefelein, J.C., “A Priori Analysis of Flamelet-Based Modeling for a Dual-Mode Scramjet Combustor,”

- in *66th Division of Fluid Dynamics Meeting of the American Physical Society*, Pittsburgh, PA, 2013.
- [91] Quinlan, J.R., Drozda, T.G., McDaniel, J.C., Lacaze, G., and Oefelein, J., “A Priori Analysis of a Compressible Flamelet Model using RANS Data for a Dual-Mode Scramjet Combustor,” *22nd AIAA Computational Fluid Dynamics Conference*, 2015.
- [92] Quinlan, J.R. and McDaniel, J.C., “Toward Large-Eddy/Reynolds-Averaged Simulation of Supersonic Combustion,” *Virginia Space Grant Consortium Student Research Conference*, 2013.
- [93] White, J.A., Baurle, R.A., Fisher, T.C., Quinlan, J.R., and Black, W.S., “Low-Dissipation Advection Schemes Designed for Large-Eddy Simulations of Hypersonic Propulsion Systems,” *48th AIAA/ASME/SAE/ASEE Joint Propulsion Conference & Exhibit*, 2012.
- [94] Quinlan, J.R., McDaniel, J.C., and Baurle, R.A., “Hybrid Large-Eddy/Reynolds-Averaged Simulation of a Supersonic Cavity using VULCAN,” in *IEEE Aerospace Conference*, Big Sky, MT, 2013.
- [95] Quinlan, J.R. and Baurle, R.A., “Simulation of a Wall-Bounded Flow using a Hybrid RANS/LES Approach with Turbulence Recycling,” in *AIAA Fluid Dynamics Conference*, New Orleans, LA, 2012.
- [96] Quinlan, J.R. and McDaniel, J.C., “Case Study of a Hybrid LES/RAS Approach Utilizing Turbulence Recycling,” *Virginia Space Grant Consortium Student Research Conference*, 2012.
- [97] Pope, S.B., “PDF Methods for Turbulent Reactive Flows,” *Prog. Energy Combust. Sci.*, **11**:119–192, 1985.
- [98] Baurle, R.A., *Modeling of Turbulent Reacting Flows with Probability Density Functions for SCRAMJET Applications*, Ph.D. thesis, North Carolina State University, Raleigh, 1995.
- [99] Pope, S.B., “Turbulence Combustion Modeling: Fluctuations and Chemistry,” in G.D. Roy, S.M. Frolov, and P. Givi, eds., *Advanced Computation & Analysis of Combustion*, pp. 310–320, ENAS Publishers, Moscow, Russia, 1997.
- [100] Drozda, T.G., *Implementation of LES/SFMD for Prediction of Non-Premixed Turbulent Flames*, Ph.D. thesis, University of Pittsburgh, Pittsburgh, PA, 2005.

- 
- [101] Oefelein, J.C., Drozda, T.G., and Sankaran, V., “Large Eddy Simulation of Turbulence-Chemistry Interactions in Reacting Flows,” *J. Phys. Conf. Ser.*, **46**:16–27, 2006.
- [102] James, S., Zhu, J., and Anand, M.S., “Large Eddy Simulations of Turbulent Flames using the Filtered Density Function Model,” *Proc. Combust. Inst.*, **31**(2):1737–1745, 2007.
- [103] Borghi, R., Argueyrolles, B., Gauffe, S., and Souhaite, P., “Application of a Presumed PDF Model of Turbulent Combustion to Reciprocating Engines,” in *Proceedings of 21st Symp. (Int.) on Combustion*, pp. 1591–1599, The Combustion Institute, Pittsburgh, PA, 1986.